Low-Platinum and Platinum-Free Electrocatalysts for Energy Applications

Thesis Submitted to AcSIR for the Award of the Degree of

DOCTOR OF PHILOSOPHY
In Chemical Sciences

By
Mr. Vishal M. Dhavale
Registration Number: 10CC12A26006

Under the Guidance of
Dr. Sreekumar Kurungot

CSIR-National Chemical Laboratory,
Pune - 411 008, India.

February 2015

सीएसआयआर–राष्ट्रीय रासायनिक प्रयोगशाला
(वैज्ञानिक तथा औद्योगिक अनुसंधान परिषद)
डॉ. होमी भाभा मार्ग, पुणे – 411 008. भारत
CSIR-NATIONAL CHEMICAL LABORATORY
(Council of Scientific & Industrial Research)
Dr. Homi Bhabha Road, Pune - 411008. India

CERTIFICATE

This is to certify that the work incorporated in the thesis entitled, "**LOW-PLATINUM AND PLATINUM-FREE ELECTROCATALYSTS FOR ENERGY APPLICATIONS**" submitted by **Mr. Vishal M. Dhavale**, has carried out by him under my supervision at the Physical and Materials Chemistry Division, CSIR-National Chemical Laboratory, Pune–411 008, India. All the materials from other sources have been duly acknowledged in the thesis.

Date: February 16th, 2015

Place: Pune, India.

Dr. Sreekumar Kurungot

(Research Guide)

Communication Channels
NCL Level DID : 2590
NCL Board No. : +91-20-25902000
EPABX : +91-20-25893300
FAX
Director's Office : +91-20-25902601
COA's Office : +91-20-25902660
COS&P's Office : +91-20-25902664
WEBSITE
www.ncl-india.org

DECLARATION

I, hereby declare that all the experiments in this thesis entitled, "**LOW-PLATINUM AND PLATINUM-FREE ELECTROCATALYSTS FOR ENERGY APPLICATIONS**" submitted for the degree of Doctor of Philosophy in Chemical Sciences, to the AcSIR-National Chemical Laboratory have been carried out by me at the Physical and Materials Chemistry Division, CSIR-National Chemical Laboratory, Pune-411 008, India, under the supervision of Dr. Sreekumar Kurungot. The work is original and has not been submitted in part or full by me, for any degree or diploma to this or to any other University.

Date: February 16th, 2015 Mr. Vishal M. Dhavale

Physical and Materials Chemistry Division,

CSIR-National Chemical Laboratory,

Pune-411 008, India.

Dedicated to

My Late Grandmother….

Acknowledgements

This is conceivably the most thorny thing I intend to do, i.e., to sincerely thank and express my heartfelt appreciation to everybody who has, in one way or the other, contributed in the successful completion of my degree of Doctor of Philosophy. I wouldn't be doing justice by simply naming everybody who helped me but at the same time it will be too difficult for me to express my heartfelt thanks in the form of words, I will nonetheless try to make a genuine effort …

Firstly, my heartfelt gratitude to Dr. K. Sreekumar, my research guide, for his guidance, fruitful discussions, trenchant critiques, valuable instruction, constant support and encouragement throughout the course of this work. I must also mention that he is also a very good teacher & a wonderful research guide with vast knowledge and insight, which are often quite rare. His constant effort to implant us with several, most essential habits, like weekly seminars & group meetings, monthly reports & daily planning, makes me confident to start an independent scientific career. He has also trained us to write manuscripts independently. I must also mention that he has shown so much of patience while correcting my thesis and official documents. He is also instrumental in teaching us to effectively communicate with people, to give a better presentation, to efficiently handle multitasking simultaneously and so on. My sincere regards and reverence are for him, forever.

I am grateful to Dr. Sourav Pal, Director, CSIR-NCL, who gave me an opportunity to work in this prestigious research institute and also to CSIR for financial support. I wish to thank Dr. Anil Kumar, Chairman of Physical Chemistry Division for allowing me to use all the available facilities in the division.

I would like to offer my sincere thanks to Dr. K. Vijayamohanan for his help, support and advice during the initial stage of this study. I also extend my admiration to DAC members Dr. C. V. Rode, Dr. K. Krishnamoorthy, and Dr. J. Nithyanadhan for their valuable suggestions, advice and fruitful discussions during the DAC meetings.

I extend my gratitude to Dr. Ashish Lele, Dr. Neelima Bulakh, Dr. U. K. Kharul, and Dr. Anurag for their timely help.

I am highly indebted to Mr. Gholap, Mr. A. B. Gaikwad, and Dr. K. R. Patil, who were helpful for characterizing various samples.

I extend my gratitude to Mr. Dipak, Mr. Punekar, Mr. Akbar and other office staffs for their timely help.

My sincere thanks to the library staff, members of Glassblowing, Sores and Purchase and Workshop sections. I would also like to thank the members of SAO and Security for their help during my stay in CSIR-NCL.

I am forever indebted to all my former teachers from School of Chemical Sciences (Solapur University), Dayanand College, Shivaji University, Walchand College of Arts and Science, Digambar Jain Gurukul High School, and SVCS School, as they built the foundation for this achievement.

My sincere thanks to, Dr. Rahul Banerjee, Dr. R. Nandini Devi, Dr. S. K. Asha, Dr. Arun Venkatnathan (IISER, Pune), Dr. R. Vaidhyanathan (IISER, Pune), and Dr. Daya Shankar Pandey (BHU,

Varanasi) for effective collaboration. My sincere thanks to their students Dr. Pradip, Leena, Chinmay, Mrigendra, Anurag (IISER, Pune), Shalini (IISER, Pune), and Shama (IISER, Pune) for the kind helps.

My special gratitude to my seniors, Dr. R. Kannan, Dr. Beena Balan, Dr. Baskar Sathe, Dr. Dhanraj Shinde, Mr. Joyashish, Dr. T. Palaniselvam, Dr. Vrushali, Mr. Sreekuttan, and Mr. Vinayak for their mentoring & care during my initial days in CSIR-NCL.

I owe deeply to my ever-trustful friends in the lab, Bihag, Harshitha, Pandiaraj, Santosh, Pritish, Kashyap, Roby Soni, Sidheshwar, Rejith, Sachin, Ruhi, Ajinkya, Nishant, Smita, Sharath, Maya, Pranav, Ayesha, Vidyanand, Hari, Aniket, Harshal, and Anita for all their affection, help and support. I must thank again Sreekuttan especially, for the constant support and help he has provided.

I would also like to thank my CSIR-NCL-colleagues Husain, Bipin, Abizar, Ranjith and Manjoor.

Also, my heartfelt thanks to the MSc. Project student Manju for her love, help and support. My sincere thanks to my colleagues of Physical Chemistry Division, Nahesh sir, Arpan, Sachin T, Amit, Pradip, Tamas, Chandan, Arijith, Tanay, Dr. Digamber, Mrs. Jayashree, Bikas, Suman, Appa, Nagesh, Shekhar, Swapnil, Dr. Datta, Dr. Omkar, Rohan, Ronak, Deepti, Vishal, Satish, Dr. Shruti, Reshma, Abik, Yogesh, Raja P, Anil, Dhanya, Chaytu, Kali, Sandy, Harami, Bhendi, Rup, Rajashree, Satej, Manik, Arul, Neeta, Bhanu, and Dhanlaxmi for providing me an excellent working ambience during the course of this work.

My special thanks to the old roommates-cum-friends Chandu, Sandip Master, Umesh, Bandu and Sumit. I also extend my gratitude to all my friends of Mi-marathi group of CSIR-NCL for their help.

I find no words to express my feelings for my Aai-Dada. Their love, support, blessings have always been my strength. Their patience and sacrifice will remain my inspiration throughout my life. I also express my heartfelt gratitude to my Uncles; Laximan and Ram, Aunties; Shardha and Meena; Brothers and Sisters; Gampa, Sagar, Datta, Govind, Nagu, Nitin, Jyoti, and Pama; and Vaini: Pooja and Varsha, whose moral support, love and constant encouragement are instrumental to achieve this feet of goal. The presence of the little angels 'Piyush', 'Gudu', 'Sanu', 'Arush', 'Advita', and "Advika" is always refreshing, making me feel relaxed, comfortable and which provides me energy to work. Finally, a very special appreciation is due to my life partner 'Bhagyashree (Swarali)' not only for her constant encouragement but also for her patience & understanding throughout.

Above all, I thank God; the almighty for guiding me in my life.

Though, many have not been mentioned, none is forgotten.

Vishal Mahesh Dhavale

List of Abbreviations

Abbreviations	Expansions
AFC	Alkaline Fuel Cells
AA	Ascorbic Acid
AEMFCs	Anion Exchange Membrane Fuel Cells
BSE	Back-Scattered Electron
CNFs	Carbon Nanofibers
CNTs	Carbon Nanotubes
CA	Chronoamperometry
CE	Counter Electrode
CV	Cyclic Voltammetry
DOE	Department of Energy
DMFCs	Direct Methanol Fuel Cells
EDAX	Energy Dispersive X-ray Analysis
F-C	Functionalized Vulcan Carbon XC-72
Gr	Graphene
GO	Graphene Oxide
GC	Gas Chromatography
HR-TEM	High Resolution Transmission Electron Microscopy
ICEs	Internal Combustion Engines
K-L equation	Koutecky-Levich equation
LSV	Linear Sweep Voltammetry
MEA	Membrane Electrode Assembly

MCFCs	Molten Carbonate Fuel Cells
NGr	Nitrogen-doped Graphene
ORR	Oxygen Reduction Reaction
PFSA	Perflouro Sulfonic Acid
PAFC	Phosphoric Acid Fuel Cells
PBI	Polybenzimidazole
PEMFCs	Polymer Electrolyte Membrane Fuel Cells
RGO	Reduced Graphene Oxide
RE	Reference Electrode
RDE	Rotating Disk Electrode
RRDE	Rotating Ring Disk Electrode
SEM	Scanning Electron Microscopy
SOFC	Solid Oxide Fuel Cells
slpm	Standard Liter Per Minute
SE	Secondary Electron
SMcA	Surface-Modification-cum-Anchoring
TEM	Transmission Electron Microscopy
WE	Working Electrode
W/O	Water-in-Oil
XRD	X-ray Diffraction
XPS	X-ray Photoelectron Spectroscopy
Z	Atomic Number
1D	One Dimensional

2D	Two Dimensional
3D	Three Dimensional

Table of Contents

Chapter 2

Chapter 3

Chapter 4

Chapter 5

Chapter 6

Chapter 7

Abstract

The commercialization potential of energy conversion and storage devices like fuel cells and metal-air batteries is mainly held back due to the use of costly platinum (Pt) and its sluggish oxygen reduction reaction (ORR) activity. Therefore, combination of noble metal Pt with non-noble metals like Cu, Fe, Ni, etc. makes the system more efficient than the Pt alone. Specifically, the strategy of combing a lower concentration of Pt with a higher concentration of non-noble metals (Cu, Fe, Ni, etc.) by maintaining a core-shell structure has been gained substantial attention. Moreover, to improve the activity, 3-D, nanocages, rods, cubes, sheets of Pt and combination with other 3d metals have been reported to be better than the state-of-the-art Pt/C. However, dispersion of such engineered structures on a support substrate is a challenging task.

In line with these recent advancements, I focused on the synthesis of low-Pt and Pt-free engineered structures by using simple and easily scalable techniques for ORR and counter reaction of metal-air battery, *i.e.,* oxygen evolution reaction. The electrocatalysts illustrated in the thesis are originated through a focused effort made to narrow down the aforementioned existing gaps by logically selecting the reducing agents, metal precursors and reaction parameters while performing the synthesis. Overall, the thesis is divided into seven chapters. The contents of the chapters are briefly highlighted below:

Chapter 1 gives a discussion on the energy devices such as fuel cells and metal-air batteries. The principles of different type of fuel cells and a concise literature review on the designing of Pt-based and Pt-free electrocatalysts and carbon support materials are included in this chapter. Subsequently, potential advantages and disadvantages of each material are described categorywise. In conjunction, the significance of metal-air battery and requirements on the modification of the cathode electrode are also discussed in the chapter. Finally, the clear objectives of the present work are listed at the end of the chapter.

In **Chapter 2**, a discussion on the different procedures adopted for the synthesis of low-platinum (low-Pt) and platinum-free (Pt-free) structures, namely, Cu@Pt and Fe_2O_3@Pt core-shell structures supported on Vulcan carbon (C) by using ascorbic acid (AA) reduction method, Au@Gr and Au@NGr core-shell structures by using water-in-oil (W/O) emulsion method, CuPt nanocage (CuPt-NC) structures by galvanic displacement technique and Ni-NGr nanocage

structures by similar W/O emulsion method is given. Additionally, the working principles of different spectroscopic and diffraction techniques used for the investigation of the structural properties of the synthesized electrocatalysts are explained. A discussion on the working principles of various electrochemical techniques which are used for the structural and activity characterization is also included in this chapter.

Chapter 3 deals with a detailed illustration on the *in situ* modification of the carbon support surface and subsequent anchoring of core-shell structures (Cu@Pt/C, Fe_2O_3@Pt/C) in a one-pot synthesis technique. The chapter portraits the systematic studies undertaken to understand the decisive role played by the core material and the oxidative products of the reducing agent (ascorbic agent) during the synthesis in order to accomplish the homogeneous dispersion of the nanoparticles on the carbon surface while ensuring the formation of the well featured core-shell growth pattern for the particles. Some of the prepared catalysts have been systematically investigated for oxygen reduction reaction in liquid as well as in semi-vapour phase conditions. A detailed discussion on the electrochemical activity characteristics of the prepared materials also is included in this chapter.

In **Chapter 4**, a discussion on the preparation of hollow Cu-Pt nanocage (CuPt-NC) structure by adopting a galvanic displacement technique and its application as cathode electrode for Zn-air battery is included. CuPt-NC is found to be displaying higher ORR activity and stability than that of Pt/C in alkaline medium. Taking the advantage of its better oxygen reduction reaction activity, the material has been explored as a cathode for the primary Zn-air battery. The chapter gives the important findings of the study along with a discussion on the activity characteristics by correlating the structural features of the material.

Chapter 5 deals with the a simple water-in-oil (W/O) emulsion technique, which could be successfully developed for the synthesis of a Pt-free core-shell structure containing Au as the core and nitrogen doped graphene as the shell (*i.e.* Au@NGr). The process illustrated in this chapter stands out as an efficient strategy to tune the properties of NGr shell by creating intimate contact between the Au-core and NGr-shell. The adopted strategy could help to increase the overall electronic conductivity of the system, which is an important criterion in reducing the ohmic overpotential in electrochemical devices. In addition to this, the wrapping of NGr around the Au nanoparticle helped the system to decrease the formation of hydrogen peroxide during

oxygen reduction reaction. This shift from the 2 to 4 electron reduction pathway is highly desirable to utilize the material for oxygen reduction applications in PEM fuel cells and these results are also discussed in the chapter. A discussion on the structure-property relationship in achieving the modulated activity characteristics is also included in this chapter.

Chapter 6 comprises the discussion on the formation and activity characteristics of a Ni-nitrogen doped graphene (Ni-NGr) nanocage structure, which was formed by the effective utilization of the surface plane energy of Ni for carbon adsorption and diffusion. The intrinsic property of carbon dissolution in Ni under the pressure created by water vapour in tiny water-in-oil nanoreactor gave beautiful 3-D structured NGr interpenetrated Ni-NGr nanocages having high surface area and roughness factor. The chapter discusses in detail about the structural characterization of the fancy nanocages and proposes a mechanism based on the carbon adsorption/dissolution property of Ni that could trigger the formation of the structure. The material has been investigated as an electrocatalyst for oxygen evolution reaction. A detailed discussion on the electrochemical data is also included in this chapter.

Finally, the key results of the work done during the tenure are summarized in **Chapter 7**. The chapter gives a concise summary of the major findings of the work illustrated in the thesis. The main aspects with respect to the synthesis strategies adopted, structural features attained and performance modulations achieved are highlighted in the chapter. The chapter also highlights the future prospects of the work.

Chapter 1
Scenario of Electrocatalyst Development for Energy Applications: An Overview

The present chapter commences with a short description about the energy devices (mainly, fuel cells, metal-air batteries etc.). The principles of different types of fuel cells, with detailed discussion on the polymer electrolyte membrane fuel cells (PEMFCs) along with the set-up, major components, advantages and challenges have been included. In continuation, a concise literature review on the designing of Pt-based and Pt-free electrocatalysts and carbon support materials is also included. Subsequently, potential advantages and disadvantages of these classes of materials are described categorywise. The use of intrinsic properties of carbon allotropes in the field of energy devices is also discussed. Followed by this, a discussion on the significance of the metal-air batteries by highlighting the existing challenges on attaining the requirements on the cathode electrode and the ways to overcome the energy density issues of the traditional batteries with the metal-air battery is also included in this chapter. Finally, the objective and scope of the present thesis are listed at the end of the thesis.

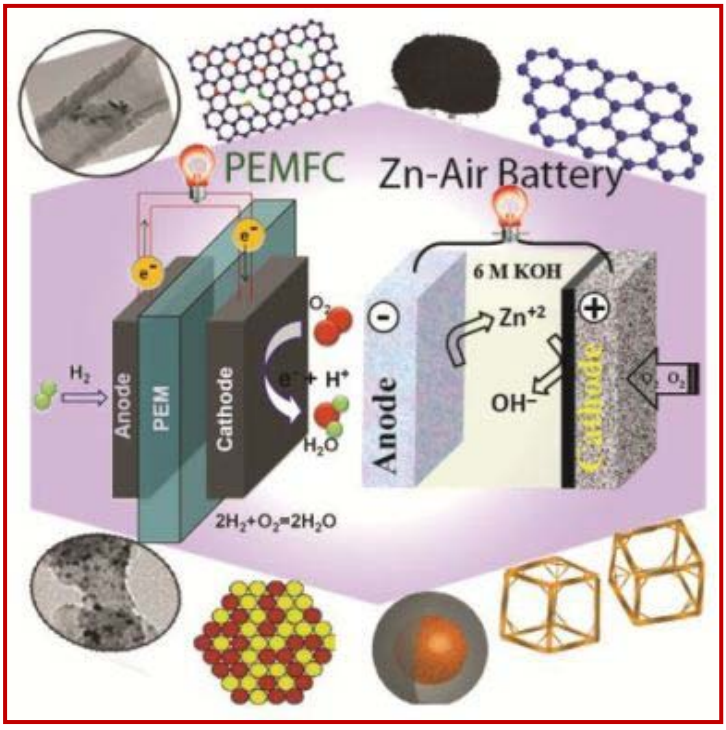

1.1. General Introduction

The overlapping issues on the increasing energy demand, depleting fossil fuels and adverse environmental impacts of the fossil fuel based technologies are raising big challenges to the scientific community to introduce environmentally benign, alternative energy conversion systems for future energy applications.[1-5] Hitherto, the fossil fuels (coal, petroleum products, natural gas, etc.) are being used for power generation.[1-5] But, the scarcity of fossil fuels and their increasing demand for energy generation are expected to lead the mankind to a big crisis in the future unless we switchover to suitable alternate energy generation technologies.[2, 6] According to the 2013 scenario of the World Energy Outlook (WEO), the demand for coal, gas and oil will increase by 0.7, 1.6 and 1.1 %, respectively, per year up to 2020/2030.[3, 6] As far as electricity generation is concerned, the coal requirement will shoot up by 33-35 %, and the oil and natural gas demand will increase by ~72 % by 2035.[6] In short, the mismatch between the global consumption and supply of energy will increase rapidly. Therefore, to accomplish more sustainable colonies with sufficient renewable energy and substantial reduction in pollution, more robust and efficient approaches in the electrical energy conversion and storage are needed. Keeping this in mind, researchers are focussing on the various renewable energy resources (sunlight, wind, rain, tides, waves, geothermal energy, etc.) and nuclear power, as alternatives to the fossil fuels.[3-4, 6-8] Currently, the hydrogen and solar energies are being considered as important renewable energy resources.[4, 7-9] Thus, the fuel cells, solar cells and batteries are gaining ample attention of the researchers primarily due to their independency on fossil fuels.[4, 7-14] It is now widely believed that the fuel cells may become an integral part of the energy sustainability and a pollution-free environment during the course of implementation of the alternate energy technologies in future. Going directly from the chemical to the electrical energy avoids the entropy penalty of converting heat into mechanical work.[4, 7-9] Thus, the fuel cell has the potential to change the world by providing the low-cost and pollution-free power, which is a dream for the modern generation.[15]

Although fuel cells have many advantages, batteries are good partners to store/convert energy. Batteries convert the stored chemical energy to electrical energy by means of electrochemical reaction within the system.[16] Fuel cells need a continuous fuel supply, whereas batteries deliver power from the stored chemical energy whenever and wherever it is required.[10-

[12] In addition, compared to the current available batteries (*i.e.* metal-ion, metal-air etc.; where the metal can be Li, Na, Zn, etc.), mainly, the metal-air (Zn-air) batteries have higher achievable energy density in a non-safety environment (*i.e.* use of aqueous electrolyte), whereas, Li-ion batteries need to be fabricated by ensuring non-aqueous (due to high moisture-sensitivity) encapsulation conditions.[10-12, 16-23]

Importantly, both the electrochemical power sources (*i.e.* fuel cells and Zn-air batteries) have similar working principle, which involves conversion of the chemical energy stored in the fuel (H_2/Zn) to electrical energy, where, oxidation of H_2/Zn takes place at the anode and reduction of oxygen occurs at the cathode.[11, 15, 24-27] In addition, the Zn-air batteries possess high energy densities and they are relatively inexpensive as they employ very cheap material (Zn). In spite of their moderate efficiencies, fuel cells and metal-air batteries have gained great attention world-wide for commercial applications in the areas of transportation, electronic devices and colonized applications since last few decades. Even when they enjoy these advantages, these systems lack prospects in heavy applications due to the sluggish cathodic reaction, which actually decides the overall efficiency of the system.[1-4, 7, 16-23]

The following few sections provide details of the chemistry behind the fuel cells and Zn-air batteries. A discussion on the main bottlenecks involved in the commercialization aspects of these systems is also included. The strategies adopted for modifying the activity characteristics of the electrocatalysts along with the available potential synthetic methodologies are also highlighted in the following sections.

1.2. Fuel Cells

Direct conversion of chemical energy stored in fuels to the useful electrical energy can be achieved by an electrochemical power source such as fuel cells, batteries, etc.[2-4, 16-24, 27] These electrochemical power sources are expected to be the main systems for fulfilling the energy demands in future. Despite of their common function, the energy gets released due to the nature of the electrochemical reactions taking place at the electrode-electrolyte boundary during energy conversion or storage. Since the fuel cells have great potential for higher energy conversion, environmentally safe fabrication and operating conditions make the system more viable in the energy market. Fuel cells are used for primary and backup power for commercial, industrial and

residential buildings and in remote or inaccessible areas. They are also used to power fuel-cell vehicles, including forklifts, automobiles, buses, boats, motorcycles and submarines.[2, 4, 24, 27]

Mainly, the fuel cell consists of two electrodes separated by an electronically insulating layer. The insulating layer (*i.e.* electrolyte) allows the charges to travel between the two sides of fuel cells. The reaction at the anode generates the electron which travels to the cathode through the external circuit and produces the direct current. Fuel cell comes in variety of sizes. A single cell produces an electrical potential of ~0.90 V, even though the theoretical potential is 1.24 V. Therefore, cells are stacked or arranged in series to increase the voltage to meet the application requirements.[28] Moreover, apart from electricity, fuel cells produce water, heat and depending upon the fuel source, small amount of nitrogen dioxide and other emissions. The energy efficiency of the fuel cell is around 40-60 %, which can be increased up to 85 %, if the waste heat can be captured for use. A brief discussion on the advantages of the fuel cells is included in the next section.

1.3. Advantages of Fuel Cells

Fuel cells are noise- and pollution-free energy conversion devices, which provide energy until we stop the inputs, *i.e.* fuel and oxidant.[2, 15, 24] Fuel cells produce water and heat as the by-products as a result of the reaction between the fuel (H_2) and oxidant (O_2) ions formed at the anode and cathode, respectively, in presence of the electrocatalyst. Therefore, fuel cells are environmentally clean and noise-free systems as compared to the combustion engines.[2, 15, 24] Fuel cells are efficient, but, they are currently lagging behind the conventional technologies in the energy market due to their cost and size. Despite of their low power density, fuel cells have higher efficiency than that of the combustion engines.[2, 15, 24] On the other hand, the fuel cells do not need the fossil fuels like the combustion engines. Importantly, the fuel cells can be operated at wide-range of temperatures up to 1000 ^{o}C.[2, 15, 24] Depending upon the operating temperatures, electrochemical reactions involved and the electrolytes used, fuel cells can be classified into different types. A brief discussion on the types of fuel cells is given in the following section.

1.4. Types of Fuel Cells

The categorizations of the fuel cells is based on the type of the electrolyte used and are mainly exemplified based on the operating temperature.[2, 15, 24] **Figure 1.1** provides a clear picture of the categorization of the fuel cells.

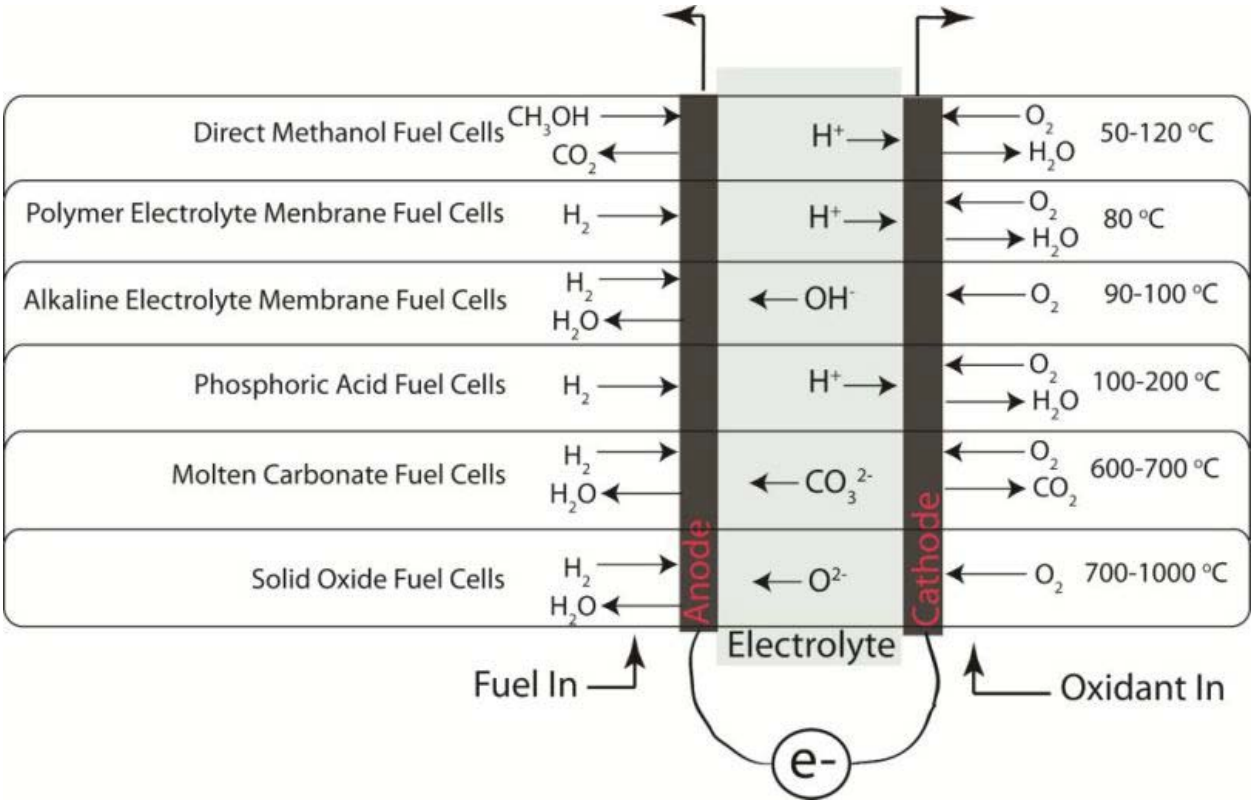

Figure 1.1: *A schematic illustration of the different types of fuel cells.*

1.4.1. Solid Oxide Fuel Cell (SOFC)

Solid oxide fuel cell (SOFC) has a great scope due to its high temperature operation and fuel flexibility, which delivers a normal efficiency of 60 %.[2, 15, 24] Typical operating temperature of SOFC is 700-1000 ^{o}C; hence, it does not require very costly Pt-catalyst and is also not vulnerable to CO-poisoning.[2, 15, 24] Mainly, the ceramic materials or solid oxides (yttria and scandia-stabilized zirconia (YSZ, ScSZ), gadolinium doped ceria (GDC), etc.) are being used as the electrolytes, which possess higher oxygen ion conductivity from the cathode to the anode.[2, 15, 24] In principle, the Co/Ni-Zirconium oxide cermet and Sr-doped $LaMnO_3$ are being used as the anode and cathode materials, respectively.[27, 29] During operation, the electrochemical oxidation of oxygen ions takes place in presence of H_2/CO at the anode side, which generates

water as the by-product.[27, 29] In addition, SOFC has gained great attention as a variety of light and heavy hydrocarbon (gasoline, diesel, bio-fuels) fuels can be used for running the system. These fuels do not require any external reformer for hydrogen generation. Generally, the light hydrocarbons get internally reformed within the anode, during operation, and generate hydrogen and CO, which will react with the incoming oxygen ions from the cathode, as mentioned above. Hence, SOFC has more options for the use of fuels. Therefore, better output of SOFC can lead great applications in auxiliary power units in vehicles to stationary power generation with an output range of 100 W to 2 MW.

1.4.2. Molten Carbonate Fuel Cell (MCFC)

Molten carbonate fuel cell (MCFC) is a type of high operating temperature fuel cell. Hence, MCFC also possesses better efficiency of 60 %, like SOFC.[30-31] Similar to the SOFC, MCFC works with a variety of hydrocarbon fuels, including light and heavy hydrocarbon fuels. Importantly, like SOFC, MCFCs does not require any external reformer to generate hydrogen.[30-31] Porous Ni and Ni-oxides are being used as the anode and cathode materials, whereas, a combination of alkali (Na/K/Li) carbonates, which is retained in a ceramic matrix of $LiAlO_2$, is generally used as the electrolyte.[30-31] In principle, MCFC operates at 600-700 ^oC, where the alkali carbonates form a highly conductive molten salt with carbonate ions provide the ionic conduction.[30-31] Due to the high temperature operation, the most expensive Pt-based catalysts can be avoided and also the issue of CO-poisoning can be disregarded.

1.4.3. Phosphoric Acid Fuel Cell (PAFC)

Among the proton transfer fuel cells, the phosphoric acid fuel cell (PAFC) has the advantage of having the relatively high operating temperature (100-200 ^oC) and high CO-tolerance (up to 1.5 %).[24, 27, 32] In PAFC, 100 % concentrated phosphoric acid is used as the electrolyte at 150-200 ^oC, due to its poor ionic conductivity and severe CO-poisoning at lower temperature. Generally, silicon carbide is used as a matrix to retain the acid in PAFC.[24, 27, 32] The relative stability of concentrated phosphoric acid is high compared to the other common acids and it also minimizes the water vapor pressure, which makes the water management in the cell less problematic. The existing PAFCs have normal capacities of around 200 kW, which

make them useful for stationary power plants and mobile towers etc. In spite of this, the use of Pt-based electrocatalysts and slow-startup are the major stumbling blocks in the way towards their large scale commercialization.

1.4.4. Direct Methanol Fuel Cell (DMFC)

Direct methanol fuel cell (DMFC) has good capability to deliver high energy density, because, methanol has one order magnitude higher energy density compared to compressed hydrogen.[24, 27] Pt-based or Pt-Ru based electrocatalysts are being used as the anode and cathode materials. In principle, methanol is used as the fuel, which undergoes oxidation at the anode and results into the formation of protons and CO and/or CO_2 with release of electron.[24, 27] These protons are transported to the cathode through the proton exchange membrane and neutralize the reduced oxygen in presence of electron, generating water as the by-product.[24, 27] General operating temperature of DMFC is 50-120 ^{o}C. Hence, DMFC possesses low efficiency and it generally finds applications in the portable and electronic devices, where energy and power density are more important than efficiency.[24, 27]

1.4.5. Alkaline Fuel Cells (AFC)

Alkaline fuel cell (AFC) is one of the well-developed fuel cell technologies. AFC is also termed as Bacon fuel cells, because, the English engineer Francis Thomas Bacon used KOH instead of sulfuric acid (William-Grove fuel cells) in mid nineteen century and demonstrated AFC.[15, 24, 33] After that, NASA has used AFC in Apollo series mission and on the space shuttle.

In principle, AFC consists of two electrodes which are separated by a porous matrix saturated with an aqueous alkaline solution, such as KOH.[15, 24, 33] AFC operates at ~250 ^{o}C and they are capable of attaining an efficiency of 70 %.[15, 24, 33] Basically, the electrolyte used is 85 wt. % KOH for high temperature (~250 ^{o}C) and 35-50 wt. % KOH for lower temperature (< 120 ^{o}C) operation. The electrolyte is retained in an asbestos matrix and a wide range of electrocatalysts (e.g., Ag, Ni, spinels, metal oxides, and non-Pt) can be used.[15, 24, 33] In AFC, the hydrogen and oxygen get consumed and result into the formation of water, heat and electricity. During the operation, trace amount of CO_2 can react with the KOH to form K_2CO_3, thus altering the electrolyte.[15, 24, 33] Therefore, AFC typically needs to be operated on pure oxygen or purified

air by passing through a 'scrubber', which cleans out as much as of CO_2 as possible. These tedious processes of generation and storage requirements of oxygen make AFC more expensive.

1.4.6. Anion Exchange Membrane Fuel Cell (AEMFC)

Anion exchange membrane fuel cell (AEMFC) is also termed as hydroxide ion exchange fuel cells, although it is a type of AFC.[15, 24] The typical operating temperature of AEMFC is 90 ^{o}C, possessing the higher electrical efficiency compared to the other fuel cells.[15, 24]

Working principle of AEMFC is similar to AFC but differs in usage of the solid electrolyte; AFC works with aqueous KOH, whereas, AEMFC works with a solid polymer electrolyte.[15, 24] In an AEMFC, the humidified fuel (hydrogen/methanol) and oxygen will be provided to the anode and cathode, respectively. The fuel gets oxidized at the anode and oxygen gets reduced at the cathode. At the cathode, reduction of oxygen generates hydroxides ions (OH^-) that migrate through the electrolyte towards the anode. At the anode, OH^- reacts with the fuel to produce water and electrons. Electrons will go through the external circuit and produce current.[15, 24] Main advantage of AEMFC is the negligible methanol crossover due to transport of ions in opposite direction compared to DMFC. In addition, AEMFC possesses additional benefits like, faster electrode kinetics, better corrosion resistance in alkaline conditions and use of cheap non-noble electrocatalysts as the cathode material.[15, 24] The main drawback of AEMFC is the use of solid polymer electrolytes having poor ionic conductivity and mechanical strength. The ionic conductivity of the alkaline membranes is normally two times less than that of the conductivity of the proton conducting membranes which are being used in polymer electrolyte membrane fuel cells.[15, 24]

1.4.7. Polymer Electrolyte Membrane Fuel Cell (PEMFC)

Polymer electrolyte membrane fuel cell (PEMFC) is also known as proton exchange membrane fuel cell. An electrically insulating, proton conducting, solid, flexible, non-porous, ion exchange membrane like the ones based on *perfluoro-sulfonic acid polymer or other similar polymers* will be used as an electrolyte in PEMFCs.[15, 24] Performance of the PEMFCs depends largely upon the proper humidification of the polymer electrolyte membrane and overall water management during the actual operation in case when the commercial Nafion® type membranes

are used.[15, 24] In order to avoid the excess use of external water for humidification, the water formed as the by-product itself will be utilized internally to keep the membrane hydrated. Therefore, a PEMFC must be operated under the conditions where the by-product does not evaporate faster than it is produced. Because of this, PEMFCs need to be operated at less than 100 ^{o}C. Due to the low-temperature operation and necessity of water within the system, pure hydrogen (very low CO content) must be used in PEMFCs. The impure fuel has negative impact on the fuel cell performance. The CO impurity of the fuel poisons the electrocatalysts.[15, 24]

Recently, depending up on the use of the electrolyte and its operating temperature, the PEMFCs are classified into two types, *viz.*, low-temperature and high-temperature.[15, 24] The low-temperature PEMFCs (LT-PEMFCs) need the humidification and the proton exchange membrane must be hydrated throughout the operation. The perfluoro-sulfonic acid (*i.e.* Nafion®) is used as an electrolyte in LT-PEMFCs. Here, the sulfonic acid groups act as water holder and path for proton transport. Hence, this necessitates their operation below 100 ^{o}C.[15, 24] In contrast, high-temperature PEMFCs (HT-PEMFCs) can be operated at 180-200 ^{o}C, in which phosphoric acid doped polybenzimidazole (PBI) is being used as the electrolyte. The phosphoric acid acts as the proton transporter whereas PBI as a matrix to hold the acid. The main advantage of HT-PEMFCs is the higher CO-tolerance (~1.5 %) compared to LT-PEMFCs.[15, 24] Hence, reformate hydrogen can also be used as the fuel. The PEMFCs find wide range of applications, including residential and transportation.[15, 24] Since the use of costly Pt-based electrocatalyst on both the electrodes and the sluggish cathodic reaction raise challenges on the cost and efficiency of PEMFCs, there is a significant focus by the researchers to develop new catalysts having low or no Pt content and simultaneously possessing improved ORR activity.

1.5. Principle of Polymer Electrolyte Membrane Fuel Cells

The heart of a PEMFC is a membrane electrode assembly (MEA). MEA is a seven layered assembly consisting of electrocatalyst (Pt, Pt-based multi-metallic structures) coated on the carbon coated porous carbon paper sandwiched with the polymer electrolyte membrane.[15, 24] Generally, Nafion® and phosphoric acid doped PBI have been used as the polymer electrolyte membrane in PEMFCs. The structures of Nafion® and PBI are shown in **Figure 1.2**. The main function of the polymer electrolyte membrane is to pass the protons from the anode to the

cathode.[15, 24] In principle, the MEA performance is investigated by passing ultra-pure compressed or reformate hydrogen at the anode and oxygen/air at the cathode side. The fuel is oxidized at the anode, releases protons and electrons. The proton transports from the anode to the cathode through the polymer electrolyte membrane and the electron travels through the external circuit and reaches the cathode side. At the cathode, the incoming electron reduces the oxygen in presence of the Pt-electrocatalyst. Finally, the reduced oxygen species are neutralized by the proton which leads to the production of heat and water.[15, 24] Overall efficiency of PEMFC depends on the cathodic reaction. Hence, the sluggish kinetics of oxygen reduction reaction (ORR) should be improved by modifying the physical and chemical properties of the Pt-electrocatalysts and also by tuning the electrode-electrolyte interface.[15, 24] In PEMFCs, the electrode-electrolyte interface mainly talks about the effective interaction between the electrode, electrolyte and reactant, and this interface has been termed as the triple phase boundary (TPB).[15, 24]

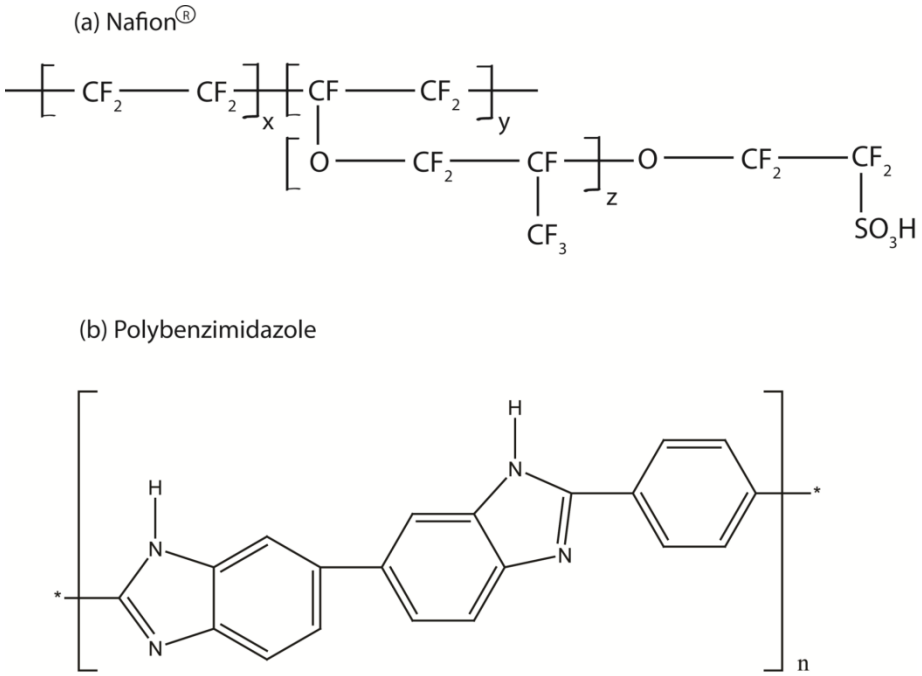

Figure 1.2: *Structure of (a) Nafion® and (b) polybenzimidazole.*

A major theme of development of PEMFCs is lying at the effective modification at TPB, where the actual reaction takes place.[15, 24] The reactions occurring in a PEMFC are presented below:

Acidic Condition:

$$At\ Anode: \quad 2H_2 \longrightarrow 4H^+ + 4e^- \quad E^0 = 0.00\ V \qquad (1.1)$$

$$At\ Cathode: \quad O_2 + 4H^+ + 4e^- \longrightarrow 2H_2O \quad E^0 = 1.23\ V \qquad (1.2)$$

$$Overall: \quad 2H_2 + O_2 \longrightarrow 2H_2O \quad E^0 = 1.23\ V \qquad (1.3)$$

An AEMFC also involves the similar structural features as that of a PEMFC involving proton transport. Here also, the establishment of TPB is one of the challenging steps in the system fabrication. AEMFC also falls under PEMFC as both involve usage of the polymer membranes; the general reactions occurring at the electrodes under the alkaline conditions are given below:

Alkaline Condition:

$$At\ Anode: \quad H_2 + 2OH^- \longrightarrow 2H_2O + 2e^- \quad E^0 = 0.83\ V \qquad (1.4)$$

$$At\ Cathode: \quad \tfrac{1}{2}\ O_2 + H_2O + 2e^- \longrightarrow 2OH^- \quad E^0 = 0.40\ V \qquad (1.5)$$

$$Overall: \quad H_2 + \tfrac{1}{2}\ O_2 \longrightarrow H_2O \quad E_{cell} = 1.23\ V \qquad (1.6)$$

The reactions occurring in PEMFCs under acidic condition are shown by **Equation 1.1** and **Equation 1.2**. **Equation 1.1** represents the oxidation reaction of hydrogen at the anode and **Equation 1.2** shows the oxygen reduction at the cathode. Overall, a 1:0.5 mole ratio of hydrogen and oxygen generates heat and one mole of water. During this process, the oxidized product of hydrogen is transferred from the anode to the cathode through the proton conducting membrane, where, it neutralizes the reduced product of oxygen and form water (**Figure 1.1**).

Moreover, the reactions take place under the alkaline condition is shown by **Equations 1.4** and **1.5**. **Equation 1.4** represents the oxidation reaction of hydrogen at the anode and **Equation 1.5** stands for the oxygen reduction at the cathode. Similar to the acidic reaction of PEMFCs, a 1:0.5 mole ratio of hydrogen and oxygen generates heat and one mole of water in the alkaline condition. During this process, at the cathode, the hydroxide ions are formed due to the reduction of oxygen. These hydroxide ions are transferred to the anode *via* the anion conducting membrane and combination of the hydroxide ions with hydrogen results into the formation of

water.[15, 24] These anodic and cathodic reactions take place only in presence of the electrocatalysts (*i.e.* Pt-based electrocatalysts) (**Figure 1.1**).

1.6. Roadblocks of Polymer Electrolyte Membrane Fuel Cells

Despite the better performance of PEMFCs, the cost of the individual components of the system is the major stumbling block in the way of commercialization of PEMFCs. As shown in **Figure 1.3**, out of the total cost of PEMFC, 83 % is contributed by the electrocatalyst and the GDL support alone. Whereas, out of the remaining 17 %, 7 % is contributed by the polymer electrolyte membrane, 6 % by the bipolar plate, etc.[34] In short, the high cost of the electrocatalyst impedes the prospects of commercialization of PEMFCs.

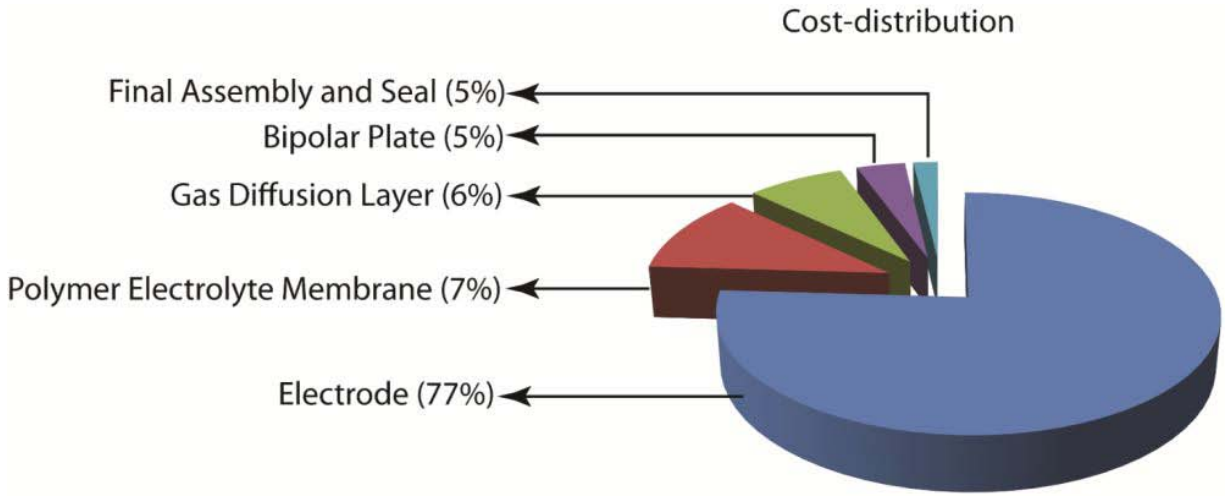

Figure 1.3: *Cost-distribution of the PEMFC components.*[34]

In the case of PEMFCs, Pt is being considered as the promising electrocatalyst. Generally, the Pt nanoparticles supported on high surface area carbon (Pt/C) has been widely used as the electrocatalyst in PEMFCs. In spite of its better activity, elimination or at least minimization of Pt from the PEMFC electrodes has become a necessity mainly due to the high cost of the material. Sluggish cathodic reaction and the issues associated with the stability of Pt also give a push towards the development of better systems. Practically, during the long-term stability tests, the carbon support undergoes oxidation, eventually leading to the agglomeration of the Pt particles (decrease the surface-to-volume ratio), thereby to the reduction in the overall performance of the system.[15, 24] On the other hand, the Nafion® type membranes used in

PEMFCs are limited by their ionic conductivity and performance dependency on humidification. Other issues like, the fuel crossover and lower stability and disintegration of the membrane due to the hydroxyl radicals are also being identified as major obstacles in the way of full utilization of the integrated system.[15, 24] At last, the brittle nature of the bipolar plates and their corrosion under high acidic environment are also adding to the issues. Therefore, all these limitations need to be tackled effectively without losing the overall efficiency of the system.

1.7. Electrocatalysts in PEMFCs

Kinetics of any kind of reaction can be improved by use of an appropriate catalyst, whose properties do not change during the reaction. In PEMFC, the oxidation of hydrogen and/or reduction of oxygen are achieved by using a Pt/C as an electrocatalyst.[15, 24] The kinetics of ORR is very sluggish and involves very high overpotential.[15, 24] In conjunction, during ORR, the oxide and/or hydroxide formation of Pt also decreases the activity and directly affect the performance.[15, 24] Hence, to tackle these issues we need innovative research ideas to develop a cheap and efficient electrocatalyst for real applications. So far, various metallic and non-metallic nanostructured electrocatalysts have been tested.[15, 24] Along with that, the chalcogenides, pervoskites, transition metal carbides etc. have also been studied for ORR.[15, 24] However, till date, there is not a concrete and solid result which can guaranty the replacement of existing electrocatalysts from PEMFCs. The scenario of the design strategies of different nanostructured electrocatalysts based on low-Pt and Pt-free active centres has been discussed in a subsequent section.

1.8. Mechanisms of Oxygen Reduction Reaction (ORR)

The mechanism of ORR is not fully disclosed due to the complexness and changing behaviour of the process depending upon the electrode materials, catalysts, and the electrolyte. Literature says that ORR follows two kinds of mechanistic pathways in acidic and alkaline media, *i.e.* four-electron and two-electron reduction pathways.[15, 24] In acidic media, the protons combine with the reduced oxygen, whereas, in alkaline media, the hydroxyl ion plays a critical role. Moreover, during ORR, the way of interaction of the oxygen molecules with the catalyst decides the pathway. The most desired reduction pathway is the four-electron pathway, where, the combination of proton and the reduced form of oxygen produces water as the product.

However, in another case, the combination of proton and the reduced form of oxygen produces the water as the product *via* hydrogen peroxide as an intermediate, by the two-electron reduction pathway. The stages of reactions in the four-electron reduction pathway in acid and alkali are already given in **Section 1.5**. The reactions involving in the two-electron reduction pathway are given below:

Acidic Condition:

$$ORR:\ O_2 + 2H^+ + 2e^- \longrightarrow H_2O_2 \qquad E^0 = 0.67\ V \qquad (1.7)$$

$$H_2O_2 + 2H^+ + 2e^- \longrightarrow 2H_2O \qquad E^0 = 1.76\ V \qquad (1.8)$$

Sometimes, the hydrogen peroxide formed *via* **Equation 1.7** can undergo alternate decomposition process and can lead to the formation of water and oxygen as,

$$2H_2O_2 \longrightarrow 2H_2O + O_2 \qquad (1.9)$$

Alkaline Condition:

$$ORR:\ O_2 + H_2O + 2e^- \longrightarrow HO_2^- + OH^- \qquad E^0 = -0.065\ V \qquad (1.10)$$

$$HO_2^- + H_2O + 2e^- \longrightarrow 3OH^- \qquad E^0 = 0.867\ V \qquad (1.11)$$

Sometimes, the peroxide ions formed *via* **Equation 1.10** can undergo alternate decomposition process and can lead to the formation of hydroxide ion and oxygen as,

$$2HO_2^- \longrightarrow 2OH^- + O_2 \qquad E^0 = 0.867\ V \qquad (1.12)$$

The undesired products formed during the two-electron reduction pathway create additional problem for the polymer electrolyte membrane. During the operation, the hydrogen peroxide may decompose the polymer electrolyte membrane, causing the fuel crossover and direct recombination of hydrogen and oxygen in presence of the Pt-catalysts and blasting of the system. The four-electron reduction pathway is more desirable and it possesses higher efficiency than that of the indirect pathway (two-electron reduction pathway). Hence, PEMFC needs the electrocatalysts which can convert the hydrogen and oxygen in water by the direct mechanistic pathway.

1.9. Platinum-based Electrocatalysts for Oxygen Reduction Reaction

The high cost of Pt has already put a big challenge to the fuel cell researchers. A long attempted way of dealing this issue is to achieve reduction of Pt usage by making a composition of Pt with other transition metals to get bi-metallic and/or multi-metallic systems.[35-41] Moreover, researchers have adopted another way to increase the activity of Pt by tuning the dispersion of Pt-particles by using different carboneous and non-carboneous supports [41-45] for ORR. Along with this, tuning the physical properties of Pt at the nanoscale can also play a decisive role in the electrocatalytic reactions.[46-49]

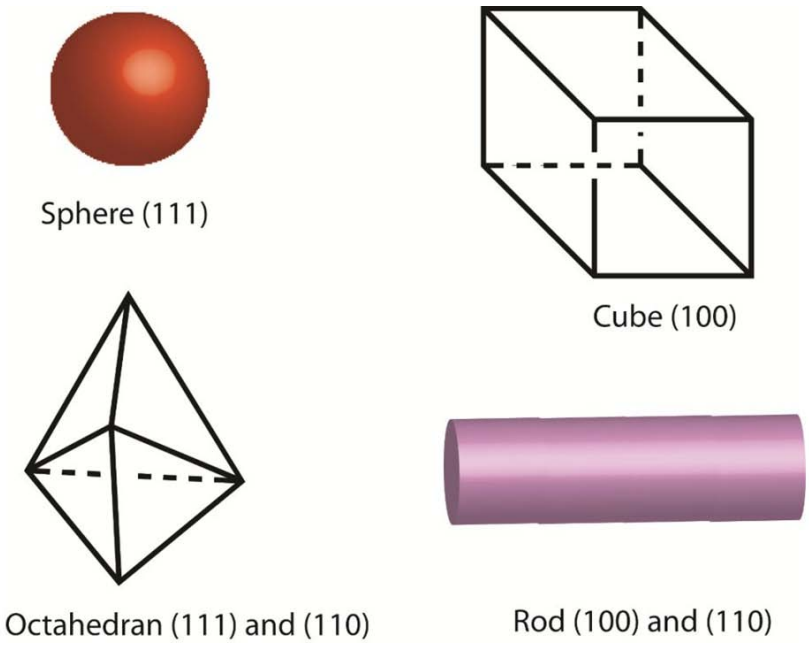

Figure 1.4: *Representation of the possible physical structures of Pt and the lattice facets they enclose (in parentheses).*

These physically changed nanoparticles have special property characteristics as originated by their geometry, which promote the catalytic reactions to different magnitudes. The fundamental principle orbits around the prevalence of various crystal lattice planes, which prevail as a function of particle morphology and the options of these lattice planes towards the interested reaction pathway. As per the literature, the interaction of Pt with oxygen and its subsequent reduction is more favourable and more selective to H_2O over the Pt (110) than the Pt (100) and (111).[50] The said activity can be correlated to the surface coordination number, which

is in the order of 7 [(110)] > 8 [(1 0 0)] > 9 [(1 1 1)], respectively.[50] This trend indicates that the modification of the structural features of the catalyst surface could be an important strategy to increase the kinetics of ORR. Recently, density functional theory (DFT) has given a clear understandable study, based on which, we can design potential alternative materials which can eventually replace the use of Pt in PEMFCs.[51] Based on the various theoretical studies, it is now possible to rank different materials depending on how their surface interacts with oxygen. Moreover, the energy of the d-band center and the Pt-Pt inter-atomic distance also play major roles towards ORR and, hence, these factors also have to be taken under consideration while designing new electrocatalysts.[55]

Norskov *et al.*,[51] have studied the interaction of the surfaces of different materials with oxygen and prepared a ranking list, which is illustrated in the form of a volcano plot (**Figure 1.5**), where, the oxygen reduction activity is plotted as a function of the oxygen binding energy.

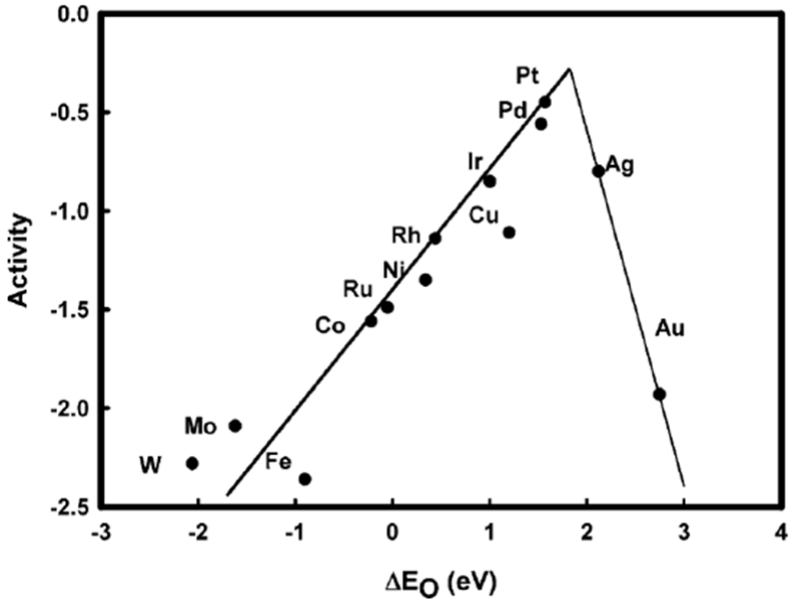

Figure 1.5: *A volcano plot (ORR activity vs. energy of oxygen interaction) indicating the ORR activity of different metals on the (111) surface plane.*[51] *[Reprinted with permission from (J. Phys. Chem. B 2004, 108, 17886–17892). Copyright (2004) American Chemical Society]*

From the volcano plot (**Figure 1.5**), the exact reason behind the acceptance of Pt as an ideal catalyst for ORR becomes evident. It can be seen from the plot that, next to Pt, Pd is appearing as the best electrocatalyst due to its slightly lower binding energy. Along with this, the cost of Pd is

approximately half of that of Pt. Therefore, it is a potent contender to replace Pt as an electrocatalyst for PEMFCs.

1.9.1. Oxygen Reduction Reaction Mechanism on Pt-Surface

As per the theoretical studies, ORR on the surface of Pt follows the two types of mechanistic pathways: (i) associative and (ii) dissociative.[51-54]

(i) Associative Mechanism:

During the reaction of oxygen and Pt, the oxygen gets adsorbed without cleavage of the O-O bond and results into the formation of H_2O *via* the reactions presented below (**Equations 1.13-1.17**).

$$Pt + O_2 \longrightarrow Pt\text{-}O_{2\text{-}ads} \quad (1.13)$$

$$Pt\text{-}O_{2\text{-}ads} + H^+ + e^- \longrightarrow Pt\text{-}HO_{2\text{-}ads} \quad (1.14)$$

$$Pt\text{-}HO_{2\text{-}ads} + H^+ + e^- \longrightarrow H_2O + Pt\text{-}O_{ads} \quad (1.15)$$

$$Pt\text{-}O_{ads} + H^+ + e^- \longrightarrow Pt\text{-}OH_{ads} \quad (1.16)$$

$$Pt\text{-}OH_{ads} + H^+ + e^- \longrightarrow H_2O + Pt \quad (1.17)$$

The subscripts “ads” indicate that the corresponding species are adsorbed on the electrode (here, Pt) surface. The O-O bond may not be broken, as shown in **Equations 1.13-1.17**. Probably, it forms hydrogen peroxide and which could be further reduced to water or could be remained as such as a final product. Therefore, this mechanism is also termed as the indirect pathway, where instead of water (four-electron reduction), hydrogen peroxide (two-electron reduction) gets formed.

(ii) Dissociative Mechanism:

During the reaction of oxygen with Pt, the oxygen gets adsorbed with cleavage of the O-O bond and forms the Pt-O bond, which results into the formation of H_2O by gaining two electrons. The corresponding reactions are presented as below (**Reactions 1.18-1.20**):

$$Pt + ½\ O_2 \longrightarrow Pt\text{-}O_{ads} \quad (1.18)$$

$$Pt\text{-}O_{ads} + H^+ + e^- \longrightarrow Pt\text{-}OH_{ads} \quad (1.19)$$

$$Pt\text{-}OH_{ads} + H^+ + e^- \longrightarrow H_2O + Pt \quad (1.20)$$

From the above equations, it can be seen that, there is no adsorbed oxygen molecule on the surface of Pt. As a result, the oxygen gets transformed directly to water without any hydrogen peroxide formation. This mechanism is considered to be more viable and fruitful to convert oxygen to water with the direct reduction pathway.

Overall, considering the orbital concept during the ORR, the electrons are transferred from Pt-metal surface to the anti-bonding orbital of oxygen. This process decreases the bond order and increases the bond length of the O-O bond, which finally results into its dissociation.

1.10. Development of Platinum-based Electrocatalysts

Based on the DFT calculations on the oxygen interactions with different metal surfaces,[51-54] clear idea about the coupling of Pt metal with selective transition metals can be deduced. Moreover, the energy level of the d-band center with respect to oxygen and the inter-atomic distance between the Pt contribute more to improve the ORR activity (**Figure 1.6**). Furthermore, the things will be more interesting and more understandable when we consider the communication of the bonding state of oxygen with the d-band of the metal.[55] During the aforementioned communication, the d-band of the metal and the sigma (bonding) orbital of the oxygen form the bonding (d-σ) and anti-bonding $(d\text{-}\sigma)^*$ states, as shown in **Figure 1.6**. Importantly, the level of filling of the anti-bonding states has been administered by the density of states (DOS) at the surface of the metal, whereas, the bonding orbitals have been considered as full. The extent of filling of the anti-bonding states is indirectly proportional to the stabilization of the metal-oxygen interaction, *i.e.*, the interaction of the metal and oxygen becomes weak. Overall, the extent of filling of the anti-bonding orbitals is depending on the position of the d-band center.[56]

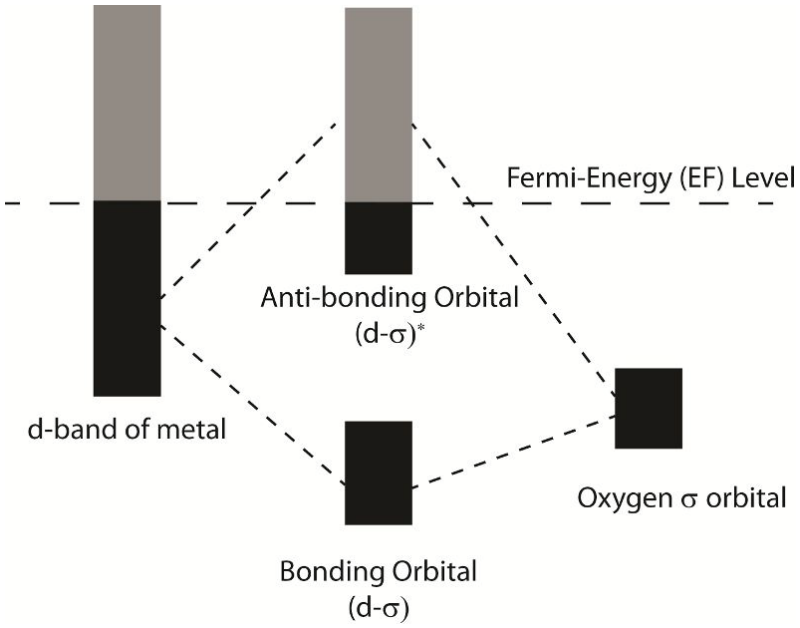

Figure 1.6: *Diagram illustrating the position of the d-band of Pt-metal and the σ-orbitals of oxygen with respect to the Fermi energy level.*[57] *Here, black and grey colours indicate the extent of the filled and unfilled orbitals of metal and oxygen.*

Mainly, the interaction of metal (here, Pt) and oxygen is depending on the position of the d-band center of the metal with respect to the Fermi level (EF). Therefore, higher d-band center results in stronger bonding and a lower d-band center results weaker bonding between the metal surface and oxygen.[57] Here, the term "dbc" stands for the d-band center and "EF" stands for the Fermi energy level.

Overall, the interaction between Pt and oxygen is too strong, which gives the intimation that its d-band center is too high.[57] Therefore, alloying of platinum with other transition metals lowers the d-band center by altering the electronic structure and inducing a degree of irregularity in the Pt lattice, which results in weakening of the metal-oxygen binding. This eventually leads to easy dissociation of oxygen and, thereby, better ORR activity.[58] Thus, researchers have focussed on the coupling of Pt with different transition metals to achieve better activity, by tweaking the surface electronic structure. In view of this, recently, alloys, core-shell structures, and cage structures have been developed and studied for ORR.[53, 59-73] The details of the important features of the aforementioned engineered structures are given in the subsequent sections.

1.10.1. Alloys

ORR on Pt is strongly depending on three aspects: (i) oxygen adsorption energy, (ii) dissociation energy of the O-O bond and (iii) binding energy of OH on the surface of Pt. The Pt d-band vacancy, *i.e.*, the electronic structure of Pt, and the Pt-Pt inter-atomic distance can strongly affect these energies (explained in **Section 1.9 and 1.10**).[59-60, 74] As per the DFT calculations, the predicted energy of oxygen adsorption on different metal surfaces and subsequent dissociation (**Figure 1.5**) are more favourable on the Pt surface. On the other hand, Pt-alloys (Pt-M; M = Fe, Co, Ni, Cu, etc.) should possess higher activity than that of pure Pt, as proven by the investigations.[51, 53] The improved activity of Pt-alloys is explained on the basis of the change in the electronic structure, *i.e.,* increase of the d-band vacancy, geometric effect, steric effect and ligand effect (decrease of the Pt-Pt interatomic distance) (as explained in **Section 1.10**).[51, 53] Mainly, whenever an alloy forms, it creates the lattice contraction and eventually, leads to change in the Pt-Pt inter-atomic distance, which favours the dissociative adsorption of oxygen. As a result, it tunes the ORR activity of alloys compared to the pure Pt alone. Arico *et al.*[59] studied ORR activity of the Pt-Fe system and the exchange current density is found to be 2.15 x 10^{-7} A/cm^2, which is higher than that of the Pt-catalyst (1.63 x 10^{-8} A/cm^2). Stamenkovic *et al.*[58] recently found that ORR is 90 times faster on Pt_3Ni than on the pure Pt-surface. Unfortunately, despite their good activity, dissolution of the transition metal alloyed in the Pt-M catalysts is a major drawback because these transition metals (M) are electrochemically soluble at a potential range between 0.3 to 1 V *vs.* NHE in low pH conditions.[59] Hence, extensive research is needed to solve the stability issues and their intimate contact within the system.

1.10.2. Core-Shell Structures

To overcome the issues related to the alloys such as leaching of non-noble metal and less structural stability in acidic conditions, very recently, researchers have come up with a new approach, where, the non-noble metal is protected with the noble metal layer. This structure is generally termed as core-shell structure and a representation of the structure is shown in **Figure 1.7**. Here, the problem associated with the leaching out of the non-noble metal and structural stability issue are sorted out and the interaction of the two metals is expected to change the

properties of Pt, as in the case of the alloys. Therefore, this strategy could simultaneously address the cost and performance requirements in the PEMFCs applications.

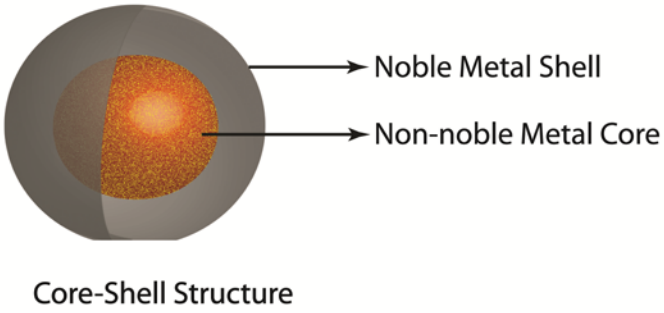

Figure 1.7: *A schematic representation of a core-shell structured electrocatalyst possessing non-noble metal core and noble metal shell.*

Mainly, Pt based core-shell systems are exceptionally important due to the coexistence of ensemble, ligand and geometric effects which modulates the characteristics and thereby lead to enhanced ORR activity.[62-65] In detail, the ensemble effect is due to the involvement of desperate surface atoms to take on distinct functionalities. The ligand effect occurs when two dissimilar surface neighbourhood atoms induce electronic charge transfer between the atoms, which eventually leads to change in the electronic band structure of the interacting atoms.[66] The geometric effect implies differences in reactivity based on the atomic arrangement of the surface atoms, which is expected to include compressed or expanded organization of the surface atoms termed as surface strain.[66]

Pt based core-shell structured systems are exceptionally important in this context due to the coexistence of all the aforementioned three favourable effects in modulating the characteristics and thereby enhancing the oxygen reduction abilities. There is ample evidence that core metals such as Cu, Fe, Ni etc. lower the d-band of the shell with respect to the Fermi level, making oxygen reduction by the Pt-shelled particles more feasible compared to that of bulk Pt nanoparticles.[62-64, 66-68, 70] While both ligand and strain effects determine the d-band center of the Pt-shell, a greater surface relaxation reduces the strain in the nanoparticles as compared to metal atoms present at the interface of the core and shell. Thus, addition of a non-noble metal can change the geometric as well as electronic structure of Pt, which ultimately enhances its activity and utilization during ORR.[62-64, 66-68, 70] The feasibility of achieving Pt in

the form of a monolayer in Pt-based core-shell systems essentially decreases the amount of Pt to be loaded in the system while the non-noble metal core modifies the electronic environment of Pt by reducing the inter-atomic distances.[62-64, 66-68, 70] Overall, Pt in the form of a thin shell on the non-noble metal core leads to enhanced catalyst utilization, better efficiency, and higher catalytic activity, thus giving immense scope for validating the techno-commercial prospects of PEMFCs by utilizing this new-class of materials. Literature review suggests plenty of methods for the synthesis of core-shell structures such as seed mediated growth, electrochemical methods, galvanic displacement method, etc.[71-73, 75-77] However, the ability to fabricate core-shell particles with uniform thickness, controllable composition, and uniform dispersion on a support is really a challenging task.

1.10.3. Hollow and 3-Dimensional Structured Electrocatalysts

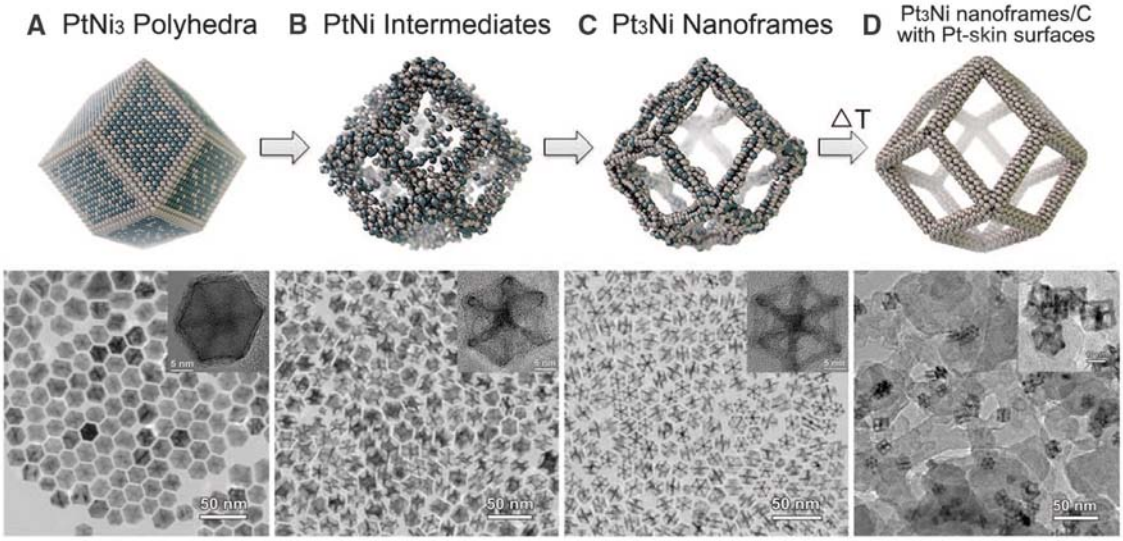

Figure 1.8: *A schematic representation and TEM images of the Pt-Ni nanoframe structures obtained at different stages, from polyhedra to nanoframes. [Reprinted with permission from {**Science**, 2014, 343, 1339}. Copyright {2014} The American Association for the Advancement of Science, License Number: 3503040027760]*

After successful journey of the core-shell structures as electrocatalysts for the PEMFC applications, still, researchers are trying to improve the Pt-activity by changing the morphology and by keeping the Pt-content as low as possible.[77] Importantly, the morphology tuning in the form of hollow, porous structures of Pt and/or Pt-coupled with transition metals gives higher

electrochemically active surface area and molecular accessibility within the structure.[77] During the actual formation the nanocage structure, atom of adsorbed metal entities moves into the lattice sites of the metal and effectively causing position switching between them. Also, at the interface of the two metals, diffusion and/or replacement reaction takes place and based on the difference in the surface segregation energy of the two metals, the surface of the particle will be dominated by only one metal.[78-80] This phenomenon is termed as "Kirkendall effect".

Recently, Han *et al*.[81] reported the synthesis of hollow Pt nanostructures with octahedral and hexagonal frame-like morphologies by a self-template route. The prepared material has shown good catalytic activity towards the CO-oxidation. Shao *et al*.[82] reported the synthesis of hollow Pd-Pt nanocage structures by potential cycling (0.6 to 1.2 V *vs.* NHE) in acid solution, where, the Pd core got dissolved due to the dendritic form of Pd@Pt structure, and Pd@Pt dendritic core-shell structure was transformed to hollow nanocage structure. These structures showed better activity compared to the Pd-Pt dendrites and pure Pt with better stability and without change in the structure. Yang *et al*.[83] (**Figure 1.8**) recently reported the synthesis of Pt-Ni nanoframes by employing a chemical reduction of metal precursors followed by controlled thermal treatment. The formed Pt-Ni nanoframe structure has shown 36- and 22-fold enhanced mass and specific activity, respectively. Recently, many more researchers involved on the synthesis of nonzero cage structures based on the Kirkendall effect and galvanic displacement method have explored such materials for the application of ORR.[73, 77, 83-89] Overall, the hollow nanocage structures have shown improved performance and stability in fuel cell applications.[73, 77, 81, 83-94] This property modulation is credited to the possible electronic changes, systematic atomic arrangement, presence of more voids and edges, higher surface-to-volume ratio and more accessible active sites etc.[73, 77-81, 83-94] Therefore, the porous nanocage structures have a potential to replace the existing Pt, so that, high utilization could be achieved during uses.

1.11. Role of Carbon Structures

The electrochemical devices and energy technology have been sustained by advanced nano-materials, mainly, carbon based. The promising properties like high mechanical strength, higher electronic conductivity and peculiar morphology, make the carbon material more useful in the field of energy market. Hence, scientists are intrigued by the development of carbon based

material for different energy conversion and storage devices.[97-107] Specifically, the carbon structures have potential to replace a metal from fuel cells and could function as electrocatalysts and/or catalyst supports. Moreover, the different allotropes of carbon (graphite, fullerenes and diamond) have gained much attention in the field of material science. The discovery of buckyball (fullerene),[95] one dimensional (1-D) nanotube and fiber and two dimensional graphene (**Figure 1.9**) have opened up new area of research by utilizing them in the energy technologies.

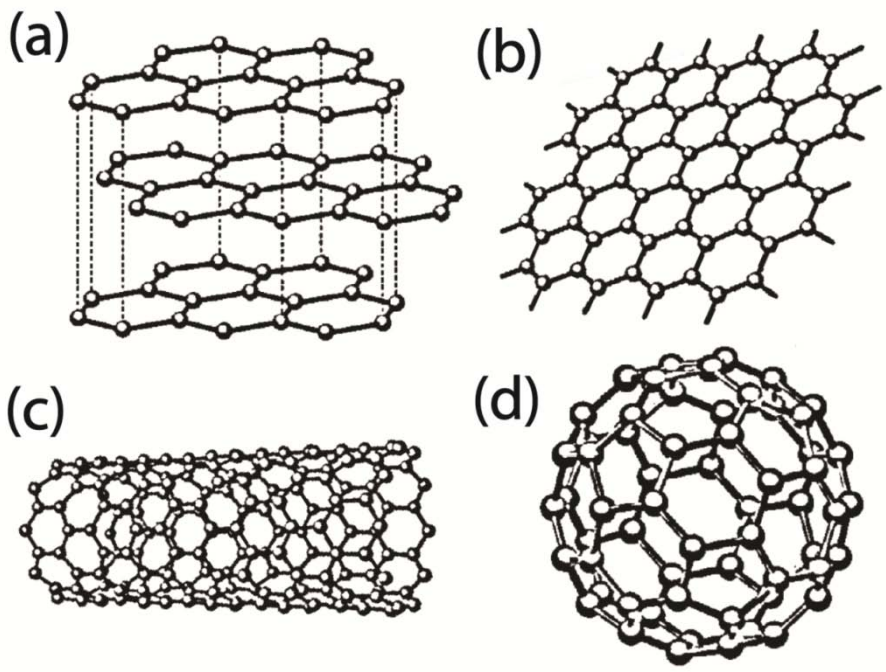

Figure 1.9: *Model structures of carbon allotropes: (a) graphite, (b) graphene, (c) carbon nanotube and (d) fullerene.*

A detailed discussion on the morphological and property characteristics of the various carbon allotropes is given below.

1.11.1. Carbon Nanotubes

Carbon nanotubes (CNTs) are allotrope of carbon possessing hollow cylinder nanostructure composed of one-atom-thick sp^2 carbon framework. These carbon sheets are rolled in a definite manner, which decides the overall properties of CNTs. This pioneering work was done by Iijima in late nineteenth century.[96] Based on the rolling, they are classified into three categories; (i) Armchair (n, n) i.e. m=n, (ii) Zigzag (n, 0) and (iii) Chiral (n, m). The integers “n”

and “m” signify the number of unit vector along the two directions in the honeycomb crystal lattice of graphene. Hence, based on the values of the unit vector (n and m), the properties of CNTs will change. Conversely, more or less, the common properties remain same, for example, tensile strength and elastic modulus. Moreover, CNTs possess high mechanical strength due to the covalent bonding between the neighbouring carbon atoms and high thermal and uni-directional electrical conductivity. Therefore, CNTs have found applications in nanotechnology, electronics and material science and the related technologies. The CNTs have dual characteristics of metallic and semiconducting and the band gap can be tuned from zero to 2 eV, which has great scope of use in miniature electronic devices. Along with this, they are being used as filler/additives for several structural materials.

Owing to the promising properties of CNTs, they have been utilized not only as catalyst support but also as electrocatalysts in the field of energy devices, specifically for fuel cells.[30]One way to use them is by modifying the surface and another way is by changing the electronic structure through hetero-atom doping.[97-101] In view of this, CNTs are modified by chemical treatment to achieve a good fertile surface for nanoparticle decoration and explored as electrocatalysts for fuel cells.[97-101] Secondly, the CNTs are doped with hetero-atoms (namely, N, S, P, and B) to use as electrocatalyst-cum-support.[101]

1.11.2. Carbon Nanofibers

Carbon nanofibers (CNFs) are graphene layers arranged as stacked cones, cups or plates in a cylindrical manner. They are synthesised by vapour grown techniques at temperatures higher over 800 ^{o}C. CNFs with particular dimensions have drawn lots of attention in the field of energy applications, thanks to their potential properties which make them simple to use, like, high thermal, electrical, frequency shielding and mechanical property. They are being extensively utilized in several applications, including selective adsorption, hydrogen storage, polymer reinforcement and catalysts support. There are mainly three types of CNFs[102] (**Figure 1.10**): (i) Herringbone: in which the graphene layers are stacked obliquely with respect to the fiber axis, (ii) Platelet: in which the graphene layers are perpendicular to the fiber axis, (iii) Ribbon: in which the graphene layers are parallel to the growth axis. The above three types of CNFs have different

properties and their characteristics decide their application. However, the herringbone CNF has attracted particular attention due to its peculiar graphene sheets arrangements, which ultimately give higher active centers, better conductivity and surface area.

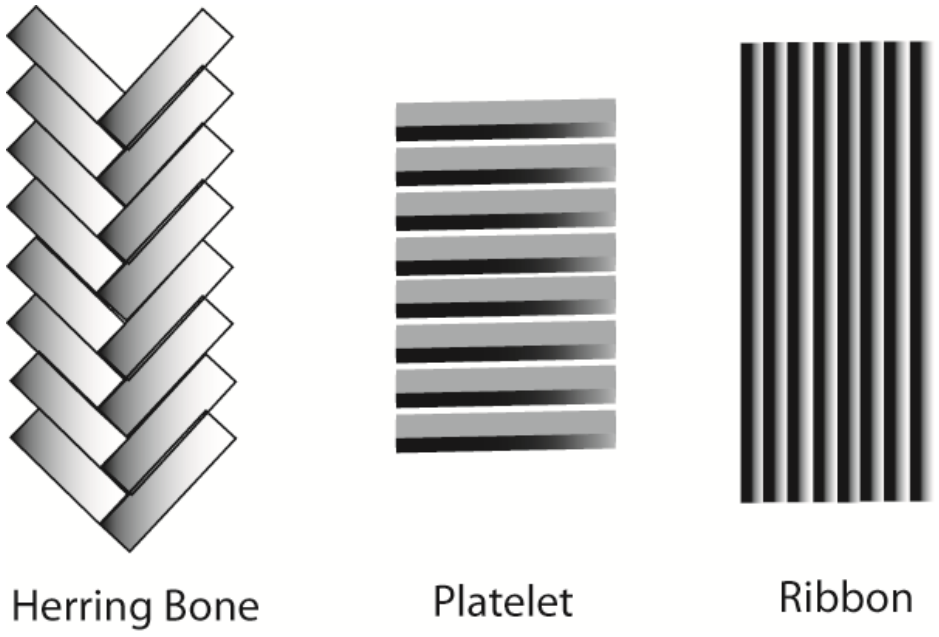

Figure 1.10: *Pictorial representations of the three types of CNFs: (i) herringbone, (ii) platelet and (iii) ribbon.*

High surface area, controlled pore size and pore size distribution are necessary for the application of these materials in a specific end use. Thus, the specific surface area and porosity of CNFs can be significantly modified by an activation process that removes the most reactive carbon atoms from the surface of the structure. The porous texture of the activated carbons depends strongly on the activation process and the nature of the precursor used for the chemical and/or physical treatment. Moreover, it has been reported that the experimental variables have great influence on the porosity of the activated carbons prepared by the chemical activation.[102] Owing to their promising properties CNFs have great future in energy applications. Recently, Beena *et al.*[103] could utilize CNF by decorating Pt nanoparticles on the inner and outer walls and demonstrate its application as an electrocatalyst for PEMFC. Palaniselvam *et al.*[104] also used the CNF as a metal-free electrode for PEMFC applications by doping the surface with hetero atoms.

1.11.3. Graphene

After ground-breaking experiment of Andre Geim and Konstantin Novoselov at the University of Manchester, attention on graphene has increased dramatically. This discovery of nearly single layer graphene brought the Nabel Prize of physics (2010). Mainly, graphene (**Figure 1.9**) is a crystalline allotrope of carbon composed of sp^2 carbon in the form of very thin and nearly transparent sheet possessing 2-dimentiaonal (2-D) properties. It can be described as one-atom thick layer of graphite (**Figure 1.9**). Graphene is a fascinating material in terms of its thermal and electrical conductivity along with good mechanical strength. The most useful property of graphene is that it is a zero-band gap semiconductor, in which both electron and hole are charge carriers. Owing to these extraordinary properties, graphene is now being utilized as flexible and stretchable conductors.

Recently, the properties of graphene have been significantly utilized in the field of electrochemical devices, which include the PEMFCs, batteries, solar cells and supercapacitors. In PEMFCs, graphene is being used as the catalyst support, which increases the electron conductivity during operation. Along with this, since, last two years, graphene has gained attention as a metal-free electrocatalyst in the field of energy conversion devices, especially, in PEMFCs. Palniselvam *et al.*[104] recently have explored the nitrogen doped graphene has a potential catalyst to replace the existing Pt-based electrocatalysts from PEMFCs. Dai *et al.*[105] also could apply N and P-doped CNTs as replacements of Pt. Moreover, Kannan *et al.*[106-107] have reported that the composites of graphene with Nafion and PBI can increase the performance as well as stability of the proton conducting membranes in PEMFCs. Owing to the properties and recent applications of graphene, it has a great future in the energy conversion and storage devices.

1.12. Non-Platinum based Electrocatalysts for Oxygen Reduction Reaction

Replacement of Pt from the PEMFC electrode is a big challenge in front of the scientific community. Therefore, the transition metals like, Fe, Co, Ni, Cu, Mn, Au, Pd, Au-Pd, Cu-Pd, Fe-Pd, Ni-Pd, Fe-Co, Fe-Ni, Co-Ni, Fe- and Cu-complexes have been extensively studied for ORR, in the unsupported and/or supported format.[97-107] Amongst these metals, Fe, Co and Ni are the champions, which have a potential to solve at least the cost issue. In addition to the metal oxides,

some conducting polymers and metallo-phorphyrins are also being positioned as potential materials to substitute the state-of-the-art catalysts (Pt/C). Although it is extensively researched, still there are debates on the structure and nature of the active centers. There are also concerns and claims on the activity and stability of these systems under the real operating conditions. Recently, hetero-atom doped carbon materials have gained a wide attention due to their ability to display nearly comparable ORR activity with Pt/C. In addition, the transition metals dispersed on the hetero-atom doped carbons have shown promising activity in acidic as well as basic environments. Consequently, these materials are expected to have great prospects for future applications in the field of electrochemical devices. In the subsequent section, a discussion on the various approaches used for the synthesis of hetero-atom doped carbon materials, use of NGr for the synthesis of novel metal@NGr core-shell structures and their basic active centers for ORR is included. On the same track, the intrinsic properties of the transition metals to achieve exquisite 3-D structures based on metal-NGr interaction have also been explained.

1.12.1. Hetero-Atom Doped Carbon Allotropes

Taking advantage of different properties of graphene and its reasonable activity towards ORR in alkaline conditions, there has been a great attention by the researchers to build new materials which can display activity not only in alkaline medium but also in acidic conditions. In view of this challenge, recently various hetero-atom (N, S, P and B) doped carbon allotropes have been synthesized by hydrothermal, carbonization, annealing and vapour deposition methods.[108] Under such conditions, the precursor may be used internally or externally to get the desired product. The doped hetero-atom and its nature plays a major role in deciding the ORR pathway.[108] As per the literature reports, in the case of the N-doped materials, various theoretical studies point towards the involvement of the pyridine-N sites towards ORR.[108]

Recently, Dai *et al.*[105] have explored N, P and S ternary-doped metal-free porous carbon materials using metal organic frameworks (MOFs) as templates for ORR by annealing N, S, and P containing MOFs at higher temperature. The synergistic effect of N, P and S ternary-doping helped to achieve positive onset potential for ORR compared to the commercial Pt/C catalyst.

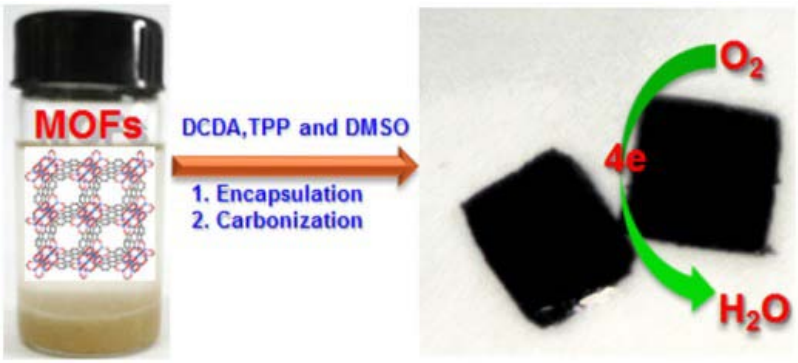

Figure 1.11: *Synthesis scheme of N, S and P co-doped porous carbon material from MOF. [Reprinted with permission from {Scientific Reports, 2014, 4, 51303}, and we fully acknowledge the authors of the paper Dai et al.]* [105]

Banerjee *et al.*[109] have reported the nitrogen containing porous organic framework (POF) as a template to achieve highly porous and conducting N-doped carbon (**Figure 1.12**), which has shown better kinetics towards ORR compared to the state-of-art Pt/C electrocatalyst.

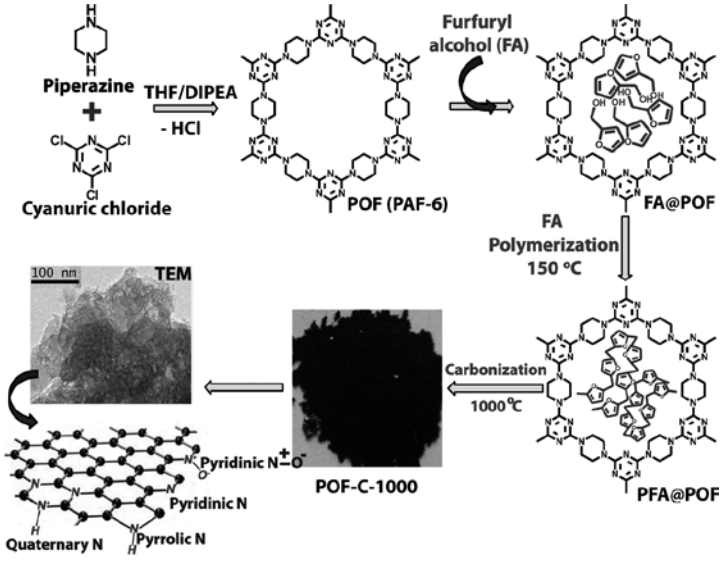

Figure 1.12: *Synthesis of N-rich porous carbon material POF-C-1000 from a porous organic framework (POF)at 1000 °C by using a nanocasting method.*[109] *[Reprinted with permission from {Chemistry - A European Journal, 2013, 19, 974-980}. Copyright © 2013 WILEY-VCH Verlag GmbH & Co. KGaA, Weinheim, John Wiley and Sons, License Number: 3505791145047]*

Dai *et al.*[110-111] in a recent report highlighted the synthesis of *in-situ* N-doped vertically aligned carbon nanotubes (VA-NCNTs) by chemical vapor deposition technique for alkaline fuel

cells (**Figure 1.13**). During a real application validation in air-saturated 0.1 M KOH, the authors observed a steady-state output potential of -80 mV and a current density of 4.1 mA/cm^2 at -0.22 V whereas the Pt/C electrode delivered the steady-state voltage of -85 mV and current density of 1.1 mA/cm^2 at -0.20 V. The incorporation of electron-accepting nitrogen atoms in the conjugated nanotube carbon framework appears to impart a relatively high positive charge density on adjacent carbon atoms. This effect, coupled with aligning the NCNTs, provides a 4e$^-$ oxygen reduction pathway with excellent performance.

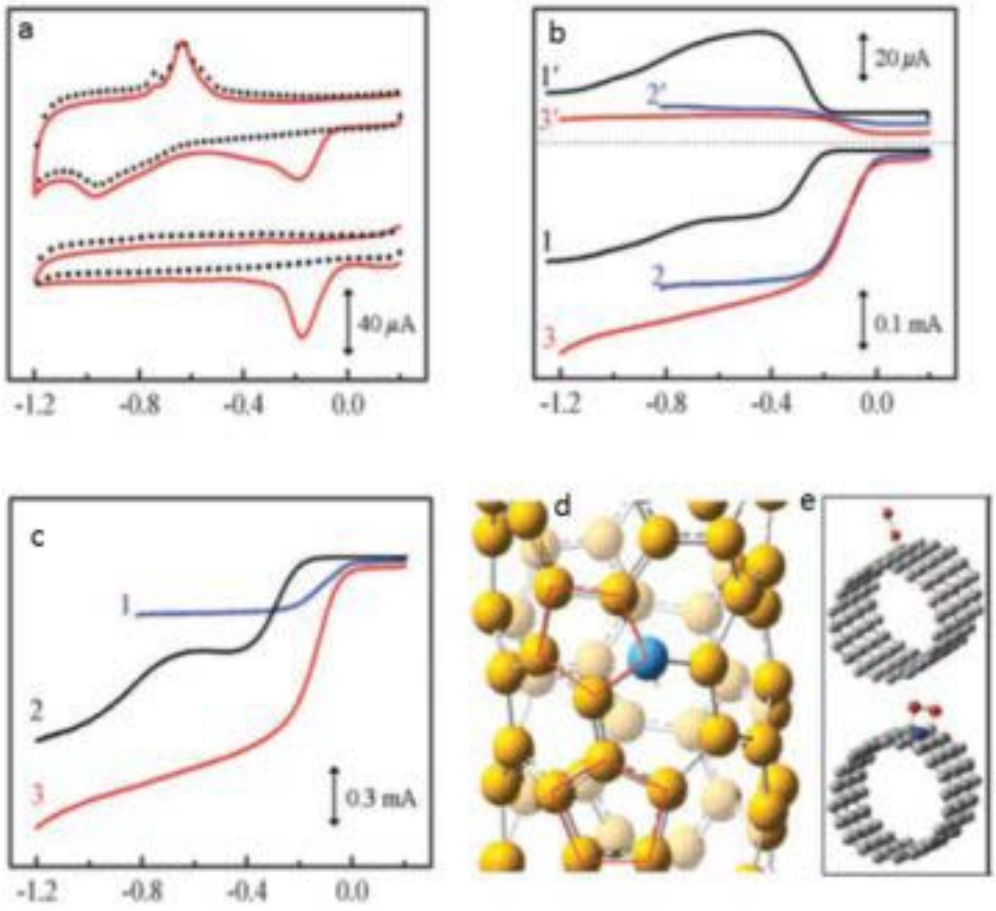

Figure 1.13: *(a) CVs for oxygen reduction at the unpurified (upper) and electrochemically purified (bottom) VA-NCNT/glassy carbon (GC) electrodes in the argon-protected (dotted curves) or air-saturated 0.1 M KOH (solid red curves) at the scan rate of 100 mV/s, (b) RRDE voltammograms and the corresponding amperometric responses for oxygen reduction in air-saturated 0.1 M KOH at the NA-CCNT/GC (curves 1 and 1′), Pt-C/GC (curves 2 and 2′), and NA-NCNT/GC (curves 3 and 3′) electrodes at the scan rate of 10 mV/s. The electrode rotation rate was 1400 revolutions per minute (rpm), and the*

*Pt-ring electrode was poised at 0.5 V, (c) RRDE voltammograms for oxygen reduction in air saturated 0.1 M KOH at the Pt-C/GC (curve 1), VA-CCNT/GC (curve 2), and VA-NCNT (curve 3) electrodes (because of the technical difficulties associated with the sample mounting, amperometic responses with the Pt ring electrode were not measured for the vertically aligned carbon nanotubes), (d) calculated charge density distribution for the NCNTs and (e) Schematic representations of the possible adsorption modes of an oxygen molecule at CCNTs (top) and NCNTs (bottom).[Reprinted with permission from {**Science**,2009, 323, 760-764}. Copyright {2009} The American Association for the Advancement of Science, License Number: 3505811024438].*[111]

Also, Dai *et al.*[110] have reported the *in-situ* N, and P co-doped vertically aligned carbon nanotubes prepared by a chemical vapor deposition technique (**Figure 1.14**), which showed better activity than Pt/C.

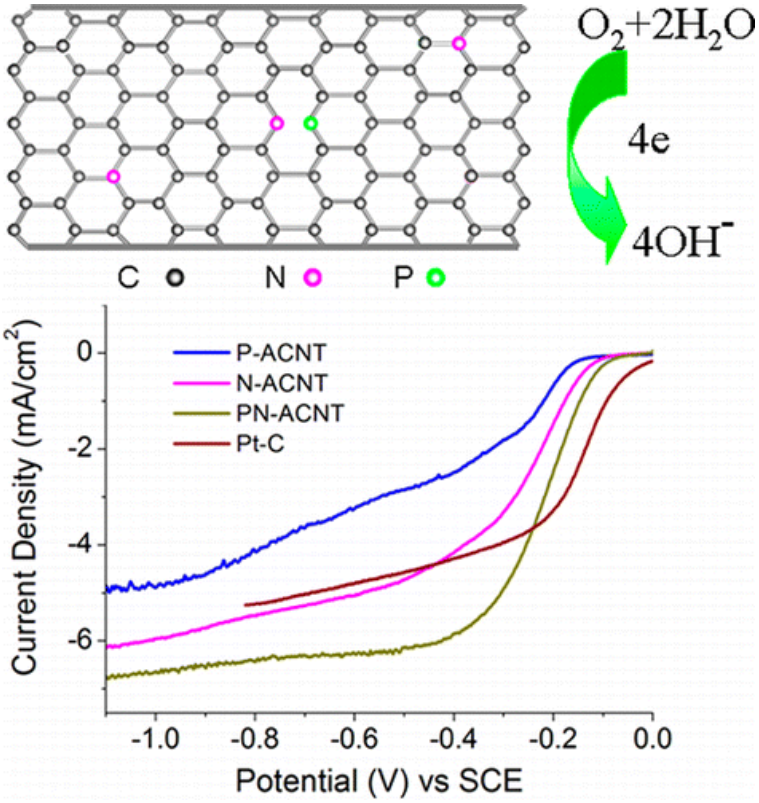

Figure 1.14: *A schematic illustration of the in-situ prepared N and P co-doped CNT and its performance characteristics for ORR. [Adopted with permission from (J. Phys. Chem. Lett. 2012, 3, 2863-2870). Copyright (2012) American Chemical Society].* [110]

Collectively, the hetero-atom doped carbon materials have great scope in near future. Therefore, it has attracted the attention of the fuel cell researchers who are looking for cost effective alternatives for the Pt based catalysts. Although so much of work is reported in the literature, still there are some pin holes which need to be filled effectively like improving the conductivity, understanding the exact nature of the active centers and reducing the overpotential associated with the ohmic drop, etc. Hence, coupling of hetero-atom doped carbon with metal particles is being considered as an effective way to sort out this issue, where the synergistic effects of the metal and carbon is expected to help to tune the properties of the catalyst towards improved ORR.

1.12.2. Non-Noble Metal Based Electrocatalysts

The non-noble metal supported on the conducting substrates or bi-non-noble metal based engineered structures have been come up as good contestants to replace the expensive Pt. However, despite the enormous research in the field of non-noble metal based electrocatalysts, the activity still is lagging behind that of the Pt based systems due to the lower number of the active centers in the former case. These systems also possess higher ohmic drop, which adds to the reduction in the performance. Therefore, non-noble metals (Cu, Co, Ni, and Fe, etc.) supported on or capped by carbon materials (graphene, CNTs, CNFs, carbon nanohorns (CNHs), etc.) with covalent bonding between them could be a promising solution to this issue.[5, 112-115] These systems have been synthesised by both *in-situ* and *ex-situ* methods. Some of the findings are discussed in the sub-sections.

1.12.2.1. Metal-Carbon Core-Shell Structures

Since last few years, the metal-carbon core-shell structures have gained significant attention due to their structural benefits which can help to meet the requirements on cost as well as activity.[5, 112-115] Main advantage of these metal-carbon materials is the modulated properties of the carbon shell owing to the interaction of the s-orbital of the surface carbon atom with the d-orbital of the inner metal core.[5, 112-115] This mutual interaction between the orbitals of the two dissimilar neighbouring atoms changes the electronic structure of the surface carbon atom and thereby indirectly increases the overall conductivity as well as activity towards the

electrocatalysis. Specifically, in case of ORR, the distribution of charges from the core to shell makes the non-metallic shell more reactive towards the dissociative adsorption of oxygen prior to its reduction.

There is a report by Chen *et al.*[112], which highlights the synthesis of a novel core-shell-structured hybrid ORR catalyst possessing nitrogen-doped porous Fe/Fe_3C@C nanoboxes supported on graphene (N-Fe/Fe_3C@C/Gr) sheets *via* simple pyrolysis of graphene oxide-supported iron-based MOFs (F**igure 1.15**). N-Fe/Fe_3C@C/Gr exhibited higher electrocatalytic activity than Pt/C by maintaining long-term stability and superior methanol tolerance.

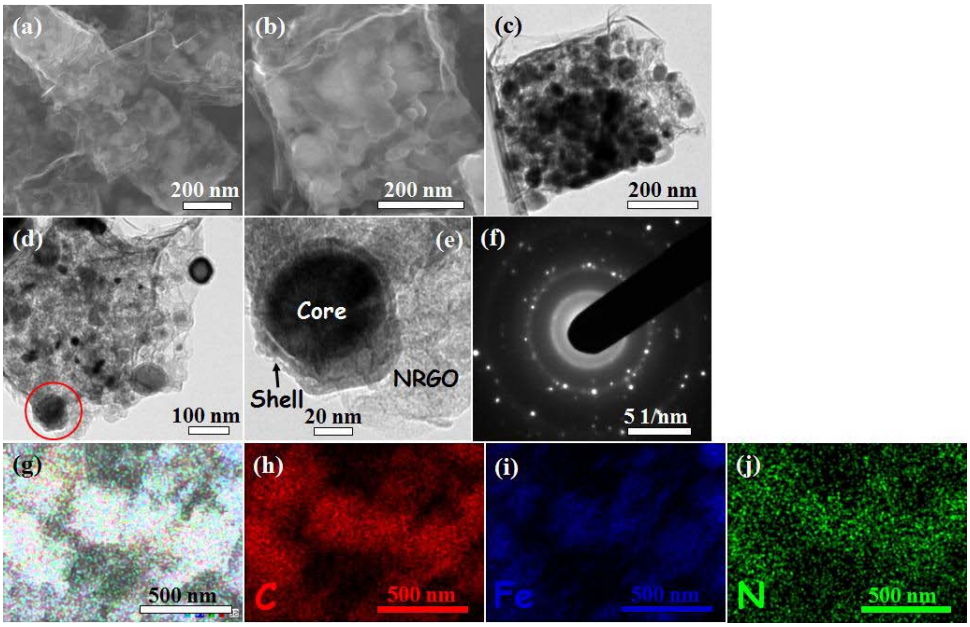

Figure 1.15: *FESEM images (a-b), TEM images (c-e), SAED pattern (f) and corresponding elemental mappings (g-j) of N-doped Fe/Fe_3C@C/RGO.* [112] *[Reprinted (adapted) with permission from {Advanced Energy Materials, 2014, 4. DOI:10.1002/aenm.201400337}. Copyright © 2014 WILEY-VCH Verlag GmbH & Co. KGaA, Weinheim, John Wiley and Sons, License Number: 3506380068170]*

Similarly a report by Chan *et al.*[5] illustrates preparation of a core-shell catalyst possessing high surface area and large pore volume iron-nitrogen-doped hollow core and mesoporous carbon shell (Fe-N-HCMS), which provides high activity for the ORR with excellent mass transfer, durability, and methanol tolerance characteristics.

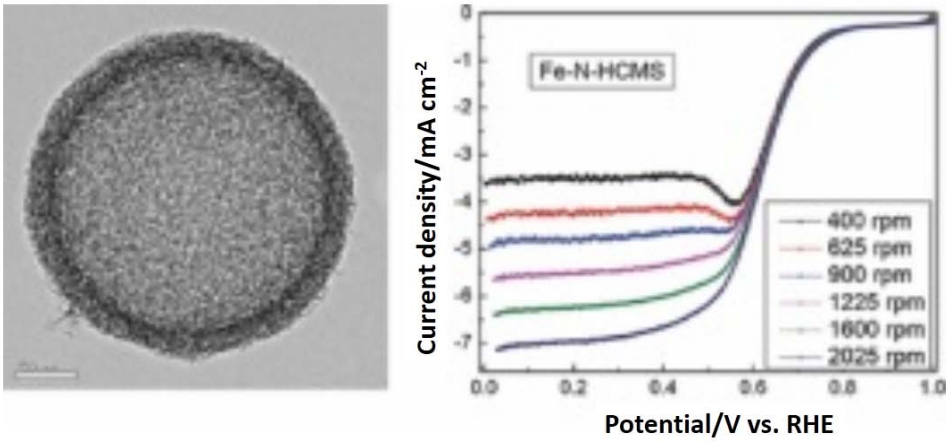

Figure 1.15: *(left) TEM image of iron-nitrogen-doped hollow core and mesoporous carbon shell (Fe-N-HCMS), (right) LSVs recorded at different rotation rates of the working electrode.*[5] *[Reprinted with permission from {Advanced Energy Materials, 2014. DOI:10.1002/aenm.201400840}. Copyright © 2014 WILEY-VCH Verlag GmbH & Co. KGaA, Weinheim, John Wiley and Sons, License Number: 3507610020181]*

Liu *et al.*[113] have reported a one-step technique for the controllable creation of metal-graphene core-shell structures, hollow graphene nanospheres and metal nanoparticles dispersed on graphene. These metal-graphene nanostructures were used for the organic molecule conversion, like, oxidation of cyclohexene to cyclohexanol.

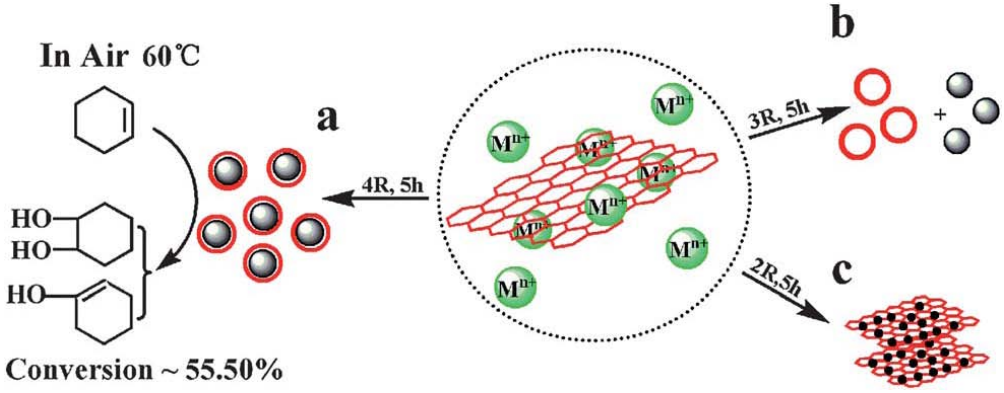

Figure 1.16: *Synthesis strategy for obtaining different metal–graphene complex nanostructures by varying the molar ratios of graphene to metal salts: (a) core– shell nanostructures, (b) hollow graphene nanospheres and (c) a high density of metal nanoparticles supported on graphene (M and n are respectively representative of metal ion and valence; R = 1 $mg_{(graphene)}$ per 100 $mM_{(metal\ salt)}$.*[113] *[Reprinted with permission from {Nanoscale, 2014, 4, 4964-4967}, and we fully acknowledge the authors of paper].*

In brief, the non-noble metal encased by another non-noble metal has shown favourable activity modulation towards the electrocatalytic activity. However, due to its limited scope or structural instability in acidic conditions, these systems are still being considered as lying in their early evolving stage. However, as discussed above and as cited in some of the recent literatures, some strategies could be developed to solve at least the stability issue. It is found that, shielding of the non-noble metal with more stable and active layer of carbon (such as heteroatom doped carbon) could tackle the issue effectively. Some of the findings in this direction have already shown better activity and stability towards the electrocatalysis.[5, 112-115]

1.12.2.2. Non-Zero Dimensional Electrocatalysts

As discussed earlier in **Section 1.10.3**, some Pt-based hetero-nanostructures possesses beautiful geometry with higher number of active centred hollow structures. These structures possess better molecular accessibility and are reported to be functioning as better catalysts for the applications like fuel cells, metal-air batteries and water splitting reactions etc. In view of these and further to reduce the cost without sacrificing the overall activity, recently, new non-noble metal based (coupled with/without carbon) structures have been reported for ORR, hydrogen evolution reaction (HER), oxygen evolution reaction (OER), etc. Some-of-the findings are highlighted below.

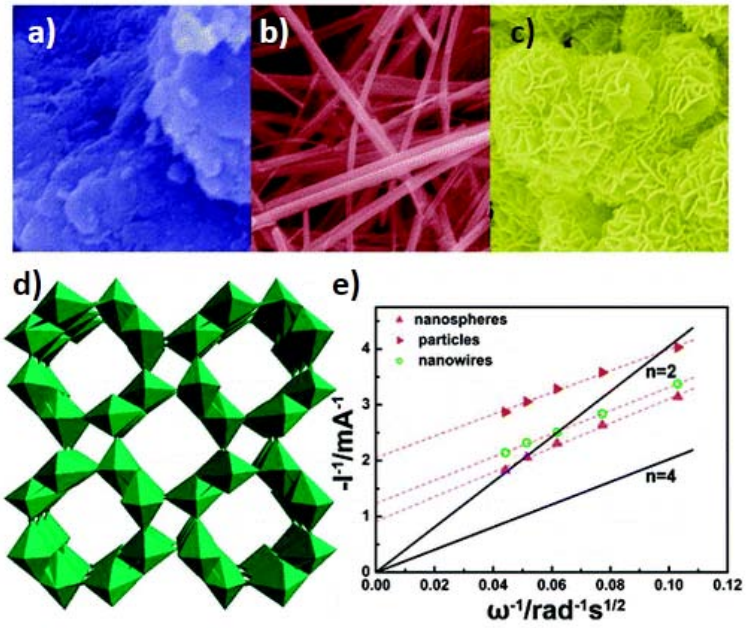

Figure 1.17: *SEM images of (a) α-MnO_2 bulk particles, (b) nanowires, (c) flowerlike nanospheres, (d) crystal structure of α-MnO_2 and (e) K-L plots for the three α-MnO_2 samples at -0.3 V (vs. Ag/AgCl).*[116] *[Reprinted with permission from {Chemistry of Materials* ***2009****, 22, 898-905}. Copyright (2010) American Chemical Society].*

Chen *et al.*[116] reported the geometrical effect of MnO_2-based nanostructures (sheet, wires and flowers) for ORR in alkaline media. The activity of the MnO_2 based nanostructures is found to be strongly depending on the crystallographic structure and the morphology. Moreover, excluding the structural impact on the activity, it follows an order of α- > β- > γ-MnO_2. Furthermore, among the α-MnO_2, nanospheres and nanorods are shown to be superior compared to the microparticles in terms of the positive oxygen reduction potential and improved current density (**Figure 1.17**). The α-MnO_2 followed a 4-electron reduction pathway. Despite this, Ni nanoparticles dispersed on α-MnO_2 nanowires (MnO_2-NWs@Ni-NPs) further improved the overall ORR catalytic activities. Therefore, the alignment of the MnO_2 in the particular direction or an assembly of MnO_2 in the form of flower makes the system more viable for the electrocatalysis.

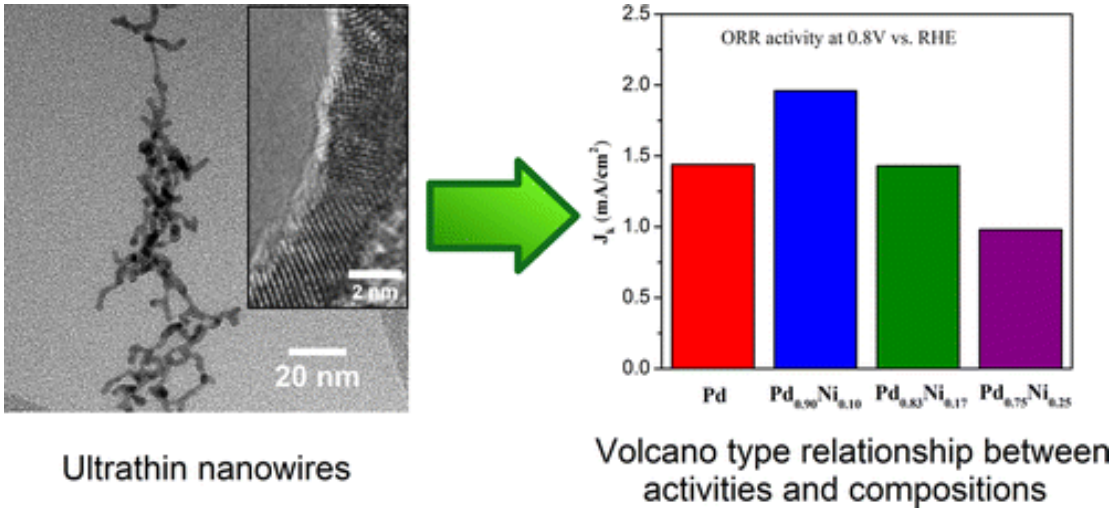

Figure 1.18: *(left) TEM image of $Pd_{0.90}Ni_{0.10}$ nanowires and (right) volcano type relationship between the activity and compositions.*[117] *[Reprinted with permission from {ACS Catal.,* ***2014****, 4 (8), 2544–2555}. Copyright (2014) American Chemical Society].*

Wang *et al.*[117] have reported the synthesis of Pd-Ni 1-D nanowires by using surfactant and later, purified by butylamine-based surfactant-exchange process. The performance of the

different compositional Pd-Ni nanowires has been utilized for the ORR (**Figure 1.18**). Moreover, this work represents the volcano-type relationship between the chemical compositions with respect to the activity towards the ORR. As per the authors, the $Pd_{0.90}Ni_{0.10}$ sample exhibited highest specific activity of 1.96 mA/cm^2 at 0.8 V (*vs.* RHE) as compared to all the prepared different compositional Pd-Ni nanowires. Therefore, the 1-D nanowires of Pd-Ni have shown better activity and stability under the operating conditions compared to Pt/C.

Lee *et al.*[118] have given an explanation on the activity of nanowires (NW) and their porous structure for ORR. The authors described the preparation of 1-D nanocomposite wires of Ag, Au and AgCl (Ag/Au/AgCl) and studied the effect of systematic change in the relative composition of Au and Ag on the ORR activity in alkaline medium. The Ag-wires were galvanic displaced with Au to get Ag/Au/AgCl composite NW. The Ag/Au/AgCl core-shell structures were changed to the porous hollow 1-D wires, as the Au precursor concentration increases (**Figure 1.19**). As a result, the Ag and AgCl concentration got decreased with increase in the Au content. The compositional ratio of Ag, Au and AgCl as 4 : 86 : 10 has shown high ORR current with positive onset potential, better stability and ethanol tolerance under the operating conditions. Overall, this study revealed that the Ag-Au nanocomposites could be a good alternative to the Pt-based cathode catalysts in fuel cells as well as in metal-air batteries.

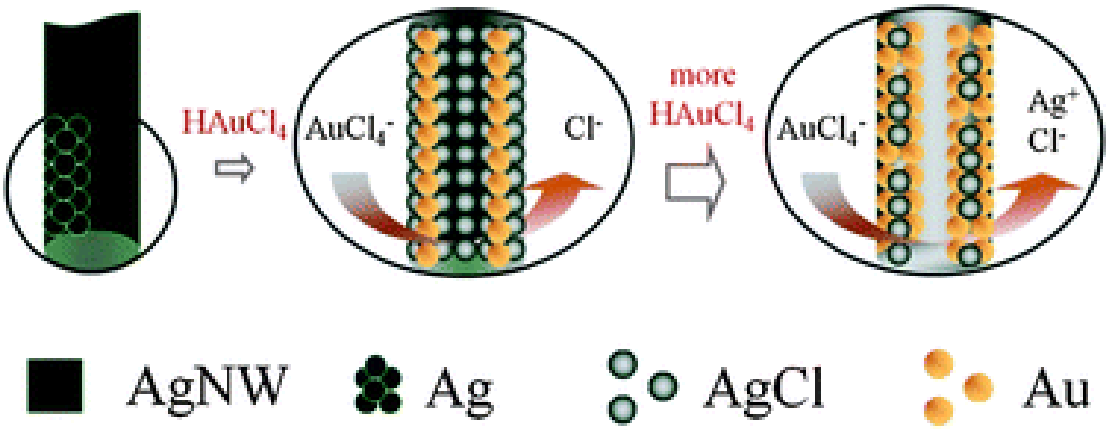

Figure 1.19: *Schematic illustration for the galvanic replacement reaction between AgNW and $AuCl_4^-$ as a function of the concentration of $AuCl_4^-$. Step (I): deposition of Au and formation of AgCl; step (II): deposition of Au and dissolution of AgCl.*[118] *[Reproduced from {J. Mater. Chem.,* ***2012****, 22, 15285-15290} Copyright (2012) with permission of The Royal Society of Chemistry, Licence Number: 3530160418846].*

The systematic structural transformation of Cu_2O in the form of nanocages, nanoframes and truncated rhombic dodecahedral structures is illustrated by Hung *et al. in a recent report*[119] (**Figure 1.20**). After mixing the reagents, the nanoframes (Type-I) is just a skeleton of the (110) faces (**Figure 1.20**). Further crystal growth transforms these nanoframes into nanocages with predominantly enclosed (100) faces. In addition, the effect of addition of ethanol in the nanocage solution and subsequent HCl etching disrupted the adsorption of the surface-capped sodium dodecyl sulfate and assisted the favoured engraving of the (110) faces. This complicated process results in the formation of nanoframe structures (Type-II) (**Figure 1.20**). These core-cage composite materials can find possible applications in various areas such as drug delivery, molecular sensing, and so on.

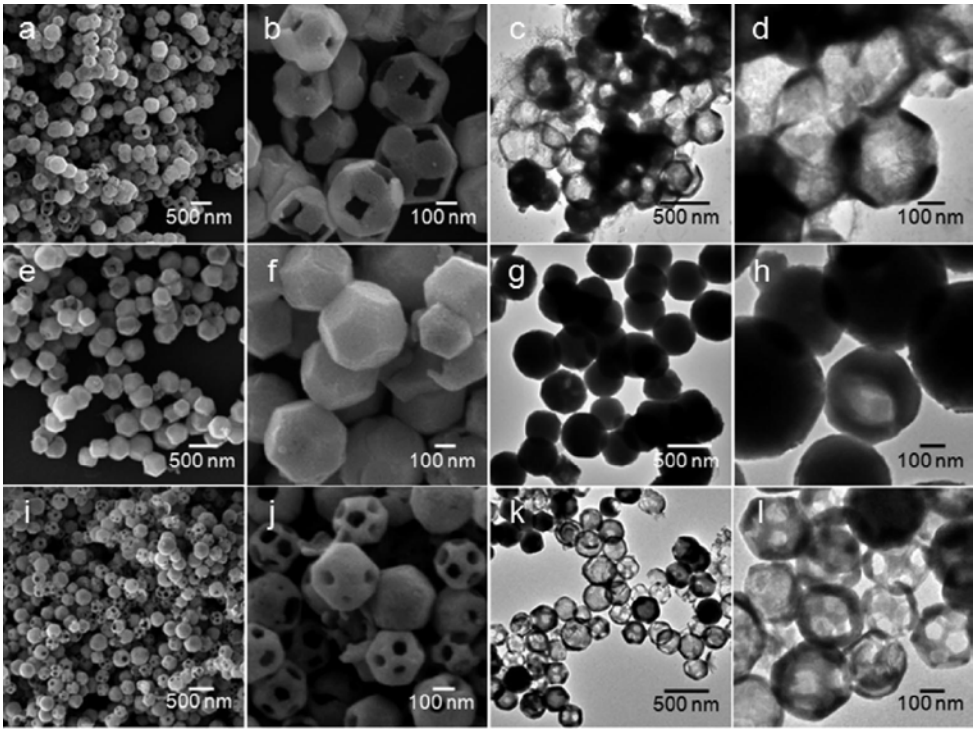

Figure 1.20: *SEM and TEM images of the truncated rhombic dodecahedral Cu_2O nanoparticles: (a-d) Type-I nanoframes, (e-h) nanocages and (i-l) Type-II nanoframes. The magnified images clearly show the hollow structures of the nanoparticles.*[119] *[Reprinted with permission from (J. Am. Chem. Soc. 2008, 130, 12815–12820). Copyright (2008) American Chemical Society].*

Wiley *et al.*[120] have summarised all the possible way of synthesis of noble/non-noble metal based anisotropic structures by simple oxidative etching methods. These authors have

claimed the oxidative etching as a versatile technique to achieve systematic nucleation and growth of the metal particles at atomic level itself. Furthermore, the same technique could be used to reorganize nanocrystals through the atomic addition and/or subtraction. Mainly, in the nanocrystals synthesis, nucleation, evolution from nuclei into seeds and finally growth of seeds to crystals are the three major stages involved. The oxidative etching plays a major role at these mentioned stages. Moreover, the etching can have several roles, like, control of single crystal vs. twinned structures, directional or sequential rate of atomic addition, and surface activation to supply the spot or centers for atomic additions. These things can be accomplished in a single stage. The oxidative etching results into different anisotropic structures, which possess unique properties (**Figure 1.21**). This could have direct or indirect role in deciding the overall characteristics of the material during electrolysis, which has been explained by Prof. Wiley and Xiong. [120]

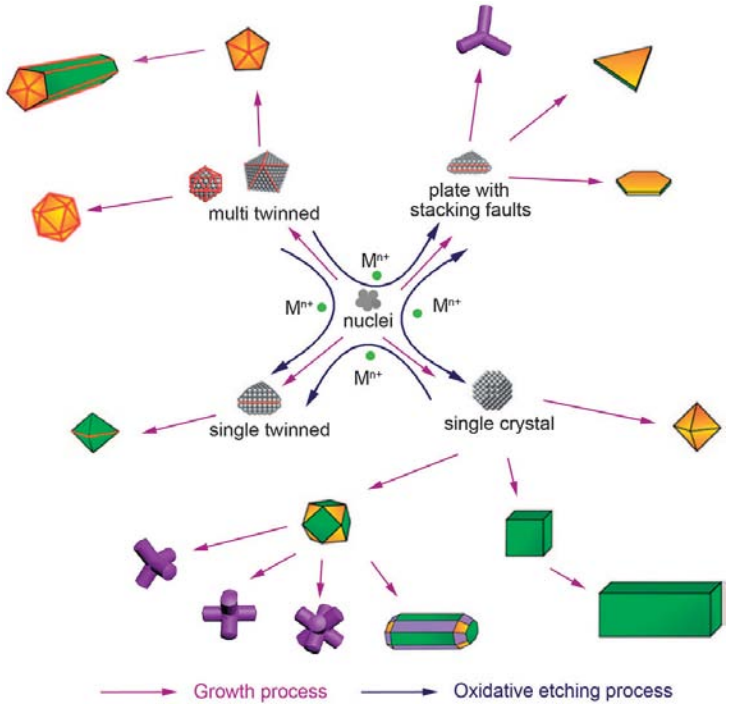

Figure 1.21: *Summary of the reaction pathways affected by oxidative etching, leading to fcc metal nanocrystals with different shapes.*[120] *[Reproduced from (Chem. Soc. Rev., 2014, 43, 6288-6310) with permission of The Royal Society of Chemistry, License Number: 3530691129777].*

In 2011, Gonzalez *et al.*[121] presented the beautiful structures of Ag-Au, carving the Ag seeds at the nanoscale. The sequential galvanic exchange between the Ag-seed (template) with

gold chloride followed by Kirkendall growth could resulted into the well-defined atomically arranged hollow structures. Authors have explained how the difference in the reduction potential values of the two different metals can be utilized to build these kinds of materials. Moreover, the systematically complex chemistry between the Ag particles with the gold chloride resulted into selective displacement reaction and formed AgCl and Ag-Au nanostructures within the reaction conditions. **Figure 1.22** represents the spherical, cubic and cylindrical morphologies of Ag-Au by galvanic exchange and Kirkendall effect. A discussion on the Kirkendall effect is already given in S**ection 1.10.3**.

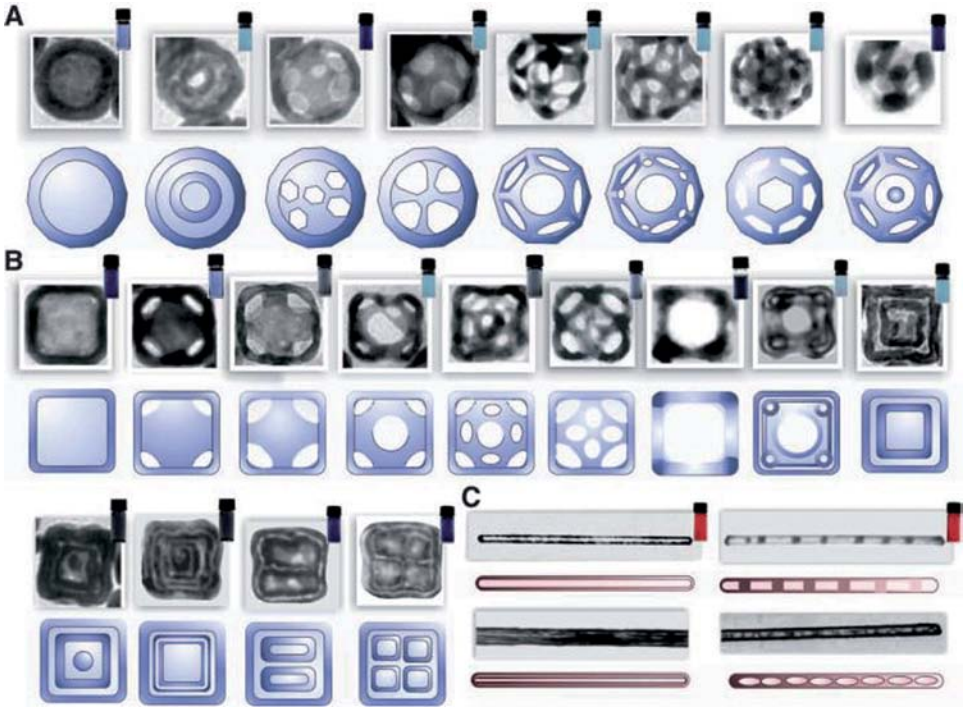

Figure 1.22: *The synthetic route reported in this work produces structures with (**A**) spherical, (**B**) cubic, and (**C**) cylindrical topologies. TEM images are accompanied by drawings that represent the morphology of each nanostructure.*[121] *[Reprinted with permission from {**Science**, 2011, 334, 1377-1380}. Copyright {2011} The American Association for the Advancement of Science, License Number: 3530730599037].*

Overall, from the non-zero dimensional Pt-free structures as cited above, it can be concluded that the non-zero dimensional structures possess higher number of active sites due to their ordered arrangement and intra-molecular connectivity within the structure. Moreover, along with the different anisotropic structures (cube, sphere, rods, wires, etc.), the carved/hollow/surface defective/3-D active nanocage structures are more effective as they

possess more surface-to-volume ratio with better molecular accessibility within the structure. These properties make the system more viable and interesting in the field of energy conversion as well as storage.

1.13. Importance of Oxygen Reduction Reaction Electrocatalysts for Metal-Air Battery Applications

The aforementioned materials developed for ORR are important not only in the application of PEM fuel cells but they also have great scope in the field of metal-air batteries. Commonly, the overall efficiency of both the systems has been administrated by the cathode material activity. Hence, the materials which have the potential to serve as efficient cathode catalysts for PEMFC can be effectively used as cathode materials in the field metal-air batteries. Therefore, use of better ORR catalyst as the air electrode in the metal-air batteries can broaden the scope of the materials.

1.13.1. Superiority of Zn-Air Battery Compared to Li-ion/Li-Air Battery

Rechargeable Li-ion batteries are being conventionally televised as the most efficient and trustworthy devices compared to the various electrical storage devices (primary Zn-MnO_2 (Zn-Mn), rechargeable lead-acid and nickel-metal hydride (Ni-MH), etc.), which could convert chemical energy directly into electrical energy and/or electrical to chemical energy by reversible redox reactions.[16, 18] Moreover, Li-ion battery is being considered as the most capable storage device, because of its relatively long-cycling life (>5000 cycles) and high-energy efficiency (>90%). Conversely, the Li-ion batteries are facing drawbacks due to their lower energy density (theoretical value of energy density is ~400 Wh/kg).[16, 122-124] Even with the use of the currently available materials during fabrication, it is still tough to achieve the high energy demands required for transport vehicles.[125]Along with this, Li-intercalation during the charging and discharging limits the energy density of the Li-ion batteries. In this perspective, it is an obligatory to develop a high energy density storage device. To overcome this issue, one needs to avoid the intercalation mechanism during charge-discharge. Therefore, substitution of intercalation material (cathode electrode) with a catalytically active ORR and OER electrode may solve the existing energy density issue in the storage devices.[16, 18, 21, 122-129] These devices are termed as metal–air batteries, namely, Zn–air and Li–air batteries. These metal-air batteries

have gained ample attention of researchers because of their extremely high energy density, low cost, and environmentally friendly operation.[21, 126-129] Additionally, the metal-air batteries produce energy *via* redox reaction between the metal (Zn/Li) and the oxygen in air.[21, 126-129] Among the metal-air batteries, mainly, the Li-air and Zn-air batteries possess very high theoretical energy density of 11700 and 1100 Wh/kg, respectively.[21, 126-129] Even, these values are better than that of the other traditional batteries (primary Zn-MnO_2 (Zn-Mn), rechargeable lead-acid, nickel–metal hydride (Ni-MH), Li-ion etc.).[18] In addition, among the metal-air batteries (*i.e.* Zn-air and Li-air), Zn-air batteries have added advantages, such as a flat discharge voltage plateau, high safety, low cost, open system, long shelf-life and higher achievable energy density.[16, 18, 21, 122-129]

1.13.2. General Characteristics of Zn-Air Battery

The characteristics of the Zn-air batteries are listed as:

1. Highest capacity-to-volume ratio
2. Relatively flat discharge curve
3. More stable voltage at high current
4. Constant internal resistance
5. Activated by just exposing cathode side for air access
6. Better service maintenance
7. Low cost
8. Higher energy density
9. Easy fabrication
10. Open set-up

1.14. Working Principle of Zn-Air Batteries

Basic fundamental reactions of a Zn-air battery are similar to the fuel cells. Here, instead of hydrogen oxidation in the case of a fuel cell, Zn-oxidation takes place at anode side of the Zn-air battery. On the other hand, the cathodic reaction, *i.e.* ORR, is same in both the systems. Hence, the Zn-air battery is also called as Zn-air fuel cells. In both the devices, sluggish ORR decides the overall efficiency of the system.

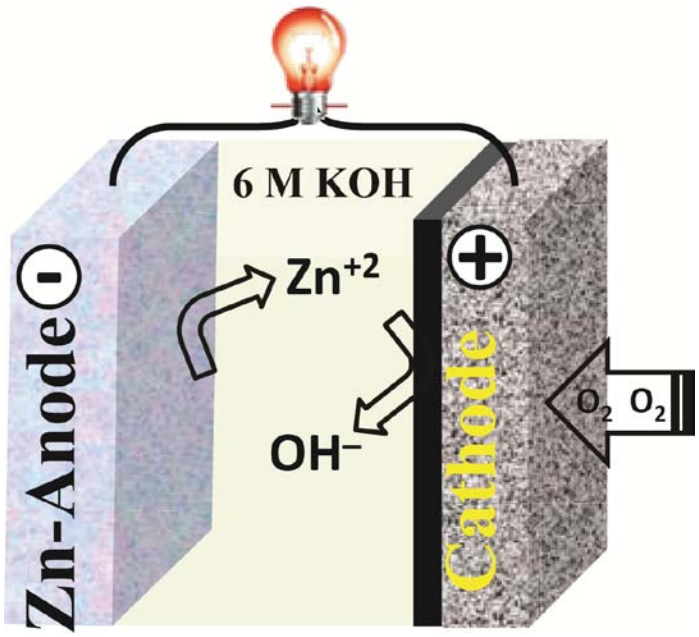

Figure 1.23: *The schematic illustration of a Zn-air battery.*

In brief, a Zn-air battery generates the electricity from the chemical reactions occurring at the anode and cathode as represented in the figure (**Figure 1.23**). Mainly, the Zn-air battery is consisted of having three main parts, namely, (i) anode (Zn-metal), (ii) cathode (ORR catalysts), and (iii) alkaline medium (ionic conductor). During the actual chemical reaction, at the cathode, the oxygen enters the cell through the porous gas diffusion electrode (GDE) and comes into contact with the positively charged electrode and generates the hydroxyl (OH^-) ions. These OH^- ions transport to the anode side through the aqueous KOH electrolyte and react with the Zn-metal (at anode), which results into the oxidation of Zn to form a zincate ion, which eventually, splits into two hydroxyls, water molecule and zinc oxide, liberating two electrons. These electrons travel through a circuit to power up a device (**Figure 1.23**). The reactions in the Zn-air alkaline battery during the discharge is shown below (**Equation 1.21-1.23**):

Cathode : $O_2 + 2H_2O + 4\,e^- \rightarrow 4OH^-$ (1.21)

Anode : $2Zn \rightarrow 2Zn^{+2} + 4e^-$ (1.22)

Overall : $2Zn + O_2 + 2H_2O \rightarrow 2Zn(OH)_2$ (1.23)

1.15. Roadblocks of Commercialization of Zn-Air Batteries

Similar to PEMFCs, Zn-air battery is facing issues due to the sluggish cathodic reaction, *i.e.* ORR, which limits its overall efficiency. Zn-air batteries have very high achievable energy density compared to the traditional Li-based batteries. It is mainly attributed to the absence of intercalation-deintercalation process during the charging-discharging process due to the use of an electro-catalytically active material as the air electrode. Although the Zn-air battery has been studied from decade, it still needs improvement in efficiency by deploying better ORR electrocatalysts in the system. Along with this, oxidation of the Zn-metal produces the inactive Zn-oxide which will be accumulated on the surface of the electrode, creating barricade for further reaction. This is also being considered as a big challenge to fabricate the reversible (secondary) Zn-air battery.[22] To achieve reversibility, dual characteristic electrocatalyst which possesses ORR and oxygen evolution reaction (OER) activity has great future. Therefore, the sluggish cathode reaction (ORR/OER) is the major stumbling block in front of its wide-spread applications in the field of energy generation. Along with this, the fabrication strategy, electrolyte leakage and porosity of the conducting support material also decide the overall performance.

In addition, the performance of the Zn-air battery is affected by the factors like, voltage drop during the polarization, carbonation of the electrolyte, transpiration of water, and efficiency.[130] During polarization, the initial voltage drop is found to be very sharper with increasing the current compared to the other types of batteries, may be due to the oxygen diffusion limitations.[130] Another factor is the vaporization and carbonation of the electrolyte, since the Zn-air battery is an open system. The KOH electrolyte is vulnerable to absorbing CO_2 from ambient air which leads to crystallization of carbonate in the porous cathode electrode (**Equation 1.24 and 1.25**) and causes mechanical damage, which leads to deterioration of the performance. The reactions of CO_2 with the KOH electrolyte can be represented as below:[130-132]

$$CO_2 + OH^- \longrightarrow CO_2^{3-} + H_2O \qquad (1.24)$$

$$CO_2 + KOH \longrightarrow K_2CO_3 + H_2O \qquad (1.25)$$

During this process, the water molecules get transferred to atmosphere in the presence of partial pressure difference between the electrolyte and the air. Hence, loss of water increases the concentration of the electrolyte and ultimately increases its viscosity and eventually drying out and premature failure. Overall, the greatest challenges lie within the air electrode of the zinc-air battery. The problem associated with the air electrode has already been mentioned above (sluggish ORR and OER, high overpotential, etc).[133] In addition, parasitic products such as hydroperoxyl radicals generated during the ORR can lead to earlier degradation of the active catalysts, which will impact the durability and the efficiency of the zinc-air battery. Therefore, this thesis will further investigate towards developing stable and effective catalysts for ORR.

1.16. Scope of the Research and Objective of the Present Work

Based on the solid groundwork done by the researchers and critical literature survey, it is very much clear that, both the energy conversion and storage devices are struggling for the wide-spread applicability due to improper implementation of the components in the systems and major prevailing issues like lower activity (in terms of higher overpotential) and cost of the electrocatalysts used. Therefore, lots of efforts have been taken by the researcher to reduce the overpotential gap by tuning the electronic and geometrical properties of the electrocatalysts. The synthesis of definite shaped mono- or multi-metallic electrocatalysts in the supported and/or unsupported form has large scope of research to overcome some of the pertinent issues in this field. Specifically, combination of the noble metal Pt with non-noble metals like Cu, Fe, Ni, etc. can make the system more efficient than the Pt alone. In view of this, engineered structures of Cu-Pt, Ni-Pt, and Fe-Pt, etc. in the form of alloy, core-shell, and hollow nanocage have been developed, which are found to be displaying better activity compared to Pt alone. Moreover, the dispersion of such engineered structures on a support substrate is a challenging task. Hence, there is a scope to develop suitable one-pot synthesis techniques, which can resolve the issues related physical and chemical aspects of the materials being used in energy applications like fuel cells, metal-air batteries etc.

In line with that, I focused on the synthesis of low-Pt and Pt-free engineered structures by using simple and easy techniques for ORR along with the counter reaction of metal-air battery, *i.e.*, oxygen evolution reaction. The main objectives of the present work are listed below:

1. One-pot synthesis of low-Pt based core-shell structures by shielding the concentrated non-noble metal core with noble metal shell and the simultaneous dispersion of the core-shell particles on the conducting substrate by developing a commercially feasible surface-modification-cum-anchoring strategy.
2. Investigation of the modulated property characteristics as accomplished by the interactions between the core and shell phases in the core-shell systems by adopting various physical and electrochemical characterization methodologies.
3. Fundamental understanding on the influence of the shell thickness on the intrinsic ORR activity of the core-shell catalysts and the catalyst layer thickness on the single cell performance characteristic in the electrodes derived from the core-shell structured catalysts.
4. Investigation of the effect of electro-catalytically active 3-D hollow nanocage (Pt and Pt-free) structures towards electrocatalysis (specifically, PEMFC and metal-air battery).
5. To study the effect of a conducting core on the ORR characteristics of the nitrogen doped graphene by preparing core-shell structured nanoparticles possessing the conductive core encapsulated by the nitrogen doped graphene shell.
6. To make use of the influence of the carbon dissolution property of some metals such as Ni for tuning the growth pattern of the carbon-metal nanostructures and evaluation of their structural and electrochemical properties.

1.17. References

[1] H. I. Karunadasa, C. J. Chang, J. R. Long, *Nature* **2010**, *464*, 1329-1333.

[2] J. M. Andújar, F. Segura, *Renewable and Sustainable Energy Reviews* **2009**, *13*, 2309-2322.

[3] J. M. Tour, C. Kittrell, V. L. Colvin, *Nature Materials* **2010**, *9*, 871-874.

[4] J. Tollefson, *Nature* **2010**, *464*, 1262-1264.

[5] M. Zhou, C. Yang, K.-Y. Chan, *Advanced Energy Materials* **2014**, *4*, DOI: 10.1002/aenm.201400840.

[6] *http://www.world-nuclear.org/info/Current-and-Future-Generation/World-Energy-Needs-and-Nuclear-Power/*.

[7] S. Ahmad, R. M. Tahar, *Renewable Energy* **2014**, *63*, 458-466.

[8] *http://www.world-nuclear.org/info/Energy-and-Environment/Sustainable-Energy/.*

[9] *https://books.google.co.in/books?hl=en&lr=&id=SuvgHnJzTJIC&oi=fnd&pg=PR5&dq=renewable+energy+sources+for+sustainable+development&ots=LNIdJcCqfR&sig=sbzyzkoAwBhFxEi9KrFi59gbMKk#v=onepage&q=renewable%20energy%20sources%20for%20sustainable%20development&f=false.*

[10] T. R. Cook, D. K. Dogutan, S. Y. Reece, Y. Surendranath, T. S. Teets, D. G. Nocera, *Chemical Reviews* **2010**, *110*, 6474-6502.

[11] M. Gong, Y. Li, H. Wang, Y. Liang, J. Z. Wu, J. Zhou, J. Wang, T. Regier, F. Wei, H. Dai, *Journal of the American Chemical Society* **2013**, *135*, 8452-8455.

[12] B. Varghese, M. V. Reddy, Z. Yanwu, C. S. Lit, T. C. Hoong, G. V. Subba Rao, B. V. R. Chowdari, A. T. S. Wee, C. T. Lim, C.-H. Sow, *Chemistry of Materials* **2008**, *20*, 3360-3367.

[13] J. Rossmeisl, Z. W. Qu, H. Zhu, G. J. Kroes, J. K. Nørskov, *Journal of Electroanalytical Chemistry* **2007**, *607*, 83-89.

[14] M. G. Walter, E. L. Warren, J. R. McKone, S. W. Boettcher, Q. Mi, E. A. Santori, N. S. Lewis, *Chemical Reviews* **2010**, *110*, 6446-6473.

[15] L. Carrette, K. A. Friedrich, U. Stimming, *Fuel Cells* **2001**, *1*, 5-39.

[16] Z.-L. Wang, D. Xu, J.-J. Xu, X.-B. Zhang, *Chemical Society Reviews* **2014**, *43*, 7746-7786.

[17] V. Caramia, B. Bozzini, *Mater Renew Sustain Energy* **2014**, *3*, 1-12.

[18] F. Cheng, J. Chen, *Chemical Society Reviews* **2012**, *41*, 2172-2192.

[19] S. B. Chikkannanavar, D. M. Bernardi, L. Liu, *Journal of Power Sources* **2014**, *248*, 91-100.

[20] P. Hartmann, C. L. Bender, M. Vračar, A. K. Dürr, A. Garsuch, J. Janek, P. Adelhelm, *Nature Materials* **2013**, *12*, 228-232.

[21] J.-S. Lee, S. Tai Kim, R. Cao, N.-S. Choi, M. Liu, K. T. Lee, J. Cho, *Advanced Energy Materials* **2011**, *1*, 34-50.

[22] Y. Li, M. Gong, Y. Liang, J. Feng, J.-E. Kim, H. Wang, G. Hong, B. Zhang, H. Dai, *Nature Communications* **2013**, *4*, 1805.

[23] M. A. Rahman, X. Wang, C. Wen, *Journal of The Electrochemical Society* **2013**, *160*, A1759-A1771.

[24] F. Barbir, *PEM Fuel Cells: Theory and Practice*, 2nd edition, San Diego,CA, Elsevier, **2005**.

[25] T. A. Centeno, F. Stoeckli, *Journal of Power Sources* **2006**, *154*, 314-320.

[26] I. M. Chan, F. C. Hong, *Thin Solid Films* **2004**, *450*, 304-311.

[27] X.-Z. Yuan, H. Wang, in *PEM Fuel Cell Electrocatalysts and Catalyst Layers* (2nd ed.: J. Zhang), Springer London, **2008**, pp. 1-87.

[28] K. Nice, J. Strickland, *How Fuel Cells Work* **2011**.

[29] A. B. Stambouli, E. Traversa, *Renewable and Sustainable Energy Reviews* **2002**, *6*, 433-455.

[30] http*://americanhistory.si.edu/fuelcells/mc/mcfcmain.htm*.

[31] http:*www.fuelcellmarkets.com/fuel_cell_markets/molten_carbonate_fuel_cells_mcfc/4,1,1,2505.html.*

[32] http: *//energy.gov/eere/fuelcells/types-fuel-cells*.

[33] http*://www.ieeeghn.org/wiki/index.php/Bacon%27s_Fuel_Cell*

[34] http*://www.hydrogen.energy.gov/pdfs/review12/fc088_popov_2012_o.pdf*.

[35] Y. Bing, H. Liu, L. Zhang, D. Ghosh, J. Zhang, *Chemical Society Reviews* **2010**, *39*, 2184-2202.

[36] L. Demarconnay, C. Coutanceau, J. M. Léger, *Electrochimica Acta* **2008**, *53*, 3232-3241.

[37] B. Du, O. Zaluzhna, Y. J. Tong, *Physical Chemistry Chemical Physics* **2011**, *13*, 11568-11574.

[38] H. Lang, S. Maldonado, K. J. Stevenson, B. D. Chandler, *Journal of the American Chemical Society* **2004**, *126*, 12949-12956.

[39] Y. Kang, C. B. Murray, *Journal of the American Chemical Society* **2010**, *132*, 7568-7569.

[40] I. N. Leontyev, D. Y. Chernyshov, V. E. Guterman, E. V. Pakhomova, A. V. Guterman, *Applied Catalysis A: General* **2009**, *357*, 1-4.

[41] Y. Wang, N. Toshima, *Journal of Physical Chemistry B* **1997**, *101*, 5301-5306.

[42] M. A. Scibioh, S.-K. Kim, E. A. Cho, T.-H. Lim, S.-A. Hong, H. Y. Ha, *Applied Catalysis B: Environmental* **2008**, *84*, 773-782.

[43] *S. Srivastava, S. Abraham, C. Singh, M. A. Ali, A. Srivastava, G. Sumana, B. D. Malhotra, RSC Advances **2015**, 5, 5406-5414.*

[44] W. He, M. Chen, Z. Zou, Z. Li, X. Zhang, S.-A. Jin, D. J. You, C. Pak, H. Yang, *Applied Catalysis B: Environmental* **2010**, *97*, 347-353.

[45] O. Antoine, Y. Bultel, R. Durand, *Journal of Electroanalytical Chemistry* **2001**, *499*, 85-94.

[46] J. N. Kuhn, W. Huang, C.-K. Tsung, Y. Zhang, G. A. Somorjai, *Journal of the American Chemical Society* **2008**, *130*, 14026-14027.

[47] C.-K. Tsung, J. N. Kuhn, W. Huang, C. Aliaga, L.-I. Hung, G. A. Somorjai, P. Yang, *Journal of the American Chemical Society* **2009**, *131*, 5816-5822.

[48] S. Xie, X. Liu, Y. Xia, *Nano Research.* **2015**, *8*, 82-96.

[49] Y. Zhang, M. E. Grass, S. E. Habas, F. Tao, T. Zhang, P. Yang, G. A. Somorjai, *The Journal of Physical Chemistry C* **2007**, *111*, 12243-12253.

[50] H. A. Gasteiger, S. S. Kocha, B. Sompalli, F. T. Wagner, *Applied Catalysis B: Environmental* **2005**, *56*, 9-35.

[51] J. K. Norskov, J. Rossmeisl, A. Logadottir, L. Lindqvist, J. R. Kitchin, T. Bligaard, H. Jonsson, *The Journal of Physical Chemistry B* **2004**, *108*, 17886.

[52] J. Greeley, I. E. L. Stephens, A. S. Bondarenko, T. P. Johansson, H. A. Hansen, T. F. Jaramillo, RossmeislJ, ChorkendorffI, J. K. Nørskov, *Nature Chemistry* **2009**, *1*, 552-556.

[53] J. Rossmeisl, G. S. Karlberg, T. Jaramillo, J. K. Norskov, *Faraday Discussions* **2009**, *140*, 337-346.

[54] Q. Jia, K. Caldwell, J. M. Ziegelbauer, A. Kongkanand, F. T. Wagner, S. Mukerjee, D. E. Ramaker, *Journal of The Electrochemical Society* **2014**, *161*, F1323-F1329.

[55] V. Stamenkovic, B. S. Mun, K. J. J. Mayrhofer, P. N. Ross, N. M. Markovic, J. Rossmeisl, J. Greeley, J. K. Nørskov, *Angewandte Chemie International Edition* **2006**, *45*, 2897-2901.

[56] B. Hammer, J. K. Norskov, *Nature* **1995**, 238-240. .

[57] http*://sites.google.com/site/orrcatalysiswithptbasedcsnps/home/d-band-theory*.

[58] V. R. Stamenkovic, B. Fowler, B. S. Mun, G. Wang, P. N. Ross, C. A. Lucas, N. M. Marković, *Science* **2007**, *315*, 493-497.

[59] A. Stassi, C. D'urso, V. Baglio, A. Di Blasi, V. Antonucci, A. S. Arico, A. M. Castro Luna, A. Bonesi, W. E. Triaca, *Journal of Applied Electrochemistry* **2006**, *36*, 1143-1149.

[60] R. N. Singh, R. Awasthi, C. S. Sharma, *International Journal of Electrochemical Science* **2014**, 5607 - 5639.

[61] S. Guo, D. Li, H. Zhu, S. Zhang, N. M. Markovic, V. R. Stamenkovic, S. Sun, *Angewandte Chemie International Edition* **2013**, *52*, 3465-3468.

[62] N. N. Kariuki, X. Wang, J. R. Mawdsley, M. S. Ferrandon, S. G. Niyogi, J. T. Vaughey, D. J. Myers, *Chemistry of Materials* **2010**, *22*, 4144-4152.

[63] J. H. Sinfelt, *Bimetallic Catalysts: Discoveries, Concepts and Applications, John Wiley & Sons, London* **1983**.

[64] F. Maroun, F. Ozanam, O. M. Magnussen, R. J. Behm, *Science* **2001**, *293*, 1811-1814.

[65] P. Strasser, S. Koh, T. Anniyev, J. Greeley, K. More, C. Yu, Z. Liu, S. Kaya, D. Nordlund, H. Ogasawara, M. F. Toney, A. Nilsson, *Nature Chemistry* **2010**, *2*, 454-460.

[66] J. R. Kitchin, J. K. Nørskov, M. A. Barteau, J. G. Chen, *Physical Review Letters* **2004**, *93*, 156801.

[67] S. J. Hwang, S. J. Yoo, S. Jang, T.-H. Lim, S. A. Hong, S.-K. Kim, *The Journal of Physical Chemistry C* **2011**, *115*, 2483-2488.

[68] K. D. Beard, D. Borrelli, A. M. Cramer, D. Blom, J. W. Van Zee, J. R. Monnier, *ACS Nano* **2009**, *3*, 2841-2853.

[69] M.-K. Min, J. Cho, K. Cho, H. Kim, *Electrochimica Acta* **2000**, *45*, 4211-4217.

[70] V. Stamenkovic, B. S. Mun, M. Arenz, K. J. J. Mayerhofer, C. A. Lucas, G. Wang, P. N. Ross, N. Markovic, *Nature Materials* **2007**, *6*, 241.

[71] J. Zhang, F. H. B. Lima, M. H. Shao, K. Sasaki, J. X. Wang, J. Hanson, R. R. Adzic, *The Journal of Physical Chemistry B* **2005**, *109*, 22701-22704.

[72] J. Zhang, Y. Mo, M. B. Vukmirovic, R. Klie, K. Sasaki, R. R. Adzic, *The Journal of Physical Chemistry B* **2004**, *108*, 10955-10964.

[73] W. Tang, G. Henkelman, *The Journal of Chemical Physics* **2009**, *130*, 194504.

[74] V. Komanicky, A. Menzel, K.-C. Chang, H. You, *The Journal of Physical Chemistry B* **2005**, *109*, 23543-23549.

[75] Z. Shi, J. Zhang, Z.-S. Liu, H. Wang, D. P. Wilkinson, *Electrochimica Acta* **2006**, *51*, 1905-1916.

[76] R. A. Sidik, A. B. Anderson, *Journal of Electroanalytical Chemistry* **2002**, *528*, 69-76.

[77] P. R. Sajanlal, T. S. Sreeprasad, A. K. Samal, T. Pradeep, *Nano Reviews* **2011**, *2*, 10.3402/nano.v3402i3400.5883.

[78] S. Trasatti, O. A. Petrii, *Pure and Applied Chemistry* **1991**, *63*, 711-734.

[79] Y.-A. Zhu, Y.-C. Dai, D. Chen, W.-K. Yuan, *Carbon* **2007**, *45*, 21-27.

[80] J. D. Benck, Z. Chen, L. Y. Kuritzky, A. J. Forman, T. F. Jaramillo, *ACS Catalysis* **2012**, *2*, 1916-1923.

[81] S. W. Kang, Y. W. Lee, Y. Park, B.-S. Choi, J. W. Hong, K.-H. Park, S. W. Han, *ACS Nano* **2013**, *7*, 7945-7955.

[82] G. Zhang, Z.-G. Shao, W. Lu, F. Xie, X. Qin, B. Yi, *Electrochimica Acta* **2013**, *103*, 66-76.

[83] C. Chen, Y. Kang, Z. Huo, Z. Zhu, W. Huang, H. L. Xin, J. D. Snyder, D. Li, J. A. Herron, M. Mavrikakis, M. Chi, K. L. More, Y. Li, N. M. Markovic, G. A. Somorjai, P. Yang, V. R. Stamenkovic, *Science* **2014**, *343*, 1339-1343.

[84] Y. Yin, R. M. Rioux, C. K. Erdonmez, S. Hughes, G. A. Somorjai, A. P. Alivisatos, *Science* **2004**, *304*, 711-714.

[85] J. E. Macdonald, M. Bar Sadan, L. Houben, I. Popov, U. Banin, *Nature Materials* **2010**, *9*, 810-815.

[86] S. E. Skrabalak, J. Chen, Y. Sun, X. Lu, L. Au, C. M. Cobley, Y. Xia, *Accounts of Chemical Research* **2008**, *41*, 1587-1595.

[87] M. McEachran, D. Keogh, B. Pietrobon, N. Cathcart, I. Gourevich, N. Coombs, V. Kitaev, *Journal of the American Chemical Society* **2011**, *133*, 8066-8069.

[88] J. X. Wang, C. Ma, Y. Choi, D. Su, Y. Zhu, P. Liu, R. Si, M. B. Vukmirovic, Y. Zhang, R. R. Adzic, *Journal of the American Chemical Society* **2011**, *133*, 13551-13557.

[89] M. S. Yavuz, Y. Cheng, J. Chen, C. M. Cobley, Q. Zhang, M. Rycenga, J. Xie, C. Kim, K. H. Song, A. G. Schwartz, L. V. Wang, Y. Xia, *Nature Materials* **2009**, *8*, 935-939.

[90] D. Wang, Y. Li, *Advanced Materials* **2011**, *23*, 1044-1060.

[91] A. R. Tao, S. Habas, P. Yang, *Small* **2008**, *4*, 310-325.

[92] B. Y. Xia, H. B. Wu, X. Wang, X. W. Lou, *Journal of the American Chemical Society* **2012**, *134*, 13934-13937.

[93] Z. Zhang, Y. Yang, F. Nosheen, P. Wang, J. Zhang, J. Zhuang, X. Wang, *Small* **2013**, *9*, 3063-3069.

[94] Y. Xu, B. Zhang, *Chemical Society Reviews* **2014**, *43*, 2439-2450.

[95] H. W. Kroto, J. R. Heath, S. C. O'Brien, R. F. Curl, R. E. Smalley, *Nature* **1985**, 162 - 163.

[96] S. Iijima, *Nature* **1991**, 56-58.

[97] K. Huang, K. Sasaki, R. R. Adzic, Y. Xing, *Journal of Materials Chemistry* **2012**, *22*, 16824-16832.

[98] H. Tang, J. H. Chen, Z. P. Huang, D. Z. Wang, Z. F. Ren, L. H. Nie, Y. F. Kuang, S. Z. Yao, *Carbon* **2004**, *42*, 191-197.

[99] S. Zhang, Y. Shao, G. Yin, Y. Lin, *Journal of Materials Chemistry* **2010**, *20*, 2826-2830.

[100] S. Takenaka, H. Miyamoto, Y. Utsunomiya, H. Matsune, M. Kishida, *The Journal of Physical Chemistry C* **2013**, *118*, 774-783.

[101] D. Higgins, *Nitrogen doped carbon nanotubes and their composites as ORR electrocatalyst for LT-fuel cells* **2011**, Thesis submitted to University of Waterloo, Ontaria, Canada.

[102] S. Mori, M. Suzuki, *ISBN 978-953-7619-86-2* **2010**, DOI: 10.5772/8159.

[103] B. K. Balan, S. M. Unni, S. Kurungot, *The Journal of Physical Chemistry C* **2009**, *113*, 17572-17578.

[104] T. Palaniselvam, R. Kannan, S. Kurungot, *Chemical Communications* **2011**, *47*, 2910-2912.

[105] J.-S. Li, S.-L. Li, Y.-J. Tang, K. Li, L. Zhou, N. Kong, Y.-Q. Lan, J.-C. Bao, Z.-H. Dai, *Scientific Reports* **2014**, *4*.

[106] R. Kannan, H. N. Kagalwala, H. D. Chaudhari, U. K. Kharul, S. Kurungot, V. K. Pillai, *Journal of Materials Chemistry* **2011**, *21*, 7223-7231.

[107] R. Kannan, B. A. Kakade, V. K. Pillai, *Angewandte Chemie International Edition* **2008**, *47*, 2653-2656.

[108] H. Wang, M. Xie, L. Thia, A. Fisher, X. Wang, *The Journal of Physical Chemistry Letters* **2013**, *5*, 119-125.

[109] P. Pachfule, V. M. Dhavale, S. Kandambeth, S. Kurungot, R. Banerjee, *Chemistry – A European Journal* **2013**, *19*, 974-980.

[110] D. Yu, Y. Xue, L. Dai, *The Journal of Physical Chemistry Letters* **2012**, *3*, 2863-2870.

[111] K. Gong, F. Du, Z. Xia, M. Durstock, L. Dai, *Science* **2009**, *323*, 760-764.

[112] Y. Hou, T. Huang, Z. Wen, S. Mao, S. Cui, J. Chen, *Advanced Energy Materials* **2014**, *4*, DOI: 10.1002/aenm.201400840.

[113] H. Huang, H. Zhang, Z. Ma, Y. Liu, H. Ming, H. Li, Z. Kang, *Nanoscale* **2012**, *4*, 4964-4967.

[114] F. Banhart, *Nanoscale* **2009**, *1*, 201-213.

[115] M. Giovanni, H. L. Poh, A. Ambrosi, G. Zhao, Z. Sofer, F. Sanek, B. Khezri, R. D. Webster, M. Pumera, *Nanoscale* **2012**, *4*, 5002-5008.

[116] F. Cheng, Y. Su, J. Liang, Z. Tao, J. Chen, *Chemistry of Materials* **2009**, *22*, 898-905.

[117] H. Liu, C. Koenigsmann, R. R. Adzic, S. S. Wong, *ACS Catalysis* **2014**, *4*, 2544-2555.

[118] J. H. Shim, J. Yang, S.-j. Kim, C. Lee, Y. Lee, *Journal of Materials Chemistry* **2012**, *22*, 15285-15290.

[119] C.-H. Kuo, M. H. Huang, *Journal of the American Chemical Society* **2008**, *130*, 12815-12820.

[120] R. Long, S. Zhou, B. J. Wiley, Y. Xiong, *Chemical Society Reviews* **2014**, *43*, 6288-6310.

[121] E. González, J. Arbiol, V. F. Puntes, *Science* **2011**, *334*, 1377-1380.

[122] F. T. Wagner, B. Lakshmanan, M. F. Mathias, *The Journal of Physical Chemistry Letters* **2010**, *1*, 2204-2219.

[123] J. Wang, Y. Li, X. Sun, *Nano Energy* **2013**, *2*, 443-467.

[124] B. Scrosati, J. Garche, *Journal of Power Sources* **2010**, *195*, 2419-2430.

[125] J. Wu, H. W. Park, A. Yu, D. Higgins, Z. Chen, *The Journal of Physical Chemistry C* **2012**, *116*, 9427-9432.

[126] E. Deiss, F. Holzer, O. Haas, *Electrochimica Acta* **2002**, *47*, 3995-4010.

[127] J. Goldstein, I. Brown, B. Koretz, *Journal of Power Sources* **1999**, *80*, 171-179.

[128] X. G. Zhang, *Journal of Power Sources* **2006**, *163*, 591-597.

[129] G. Girishkumar, B. McCloskey, A. C. Luntz, S. Swanson, W. Wilcke, *The Journal of Physical Chemistry Letters* **2010**, *1*, 2193-2203.

[130] T. Reddy, *Linden's Handbook of Batteries, 4th edn., Mcgraw-hill* **2010**.

[131] G. F. McLean, T. Niet, S. Prince-Richard, N. Djilali, *International Journal of Hydrogen Energy* **2002**, *27*, 507-526.

[132] E. Gülzow, *Journal of Power Sources* **1996**, *61*, 99-104.

[133] I. Iliev, A. Kaisheva, S. Gamburzev, *Air Electrodes for Metal-Air Batteries and FuelCells. Proceedings of the 26th Intersociety Energy Conversion Engineering Conference, Vols 1-6* **1991**, C469-C470.

Chapter 2
Experimental Methods and Characterization Techniques

Present chapter gives a transitory depiction of different procedures adopted for the synthesis of low-platinum (low-Pt) and platinum-free (Pt-free) structures, namely, Cu@Pt and Fe_2O_3@Pt core-shell structures supported on Vulcan carbon (C) by using ascorbic acid (AA) reduction method, Au@Gr and Au@NGr core-shell structures by using water-in-oil (W/O) emulsion method, CuPt nanocage (CuPt-NC) structures by galvanic displacement technique and Ni-NGr nanocage structures by similar W/O emulsion method. This chapter also contains the protocol employed for the synthesis of graphene oxide (GO), reduced graphene oxide (RGO) and nitrogen-doped graphene (NGr). Additionally, the chapter provides the working principles of different spectroscopic and diffraction techniques used for the investigation of structural properties of the synthesised electrocatalysts like high resolution transmission electron microscopy (HR-TEM), scanning electron microscopy (SEM), energy dispersive X-ray analysis (EDAX), X-ray diffraction, X-ray photoelectron spectroscopy, Raman spectroscopy etc. The working principles of various electrochemical techniques like cyclic voltammetry (CV), rotating disk electrode (RDE), rotating ring disk electrode (RRDE) and chronoamperometry (CA), which are comprehensively utilized in the present work to investigate the oxygen reduction reaction (ORR) and oxygen evolution reaction (OER) characteristics of the above mentioned catalysts, have also been discussed. A fuel cell made from Fe_2O_3@Pt/C as a cathode electrode has been tested with Nafion® as the ionic conductor and a discussion on the experimental procedure on this is also included in this chapter.

2.1 Experimental Methods

2.1.1 Chemicals and Materials

Cupric chlorides ($CuCl_2$), ascorbic acid (AA), chloroplatinic acid ($H_2PtCl_6.6H_2O$), sodium hydroxide (NaOH), iron nitrate ($Fe(NO_3)_3.9H_2O$), hydrogen peroxide (H_2O_2), chloroauric acid ($HAuCl_4$), nickel chloride ($NiCl_2$), graphite, potassium permanganate ($KMnO_4$), phosphoric acid (H_3PO_4), potassium hydroxide (KOH), melamine, sulfuric acid (H_2SO_4), silicon oil copper acetylacetonate ($Cu(acac)_2$), oleylamine, cetyltributylammoniumbromide (CTAB), sodium borohydride ($NaBH_4$) and n-hexane were purchased from Sigma-Aldrich. Toluene and absolute ethanol were purchased from Thomas Baker. Perchloric acid ($HClO_4$), hydrochloric acid (HCL), nitric acid (HNO_3), ether, methanol, isopropyl alcohol and polytetrafluoroethylene (PTFE) membrane filter paper were purchased from Rankem. Zinc powder was purchased from J K Impex. Vulcan carbon XC-72 was purchased from Cabot. Nafion®-212 membrane and solutions were procured from DuPont and pre-treated with acid, peroxide and DI water before use (discussed in the present chapter **Section 2.4**). Fumion was purchased from Fumatek. All the chemicals were used as such without any further purification.

2.1.2 Synthesis of Functionalized Vulcan Carbon XC-72 (F-C)

For the functionalization of Vulcan carbon XC-72 support, H_2O_2 treatment was used.[1] During the synthesis, 500 mg of Vulcan carbon was dispersed properly in 100 ml of H_2O_2 (30 %) solution by ultra-sonication for 15 min. Further, the Vulcan carbon and H_2O_2reaction mixture was refluxed for5h at 60 ^oC. Finally, the mixture was filtered with 0.2 µm PTFE membrane filter paper and washed thoroughly with DI water. Subsequently, the material was dried at 80^oC for overnight. The functionalized Vulcan carbon XC-72 is designated as F-C.

2.1.3 Synthesis of Cu@Pt/C Core-Shell Structure Electrocatalyst

8 ml aqueous solution of 0.1 N $CuCl_2$ was reduced by adding 40 ml aqueous solution of 0.1 N AA and the solution was subsequently kept on stirring for 30 min. The pH of the reaction mixture was maintained to 12 by drop-wise addition of 10 % NaOH. Under these conditions, the copper gets reduced, indicated by a reddish colour, and instantaneously 8 ml aqueous solution of 0.01 N H_2PtCl_6 was added without altering the pH of the reaction

mixture. After the addition of H_2PtCl_6, the reaction mixture was kept on stirring for 20 min, at 60 ^oC to ensure complete reduction of Pt^{+x} preceded the colour change of the mixture to black. F-C was dispersed in DI water by ultra-sonication and instantly added to the reaction mixture and kept on stirring for 10 h. Afterwards, the catalyst (Cu@Pt/C) was filtered (PTFE membrane filter paper having 0.2 μm pore size, Rankem) and dried at 90 ^oC for 2 h.

2.1.3.1 Role of Ascorbic Acid

As mentioned above, during the synthesis of Cu@Pt/C core-shell structures, the reaction mixture was kept on stirring for 10 h. Mainly, during this ageing time, the oxidation products of AA were formed during the course of the metal ion reduction. These degradation products of AA[2] (dehydroascorbic acid and 2, 3-diketogulonic acid) help to modify the surface of F-C and create fertile platform for the anchoring of the core-shell nanoparticle.

2.1.4 Synthesis of Fe_2O_3@Pt/C Core-Shell Structure Electrocatalyst

Similar synthetic procedure was employed for the synthesis of Fe_2O_3@Pt/C core-shell structures as mentioned in the above section **(Section 2.1.3)**. Here, iron nitrate was used as the Fe-precursor instead of the Cu-precursor. The concentration of the precursor was kept same as in the previous procedure. The prepared catalyst is designated as Fe_2O_3@Pt/C.

2.1.5 Synthesis of CuPt-Nanocage Structure (CuPt-NC)

CuPt-NC structures were synthesized by adopting a reported procedure.[3] Briefly, 42.42 mg of H_2PtCl_6 solution was dispersed in 200 mg of oleylamine, and 20 mg of $Cu(acac)_2$ was dispersed in fresh 8 ml of oleylamine by sonicating it in a Branson water bath sonicator. Subsequently, 50 mg of CTAB was added and the sonication was continued for additional 30 min. Perfectly dispersed solution of H_2PtCl_6, $Cu(acac)_2$, and CTAB in oleylamine was transferred into a Teflon coated stainless steel autoclave (15 ml capacity) and was subjected to heating at 180 ^oC for 24 h. Finally, the reaction mixture was centrifuged at 10,000 rpm and washed with toluene: ethanol (3:2) mixture and dried at 60 ^oC in an oven. Material collected after this stage was used as such for further characterization.

2.1.6 Synthesis of Graphene Oxide (GO)

GO was synthesized by improved Hummer's method.[4] In short, a mixture of 3 g of graphite and required amount of $KMnO_4$ was added slowly into a 1:9 mixture of conc.

H_3PO_4:H_2SO_4; the solution was kept under stirring for overnight by maintaining the reaction mixture temperature at 60 °C. The obtained solution was poured into ice cooled water containing 3% H_2O_2. A yellow precipitate was formed, which was separated by centrifugation at 10,000 rpm and was washed well with copious DI water. Finally, the product was washed with 30% HCl to remove unwanted impurities, followed by washing with ethanol and acetone. The product was allowed to dry at room temperature and this was used as such for the further studies.

2.1.7 Synthesis of Reduced Graphene Oxide (RGO)

GO was reduced by aqueous solution of sodium borohydride. Briefly, 50 mg of GO was dispersed in 50 ml DI water and transferred in a 250 ml round bottom flask. Subsequently, the solution was kept on vigorous magnetic stirring for 30 min. Further, 0.1 M sodium borohydride (25 ml) aqueous solution was added slowly using a burette into the mixture and kept on stirring for 4 h. Finally, the reaction mixture was centrifuged at 10,000 rpm, washed with DI water and dried at 80 ^oC in an oven for 10 h. After that, the product was annealed at 900 ^oC to remove maximum functional groups. The obtained black product is termed as RGO (Gr) (**Figure 2.1**).

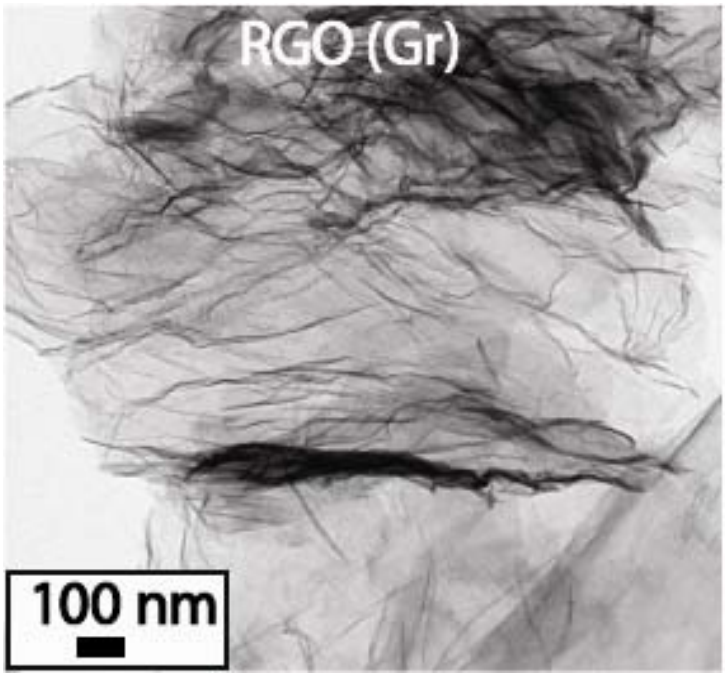

Figure 2.1: *TEM images of reduced graphene oxide (Gr).*

2.1.8 Synthesis of Nitrogen Doped Graphene (NGr)

A mixture of 1 g of RGO (Gr) and 6 g of melamine in 100 ml of DI water was prepared and stirred for 24 h. The slurry was filtered and dried in an oven at 80 ^{o}C for overnight. The obtained melamine-Gr solid powder was heated at about 900 ^{o}C in an Argon atmosphere (flow rate: 0.2 slpm) for about 4 h. The furnace was cooled down to room temperature under inert atmosphere and the obtained NGr (**Figure 2.2**) was used for the further investigation and characterization.

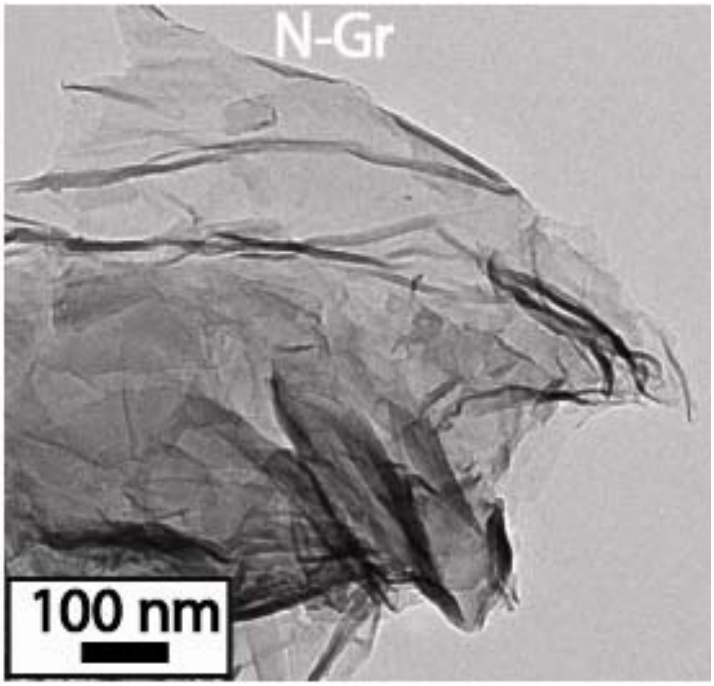

Figure 2.2: *TEM images of N-doped graphene (NGr).*

2.1.9 Synthesis of Au-Nanoparticles

For the synthesis of Au nanoparticles, a homogeneous mixture of the as-above synthesized 2 mg of Gr and 2ml of 100 mM $HAuCl_4$ solution was obtained by ultra-sonication. Here, the concentration of Gr is maintained to be veryless as required as a moiety to facilitate *in-situ* reduction of the Au precursor (a higher concentration of Gr will trigger the formation of Au@Gr core-shell particles). The mixture was then added drop-wise in a beaker containing fresh silicon oil (25 ml), under a strong magnetic stirring. After the addition, the reaction mixture was maintained at room temperature for 5h to get uniform emulsion droplets. After 5 h, this emulsified reaction mixture was transferred into a Petri dish, and was kept in an oven at 80 ^{o}C for 80 h. During this process, Gr reduces the gold precursor to gold

nanoparticles and Gr itself gets oxidized, leading to formation of gold nanoparticles and small graphene sheets. The gold nanoparticles and gold supported graphene sheets will form separately, which can be separated after the centrifugation. The product was washed several times with hexane to remove the silicon oil and finally it was dried under the lamp.

2.1.10 Synthesis of Au@Gr Core-Shell Structured Electrocatalyst

Gold@graphene (Au@Gr) core-shell nanostructures were synthesized by simple water-in-oil (W/O) emulsion technique without using any external reducing and capping agents in a size controlled manner. Briefly, 4 mg of the as-synthesized reduced graphene oxide (RGO) was mixed with 2 ml of aqueous solution of 100 mM $HAuCl_4$ and the mixture was sonicated for 30 min using a bath sonicator to form a homogenous solution. The dispersed solution was added drop-wise in previously taken 25 ml fresh silicon oil, under strong magnetic stirring. Furthermore, the reaction mixture was maintained for 5 h under stirring at 750 rpm at room temperature to get a uniform distribution of the emulsion droplets. At this stage, the transparent colour of the reaction mixture was turned to red, which is attributed to the formation of Au@Gr core-shell nanostructures. Subsequently, the W/O emulsion mixture was transferred into a Petri dish and was kept in an oven at 80 ^{o}C for 80 h. During this process, water in the emulsion droplets gets evaporated and crystallization of the solid components in the emulsion droplets occurs simultaneously. Finally, the formed Au@Gr core-shell nanostructures were centrifuged at 10,000 rpm for 15 min and the mixture was washed with excess hexane to obtain oil-free Au@Gr core-shell nanostructures.

2.1.11 Synthesis of Au@NGr Core-Shell Structured Electrocatalyst

In a similar way as discussed in the above section (*i.e.* **Section 2.1.10**), gold@N-doped graphene (Au@NGr) sample was also synthesized by using N-doped graphene (NGr), instead of Gr, in the above mentioned method.

2.1.12 Synthesis of Ni-NGr Nanocage Structure

For the synthesis of the Ni-based nanocage structures, a homogeneous mixture of 4 mg NGr and 2 ml aqueous solution of 100 mM nickel chloride were obtained by sonicating the mixture for 30 min using a Branson bath sonicator. This perfectly dispersed solution was added drop-wise in previously taken 25 ml fresh silicon oil, under strong magnetic stirring (750 rpm) at room temperature. Moreover, the reaction mixture was maintained for 5 h at

room temperature for uniform distribution of the emulsion droplets. Furthermore, the W/O emulsion was transferred into a Petri dish and it was kept in an oven at 80 °C for 80 h. The formed Ni-NGr nanocage structures were centrifuged at 10 000 rpm for 15 min and washed several times with hexane to remove the silicon oil and subsequently, dried under a lamp.

2.1.13 Synthesis of Ni-Gr Particles

To understand the role of nitrogen, we prepared a Ni-Gr sample by employing a similar synthetic procedure (as mentioned in **Section 2.1.12**) with RGO (Gr), instead of NGr, and ended with spherical particles.

2.1.14 Synthesis of Ni-Nanoparticles

The Ni-nanoparticles were synthesized by chemical reduction method. 25 mL of 100 mM nickel chloride solution was taken in 100 mL round bottom flask. Subsequently, 0.5 M aqueous solution of sodium borohydride was added slowly in to the above nickel chloride solution. After complete addition, the reaction mixture was kept under stirring for 8 h, and then, filtered by using 0.2 μm PTFE membrane filter paper. Finally, the residue was washed with DI water and dried in an oven at 80 ^{o}C for 10 h.

2.1.15 Electrode Preparation

Initially, the slurry was prepared by sonicating5 mg of the catalyst in 1 ml ethanol in water (3:2) solution mixture. Parallely, the electrode was polished by using 0.3 mm alumina slurry followed by sonication in water and ethanol.[1] After that, the working electrode was prepared by drop coating required amount of the catalyst slurry on the glassy carbon disk, followed by 2 μl of 0.01 wt. % Nafion® or Fumion (as binder).[1] This solution was applied on the whole surface of the disk electrode to yield a uniform thin film, which avoids the problem related to catalyst detachment from the surface of the electrode during the electrochemical measurements. Moreover, the electrode was dried for 4 h under an IR-lamp and this was used as the working electrode for the electrochemical investigations. An aqueous solution of 0.1 M KOH or 0.5 M H_2SO_4 or 0.5 M $HClO_4$ de-aerated with N_2 gas was used as an electrolyte for the CV, RDE and RRDE studies. Moreover, all the RDE and RRDE studies were recorded at 10 mV/s. During the RDE and RRDE investigations, the electrolyte was saturated with oxygen to achieve oxygen rich and nitrogen to achieve the inert atmosphere.

2.2 Material Characterization Techniques

2.2.1 Transmission Electron Microscopy

Transmission electron microscope (TEM) is an influential technique to obtain the highly magnified and resolution imaging of the samples of biological, chemical and material sciences.[5-6] The TEM provides the topographical, compositional and crystallographic information of the nanoparticles, through which exact size, shape and atomic arrangements can be obtained very precisely.[5-6] The high resolution-TEM (HR-TEM) allows understanding of the atomic lattice fringes of the nanoparticles up to 1 nm or even at high.

Principally, the TEM operates on the similar basic principles as the light microscope, which uses electrons instead of light.[5-6] Basically, visibility with a light microscope is restricted by the wavelength (λ) of light. However, in TEMs, electrons are being used as the light source due to its much lower λ, which makes it possible to get a thousand times better resolution than what we get with a light microscope. We will be able to take the images in the order of a few angstroms (10^{-8} cm), *i.e.* we can study small niceties in the cell or different materials down to near atomic levels. The possibility for high magnifications of TEM makes it a valuable spectroscopy technique in medical, biological and materials research.

Mainly, in the TEM, only thin specimens, which allow a fraction of the incident electron beam to go through the specimen, can be studied. When an accelerated beam of electrons illuminated upon a specimen, diverse of interactions take place. This non-uniform distribution of electrons after interaction with the specimen results into angular distribution of the scattering which could be viewed in the form of scattering patterns. This kind of patterns is referred as diffraction patterns or selected area electron diffraction (SEAD). Generally, the coherent scattering (elastic) gives spot patterns in the case of single crystals and ring pattern for polycrystalline materials.

Concrete specimen analysis conditions, the electrons get emitted from the light source (Thermission emitter: Tungsten filament or LaB_6) which will be at the top of the microscope. These emitted electrons travel through the vacuum in the column of the microscope. The electrons are focussed in to a very thin beam. For this purpose, electromagnetic lenses are used, in TEM. The electron beam travels through the specimen which is placed for examination. Depending on the density of the material present, some of the electrons get

disappeared and scattered from the beam. The unscattered electrons hit the fluorescent screen (at the bottom of the microscope), which generate the "shadow image" of the specimen. The image gets appeared with its different parts displayed in varied with various darkness with respect to their density.

In the present study, the high resolution transmission electron microscope (HR-TEM) model TECNAI G^2 F20 instrument operated at an accelerating voltage of 200 kV (Cs=0.6 mm, resolution=1.7 Å) was used to characterize the structural properties of the synthesised catalysts. For the TEM analysis, the sample was prepared by drop casting the slurry of the catalyst dispersed in isopropyl alcohol on the 200 mesh copper grid. The copper grid was coated with carbon film (purchased from Ted Pella). Before loading it in the microscope chamber, the catalyst casted copper grid was dried for almost 12 h in vacuum.

2.2.2 Scanning Electron Microscopy and Energy Dispersive X-ray Analysis

The working principle of scanning electron microscope (SEM) is quite similar to that of TEM. Instead of transmission, the specimen will be get scanned with focussed beam of electrons and produces the surface images. The focussed beam of electrons interacts with atoms in the specimen, which results into various signals. These signals can be detected and they give the information about the sample's surface features and composition.[7] However, commonly, the secondary electrons emitted by atoms after talking with the focussed beam of electrons get detected and displayed a very high resolution images of surface topography of the specimen, revealing details of <5 nm in size.[7-8] SEM imaging can be done in high and low vacuum, and at a wide range of elevated temperatures. Moreover, the biological samples also can be done in wet condition, which is termed as environmental SEM (ESEM). Specifically, due to the very narrow electron beam, SEM micrographs have a large depth of field, which can produce the distinctive 3-D appearance of the specimen with a wide range of magnifications ranging from 10 to 500,000 times higher than the best light microscopes.[7-8]

Mainly, the electrons reflected from the surface of the specimen are due to the elastic scattering, which produce the back scattered electrons (BSE). The intensity of the BSE signal is strongly linked to the atomic number (Z) of the specimen. Moreover, as mentioned above, along with the BSE, the characteristic X-rays are also being generated. The characteristic X-rays gets emitted, when the electron beam knocks off an inner shell electron from the specimen, results into the filling of the shell by a higher-energy electron and releases the

energy. These emitted characteristic X-rays could be used to find out the elemental composition in the specimen, termed as energy dispersive X-rays analysis (EDAX).[8]

More importantly, for SEM imaging, specimens must be electrically conductive, at least at the surface. While SEM, the specimen must be electrically grounded, which prevents the accumulation of electrostatic charge at the specimen surface. Noteworthy, before imaging of the non-conductive specimens, surface could be made conducting by a thin coating of electrically conducting material. This is done by depositing Au/Au-Pd alloy/Pt/Os/ Ir/Gr/W/Cr on the surface of the specimen either by low-vacuum sputter coating or by high-vacuum evaporation technique. This could be done on any specimen before imaging. Additionally, conductive thin layer coating may increase signal-to-noise ratio for the specimens of low-Z. This could be due to the enhancement in secondary electron emission for high-Z materials.[7-8]

In the present work, SEM imaging coupled with EDAX and elemental mapping were performed on an FEI, Model Quanta 200 3D instrument equipped with Phoenix energy dispersive spectral analysis setup at an operating potential of 30 kV. For SEM imaging, a small amount of the sample was dispersed well in isopropanol by ultra-sonication and drop-coated on stubs and gold sputtered at low-vacuum.

2.2.3 Powder X-ray Diffraction

Powder X-ray diffraction (PXRD) is a most widely used powerful non-destructive and rapid (< 20 min) technique for the identification of unknown crystalline materials with its unit cell dimensions.[9] It also provides the information about the phase identification of crystalline materials. XRD is now commonly used to understand the crystal structure and atomic spacing. The fundamental principle of XRD is based on constructive interference of the monochromatic X-rays and a crystalline material. The X-rays are being generated by a cathode ray tube and get filtered to obtain monochromatic radiations.[9-10]According to Bragg's Law ($n\lambda=2dsin\theta$), when an incident X-ray interacts with the specimen, it produces the constructive interference along with diffracted rays (**Figure 2.1**).[9] Basically, this law tells about the relation between the λ of electromagnetic radiation to the diffraction angle (θ) and lattice spacing (d) in a crystalline specimen. The diffracted X-rays from the atomic layers of the specimen were detected, counted and investigated. The conversion of the diffraction peaks to d-spacing allows identification of the material, because each material has a set of

unique d-spacing, which could be achieved or identified by comparing it with the standards.[10]

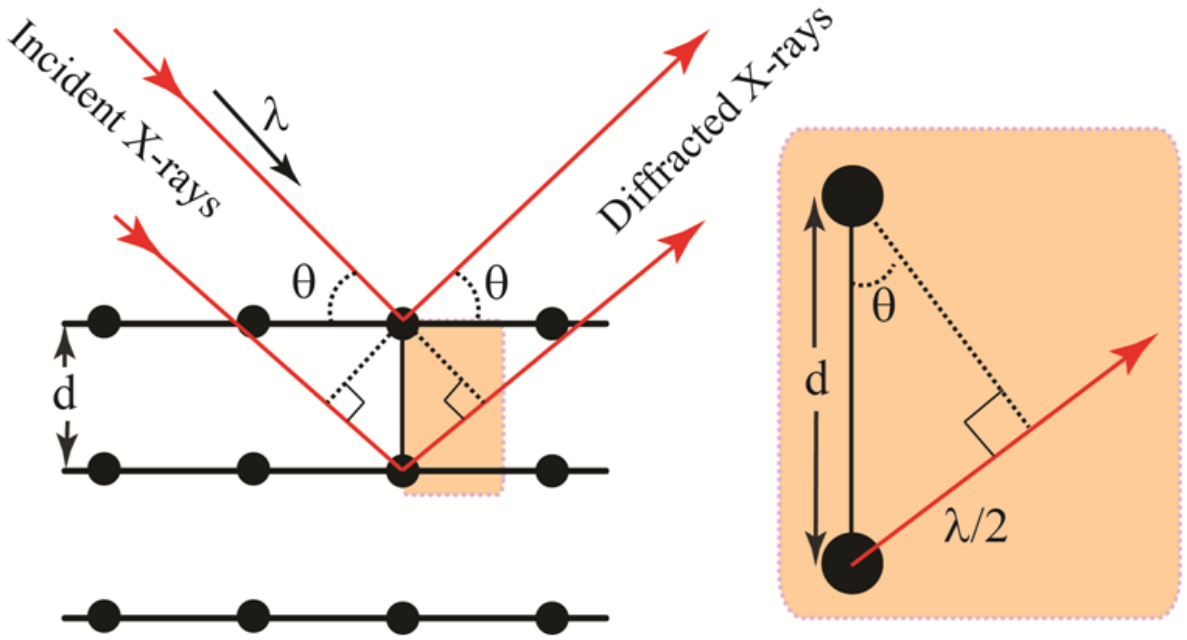

Figure 2.1: *Schematic illustration of Bragg's Law.*

More importantly, the full width at half maxima (FWHM) of the diffraction peaks gives an idea about the crystallite size of the material. As the peak becomes broader, the size becomes smaller, and *vice-versa*. The average crystallite size (*t*) of the particles could be calculated by using Scherer equation (**Equation2.1)**.[9-10]

$$t = \frac{0.94\,\lambda}{\beta\,cos\theta} \quad (2.1)$$

where, λ is the wavelength of X-ray, β is the FWHM of diffraction patterns, and θ is the Bragg's angle.

The PXRD is not only applicable to the crystalline materials but also can be used to amorphous, where, all the atoms are arranged in a random manner.[9-11]

In the present study, powder X-ray diffraction (PXRD) patterns were recorded on PANalytical instrument using Cu-K_α radiation (λ =1.5418Å). All the samples were scanned at a scanning rate of 2^o min^{-1} and a step size of 0.02^o in 2θ. The PXRD of all the samples were scanned in the range of 2θ = ~10 to 80^o. Furthermore, the obtained data were imported and analysed using X'PertHighScore Plus software.

2.2.4 X-ray Photoelectron Spectroscopy

X-ray photoelectron spectroscopy (XPS) is a surface sensitive technique used to understand the surface chemistry of the sample.[12] Therefore, it is also known as electron spectroscopy for chemical analysis (ESCA). This abbreviation was introduced by Kai Siegbahn's group to point out that the technique provides the information of chemical rather than only elemental.[13]

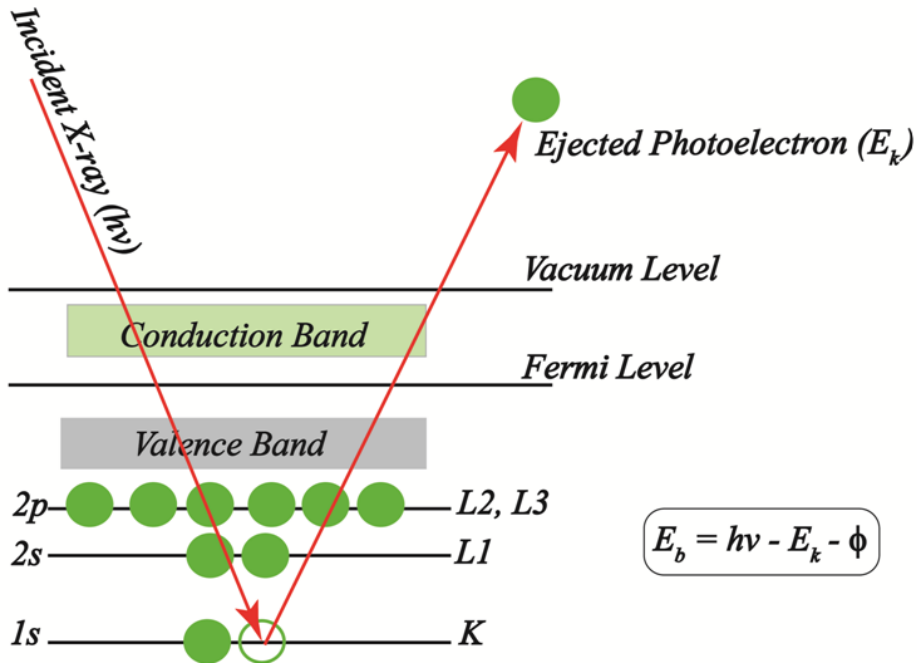

Figure 2.2:*Apictorial representation of the working principle of XPS.*

The quantitative estimation of elements present in the sample can be obtained at the parts per thousand ranges. Moreover, the chemical state/electronic configuration of the elements can be investigated by using XPS technique. Mainly, the XPS spectra are obtained by illuminating a sample with a beam of X-ray and the kinetic energy and the number of the ejected electrons from the top 0 to 10 nm of the sample, which were collected and analyzed.[13]Therefore, the XPS is mainly based on the photoelectric effect. In detail, when an X-ray beam interacts with the sample surface, the energy of the incident X-ray photon (*hv*) is absorbed by the core electron of an atom knocked out from it, if it is large enough. Then, the emitted electron with a kinetic energy of E_k is termed as a photoelectron (**Figure 2.2**). Therefore, the binding energy (E_b) of the core electron is given by the Einstein relationship (Equations **2.2 and 2.3**).[14]

$$hv = E_b + E_k + \phi \quad (2.2)$$

$$E_b = hv - E_k - \phi \quad (2.3)$$

where, *hv* is the X-ray photon energy (for Al *Kα* = 1486.6 eV, for Mg Kα = 1253.6 eV), E_k is the kinetic energy of the photoelectron; ϕ is the work function (4 ~5 eV) and E_b is the binding energy of the core electron.

Finally, E_b can be obtained by manually compensating the work function (ϕ); so, the Equation **2.3** becomes,

$$E_b = hv - E_k \quad (2.4)$$

Importantly, XPS can able to detect all the elements with a Z > 3. Therefore, Li, H, or He cannot be easily detected by this technique.[14]

In the present study, XPS measurements were carried out on a VG Micro Tech ESCA 300° instrumentat a pressure of >1 × 10^{-9} Torr (pass energy 50 eV, electron take-off angle 60°, and the overall resolution of ~0.1 eV). The collected data were imported and deconvulated by using XPSPEAK41 software.

2.2.5 Raman Spectroscopy

Raman spectroscopy is another non-destructive technique used to obtain the crystallinity and disorderness of the carbonaceous materials. Along with this, the technique is used to examine the molecules which has zero dipole moment but could be polarized under electromagnetic radiations. Raman spectroscopic technique is akin to Infra-red spectroscopy, useful to obtain the information of vibrational, rotational and other low-frequency modes in the system. The general principle of Raman spectroscopy is the collection of scattered lights generated after the interaction of a monochromatic light source (*i.e.* laser) with a sample. Commonly, the scattered light possesses the same frequency as the excitation source; this is known as Rayleigh (elastic) scattering.[15] Moreover, due to interactions between the incident electromagnetic waves and the vibrational energy levels of the molecules in the system, there occur shift in energy from the laser frequency (**Figure 2.3**). Therefore, the Raman spectrum could be obtained by plotting the graph of intensity of the shifted light *vs.* frequency, which

gives the information about the vibrational modes caused due to the polarization of the system in presence of the electromagnetic waves.[15]

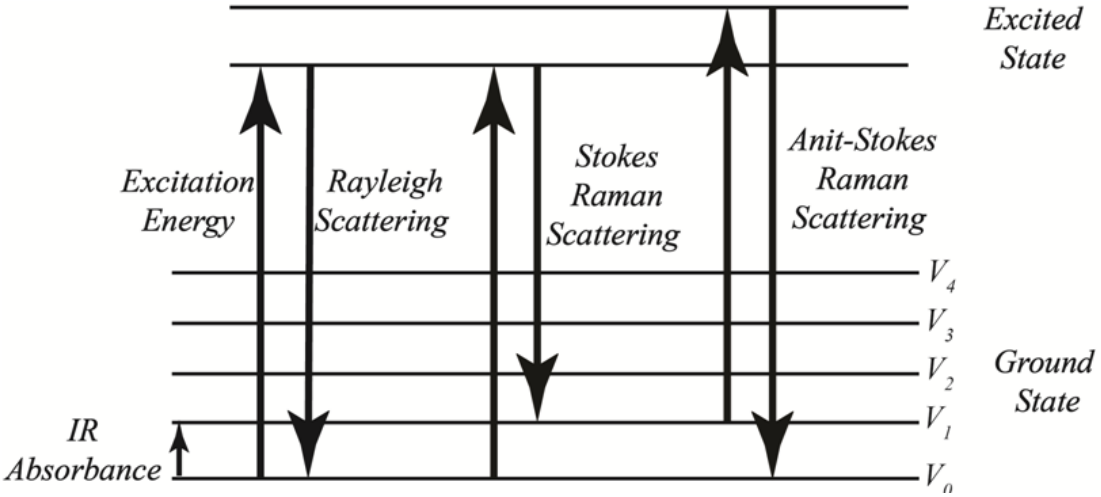

Figure 2.3: *A diagrammatic illustration of the various types of scatterings in Raman analysis.*

As shown in **Figure 2.3**, as soon as the laser light interacts with the ground state molecules, they undergo polarization and gets excited to the higher energy vibrational states and this depends on the frequency of the used light source. In Rayleigh scattering, the energy of excitation is same as that of energy of relaxation of the molecule to come back to the ground state. Whereas, in case of the stokes effect, the energy of relaxation of the excited molecule is less compared to the energy of the incident light. Moreover, it will be more in case of the anti-Stokes effect. Overall, these processes provide the information about the moment of inertia and eventually, the structure of the molecule.

In application of the Raman technique to the carbon materials, the orderness and disorderness of the carbon system can be identified by recording the defective- (D-band) and graphitic-band (G-band). The ratio of the intensity of D-band (I_D) to G-band (I_G) gives the information about the overall graphitization of the carbon materials. Along with this, the characteristic peak of 2D-band and its ratio with G-band provides the average number of the graphitic layers. Besides, the characteristic dimensions of the graphitic domains could be obtained by using the following equation (**Equation 2.5)**.[16]

$$I\,(\text{Å}) = 44\,(I_G/I_D) \qquad (2.5)$$

In the present work, Raman analysis of the synthesized electrocatalysts was performed on an HR 800 Raman spectrometer (Jobin Yvon, Horiba, France) using 632 nm green laser (NRS 1500 W) in order to understand the graphitization and defects of graphene.

2.2.6 Electrical Conductivity

The electrical conductivity of the samples was measured with a home-made set-up (shown in **Figure 2.4**). Initially, the material was coated on an ITO plate having a specified area of 0.5 cm X 0.5 cm (as shown in **Figure 2.4**). Subsequent to the coating, the plate was dried under a lamp. After that, the second ITO plate was placed on it and the entire unit was clamped with a binder clip. Later, I-V measurement was done in a potential window of -1.0 to +1.0 V with scan rate of 20 mV/s. The conductivity was calculated from the slope of the I-V data using **Equation 2.6**.

$$\text{Conductivity (S/cm)} = l/R*A \qquad (2.6)$$

where, 'l' is the thickness, 'R' is the resistance and 'A' is the area of the electrode material.

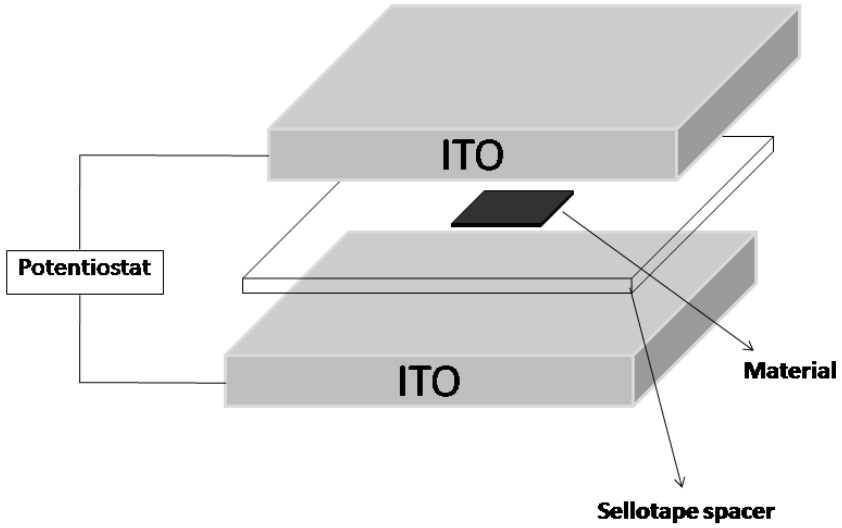

Figure 2.4: *Schematic view of the cell used for the conductivity measurement.*

2.3 Electrochemical Study

The electrochemical study of the chemical reactions taking place at the electrode-electrolyte interface could be done using different electrochemical techniques, such as, cyclic voltammetry (CV), linear sweep voltammetry (LSV) by using rotating disc electrode (RDE) and rotating ring disc electrode (RRDE) and chronoamperometry (CA) study, etc. The

electric charges shuttling between the electrode and electrolyte vicinity could be monitored by using the electrochemical techniques. Moreover, the exact reaction kinetics of oxidation, reduction, number of electron involved during reaction, and/or stability of the material and reversibility and irreversibility of the process etc. can be examined by using the electrochemical methods. In the present work, activities of the prepared samples towards oxygen reduction reaction (ORR) and oxygen evolution reaction (OER) have been screened by using numerous electrochemical techniques. The general principle and working of the different electrochemical techniques are explained in the followed sections.

2.3.1 Cyclic Voltammetry

Cyclic voltammetry (CV) is a routinely used technique to rapidly scan the Faradaic and/or non-Faradaic processes of the analyte in the solution. CV is a type of potentiodynamic electrochemical measurement which is being used to investigate the half-cell reactivity of the analyte.[17] Mainly, the CV measurements are done with a system equipped with the three different electrodes, namely, working electrode (WE), reference electrode (RE) and counter electrode (CE).[17] The three-electrode set-up resolves the issue of maintaining the constant potential while passing the current to counter redox events at the WE in the two-electrode system.

During the actual CV measurement, the potential of the electrode is ramped linearly *vs.* time (*i.e.* scan rate, V/s). Simply, the CV is the sweep which starts from the initial potential and reaches at the set potential. After that, the potential ramp of WE gets inverted and reaches back to the initial potential. Importantly, while doing CV, the potential is applied between WE and RE and the current is measured between the WE and the CE. Consequently, these data are plotted as current at the working electrode *vs.* the applied voltage, which gives the cyclic voltammogram.

Basically, the current will increase as the potential reaches the reduction and/or oxidation potential of the analyte, but, latter falls off as the concentration of the analyte is depleted close to the WE surface.[17-18] Therefore, as the electron transfer between the electrode and the analyte is fast and the current is limited by the diffusion of the species to the WE surface, the current peak will be proportional to the $\sqrt{scan\ rate}$, as explained by the Cottrell equation (**Equation 2.7**).

$$i = \frac{nFAc_j^o\sqrt{D_j}}{\sqrt{\pi t}} \qquad (2.7)$$

where, i is the current (A), n is the number of electrons (to oxidze/reduce 1 molecule of j); F is the Faraday constant (C/mol), A is the area of the electrode (cm^2), c_j^o is the initial amount of j(mol/cm^3), D_j is the diffusion coefficient (cm^2/s) and t is the time (s).

The Cottrell equation also describes the change in electric current with respect to time under the constant or controlled potential measurements, like, chronoamperometry.

In the present study, all the electrochemical investigations were carried out on a Bio-Logic (VMP-3) using a three-electrode set-up purchased from Pine Instruments. The Hg/HgO electrode was used as the reference in alkaline medium. Moreover, the $Hg/HgSO_4$ and Ag/AgCl reference electrodes were used in sulphuric and perchloric acid, respectively. In all the experiments, the Pt-flag was used as CE. The glassy carbon electrode embedded in Teflon was used as WE, and was cleaned before use (the cleaning procedure has been mentioned in **Section 2.1.15**).

2.3.2 Rotating Disk Electrode

A rotating disk electrode (RDE) is a hydrodynamic technique used to study the reaction mechanism of the analytes in a three-electrode set-up. Generally, the electrochemical reactions involving mass transport can be precisely controlled and investigated by this technique. The RDE is very easy to fabricate, where the electrode material, *i.e.* disk (may be carbon, Pt, Au, etc), is entrenched in an insulating rod (Teflon, epoxy resin or plastic) as shown in **Figure 2.5**. More importantly, there should not be solution leakage between the electrode and the insulating material. Electrical contact is made to the imbedded electrode (disk) by means of a brush contact which is attached to the shaft connected to the motor. Hence, the electrode can be rotated at definite frequency (f, revolution per second, $f = \omega/2\pi$), where, ω is the angular velocity (s^{-1}). In the present study, this technique is fully utilized to investigate the ORR mechanism of the electro-active material.

During the electrochemical reactions, the ionic movements from the bulk towards the electrode surface takes place by mainly diffusion and convection. The diffusion of ion mainly happens due to the concentration gradient and it explains the net flux of molecules from higher concentration region to lower.[17, 19] Formerly, as the concentrations become equal, the

molecular diffusion gets ceased. However, under these conditions the movement of ions take place by the self-diffusion process. As a result, the current will attain steady state. Therefore, to improve the rate of mass transport/rate of reaction/increase the rate of diffusion to the electrode, hydrodynamic technique (RDE) can be more useful to improve the same by introducing convection. The rate of reaction at the electrode surface can be improved by altering the convection rate in the solution by increasing the rotation of WE.

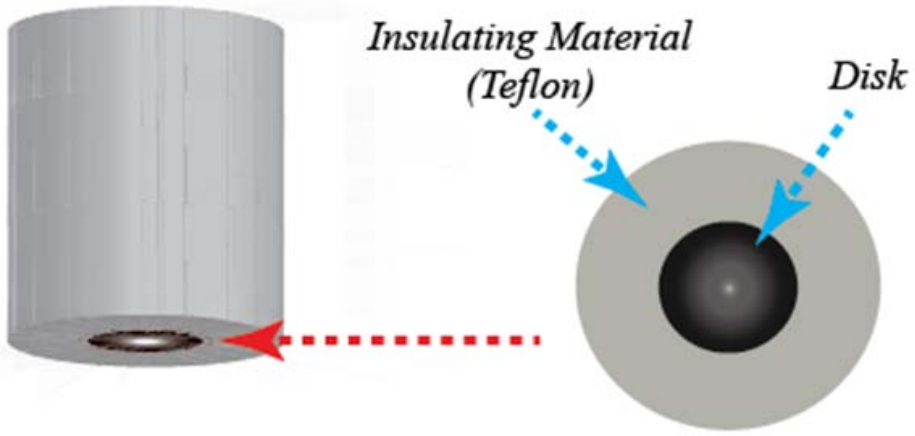

Figure 2.5: *Diagrammatic representation of RDE showing the imbedded electrode in the insulating material.*

Under the rotating conditions, the ions are pulled towards the electrode surface and concurrently, removing the resultant products, thereby, keeping the electrode surface always fresh by maintaining the minimum flux on the surface. Importantly, the net mass transport of the ions towards the electrode-electrolyte boundary is decided by diffusion + convection. In RDE, the steady-state diffusion controlled process is given by Koutecky-Levich (K-L) equation (explained below).[20]

In the other way, total current obtained in the RDE analysis is the combination of the inverse of diffusion (j_d), kinetic (j_k) and film diffusion (j_l) currents. However, in the present study, the amount of binder applied, *i.e.* Nafion® or Fumion, is significantly low. Therefore, the j_l component can be neglected. Hence, in the laminar flow region, the diffusion current density is a function of the rotational velocity and hence the kinetic current densities can be adjusted to the simple K-L equation as below.[20-21]

$$j^{-1} = j_k^{-1} + j_d^{-1} \qquad (2.8)$$

$$j^{-1} = (nFkC_O^*)^{-1} + (0.62nFD_O^{2/3}C_O^* v^{-1/6}\omega^{1/2})^{-1} \qquad (2.9)$$

where, j is the disk electrode current density, k is the rate constant of reaction, n is the number of electrons involved during reaction, F is the Faraday constant (96500 C/mol), C_o^* is the oxygen concentration in the bulk (mol/cm^3), D_o is the diffusion coefficient of molecular oxygen (cm^2/s), v is the kinematic viscosity of the electrolyte (cm^2/s) and ω is the angular rotation of the electrode. This equation gives a linear relation between j^{-1} and $\omega^{-1/2}$ with a Y-intercept equal to the j_k^{-1}. Subsequently, the kinetic current, n and k can be obtained from the above equation.

For RDE data analysis, above mentioned three non-electrochemical kinetic parameters, i.e. D_o, v, and C_o^* must be known accurately. These parameters are very sensitive towards temperature and their values are also somewhat dependent on the electrolyte used during electrochemical study. **Table 2.1** provides these parameters at various conditions.

Table 2.1: *Non-electrochemical kinetic parameters for RDE data analysis.*

Experiment conditions			Diffusion coefficient of oxygen (cm^2/s)	Kinematic viscosity of electrolyte (cm^2/s)	Solubility of oxygen (mol/cm^3)	Ref.
Electrolyte	Temperature	Pressure				
0.1 M $HClO_4$	20 ^oC	1 atm. O_2	1.67 x 10^{-5}	--	1.38 x 10^{-6}	[22]
0.1 M H_2SO_4	20 ^oC	1 atm. O_2	1.4 x 10^{-5}	0.010	1.11.38 x 10^{-6}	[23]
0.1 M KOH	20 ^oC	1 atm. O_2	1.9 x 10^{-5}	--	1.21.38 x 10^{-6}	[24]
0.1 M NaOH	20 ^oC	1 atm. O_2	1.65 x 10^{-5}	0.011	8.41.38 x 10^{-7}	[25]

2.3.3 Rotating Ring Disk Electrode

Similar to the RDE, the rotating ring disk electrode (RRDE) is a very important technique which is being used to understand and quantify the product formed on the disk electrode. The only difference between the RDE and RRDE is the addition of second WE in the form of a ring. Therefore, the RRDE is a double WE system consists of glassy carbon as the disk and Pt as the ring WE. These two electrodes are separated by a non-conducting barrier. Bipotentiostat must be needed to operate such kind of electrode. As mentioned in RDE, the laminar flow created during rotation of WE can be effectively utilized in the RRDE technique. Since, the electrode is under rotation (laminar flow), the solution gets driven to the

side of the disk and can be collected in a controlled manner. As a result, the obtained current from the disk and ring WE depends on their respective potentials, area and the separation distance between the two WEs (s). Depending on the area, size and separation distance between the two WEs, the collection efficiency (N) of the ring can be obtained. For that, the standard ferrocene/ferrocenium couple is measured by using $K_3Fe(CN)_6$ as the electro-active species. The ratio of the ring current (I_R) to the disk current (I_D) gives the value of N (N=0.37).[19, 21]

In the present study, the RRDE technique has been used to investigate the intermediates formed during ORR. During ORR, the disk electrode is scanned in a particular potential window and the product formed on the disk can be merely collected and recorded on the ring WE. The potential of the ring WE will be kept constant.

Mainly, ORR takes place *via* two-electron and/or four-electron reduction pathways. The two-electron pathway produces hydrogen peroxide as the intermediate, which can be quantified by using RRDE. The percentage of hydrogen peroxide and number of electrons involved can be obtained by using the following equations:[21]

$$H_2O_2\% = 200 * \frac{I_R/N}{(I_R/N)+I_D} \quad (2.10)$$

$$n = \frac{4I_D}{(I_R/N)+I_D} \quad (2.11)$$

where, I_R is the Faradaic ring current, I_D is the Faradaic disk current and N is the collection efficiency of the ring WE.

2.4 PEM Fuel Cell Testing

Real ORR performance of the prepared electrocatalyst can be tested using the polymer electrolyte membrane fuel cell (PEMFC) in the form of a single cell or multi-cell stack. The performance can be screed by fabricating the membrane electrode assembly (MEA) by sandwiching two electrodes with a polymer electrolyte membrane. The performance can be analysed by passing fuel (hydrogen, methanol etc.) at the anode and oxidant (oxygen or air) at the cathode side of the cell with the help of the Test Station.[26-28] The fuel gets oxidized to proton and generates electron. Proton travels through the polymer electrolyte membrane from the anode to the cathode side and, simultaneously, electron comes

through the external circuit. The oxidant gets reduced due to the electron and the intermediate product gets neutralized by combining with proton and forms water and heat as the final product.

In the present study, Nafion® (N-212) was used as the polymer electrolyte membrane. The carbon supported Fe-Pt based core-shell electrocatalyst was utilized as the cathode and commercially available 20 wt. % Pt/C as the anode catalyst. The fabricated MEAs were tested by using a FCT Test Station (Purchased from Fuel Cell Technologies, INC, USA) unit bypassing hydrogen at the anode and oxygen at the cathode side with a flow rate of 0.2standard liters per minute (slpm) and by maintaining 100% relative humidity. Moreover, to maintain the desired current profile while collecting the lifetime data (durability data), a cyclical current step protocol was written to control the output and load box setting. This protocol was based on the Set Protocol.vi from the FCT test station Labview software library, in which we can specify the current settings of the load box under constant current mode as well as the time delay for each of the current settings after the specification is reached. At the same time, individual test parameters like gas flow rates, current, voltage, and temperatures of the running MEA were examined and documented *via* an independent Lab-view file (Alone LT.vi, from FCT software library) software.

The details of Nafion® treatment and MEA fabrication are given in the following section (**Section 2.4.1)**.

2.4.1 Pre-treatment of Nafion Membrane

The as purchased Nafion membranes were pre-treated with H_2SO_4, H_2O_2 and HNO_3, prior to use. These treatments activate the Nafion film prior to its use PEMFC. The desired sized Nafion pieces were first treated with 30 % nitric acid for ~1h at 110 ^oC, which removes the metal ion impurities present in the Nafion® matrix. In the second step, the nitric acid treated Nafion films were boiled with 5 % hydrogen peroxide for ~1h at 110 ^oC. Subsequently, in the third step, the Nafion films were treated with 1 M H_2SO_4 for 1h at 110 ^oC, to get the additional -SO_3H groups. During the pre-treatment, the DI water washing was performed after each step. Finally, the Nafion films were boiled in DI water and stored in fresh DI water until it is used for making MEA.

2.4.2 Preparation of the Electrodes

The electrodes were prepared by brush coating. Before brush coating, the catalyst slurry was prepared by sonicating the required amount of the catalyst in ethanol:water mixture with appropriate amount of the Nafion® solution to achieve the Nafion to Carbon ratio equal to 0.75. The catalyst slurry was brush coated on the surface of the gas diffusion layer (GDL) till the required amount of Pt gets loaded on GDL. In the present study, we maintained the Pt-loading of 0.05, 0.1, 0.2 and 0.3 mg_{-Pt}/cm^2. Afterwards, the electrodes were brushed with 1 wt. % of Nafion® to attain a very thin layer on the surface of GDL, which helps to achieve the effective triple phase boundary conditions during the testing.

2.4.3 Fabrication of the Membrane Electrode Assembly

The brush coated electrodes were put on the either side of the Nafion® membrane and hot pressed in a Carver Press at 130 ^oC for 90 s. Subsequently, it was removed from the press and fixed in a fuel cell fixture and tested.

2.5 References

[1] B. K. Balan, S. M. Unni, S. Kurungot, *The Journal of Physical Chemistry C* **2009**, *113*, 17572-17578.

[2] A. Murugadoss, R. Pasricha, A. Chattopadhyay, *Journal of Colloid and Interface Science* **2007**, *311*, 303-310.

[3] B. Y. Xia, H. B. Wu, X. Wang, X. W. Lou, *Journal of the American Chemical Society* **2012**, *134*, 13934-13937.

[4] D. C. Marcano, D. V. Kosynkin, J. M. Berlin, A. Sinitskii, Z. Sun, A. Slesarev, L. B. Alemany, W. Lu, J. M. Tour, *ACS Nano* **2010**, *4*, 4806-4814.

[5] N. Yao, Z. L. Wang, *Handbook of microscopy for nanotechnology*, Kluwer Academic Publishers, Boston, **2005**.

[6] Z. L. Wang, in *Characterization of Nanophase Materials*, Wiley-VCH Verlag GmbH, **2001**, pp. 37-80.

[7] G. Lawes, *Scanning Electron Microscopy and X-ray Microanalysis, John Wiely & Sons, Chichester* **1987**.

[8] J. I. Goldstein, et. al., *Scanning Electron Microscopy and X-Ray Microanalysis, Kluwer Academic/Plenum Publishers, New York, 3rd ed.* **2003**.

[9] B. D. Cullity, S. R. Stock, *Elements of X-Ray Diffraction, Addision-Wesley Reading, MA,* **1978**.

[10] H. P. Klug, L. E. Alexander, *X-Ray Diffraction Procedures, Wiely New York,* **1954**.

[11] A. R. West, *Solid State Chemistry and its Applications, John Wiely & Sons, Singapore,* **2003**.

[12] J. F. Moulder, W. F. Stickle, P. E. Sobol, K. D. Bomben, *Handbook of X-ray Photoelectron Spectroscopy: A Reference Book of Standared Spectra for Identification and Interpretation of XPS Data; Physical Electronics, Division, Perkin-Elmer Corp.: Eden Prarie, MN,* **1995**.

[13] J. F. Watts, J. Wolstenholme, *An Introduuction to Surface Analysis by XPS and AES, John Wolstenholme* **2003**.

[14] G. A. Somorjai, A. S. Mujumdar, *Introduction to Surface Chemistry and Catalysis, Wiely New York* **1994**.

[15] D. A. Long, *Raman Scattering, Mcgraw Hill Bokk Company, New York,* **1977**.

[16] F. Tuinstra, J. L. Koenig, *The Journal of chemical physics* **1970**, *53*, 1126-1130.

[17] J. F. Rusling, S. L. Suib, *Advanced Materials* **1994**, *6*, 922-930.

[18] B. E. Conway, *Progress in Surface Science* **1995**, *49*, 331-452.

[19] C. Wang, L. Ma, L. Liao, S. Bai, R. Long, M. Zuo, Y. Xiong, *Scientific Reports* **2013**, *3*.

[20] V. Komanicky, A. Menzel, K.-C. Chang, H. You, *The Journal of Physical Chemistry B* **2005**, *109*, 23543-23549.

[21] A. J. Bard, L. R. Faulkner, Electrochemical Methods Fundamentals and Applications, 2nd ed.; John Wiley & Sons, Inc.: New York, **2006.**

[22] N. Wakabayashi, M. Takeichi, M. Itagaki, H. Uchida, M. Watanabe, *Journal of Electroanalytical Chemistry* **2005**, *574*, 339-346.

[23] Y. Gochi-Ponce, G. Alonso-Nuñez, N. Alonso-Vante, *Electrochemistry Communications* **2006**, *8*, 1487-1491.

[24] A. Parthasarathy, S. Srinivasan, A. J. Appleby, C. R. Martin, *Journal of The Electrochemical Society* **1992**, *139*, 2530-2537.

[25] C. Paliteiro, A. Hamnett, J. B. Goodenough, *Journal of Electroanalytical Chemistry and Interfacial Electrochemistry* **1987**, *233*, 147-159.

[26] F. Barbir, in *PEM Fuel Cells, 2nd ed.,* Academic Press, Boston, **2013**, pp. 17-32.

[27] F. Barbir, in *PEM Fuel Cell, 2nd ed.,* Academic Press, Boston, **2013**, pp. 119-157.

[28] L. Carrette, K. A. Friedrich, U. Stimming, *Fuel Cells* **2001**, *1*, 5-39.

Chapter 3

Surface Modification-cum-Anchoring Strategy for the Synthesis of Low-Pt Core-Shell Electrocatalysts for Oxygen Reduction Reaction*

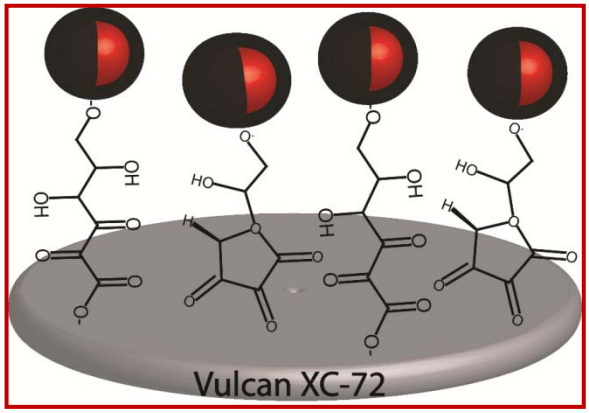

A novel ascorbic acid (AA) reduction method for the synthesis of low-Pt based core-shell structured electrocatalysts is explained in this chapter. The chapter deals with the preparation of two different types of electrocatalysts, namely, carbon supported Cu (core)-Pt (shell) (Cu@Pt/C) and carbon supported Fe_2O_3 (core)-Pt (shell) (Fe_2O_3@Pt/C). The direct dispersion of Cu@Pt and Fe_2O_3@Pt core-shell nanoparticles on a carbon support has been achieved while retaining the essential core-shell features of the nanoparticles by adopting an *in situ* surface modification-cum-anchoring strategy. AA, which was used as the reducing agent in the process, is playing a crucial role by making use of its multifunctional activities as a reducing agent, a stabilizing agent, as well as a capping agent in addition to its efficiency in functionalizing the carbon surface during the course of the reaction. Later, the prepared catalysts, *viz*. Cu@Pt/C and Fe_2O_3@Pt/C, have been investigated towards oxygen reduction reaction (ORR) in acidic condition. The single cell performance and durability characteristic of a low-Pt electrode derived from Fe_2O_3@Pt/C have been explained thoroughly. The ORR activity in both liquid and semi-vapor phase was found to be strongly influenced by the thickness of the catalyst layer owing to the ohmic contribution from the less conductive Fe_2O_3 core. The durability assessment of the electrodes is included at the end of this chapter.

*The content of this chapter has been published in "***Chem. Commun.***, 2011, ***47***, 3951-3953"
- Reproduced by permission of The Royal Society of Chemistry
http://pubs.rsc.org/En/content/articlelanding/2011/cc/c0cc05645f#!divAbstract

*The content of this chapter has been published in "***J. Phys. Chem. C***, 2012, ***116***, 7318–7326"
-Adopted with permission from (***J. Phys. Chem. C***, 2012, ***116***, 7318–7326). Copyright (2012) American Chemical Society.

3.1. Introduction

Development of Pt-based core-shell nanoparticles of non-noble metals as electrocatalysts for PEMFCs has become an emerging research area as these classes of materials can offer great scope for ensuring cost reduction as well as electrochemical stability. Pt as a protective thin shell significantly helps the non-noble metal core to attain greater electrochemical stability in the operating electrochemical environment of PEMFCs. To date, different methods have been proposed for synthesizing the core-shell nanoparticles having good electrocatalytic activity.[1-5] However, achievement of proper dispersion of core-shell nanoparticles on a carbon support, while retaining the essential core-shell features, is a challenging task owing to the counteracting inter-species interactions within the system.[2] For example, particle dispersion can be improved by adopting *in situ* reduction methods because, here reduction takes place in the presence of carbon, where the surface interaction is expected to be high.[3] Although particle dispersion will be fairly good, the preferential adsorption of the respective metal ions on the active sites of carbon makes more individual metal particle dispersion than the formation and dispersion of the core-shell nanoparticles on the surface.[2] In contrast, the *ex situ* dispersion strategy, where the process involves initial preparation of the core-shell nanoparticles and their subsequent dispersion on carbon by adding the substrate at a later stage, gives poor dispersion owing to the weak interaction between carbon and reduced surfaces of the core-shell nanoparticles.[4] However, this method gives core-shell nanoparticles possessing the required structural features.

This means that, maintaining high dispersion while retaining the core-shell characteristics of the species is an exigent task. To overcome this issue, here, a unique strategy has been developed, where the reduction process itself gives a means to interlink the core-shell particles with the carbon surface, which leads to better dispersion and improved control on particle growth. The idea is that the core-shell nanoparticles will be initially generated in the medium and will be subsequently forced to interact with the *in situ* modified carbon surface. The *in situ* functionalization of the carbon support is achieved by the intervention of the oxidation and degradation products of the reducing agent formed during the course of the reaction. Since the process helps direct anchoring of particles on the substrate surface in the medium where these particles are evolved, excellent dispersion could be achieved while retaining the nanometer size distribution and essential structural characteristics of the core-shell morphology (**Scheme 3.1**).

In this process, logical selection of the reducing agent is the key requirement for the successful accomplishment of dispersion because, as the reducing agent reduces the metal ions and creates core-shell nanoparticles, its own degradation and oxidation products play another major role by building the required surface sites on the substrate surface. A controlled interplay of these features helps to attain sufficiently good dispersion of the core-shell nanoparticles on the carbon substrates, all involving milder experimental conditions and easy workups. For examples, in the case of the carbon supported Cu-Pt core-shell catalyst, which comprises a Cu core and a Pt shell (Cu@Pt/C), the synthesis was accomplished by sequential reduction of $CuCl_2$ and H_2PtCl_6 by using ascorbicacid (AA), where AA acts as the reducing as well as stabilizing agent. Thus, both the core-shell feature and dispersion could be simultaneously maintained by using the modification-cum-anchoring strategy process. Most importantly, it has been observed that Cu@Pt/C outperforms the Pt/C catalyst during electrochemical oxygen reduction reaction in terms of the overpotential (detailed discussion is provided in **Part-A**).

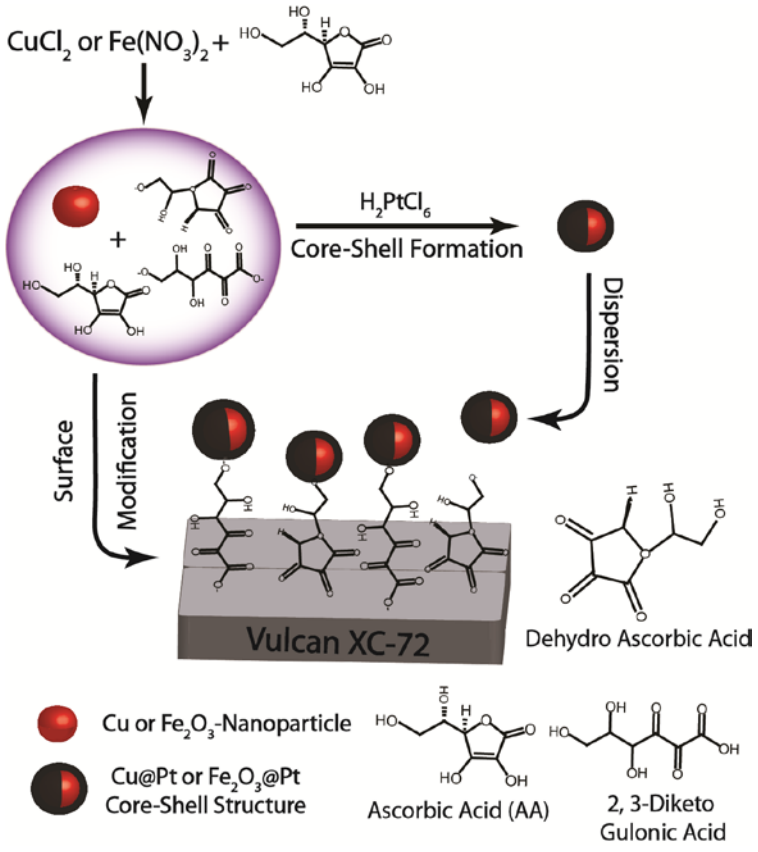

Scheme 3.1: *Schematic representation of the strategy involved in the synthesis of the Cu@Pt/C and Fe_2O_3@Pt/C core-shell nanoparticles by the sequential reduction method.*

Similar to the Cu@Pt/C catalyst, the Fe-Pt core-shell structured electrocatalyst supported on carbon (Fe_2O_3@Pt/C) was prepared by following the similar surface modification-cum-anchoring protocol and its ORR activity was screened. A single cell of PEMFC was also prepared by using this catalyst in the cathode and its performance evaluation was done, which is found to be better than that of the cell made from the state-of-the-art Pt/C as the cathode when the electrode thickness is below a threshold level (detailed discussion is provided in **Part-B**). Thus, the outstanding performance of the electrodes derived from the core-shell structured electrocatalysts opens up a great scope for realizing cost effective systems and miniature cells for various niche applications.

Part-A: Carbon Supported Cu-Pt Core-Shell Catalyst (Cu@Pt/C): Preparation, Characterization and Activity Evaluation.

3A.1. Experimental Section

3A.1.1. Synthesis of Functionalized Vulcan Carbon XC-72 (F-C)

For the functionalization of Vulcan carbon XC-72 support, H_2O_2 treatment was used.[6] During the synthesis, 500 mg of Vulcan carbon was dispersed properly in 100 ml of H_2O_2 (30 %) solution by ultra-sonication for 15 min. Further, the Vulcan carbon and H_2O_2 reaction mixture was refluxed for 5h at 60 ^oC. Finally, the mixture was filtered with 0.2 µm PTFE membrane filter paper and washed thoroughly with DI water. Subsequently, the material was dried at 80 ^oC for overnight. The functionalized Vulcan carbon XC-72 is designated as F-C.

3A.1.2. Synthesis of Cu@Pt/C Core-Shell Structured Electrocatalyst

8 ml aqueous solution of 0.1 N $CuCl_2$ was reduced by adding 40 ml aqueous solutionof 0.1 N AA and the solution was subsequently kept on stirring for 30 min. The pH of reaction mixture was maintained to 12 by drop-wise addition of 10 % NaOH. Under these conditions, the copper gets reduced, indicated by a reddish colour, and instantaneously 8 ml aqueous solution of 0.01 N H_2PtCl_6 was added without altering the pH of the reaction mixture. After the addition of H_2PtCl_6, the reaction mixture was kept on stirring for 20 min, at 60 ^oC to ensure complete reduction of Pt^{+x} preceded the colour change of the mixture to black. F-C was dispersed in DI water by ultra-sonication and instantly added to the reaction mixture and kept on stirring for 10 h. Afterwards, the catalyst (Cu@Pt/C) was filtered (PTFE membrane filter paper having 0.2 µm

pore size, Rankem) and dried at 90 ^{o}C for 2 h. Further, to study the effect of the shell thickness on the structure and properties of the core-shell materials, catalysts bearing different Pt weight percentage were synthesized (**Table 3A.1**). Mainly, three samples were prepared with 18, 15 and 10 wt. % of Pt and the prepared catalysts are designated as Cu_{50}:Pt_{18}, Cu_{50}:Pt_{15}, and Cu_{50}:Pt_{10}, respectively.

Table 3A.1: *The synthesized catalysts with varying shell concentration.*

Cu@Pt/C				
Sr. No.	**Sample Code Name**	**Cu:Pt:C ratio (wt. %)**		
		Cu	**Pt**	**C**
1	Cu_{50}:Pt_{18}	50	18	32
2	Cu_{50}:Pt_{15}	50	15	35
3	Cu_{50}:Pt_{10}	50	10	40
4	Cu_{50}:Pt_{0}	50	0	50

3A.2. Results and Discussion

3A.2.1.TEM Analysis

Structural morphology of the prepared core-shell structures of Cu@Pt/C (Cu_{50}:Pt_{18}) has been investigated by TEM analysis. **Figure 3A.1** provides the TEM images of Cu_{50}:Pt_{18} supported on Vulcan XC-72 at different magnification. **Figure 3A.1a** shows the well dispersion of Cu_{50}:Pt_{18} core-shell nanoparticles on carbon. Here, the nanoparticles are well separated from each other and monodispersity on the carbon support has been essentially maintained. The magnified portion has been shown in **Figure 3A.1b,** which indicates the clear picture of the core-shell structure. The inset of **Figure 3A.1b** reveals the essential features of the Cu_{50}:Pt_{18} core-shell structure, possessing a thin shell of Pt (~0.5 nm) on the non-noble metal (Cu) core, giving an overall particle size of 3-4 nm. Moreover, looking closely to the TEM (inset of **Figure 3A.1b**), it can be seen that Cu-core shows a diameter of 2.5 nm and it possesses higher concentration compared to the Pt-shell. In addition, the difference between the interference fringes and their interpenetration at the interface of the two layers indicate the formation of crystalline cores and shell structures, which can be seen in **Figure 3A.1c**. This intervention leads to reduction in the Pt-Pt inter-atomic distance at the surface and modifies the electronic and crystalline properties of

the Pt skin layer, which eventually helps in improving the electrocatalytic activity of the surface.[7-9] Moreover, the calculated d-spacing values at the center and surface (shown **in Figure 3A.1.c**) are found to be 0.20 and 0.23 nm, which give the evidence of Cu as a core and Pt as a shell. In addition, the measured d-spacing values from the selective area diffraction pattern (SAED) (**Figure 3A.1d**) are 3.37, 2.08 and 1.48 Å for Cu_{50}:Pt_{18}, which match with those of Pt (111), (200) and (220) planes, respectively.

More importantly, while performing the TEM investigation of the core-shell structures supported on the carbon substrate, we have to simultaneously take care of the contrast differences of Cu, Pt and carbon. Here, we faced some problems to simultaneously distinguish the contrast difference between Pt and carbon. However, this could be overcome up to some extent by focusing on the particles deposited along the curved edges (**Figure 3A.1b**). Specifically, carbon supported Cu_{50}:Pt_{18} has shown formation of continuous Pt-shell in comparison to the all other prepared samples (*i.e.* Cu_{50}:Pt_0, Cu_{50}:Pt_{10} and Cu_{50}:Pt_{15}; confirmed by the electrochemical study, discussed in **Section 3A.2.6**). Hence, Cu_{50}:Pt_{18} has been chosen for the further evaluations.

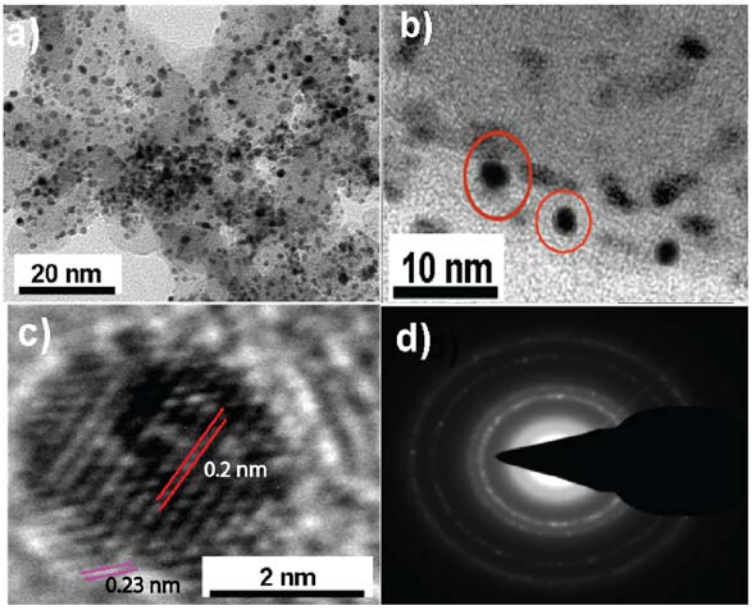

Figure 3A.1: *(a) TEM image of well dispersed Cu@Pt (Cu_{50}: Pt_{18}) particles on Vulcan XC-72, (b) magnified portion of (a) indicating core–shell features of the supported nanoparticles and inset shows the magnified single core–shell nanoparticle with its core and shell dimensions, (c) HR-TEM image of Cu@Pt ($Cu_{50:}$ Pt_{18}) with lattice fringes of Cu (red) and Pt (pink) and (d) SAED pattern of the Cu_{50}: Pt_{18}.*

Furthermore, to be more realistic and to compare the activity of the prepared core-shell structured electrocatalyst with commercially available 20 wt. % Pt/C (Pt_{20}), we have also taken the TEM images of Pt/C. As can be observed from **Figure 3A.2**, the nanoparticles of Pt are well-dispersed with a mean particle size of ~ 3-5 nm. Moreover, most of the Pt particles have a spherical shape (**Figure 3A.2a,b**). Thus, both the Pt/C and core-shell catalysts have nearly similar dispersion and shape characteristics. The HR-TEM image in **Figure 3A.2c** demonstrates good crystalline nature of the nanoparticles, matching with the Cu_{50}:Pt_{18} sample. The HR-TEM of Pt/C has shown a d-spacing value of 0.23 nm, which is corresponding to the (111) plane of Pt. This also gives information on the good crystallinity of the system. The calculated d-spacing values from the SAED pattern are matching with (**Figure 3A.2d**) with the (111), (200) and (220) planes of Pt.

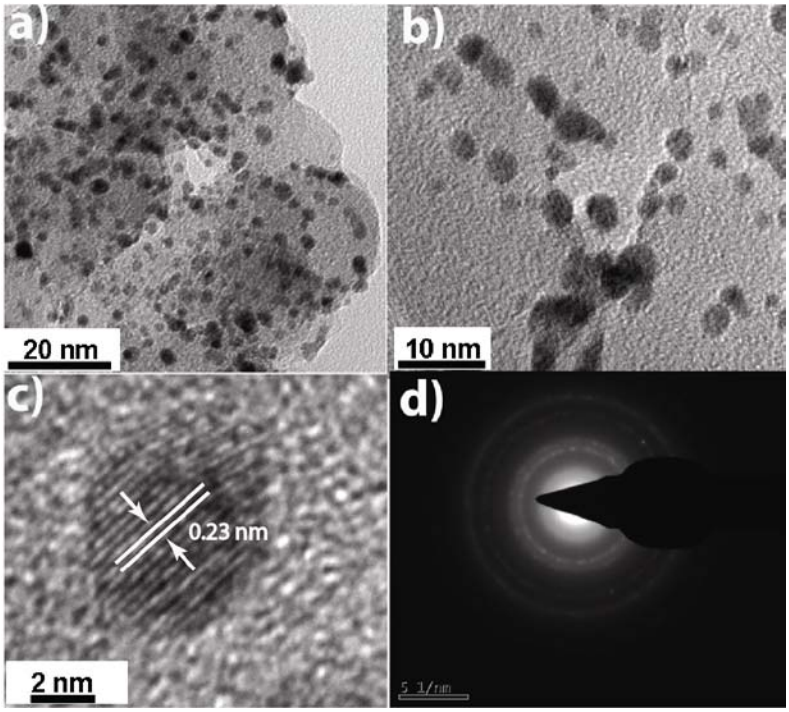

Figure 3A.2: *(a, b) TEM images of a commercially available 20 wt. % Pt/C (Pt_{20}) taken at different resolutions, (c) HR-TEM image of Pt/C showing the lattice fringes and (d) SAED pattern of the Pt/C.*

3A.2.2. XRD Analysis

XRD technique has been used to confirm the crystallinity of the prepared catalysts. **Figure 3A.3** shows the comparative XRD of Cu@Pt/C (Cu_{50}:Pt_{18}) and Pt/C. The XRD patterns

of Cu@Pt/C prepared with varying Pt content are provided in **Figure 3A.4**, along with the XRD of Cu. Slight shift in the Pt (111) and Pt (200) peak positions indicates change in the lattice of the core-shell metal as a result of the shell thickness variation and interpenetration of the lattice planes.[10] The well resolved broad peaks in the XRD patterns in comparison to the commercial Pt/C catalyst presumably indicate the high dispersion of the nanoparticles on the substrate surface.[6, 10-14] The 2θ values of ~39.1, ~46.51 and ~68.1^{o} correspond to the Pt (111), (200) and (220) planes, respectively, confirming the face centered cubic (fcc) crystal structure of Pt.

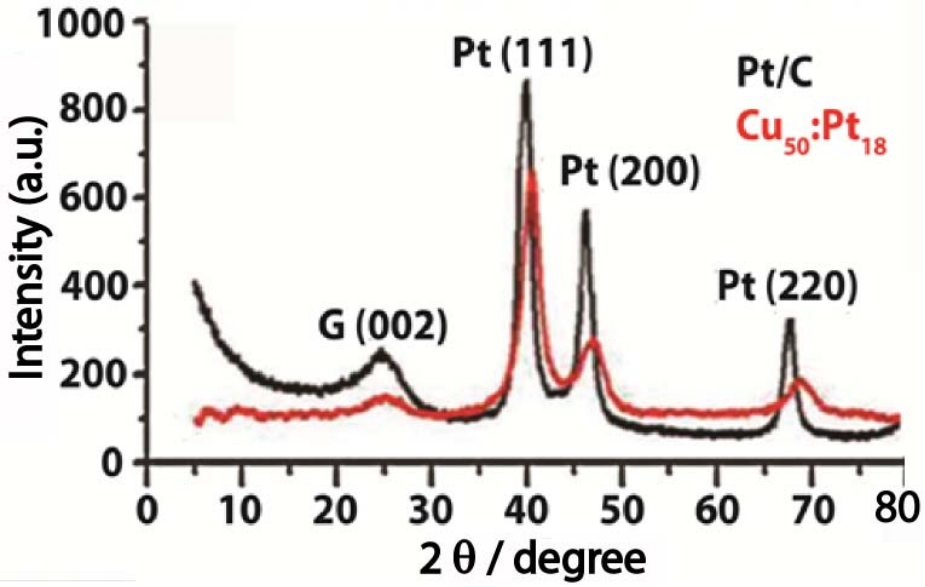

Figure 3A.3: *Comparative XRD spectra of Cu@Pt/C (Cu_{50}:Pt_{18}) and Pt/C.*

As mentioned above, to understand the exact concentration of Pt needed to completely cover the Cu-core, different samples named as Cu_{50}:Pt_{18}, Cu_{50}:Pt_{15}, Cu_{50}:Pt_{10}, and Cu_{50}:Pt_{0} were prepared by keeping the amount of Cu same in all the samples. These samples were analyzed by XRD and cyclic voltammetry (CV). Interestingly, the absence of the core metal peak/s in the XRD of Cu_{50}:Pt_{18} clearly indicates that the Cu core is well shielded by the Pt shell (**Figure 3A.3** and **3A.4**) in the sample. This has been substantiated by CV taken in acidic media, which indicates the absence of the characteristic redox peaks of Cu in Cu_{50}:Pt_{18} (a detailed discussion on the CV is provided in **Section 3A.2.6**). It can be clearly seen that the Cu (111) peak appeared between the 40-45^{o} in case of Cu_{50}:Pt_{15} (**Figure 3A.4c**) is found to be absent in case of Cu_{50}:Pt_{18} (Figure 3A.4d). This stands out as a strong evidence for the complete coverage of the Cu-core by

the Pt-shell. From these results, it can be concluded that the 18 wt. % of Pt is enough to provide the continuous shell on the Cu-core.

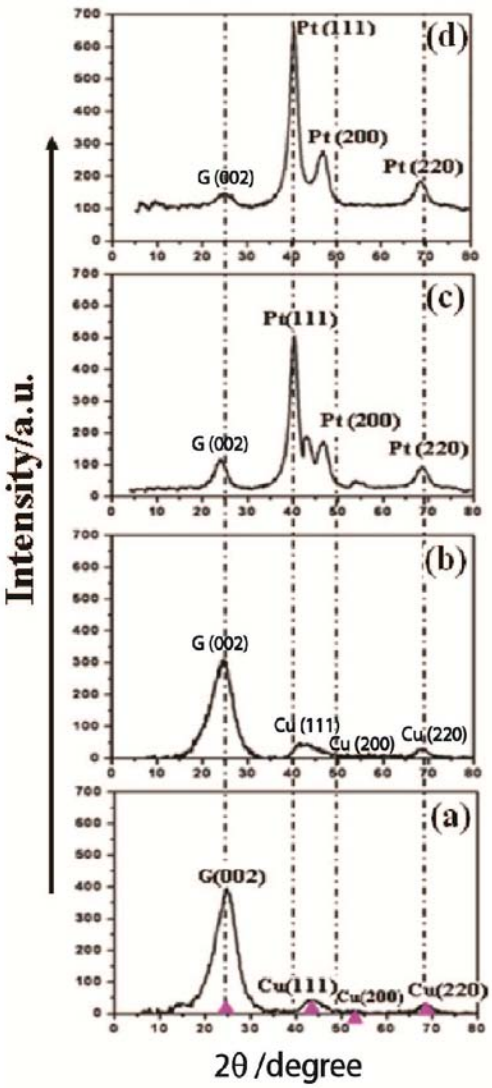

Figure 3A.4: *XRD spectra of (a) Cu_{50}:Pt_0, (b) Cu_{50}:Pt_{10}, (c) Cu_{50}:Pt_{15} and (d) Cu_{50}:Pt_{18}.*

3A.2.3. Infra-Red Spectroscopy

As mentioned earlier, to maintain better dispersion of the core-shell nanoparticles, both AA and its oxidative products formed during the synthesis process create the anchoring sites on the carbon surface and, thus, effectively prevent agglomeration of the particles on the substrate surface. The formation of the functional groups on the surface of the carbon substrate has been confirmed by IR spectroscopy. **Figure 3A.5** shows the IR spectra of AA, Vulcan XC-72, Vulcan XC-72 functionalized by H_2O_2 (FC), and AA-treated FC (AAFC) before and after washing and

after core-shell nanoparticles dispersion on AAFC. The IR band at ~1745 cm^{-1} of the AAFC is corresponding to the –C=O stretching frequency of the dehydroascorbic acid and 2, 3-diketogulonic acid moieties grafted during the reduction process (**Figure 3A.5, right side, peak marked as 'iv')**. Furthermore, the peaks at ~1055 (**Figure 3A.5, right side, peak marked as 'i'**) and ~1225 cm^{-1} (**Figure 3A.5, right side, peak marked as 'ii'**) are attributed to the -C-O stretching of acid and ether groups, respectively. These IR stretching gives confirmation on the *in situ* modification of the support surface. The analysis also reveals that dispersion of Cu@Pt/C nanoparticles on the carbon support surface eradicates the majority of the surface groups grafted on the surface. In addition, the IR-band at ~1580 cm^{-1} (**Figure 3A.5, right side, peak marked as 'iii'**) of AAFC before and after the washing is attributed to the C=C stretching frequency of the dehydroascorbic acid and 2, 3-diketogulonic acid moieties grafted during the process. The sharp peak of C=C stretching in case of AAFC after the washing in comparison to the sample collected before the washing could be due to the effective interaction of the degradation products of AA with the carbon surface (**Figure 3A.5, right side, peak marked as 'iii'**). However, in the case of the AAFC sample collected before the washing, the C=C IR-band is appeared to be very broad, which might be due to the combined effect of the grafted and non-grafted degradation products of the AA on the carbon surface.

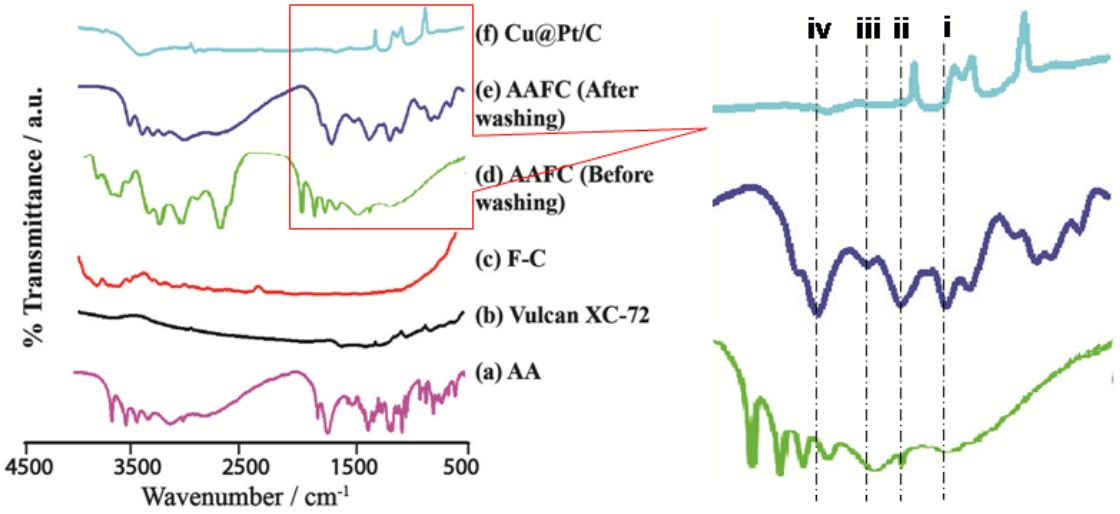

Figure 3A.5: *(Left side) IR spectra of (a) ascorbic acid (AA), (b) Vulcan XC-72, (c) functionalized carbon (F-C), (d, e) AA-treated FC (AAFC) (before washing and after washing) and (f) Cu@Pt/C. (Right side) Enlarged view of the marked area with the red color box.*

The coexistence of the reduction products and the oxidized and decomposed intermediates along with the excess reducing agent and provision for direct anchoring on the substrate surface thus ensure quality dispersion by effectively preventing extensive growth of the particles. Overall, the process leads to the conceptualization of *ex situ* dispersion of core-shell nanoparticles on *in situ* modified carbon substrate in the reaction mixture where the particles are actually originated. In this way, many multistep processes and post-synthesis treatments could be effectively eliminated, which often trigger aggregation of particles and inhomogeneity in their dispersions.

3A.2.4. XPS Study

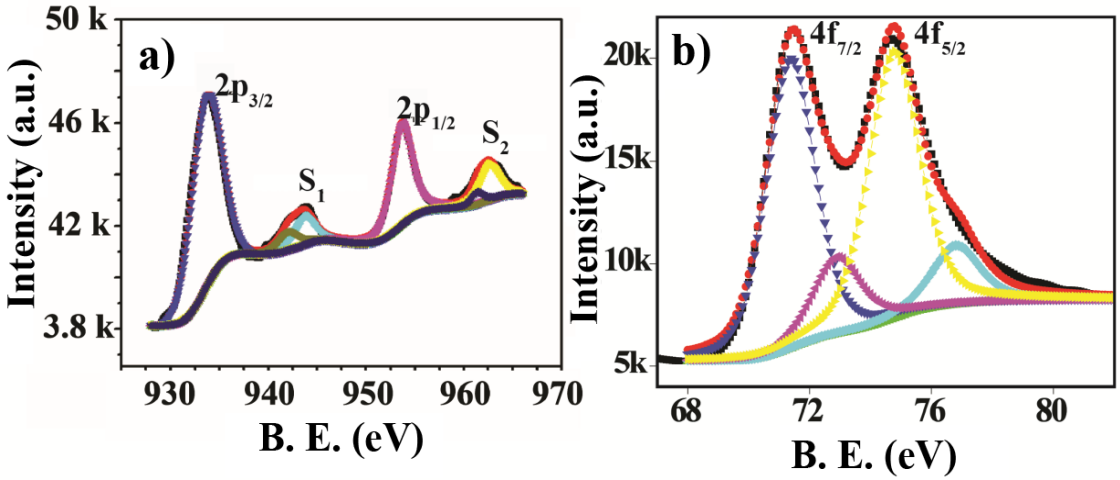

Figure 3A.6: *Deconvoluted XPS of (a) Cu 2p and (b) Pt 4f, of Cu@Pt/C.*

The change in the electronic environment of Cu@Pt/C has been confirmed by XPS analysis. The deconvoluted XPS of Cu and Pt in Cu@Pt/C, shown in **Figure 3A.6**, shed light onto the nature and states of existence of nanoparticles on the surface of carbon. The XPS of Cu (**Figure 3A.6a**) shows two main peaks at ~934.32 and 954.11 eV which are attributed to Cu^0 ($2p_{3/2}$, $2p_{1/2}$). Along with this, the corresponding satellite peaks of $2p_{3/2}$ (**S_1**) and $2p_{1/2}$ (**S_2**) are appeared at ~944.65 and ~964.60 eV, which indicate the bonding of Cu with oxygen.[15] Thus, the shake-up satellite peaks of Cu at higher binding energy embody the presence of oxide of the core metal.[16-17] Moreover, the Pt 4f spectrum (**Figure 3A.6b**) of Cu@Pt/C is fitted with four peaks originating from the spin-orbit splitting of $4f_{7/2}$ and $4f_{5/2}$ states. The peaks at the binding energies of ~71.30 (Pt $4f_{7/2}$) and ~74.50 eV (Pt $4f_{5/2}$) are attributed to the Pt^0 state whereas the two supplementary peaks at the binding energies of ~72.80 and ~76.60 eV are attributed to the

Pt^{+2} state. Overall, a comparison of the relative intensities of the peaks due to Pt^0 and Pt-O in XPS of Cu@Pt/C indicates that Pt in both the catalysts is predominately in the metallic state. The XPS of the commercially available Pt/C is presented in **Figure 3A.7**.

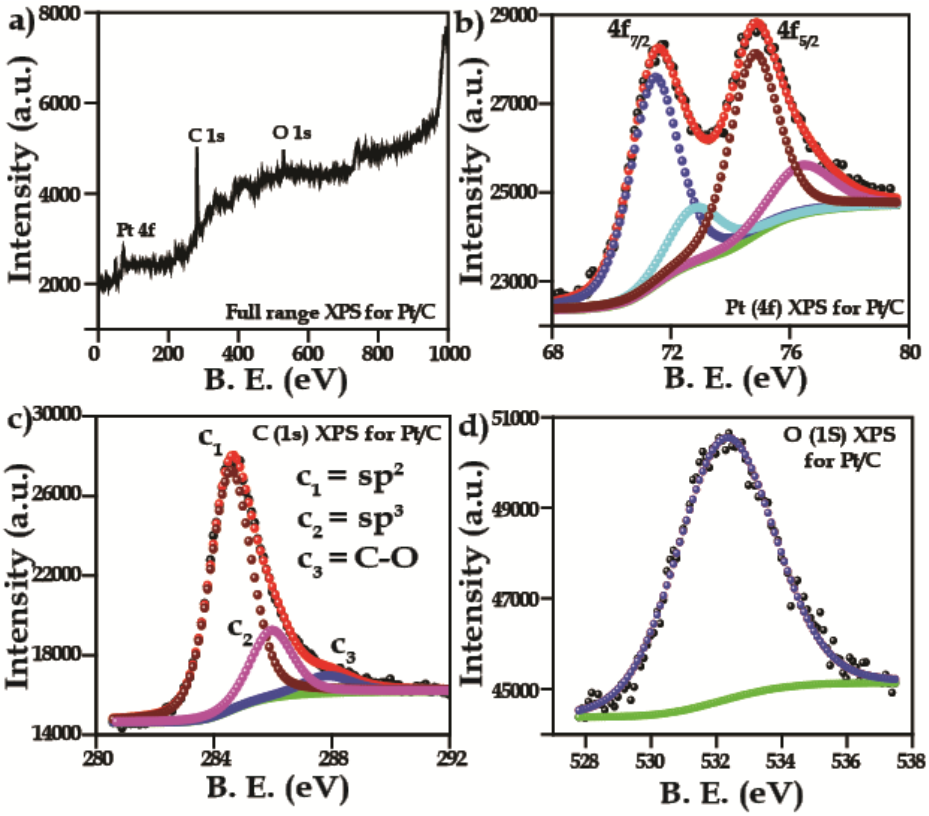

Figure 3A.7: *XPS of the commercially available 20 wt. % Pt/C; a) full scan survey, b) Pt 4f spectra, c) C 1s spectra and d) O 1s spectra.*

The XPS data of pure Pt (**Figure 3A.7**) shows only two peaks, without any supplementary peaks, at the binding energies of ~71.00 and ~74.10 eV corresponding to the Pt^0 state. Absence of the peaks corresponding to the Pt-O indicates that Pt in this system is purely metallic. Moreover, a comparison of the XPS of Pt in the core-shell structure and pure Pt indicates a shift in the peak positions. The shifting of the peak position to a higher binding energy can be due to the core-shell interface and small size of Pt, which leads to the bonding between O and Pt, altering the electronic structure of Pt.[18] Moreover, the interaction between the carbon support and the surface Pt atoms of the core-shell structures also can contribute in the binding energy shift. The exact nature of the Pt interaction with the carbon is still a matter of debate. It is reported that delocalized electrons in the p-orbital of the π-sites on carbon overlap

with a d-orbital of Pt, signifying partially a covalent bonding nature.[19] The obtained XPS results are summarized in **Table 3A.2**.

Table 3A.2: *Results of the XPS analysis.*

Sample Name	Peak	Peak Position				wt. %
Cu@Pt/C	Cu 2p	$2p_{3/2}$	$2p_{1/2}$	S_1	S_2	49.95
		934.32	954.11	944.65	964.60	
	Pt 4f	$4f_{7/2}$		$4f_{5/2}$		17.89
		71.30		74.50		
Pt/C (Pt_{20})	Pt 4f	$4f_{7/2}$		$4f_{5/2}$		20.10
		71.00		74.10		

3A.2.5. Thermogravimetric Analysis

The thermal stability of the catalysts has been evaluated by thermogravimetric analysis (TGA) in an air atmosphere. TGA plots of Vulcan XC-72, Pt/C as well as the catalysts, namely Cu_{50}:Pt_0, Cu_{50}:Pt_{18}, and AA-F-C (**Figure 3A.8**) show an initial weight loss at 100 ^oC due to the loss of moisture. A prominent weight loss region has been observed in the case of AA-F-C in the proximity of 300 ^oC, which has been attributed to the loss of organic moieties adsorbed or deposited on the surface of carbon.

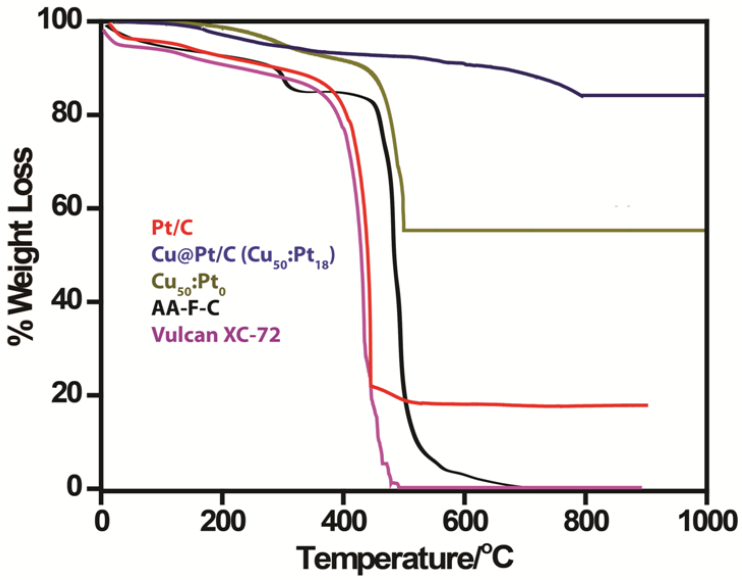

Figure 3A.8: *Thermogravimetric curves of Vulcan-XC-72, Pt/C (Pt_{20}), Cu_{50}:Pt_0, Cu@Pt/C (Cu_{50}:Pt_{18}), and AA-F-C performed in an air atmosphere.*

The samples Cu_{50}:Pt_0, and Cu@Pt/C (Cu_{50}:Pt_{18}) do not display prominent weight loss in this region, indicating nearly complete removal of the organic residues and moieties from the surface. Therefore, these results, along with the evidences from the IR and TEM analysis, rule out the possibilities of forming fibrous organic shells which can be originated during the decomposition of AA. Further loss in weight starting at 450 ^oC is attributed to the decomposition of carbon. Residual weight of 84 wt. % in the case of Cu@Pt/C (Cu_{50}:Pt_{18}) core-shell catalyst indicates the combined weight of Pt, Cu and the corresponding oxide forms of Cu. Moreover, the commercial sample of Pt/C shows the weight loss at ~400 ^oC, which is assigned to the degradation of carbon, leading to the residual weight of ~21 wt. %. This residual weight indicates the weight of Pt. Overall, the obtained weight percentage from TGA is nearly matching with the value estimated from the XPS result.

3A.2.6. Electrochemical Analysis

The combined effect of Pt strain, formation of metal oxide, modifications in the lattice planes caused by the interpenetration and changes in the electronic structure of Pt and efficient dispersion on a carbon substrate results in improved electrochemical performance of the Cu@Pt/C system. Absence of the characteristic redox couple of Cu (corresponding to Cu_{50}:Pt_0 in **Figure 3A.9**) in the cyclic voltammograms of Cu_{50}:Pt_{18} clearly indicates confinement of the Cu core within the incessant protective layer of Pt. The evolution of a continuous shell of Pt can be visualized from the set of cyclic voltammograms presented in **Figure 3A.10**.

The electrochemically active surface area (ECSA) has been calculated from the charge required for hydrogen desorption by using **Equation 3A.1**.

$$ECSA = Q_H / (0.21 * [Pt]) \qquad (3A.1)$$

where, 'Q_H' represents the charge for hydrogen desorption, '[Pt]' is the amount of Pt-loading on the electrode surface and '0.21 mC/cm^2' represents the charge required to oxidize a monolayer of hydrogen from the surface of Pt.[10]

Calculated electro-active surface area (ECSA) is 125 m^2/g for Cu_{50}:Pt_{18} and 94.5 m^2/g for Pt/C.

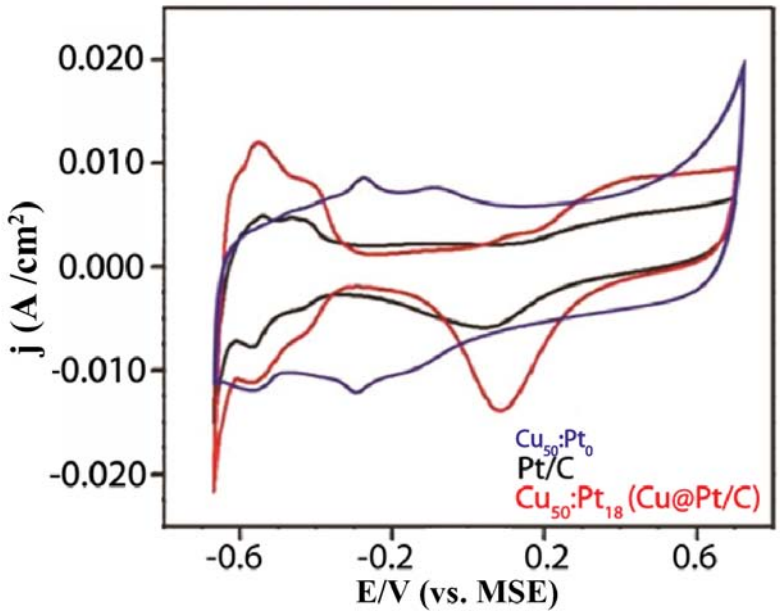

Figure 3A.9: *Comparative cyclic voltammograms of Cu_{50}:Pt_{18}, Cu_{50}:Pt_0, and Pt/C at 100 mV/s in a deaerated 0.5 M H_2SO_4 electrolyte, with Hg/Hg_2SO_4 reference electrode (MSE) and Pt-wire counter electrode. The amount of the Pt loaded on the electrode surface is 4.5 µgm.*

This clearly indicates that the formation of Pt in the form of a shell on another species helps to improve the reactive surface area as the skin layer adopts the surface geometric features of the core material. However, even though we have carried out a systematic study to optimize the Pt shell thickness, the benefit in terms of ECSA was dominant when the shell thickness was in the range of 0.5 to 1.0 nm, which corresponds to the composition Cu_{50}:Pt_{18}. The set of voltammograms presented in **Figure 3A.10** indicates the gradual growth of the protective Pt shell on the Cu core, as evidenced by the progressive elimination of the redox peak corresponding to Cu as the Pt shell grows on its surface. The cyclic voltammogram corresponding to Cu_{50}:Pt_{18} (the voltammogram numbered as 'd') gives the characteristic signatures corresponding to Pt in acid medium, which substantiates the claim that the Cu surface has been completely shielded by the protective layer of Pt.

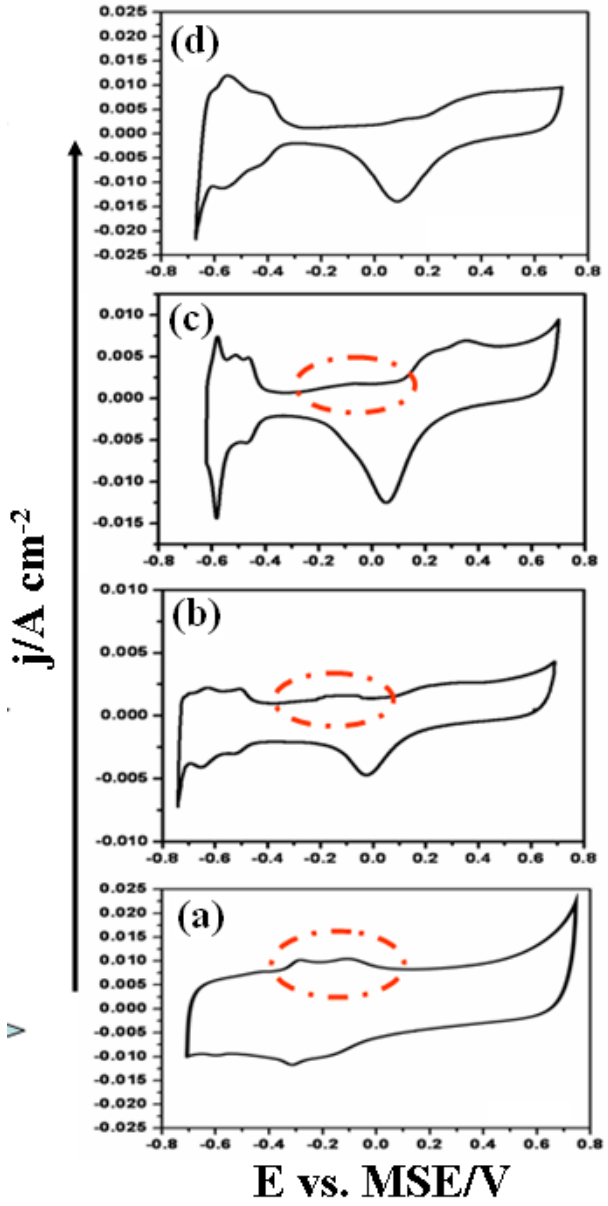

Figure 3A.10: *Cyclic voltammograms of (a) Cu_{50}:Pt_0, (b) Cu_{50}:Pt_{10}, (c) Cu_{50}:Pt_{15} and (d) Cu_{50}:Pt_{18}.*

Thicker shells heal the surface roughness originated from the core material whereas thinner shells produce exposed patches of the core material surfaces. Consequently, Cu_{50}:Pt_{18} on carbon has been taken as the choice sample for the electrochemical evaluations. An additional confirmation on the formation of an incessant shell of Pt on the Cu core has been obtained when the ECSA was continuously monitored while subjecting the catalyst to potential cycling in 0.5 M H_2SO_4. The CV profiles presented in **Figure 3A.11a** correspond to the 100 cycles taken at a scan rate of 100 mV/s. The graph of ECSA against the number of cycles (inset of **Figure 3A.11a**)

clearly verifies the excellent electro-chemical stability attained by the core material in the shell of Pt. The overall percentage loss of ECSA is merely 0.34 % during the course of the potential cycling. The electrocatalytic activities for ORR are studied by the hydrodynamic rotating disk electrode (RDE) technique at different rotations per minute (rpm).

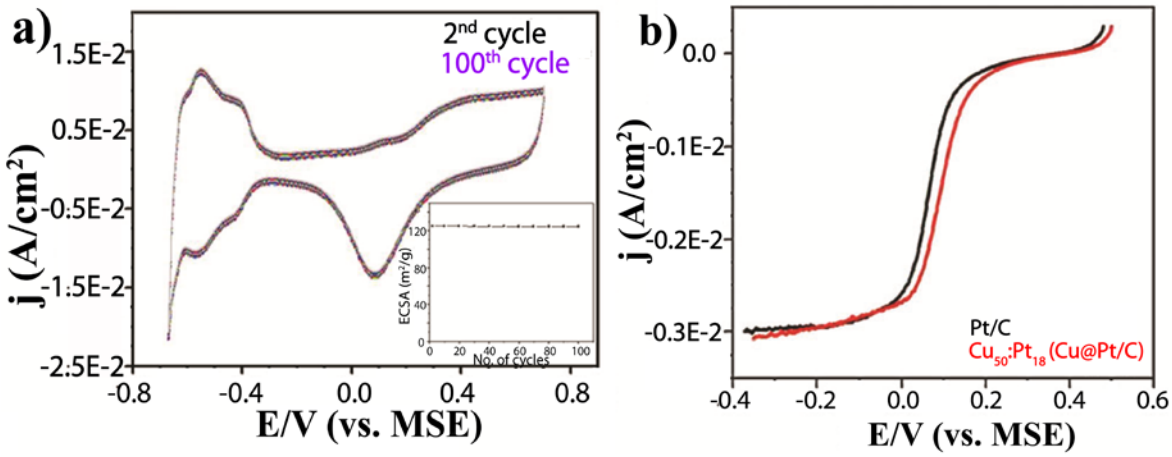

Figure 3A.11: *(a) Durability study of Cu@Pt/C (Cu_{50}:Pt_{18}) in 0.5 M H_2SO_4 electrolyte by recording 100 cycles at a scan rate of 100 mV/s. (the respective inset shows the graph of ECSA versus number of cycles), and (b) comparative LSVs of Cu@Pt/C (Cu_{50}:Pt_{18}) and Pt/C performed at 900 rpm with O_2 flow at 10 mV/s scan rate.*

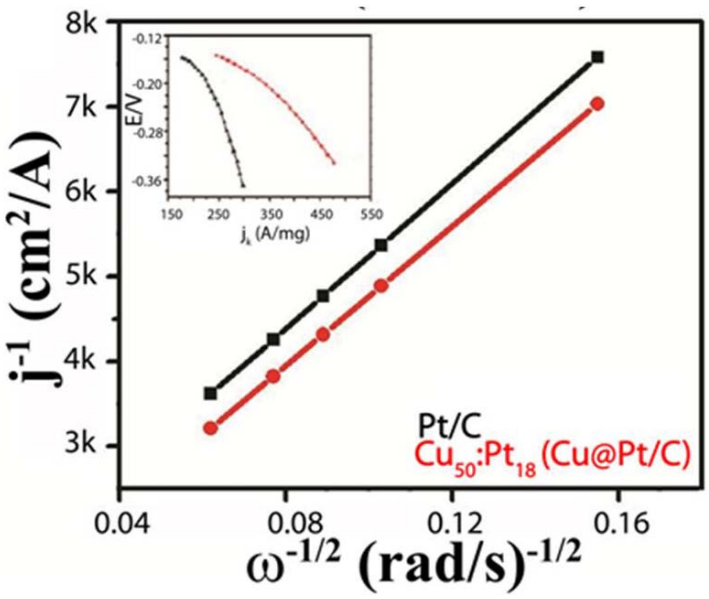

Figure 3A.12: *Koutecky–Levich (K-L) plots at -0.20 V and (inset) Tafel plots indicating the higher catalytic activity of the core-shell catalyst.*

A comparison of linear sweep voltammograms (LSVs) for the core-shell catalyst and Pt/C, performed at an electrode rotation speed of 900 rpm, is shown in **Figure 3A.11b**. The limiting current density is found to be nearly the same in both the cases, but the core-shell catalyst has more positive onset potential. The relatively similar values of diffusion limited current indicate more or less similar oxygen diffusion in these catalysts irrespective of the nanoscale structural differences of the active components. On the other hand, the positive shift in the onset potential of the core-shell system, in comparison to the conventional Pt/C, underlines the fact that the carbon supported core-shell catalyst is more efficient for ORR. The half-wave potential is found to be 30 mV more positive for Cu_{50}:Pt_{18} compared to that of Pt/C. The Koutecky-Levich (K-L) plot, which is a plot of the inverse of current density (j^{-1}) as a function of the inverse of the square root of the rotation rate ($\omega^{-1/2}$), has been used to investigate the kinetic parameters at -0.2 V (**Figure 3A.12**). The calculated rate constant is 2.5 x 10^{-3} cm/s for Cu_{50}:Pt_{18} and 1.0 x10^{-3} cm/s for Pt/C, which clearly indicates that the rateconstant of the core-shell catalyst is twice higher than that of the conventional Pt/C. The Tafel plot (inset of **Figure 3A.12**) indicates the core-shell structured electrocatalyst possesses higher catalytic activity compared to Pt/C.

Part-B: Single Cell Evaluation using the Carbon Supported Fe_2O_3-Pt Core-Shell System (Fe_2O_3@Pt/C) as the Cathode Electrocatalyst

Literature provides strong evidence on the superiority of Fe in tuning the oxygen reduction activity of Pt compared to that of Cu.[20-25] Considering this superiority of Fe over Cu,[20-25] Fe-Pt based core-shell system was prepared by adopting the same preparation protocol as developed for preparing the Cu-Pt system. Few key reasons of selecting the Fe based core-shell catalyst for making the single cell include the strong activity of Fe towards the oxygen adsorption, inherent oxygen reduction property of Fe, its association with Pt can change the oxygen adsorption capacity of Pt and the ability of Fe to lower the d-band centre of Pt by inducing a degree of irregularity in the Pt lattice etc.[20-25] Lowering of the d-band centre and creation of degree of irregularity can result in the weakening of the Pt-oxygen bond, leading to easy dissociation of oxygen and, thereby, better ORR activity.

A discussion on the synthesis of Fe_2O_3@Pt/C and characterizations using TEM, XRD, XPS, and IR-techniques is given briefly in the following sections. Followed by this, a detailed discussion on the electrochemical analysis and single cell evaluation is included.

3B.1. Experimental Section

3B.1.1. Synthesis of Functionalized Vulcan Carbon XC-72 (F-C)

The Vulcan carbon was functionalized as per the reported procedure.[6] The detailed procedure is given in **Section 3A.1.1.**

3B.1.2. Synthesis of Fe_2O_3@Pt/C Core-Shell Structured Electrocatalyst

The Fe_2O_3@Pt core-shell nanoparticles supported on Vulcan carbon catalyst (Fe_2O_3@Pt/C) was prepared by using the similar protocol used for the synthesis of Cu@Pt/C (**Section 3A.1.2, Scheme 3.1**). Here, Fe-precursor (*i.e.* iron nitrate) was used instead of Cu and all the other parameters were kept similar to those maintained for preparing the Cu system.

3B.2. Results and Discussion

3B.2.1. TEM Analysis

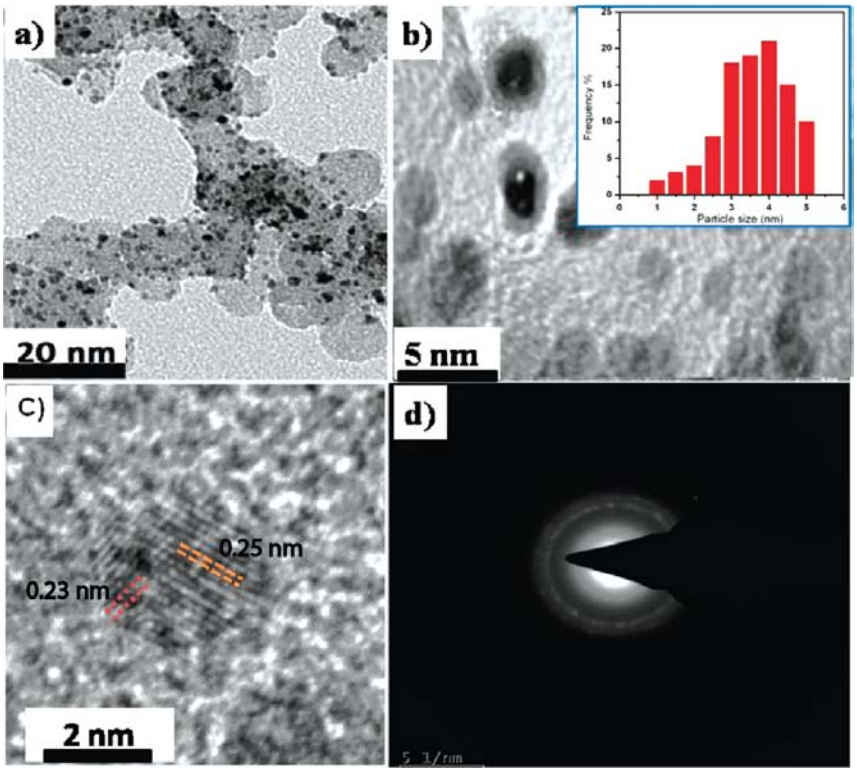

Figure 3B.1: *TEM images of (a) Fe_2O_3@Pt/C indicating the presence of well-dispersed core-shell nanoparticles on the surface of the carbon support, (b) Fe_2O_3@Pt/C core-shell nanoparticles clearly showing the boundaries of the core and shell regions of the nanoparticles, where the inset shows the particle size histogram of Fe_2O_3@Pt/C nanoparticles with an average particles size of ~3-5 nm, (c) HR-*

TEM image of a single particle showing the lattice mismatch at the edge of the core and shell region and (d) SAED pattern of the Fe_2O_3@Pt/C.

Figure 3B.1 shows the TEM image of well-dispersed Fe_2O_3@Pt/C nanoparticles with essential features of the core-shell structure (particle size is ~3-5 nm). The particles size histogram (inset of **Figure 3B.1b**) gives the evidence for the monodispersity of nanoparticles. **Figure 3B.1c** reveals lattice mismatch at the interface of the core and shell indicating the formation of crystalline core-shell nanoparticles. Moreover, the calculated lattice spacing values at the center and surface (shown **in Figure 3B.1c**) are found to be 0.25 and 0.23 nm, which give the evidence of the presence of Fe_2O_3 as a core and Pt as a shell in the system. In addition, the measured d-spacing values from the SAED pattern (**Figure 3B.1d**) are 3.35, 2.04, and 1.44 Å, which match with those of Pt (111), Pt (200), and Pt (220) planes, respectively.

3B.2.2. XRD Analysis

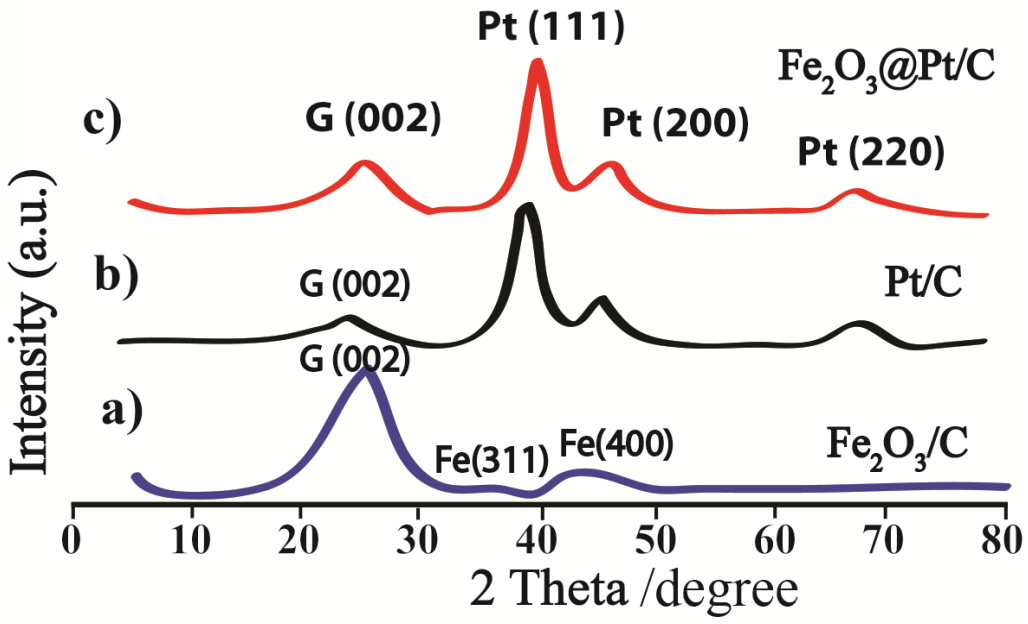

Figure 3B.2: *XRD patterns of (a) Fe_2O_3/C, (b) Pt/C and (c) Fe_2O_3@Pt/C.*

Comparative XRD profiles of Fe_2O_3/C, Fe_2O_3@Pt/C and Pt/C are provided in **Figure 3B.2.** The obtained peaks at 43 and 47° correspond to the iron oxide phase of Fe_2O_3/C. Moreover, these peaks are vanished in the case of Fe_2O_3@Pt/C and instead well-distinguished peaks at 39.8, 46.4, and 68.6°, corresponding to the (111), (200), and (220) planes of the fcc

crystal of Pt, are appeared. In addition, the clear shift of the XRD peaks toward higher 2θ value of Pt (111) certifies the lattice contraction, which indicates the change in the electronic as well as geometric nature of the Pt-shell. The observed broad peaks indicate the high dispersion of the nanoparticles possessing small particle sizes on the substrate surface.

3B.2.3. Infra-Red Spectroscopy

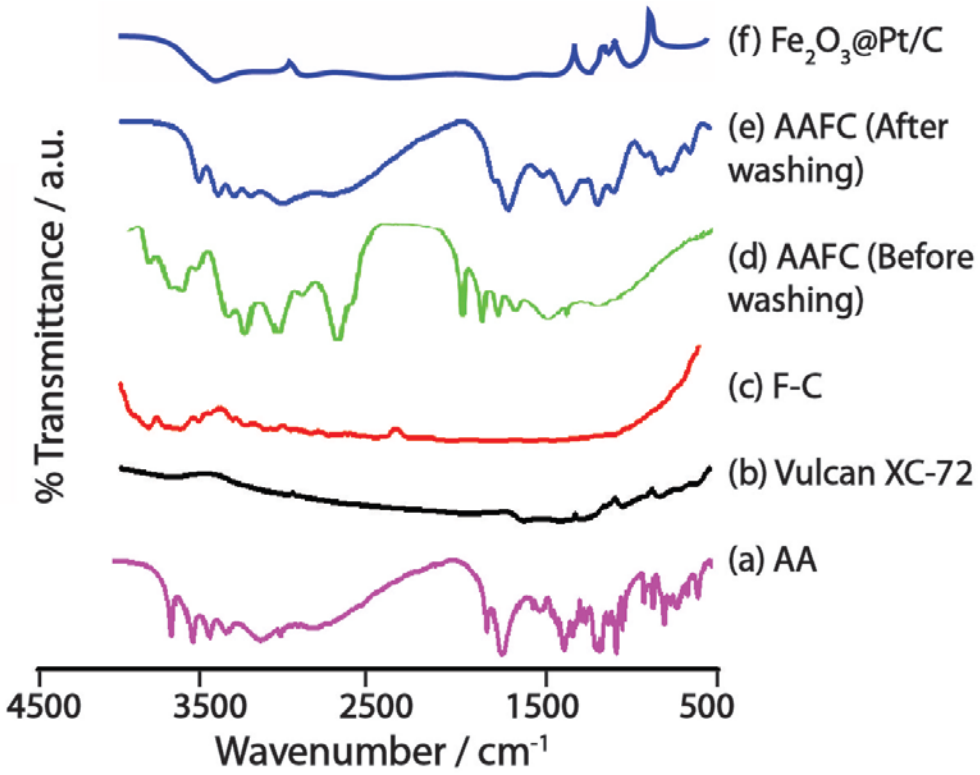

Figure 3B.3: *IR spectra of (a) ascorbic acid (AA), (b) Vulcan XC-72, (c) functionalized carbon (F-C), (d, e) AA-treated FC (AAFC) (before washing and after washing), and (f) Fe_2O_3@Pt/C.*

As mentioned earlier in **Section 3A.2.3**, in the present case also, the signature peaks corresponding to the surface functional groups grafted on the surface of the carbon substrate could be observed due to the oxidative products of AA (**Figure 3B.3**). These peaks are observed at ~1745 cm^{-1} in case of the AAFC samples (spectrum "d" and "e" in **Figure 3B.3**), which represent the -C=O stretching frequency of the dehydroascorbic acid and 2,3-diketogulonicacid moieties grafted during the reduction process. Furthermore, the peaks at ~1055 and ~1225 cm^{-1} are attributed to the-C-O stretching of the acid and ether groups (spectrum "d" and "e" in **Figure 3B.3**), respectively. Moreover, the IR-investigation reveals that dispersion of Fe_2O_3@Pt/C

nanoparticles on the carbon support surface eradicates the majority of the surface groups grafted on the surface (spectrum "f" in **Figure 3B.3**). During the synthesis, the bi-lateral interaction between the grafted functional groups and formed Fe_2O_3@Pt core-shell structures provides the quality dispersion with controlled growth kinetics of the core-shell nanoparticles (**Scheme 3.1**).

3B.2.4. XPS Analysis

Figure 3B.4 shows the deconvoluted XPS spectra of Fe and Pt in Fe_2O_3@Pt/C. The peaks at the binding energy of ~71.3 (Pt $4f_{7/2}$) and ~74.5 eV (Pt $4f_{5/2}$) are attributed to the Pt^0 state, whereas the two supplementary peaks at the ~72.8 and ~76.6 eV are attributed to the Pt^{2+} state. The relative peak intensities of Pt^0 and Pt-O indicate that the Pt is predominately in metallic form. However, the higher binding energy of the Pt peaks (**Figure 3B.4**) comparing to the pure Pt (**Table 3A.2**) can be attributed to the core and shell interface and the small size of the Pt, which lead to the bonding between O and Pt and bring alteration in its electronic structure.[19, 26] Moreover, the XPS of Fe shows peaks at 709.70 and 724.11 eV which are attributed to Fe^0 ($2p_{3/2}$, $2p_{1/2}$). There are also peaks at 712.00 and 725.60 eV along with a satellite peak at ~718.00 eV, which indicate the bonding of Fe with oxygen.[15, 27] This indicates that the core is having a mixed composition of both metallic and oxidic characteristics, even though the oxide phase predominates over the metallic phase. Furthermore, the concentrations of Fe-oxide and Pt are found to be 40 and 18 wt. %, respectively, in Fe_2O_3@Pt/C.

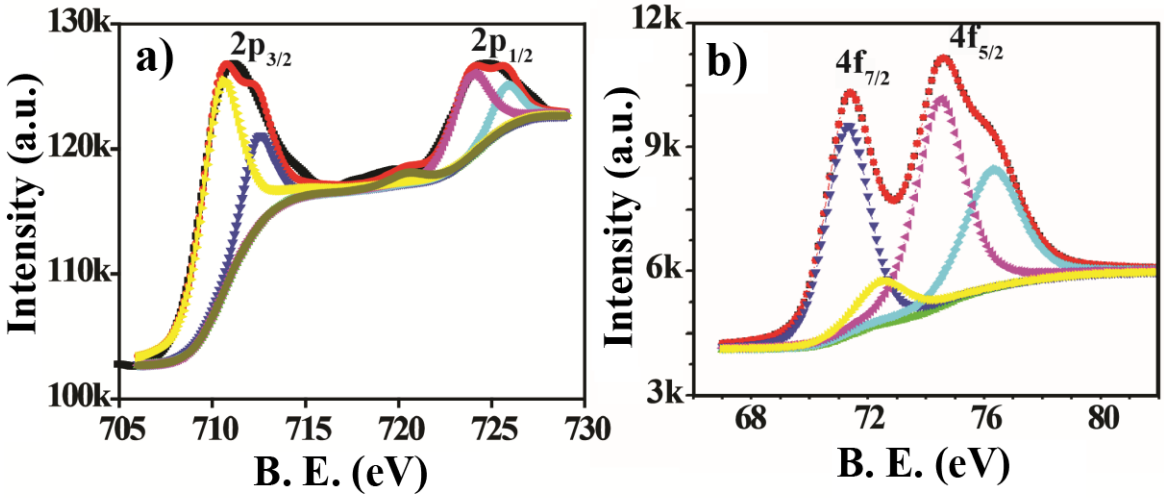

Figure 3B.4: *Deconvoluted XPS of (a) Fe 2p and (b) Pt 4f of Fe_2O_3@Pt/C.*

3B.2.5. Thermogravimetric Analysis

Comparative TGA plots of the commercial Pt/C, Fe_2O_3/C, and Fe_2O_3@Pt/C (**Figure 3B.5**) show two weight loss regions, one starting at 100 °C and another one after 400 ^oC, which are attributed to the loss of moisture and the decomposition of carbon, respectively. A residual weight of 64 wt. % in the case of Fe_2O_3@Pt/C core-shell catalyst indicates the combined weight of Pt, Fe, and the corresponding oxide forms of Fe.

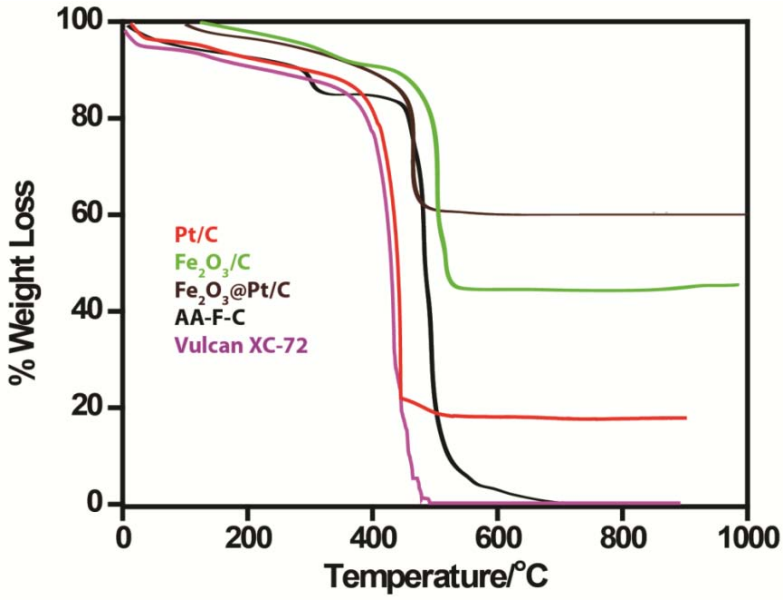

Figure 3B.5: *TGA profiles of AA-F-C, Vulcan carbon XC-72, Pt/C, Fe_2O_3/C and Fe_2O_3@Pt/C recorded in a temperature range of room temperature (RT) to 900 ^oC under air atmosphere.*

3B.2.6. Electrochemical Analysis of Fe_2O_3@Pt/C Electrocatalyst

The electrochemical analysis was carried in $HClO_4$ electrolyte, instead of H_2SO_4 to avoid the issue of sulfate poisoning. The electrochemical evaluation of the samples further augments the formation of the core-shell structure with the modulated electronic and structural properties as visualized from the aforementioned characterization data. This has been confirmed by a set of dedicated electrochemical experiments in aqueous $HClO_4$ solution. **Figure 3B.6a** and **Figure 3B.6b** respectively show the CV profiles of Fe_2O_3@Pt/C and Pt/C with different Pt loadings on the electrode recorded at a scan rate of 100 mV/s in 0.5 M $HClO_4$ with a conventional three-electrode system. The hydrogen adsorption and desorption take place in the potential range of 0-0.3 V (vs. NHE), and the features in this region resemble very much that of a polycrystalline Pt

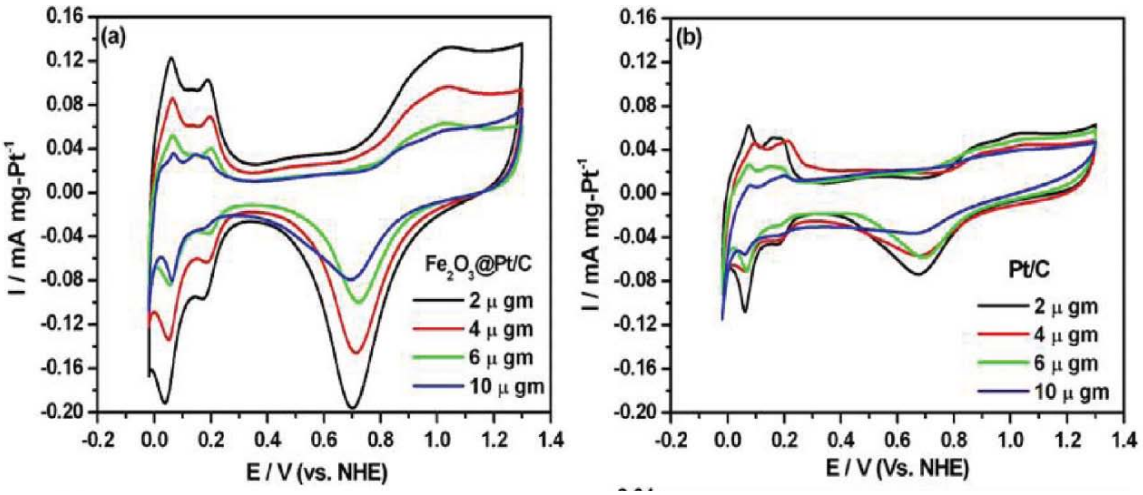

Figure 3B.6: *Combined cyclic voltammograms of (a) Fe_2O_3@Pt/C and (b) Pt/C with different Pt loadings performed at 100 mV/s in 0.5 M $HClO_4$. All the graphs are normalized with respect to NHE.*

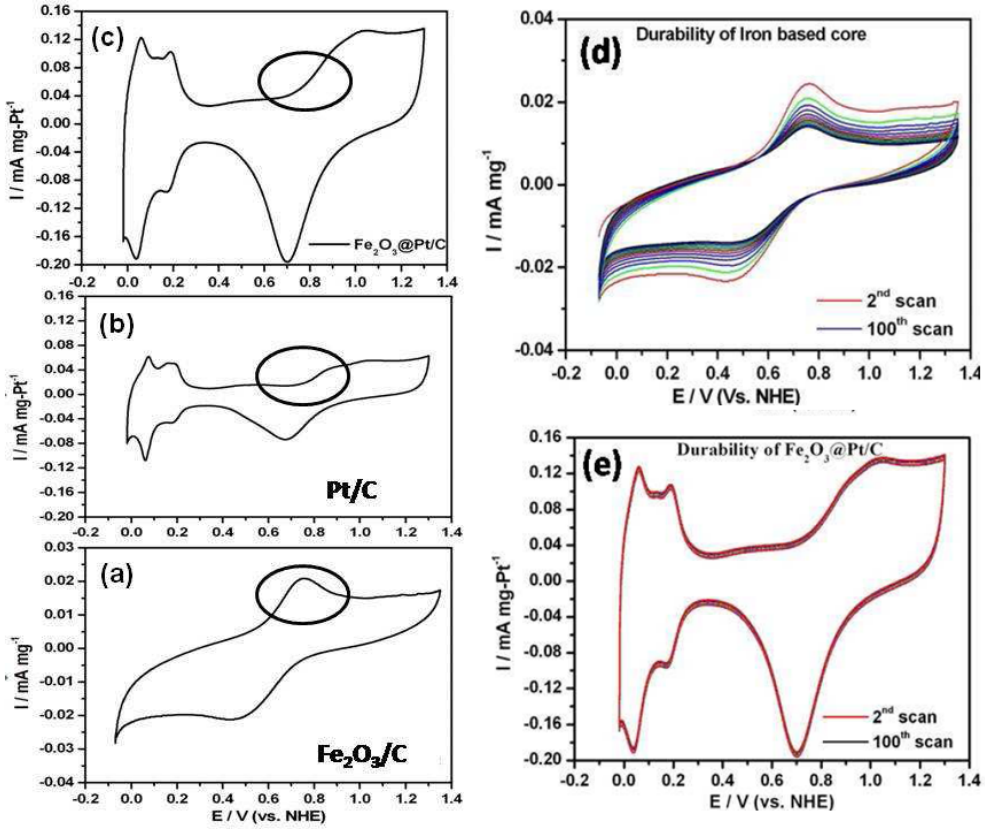

Figure 3B.7: *Cyclic voltammograms of (a) Fe_2O_3/C, (b) Pt/C, (c) Fe_2O_3@Pt/C performed with a scan rate of 100 mV/s. The absence of Fe redox peaks (shown by black circle) in case of Fe_2O_3@Pt/C confirms the formation of continuous Pt shell on the iron based core, and (d) and (e) show the durability of Fe_2O_3/C and Fe_2O_3@Pt/C performed in 0.5 M $HClO_4$ solution (100 scans) at 100 mV/s. The amount of Pt loaded on the electrode surface in the case of Fe_2O_3@Pt/C and Pt/C is maintained to be 2 µgm.*

electrode in acid solution. The absence of the redox couple corresponding to the Fe moiety clearly underlines the formation of a continuous protective layer of Pt over the iron-based core (**Figure 3B.6a** and **Figure 3B.7**).[28] Moreover, the durability assessment of Fe_2O_3/C and Fe_2O_3@Pt/C (**Figure 3B.7d, e**) catalyst has been done by subjecting potential cycling (100 cycles) between 0 and 1.3 V (vs. NHE).

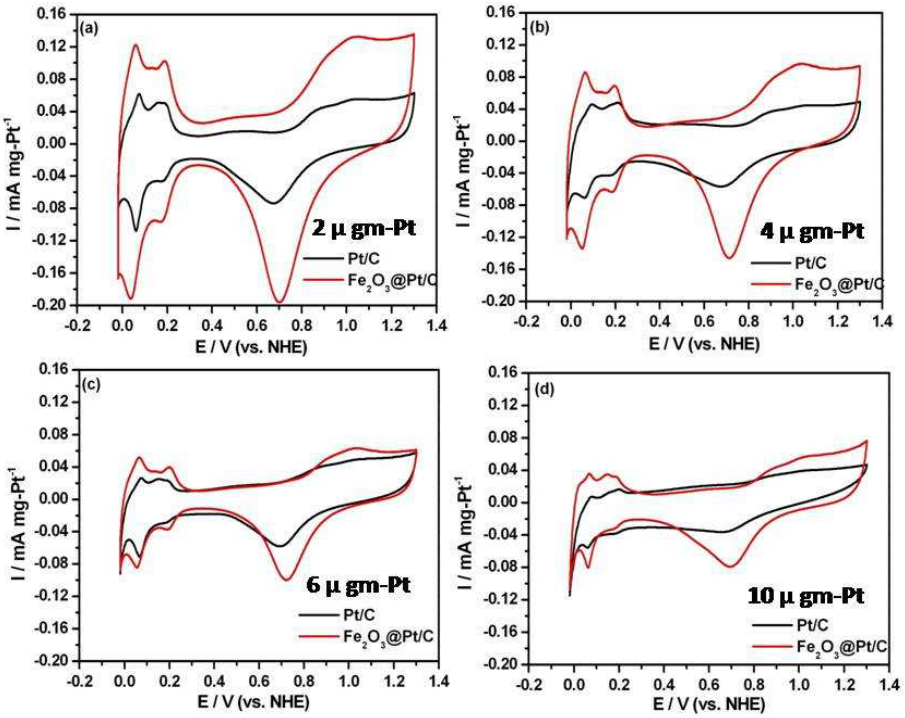

Figure 3B.8: *Comparative cyclic voltammograms of Fe_2O_3@Pt/C and Pt/C with different Pt loadings at a scan rate of 100 mV/s, in a deaerated 0.5 M $HClO_4$ electrolyte and Pt-foil as the counter electrode. The measurements were done by using Ag/AgCl reference electrode and are further normalized with respect to the potential of a NHE.*

A potential cycling can provide very useful information on the leaching of the iron-based core under acidic conditions if the core is not well protected by the Pt shell. This is a relatively fast and reliable method to confirm the formation of a protective layer of Pt on the base metal like Fe. Since the core-shell structure has been confirmed from TEM, XRD, and CV, the absence of anodic peaks of iron-based core in Fe_2O_3@Pt/C indicates the incessant shell of Pt on the surface of the iron based core. Fe_2O_3/C, which does not contain the protective Pt shell (**Figure 3B.7d**) shows gradual decrease in the redox peak intensity corresponding to Fe due to the leaching of Fe from the Fe_2O_3 matrix under the potential induced conditions. On the other hand,

such a redox peak is completely absent in the case of Fe_2O_3@Pt/C (**Figure 3B.7c, e**) as the core is completely encapsulated by the Pt shell. Also, this system maintains substantial durability during the potential cycling, signifying the structural integrity of the system. The core and shell are mutually benefitted and they together bring integrity and efficiency. As the protective case of Pt ensures the required electrochemical stability of the core in the operating potential window, the morphology and surface roughness of the core on the other hand dictate Pt growth and thereby its unprecedentedly high active surface area is attained. The electrochemically active surface area (ECSA) has been calculated by using **Equation 3A.1**.

An important behavior that we observed while measuring the ECSA of the core-shell catalystis its relatively high sensitivity to the coating thickness on the electrode surface compared to the normal Pt/C catalyst. The measured ECSA values as a function of the catalyst loading on the electrode for Fe_2O_3@Pt/C follows the order 185 m^2/g (2μg) > 140 m^2/g (4 μg) > 122 m^2/g (6 μg) > 102 m^2/g (10 μg) (**Figure 3B.8**). Even though Pt/C also displayed a similar trend for its ECSA with the loading amount as 119 m^2/g (2 μg) > 118 m^2/g (4 μg) > 107 m^2/g (6 μg) > 87 m^2/g (10 μg) (**Figure 3B.8**)**,** a notable drop in this case has been observed only when the coating thickness goes to a significantly high level.

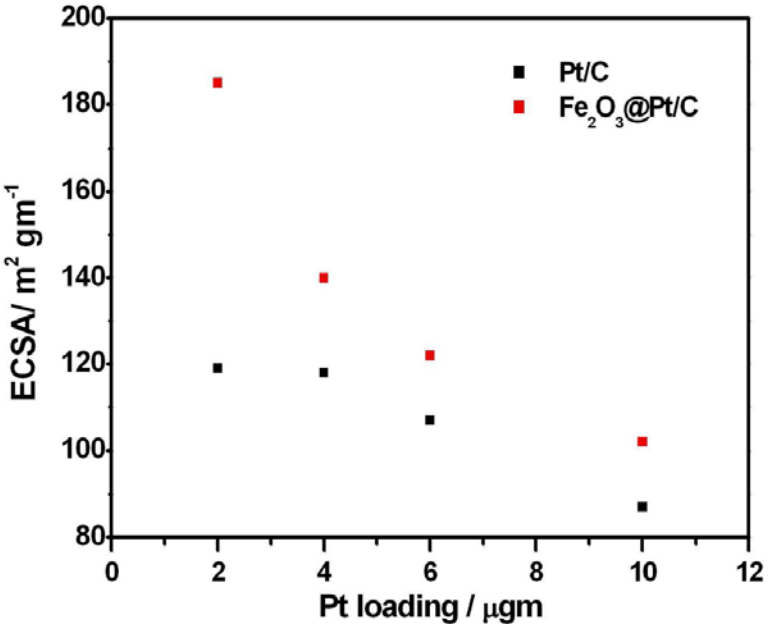

Figure 3B.9: *ECSA vs. Pt loading shows drastic drop in ECSA of Fe_2O_3@Pt/C compared to Pt/C even though the former displays superior values compared to the later throughout the experiment. It appears that the coating thickness plays a highly sensitive role in the case of the core-shell system.*

It should also be noted that the ECSAs of Fe_2O_3@Pt/C are distinctly ahead of Pt/C under low catalyst loading conditions. The calculated ECSA values are plotted in **Figure 3B.9**, which clearly highlights the need to look into the optimum loading of the electrocatalyst to effectively make use of the morphological and structural benefits of the core-shell material. The high sensitivity of the Fe_2O_3@Pt/C catalyst with its coating amount on the electrode can be attributed to the resistance imposed by the core material, which increases significantly owing to its high mass fraction compared to Pt in the system. This is an important observation in the context of developing MEAs for PEMFCs, because as can be evident from later discussions, the best performance characteristics of an electrode derived from the Fe_2O_3@Pt/C catalyst could be obtained only when the thickness of the electrode was maintained below a threshold level. Similar behavior is observed in case of Pt/C, which could be assigned to the varying internal diffusion resistance towards the accessing of the active sites.

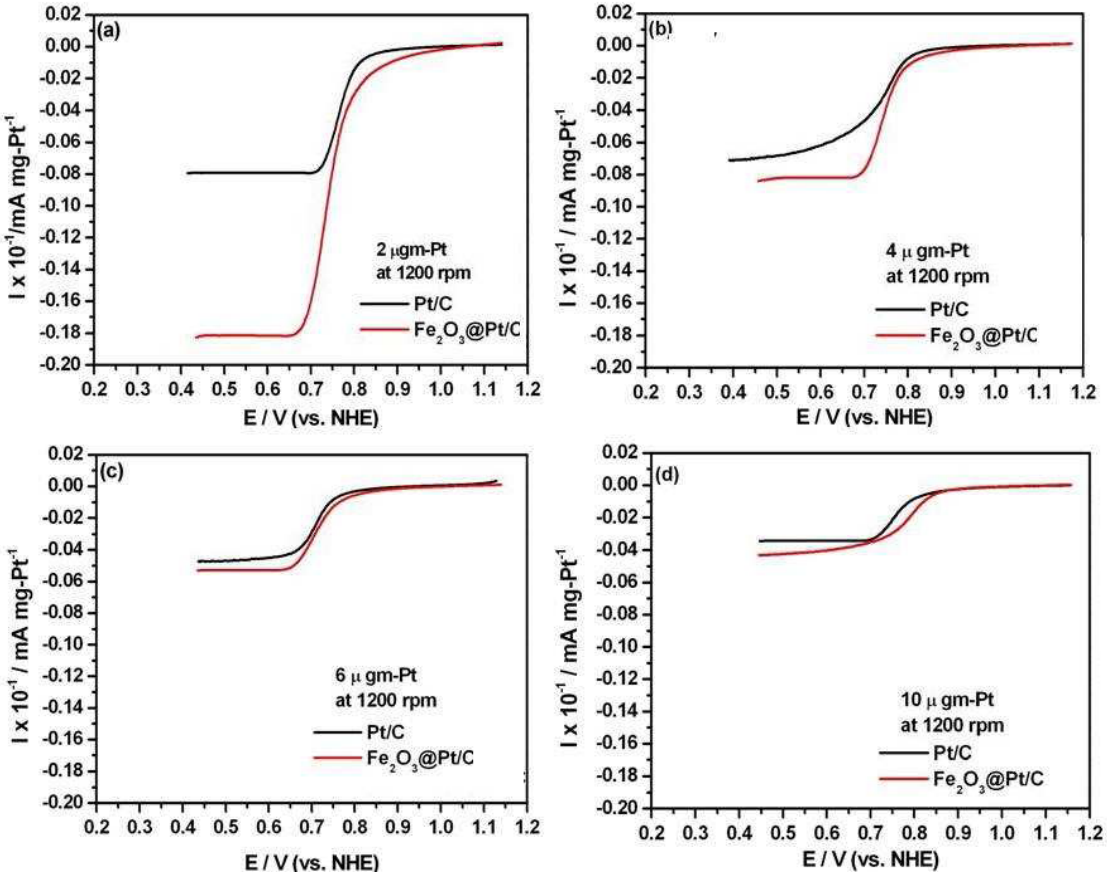

Figure 3B.10: *Comparative LSVs of Fe_2O_3@Pt/C and Pt/C performed at an electrode rotation speed of 1200 rpm with an O_2 flow at a scan rate of 10 mV/s in 0.5 M $HClO_4$ electrolyte.*

In accordance with the ECSA measurements, an analysis of the ORR activity also reveals a strong dependency on the coating thickness (**Figure 3B.9** and **Figure 3B.10**). The electrocatalytic activities for ORR are recorded by the hydrodynamic RDE technique at different rotation speeds per minute (rpm). A huge difference in the performance characteristics between the two catalysts is clearly visible when the catalyst loading was maintained as 2 μg on the electrode. The enhanced activity of Fe_2O_3@Pt/C can be ascribed to the multiple features such as high ECSA, electronic modifications, and synergistic effects enjoyed by the system all the while avoiding the chance for the ohmic component of the core material to dominate and consequently upset the expected improvement in performance. The literature[29-30] shows that addition of a second metal exhibits an increase of surface d-vacancy, which facilitates electron donation from oxygen to the surface of Pt. This brings strong interaction between Pt and oxygen, which results in enhancement of oxygen adsorption and weakening of the O-O bond, leading to fast scission of the bond and enhanced ORR activities.[16-17, 19, 29-30]

As already seen, the ORR activity of the core-shell catalyst, just like ECSA, is found to be significantly influenced by the coating amount of the catalyst on the electrode. Comparative RDE polarization curves of Fe_2O_3@Pt/C and Pt/C with varying catalyst loading performed at 1200 rpm are shown in **Figure 3B.10,** which shed light into the fact that, unless the coating thickness is maintained within a threshold level, the benefits expected from the core-shell morphology cannot be extracted effectively. It should be noted that the composional effect and loading effect together dictate the ORR activity even though the extent of domination of the factors varies with the coating levels. Under low loading conditions, the core-shell system enjoys a clear edge over Pt/C in terms of both ECSA and ORR activity, whereas the differences narrow down as the coating thickness increases. The large mass fraction of the core material, which is predominantly oxidic, makes significant ohmic overpotential contribution and clearly dictates the performance under higher loading conditions. This important observation should not be underestimated during electrode fabrication because the real performance benefits of the core-shell materials with oxide cores may not be clearly visualized beyond a coating thickness owing to the dominating role played by the ohmic component of the core materials.

Further insights into the ORR dynamics were obtained from the analysis of the Koutecky−Levich (K-L) plot, which is a plot of the inverse of current density (j^{-1}) as a function

of the inverse of the square root of the rotation rate ($\omega^{-1/2}$), as shown in **Figure 3B.11**. Total current obtained in the analysis is the sum of the inverse of diffusion, kinetic and film diffusion currents.[31] Details about the equations are provided in the **Chapter 2, Section 2.3.2**. The K-L plots generated from Fe_2O_3@Pt/C at different coating thicknesses (at 0.45 V) are shown in **Figure 3B.11**. Good linearity and parallelism of the K-L plots indicate that ORR follows first-order kinetics and similar mechanistic aspects.[31-32] The reaction proceeds *via* a four electron transfer, which has been calculated from a Levich plot analysis of the RDE data. The calculated kinetic current density (j_k) for the core-shell catalyst is 5.8 x 10^{-4} A/cm^2 when the catalyst loading was maintained as 2 μg. On the other hand, in the case of Pt/C, the same catalyst loading gives a lower j_k value of 3.8 x 10^{-4} A/cm^2.

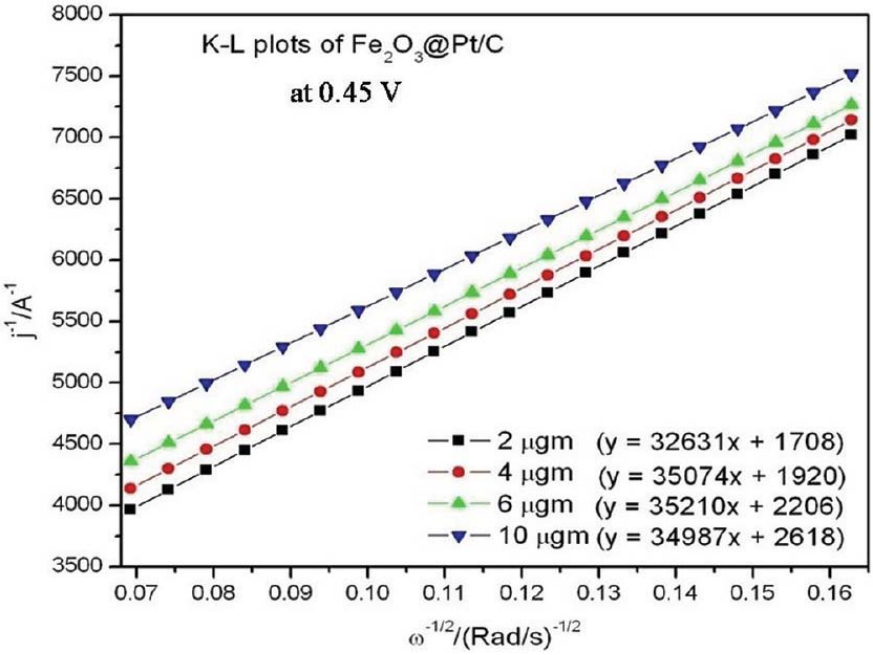

Figure 3B.11: *Koutecky−Levich plots of Fe_2O_3@Pt/C at 0.45 V generated from the LSVs taken as a function of different catalyst loading amounts.*

However, it has been noticed that the difference between the two systems in terms of the measured j_k values narrows down as the catalyst coating thickness increases.This clearly indicates that the ORR kinetics of the core-shell catalyst is clearly higher than that of the conventional Pt/C catalyst, provided the thickness of the catalyst layer does not exceed a threshold level. The obtained higher activity at low Pt loading is attributed to the low resistance and better internal diffusion of the reactant at low thickness level. Overall, it was found from the

results that the ORR activity can be affected by the contributions from ohmic and diffusion components, and the ohmic component appears to play a dominating role in the case of the core-shell system owing to the large mass fractionof the core component whose conductivity is expected to be significantly lower than that of Pt.

Overall, the Fe-Pt based system is found to be better than Pt/C and even better than that of Cu@Pt/C, in terms of ECSA and onset potential. Therefore, the Fe-Pt system has been used to understand the behavior in real fuel cell applications. This has been explained in the following section.

3B.2.7. Single Cell Testing of Fe_2O_3@Pt/C Electrocatalyst

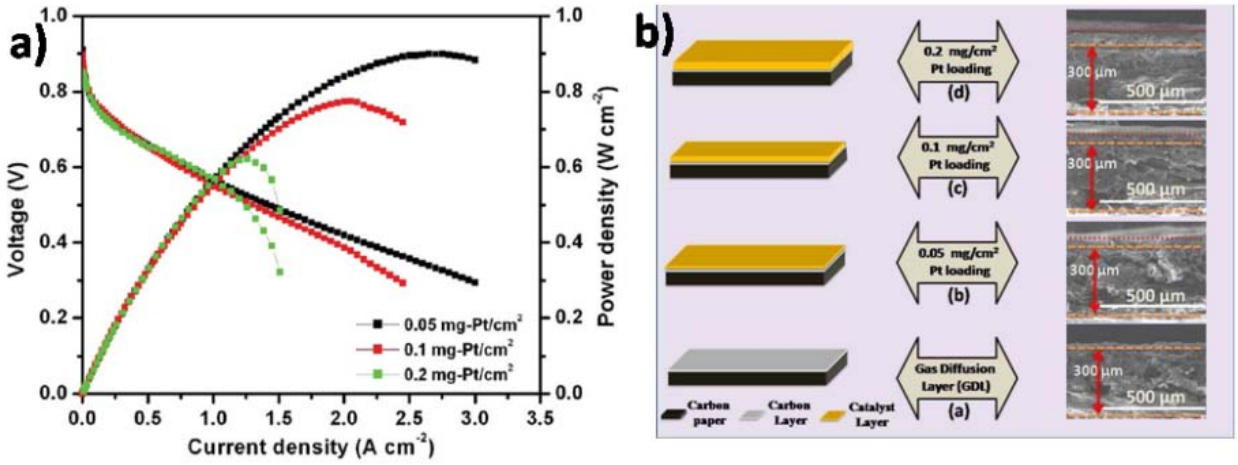

Figure 3B.12: *(a) Polarization plots of MEAs fabricated by using Fe_2O_3@Pt/C with different Pt loadings by passing ultrapure H_2 and O_2 at the anode and cathode sides respectively at a flow rate of 0.2 slpm (100% relative humidity and at 60 °C cell temperature) and (b) a diagrammatic representation of the electrodes (left side) with varying Pt loading of Fe_2O_3@Pt/C and corresponding SEM images (right side)[(a) gas diffusion layer (thickness-300 µm), (b) electrode having 0.05 mg/cm^2 Pt loading (total thickness-319.5µm; catalyst layer thickness - 19.5 µm), (c) electrode having 0.10 mg/cm^2 Pt loading (total thickness-341.0 µm, catalyst layer thickness - 41.0 µm), and (d) electrode having 0.20 mg/cm^2 Pt loading (total thickness-391.0 µm; catalyst layer thickness - 91.0 µm)].*

To investigate more clearly the effect of loading and thickness in a realistic perspective, a series of single cell performance evaluation with varying cathode Pt loading from 0.05 to 0.20 mg/cm^2 (**Figure 3B.12a**) was carried out. The thickness of the Pt-coated gas diffusion layer with varying Pt loading has been measured by the SEM analysis, and the corresponding images are

shown in **Figure 3B.12b**. The analysis reveals that the thickness of the electrode possessing the Pt loading of 0.05 mg/cm^2 is approximately 19.5 μm and this increases significantly (nearly to 90 μm) as the Pt loading goes to 0.20 mg/cm^2. It should be noted that the variation in the Pt loading has been achieved by controlling the catalyst coating thickness on the electrode. The trend in performance during the single cell evaluation is in par with the RDE results with respect to the thickness effect. The MEA corresponding to the cathode Pt loading of 0.05 mg/cm^2, *i.e.*, the one with the lowest thickness, displays the highest power density of 900 mW/cm^2, whereas the MEA prepared by Pt/C with the same Pt loading and under similar test conditions displays a power density of approximately 700 mW/cm^2 (**Figure 3B.13**).

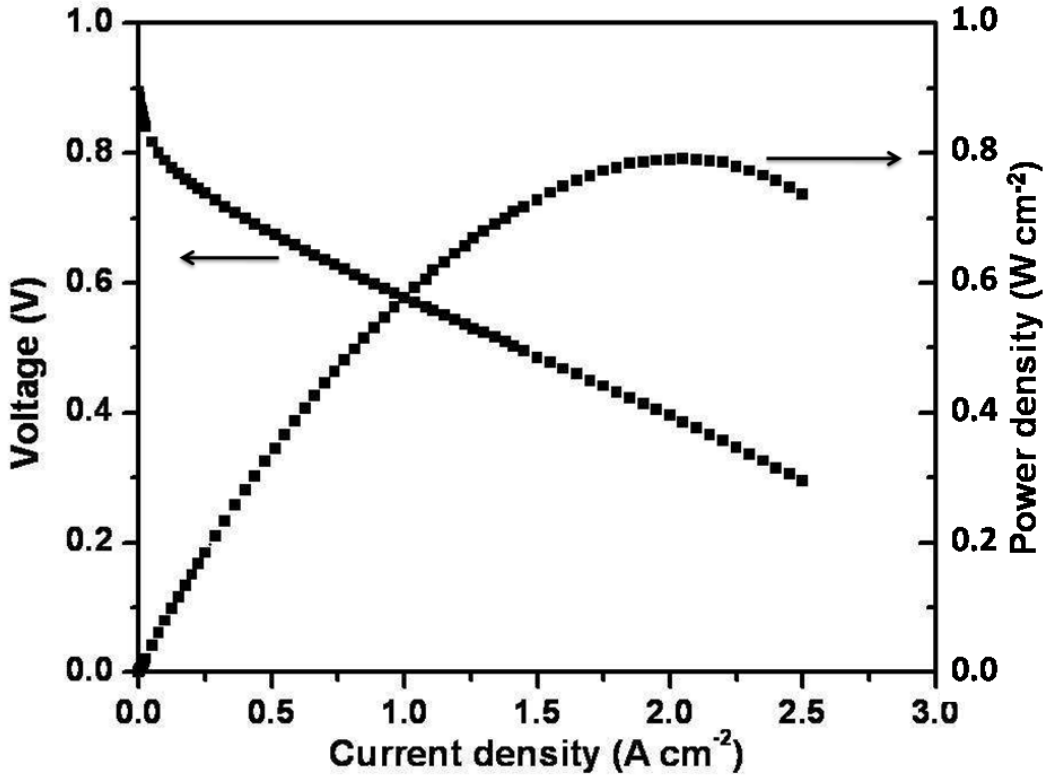

Figure 3B.13: *Polarization study of the MEA prepared with Pt/C having 0.05 mg$_{\text{-Pt}}$/cm^2 loading at the cathode side and 0.30 mg$_{\text{-Pt}}$/cm^2 in the anode side by passing ultra-pure H_2 and O_2 on the anode and cathode sides, respectively.*

One reason for the high performance at low loading for Fe_2O_3@Pt/C can be attributed to the higher ECSA of the core-shell structure, which is better accessible when the coating thickness of the electrode is low. As the thickness increases above a threshold level, along with the expected

mass transfer effects, the resistance contribution from the base metal species can be dominated in the core-shell system unlike in a Pt/C-based electrode. This leads to a technical limitation in obtaining the expected benefits from the core-shell geometry from thicker electrodes.

Further, to understand the kinetics of the fuel cell reaction, the exchange current density has been calculated from the Tafel plot. The Tafel slope is an indication of the mechanism of the electrode reaction, which is related to the change in the nature of adsorbed oxygen species and their coverage variation with the potential. The low current density region corresponds to the oxygen reduction when the adsorbed hydroxyl species at the Pt surface determines the electrode activity. Tafel plot has been created by measuring the *in situ* resistance during actual single cell testing and by making accordingly the required IR compensation in the measured voltage.

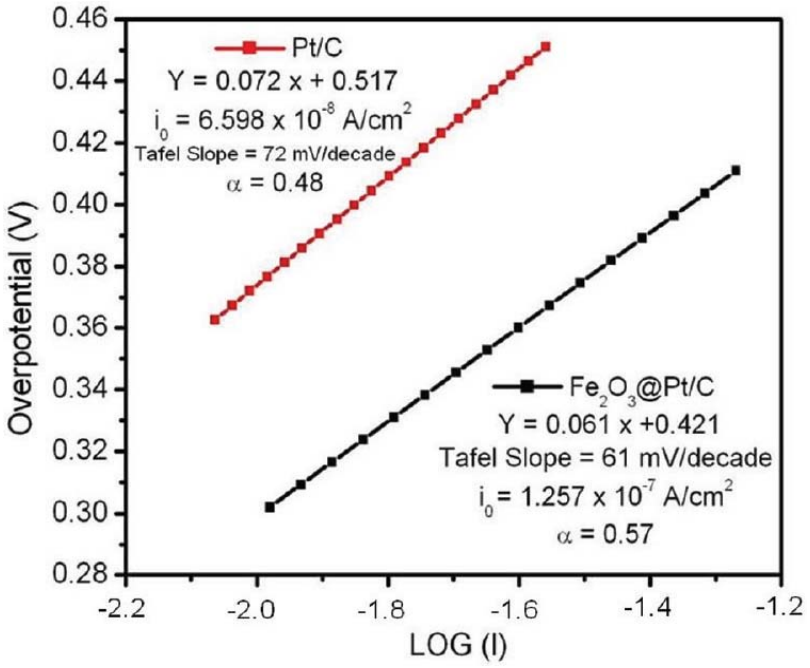

Figure 3B.14: *Comparative Tafel plots of Pt/C and Fe_2O_3@Pt/C derived from the single cell analysis.*

Both Tafel intercept and slope have been used to reveal the properties of the rate-determining step. **Figure 3B.14** shows representative comparative Tafel plots generated from the single cell polarization data based on the electrodes fabricated from Fe_2O_3@Pt/C and Pt/C. The measured Tafel slope values are 61 mV/decade for the core-shell system and 72 mV/decade for the Pt/C system. The Tafel slope can then be used to calculate the effective transfer coefficient, and the Tafel intercept gives the value of exchange current density. The calculated transfer coefficient

(α) is nearly 0.5 for both the systems. However, more than one order of the difference in the exchange current density as measured for Fe_2O_3@Pt/C (1.26 x 10^{-7} A/cm^2) and Pt/C (6.60 x 10^{-8} A/cm^2) clearly depicts the distinct benefit obtainable from a properly designed electrode based on the core-shell catalyst for PEMFC applications.

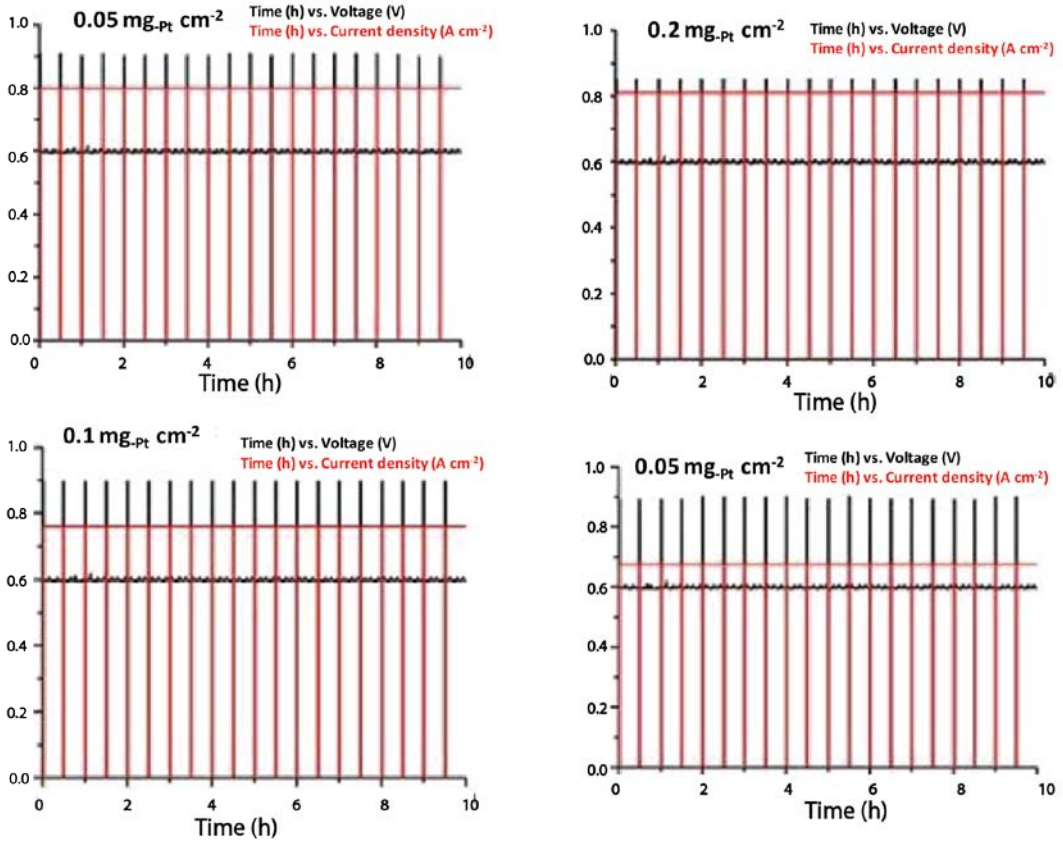

Figure 3B.15: *Durability study of the MEAs by switching the voltage between 0.6 V and OCV (10 h) by passing ultrapure H_2 and O_2 on the anode and cathode sides, respectively. Fe_2O_3@Pt/C MEA having (a) 0.05 mg of Pt/cm^2, (b) 0.10 mg of Pt/cm^2 and (c) 0.20 mg of Pt/cm^2 loading at the cathode side. (d) MEA prepared by Pt/C having 0.05 mg of Pt/cm^2 loading at the cathode side. In all the cases, the anode side Pt loading was maintained as 0.30 mg/cm^2.*

Durability of MEAs has been tested for 10 h (**Figure 3B.15**) by keeping the cell at 0.6 V for 30 min and thereafter switching the voltage to OCV and again bringing it back to 0.6 V. We found that there is little fluctuation in potential, but the current density is constant throughout the evaluation period of 10 h.The obtained results are tabulated in **Table 3B.1**. Thus, the durability assessment assures the integrity of the core-shell material and reliability of the electrodes derived

from these materials to deliver sustainable power output (voltage×current) under the operating electrochemical environments.

Table 3B.1: *Electrochemical activities of the prepared catalysts and their single cell performance data.*

Electrochemical active surface area (m^2/g)				
	2 µg of Pt	**4 µg of Pt**	**6 µg of Pt**	**10 µg of Pt**
Fe_2O_3@Pt/C	185	140	122	102
Pt/C	119	118	107	87

Single cell performance evaluation of Fe_2O_3@Pt/C			
Cathode Pt-loading	**Max. Power Density (mW/cm^2)**	**Max. Current Density (mA/cm^2)**	**OCV (V)**
0.05 mg/cm^2	900	3000	0.910
0.1 mg/cm^2	775	2450	0.896
0.2 mg/cm^2	622	1510	0.850

3.2. Conclusion

The adopted method gave an effective strategy for preparing well dispersed carbon supported core-shell nanoparticles of Pt possessing remarkable electrocatalytic activities. Sequential addition of the reactants is critical because the degradation and oxidation products of AA during the metal ion reduction and self-oxidation play pivotal role to modify the carbon surface and thereafter to anchor the as formed core-shell particles on the surface. Since the core-shell particles are allowed to form in the preceding step and subsequently anchor on the carbon surface in a sequential process, both excellent core-shell features and high dispersion could be simultaneously ensured in this process. The synthesized Cu@Pt/C and Fe_2O_3@Pt/C electrocatalysts possess core-shell features as well as good dispersion on the carbon substrate. Both the electrocatalysts have delivered better ORR activity compared to Pt/C. However, Fe_2O_3@Pt/C has delivered better ECSA and ORR activity compared to Cu@Pt/C. Most importantly, Fe_2O_3@Pt/C has shown higher performance for ORR at a significantly low Pt loading, possibly due to the less ohmic overpotential by the oxidic core moiety when the coating thickness is less. Hence, in a system possessing a less conductive core material, *i.e.* Fe_2O_3, it is mandatory to prevent the electrode thickness from exceeding a threshold level owing to the

greater dominance of the core material with its higher mass fraction in the system. Exceeding the thickness beyond a threshold level upsets the electrochemically active surface area, oxygen reduction kinetics, and polarization characteristics. On theother hand, in properly optimized systems, the core-shell (Fe_2O_3@Pt/C) material clearly outperforms the conventional Pt/C, leaving great scope for the development of high performance, cost-effective low-Pt electrocatalysts possessing excellent electrochemical stability. Realization of high-performance thin electrodes is expected to make radical changes in the design aspects of PEMFCs along with its potential to develop miniature cells for various niche applications. This could be an innovative and elegant solution for realizing micro fuel cells and better system adaptability for various applications.

3.3. References

[1] L. Carrette, K. A. Friedrich, U. Stimming, *Fuel Cells* **2001**, *1*, 5-39.

[2] X.-Z. Yuan, H. Wang, in *PEM Fuel Cell Electrocatalysts and Catalyst Layers* (2nd ed.: J. Zhang), Springer London, **2008**, pp. 1-87.

[3] K. Gong, F. Du, Z. Xia, M. Durstock, L. Dai, *Science* **2009**, *323*, 760-764.

[4] B. Lim, M. Jiang, P. H. C. Camargo, E. C. Cho, J. Tao, X. Lu, Y. Zhu, Y. Xia, *Science* **2009**, *324*, 1302-1305.

[5] M.-H. Shao, K. Sasaki, R. R. Adzic, *Journal of the American Chemical Society* **2006**, *128*, 3526-3527.

[6] B. K. Balan, S. M. Unni, S. Kurungot, *The Journal of Physical Chemistry C* **2009**, *113*, 17572-17578.

[7] F. Maroun, F. Ozanam, O. M. Magnussen, R. J. Behm, *Science* **2001**, *293*, 1811-1814.

[8] J. H. Sinfelt, *Bimetallic catalysts: discoveries, concepts, and applications*, Wiley, **1983**.

[9] P. Strasser, S. Koh, T. Anniyev, J. Greeley, K. More, C. Yu, Z. Liu, S. Kaya, D. Nordlund, H. Ogasawara, M. F. Toney, A. Nilsson, *Nature Chemistry* **2010**, *2*, 454-460.

[10] A. Pozio, M. De Francesco, A. Cemmi, F. Cardellini, L. Giorgi, *Journal of Power Sources* **2002**, *105*, 13-19.

[11] R. Huang, Y.-H. Wen, Z.-Z. Zhu, S.-G. Sun, *The Journal of Physical Chemistry C* **2012**, *116*, 8664-8671.

[12] M. Heggen, M. Oezaslan, L. Houben, P. Strasser, *The Journal of Physical Chemistry C* **2012**, *116*, 19073-19083.

[13] L. Han, H. Liu, P. Cui, Z. Peng, S. Zhang, J. Yang, *Scientific Reports* **2014**, *4*.

[14] L. Chen, L. Kuai, B. Geng, *Crystal Engineering Communications* **2013**, *15*, 2133-2136.

[15] J. F. Moulder, W. F. Stickle, P. E. Sobol, K. D. Bomben, *Handbook of X-ray Photoelectron Spectroscopy: A Reference Book of Standared Spectra for Identification and Interpretation of XPS Data; Physical Electronics, Division, Perkin-Elmer Corp.: Eden Prarie, MN*, **1995**.

[16] M.-K. Min, J. Cho, K. Cho, H. Kim, *Electrochimica Acta* **2000**, *45*, 4211-4217.

[17] V. R. Stamenkovic, B. S. Mun, M. Arenz, K. J. J. Mayrhofer, C. A. Lucas, G. Wang, P. N. Ross, N. M. Markovic, *Nature Materials* **2007**, *6*, 241-247.

[18] J. R. Kitchin, J. K. Nørskov, M. A. Barteau, J. G. Chen, *Physical Review Letters* **2004**, *93*, 156801.

[19] S. J. Hwang, S. J. Yoo, S. Jang, T.-H. Lim, S. A. Hong, S.-K. Kim, *The Journal of Physical Chemistry C* **2011**, *115*, 2483-2488.

[20] S. Guo, D. Li, H. Zhu, S. Zhang, N. M. Markovic, V. R. Stamenkovic, S. Sun, *Angewandte Chemie International Edition* **2013**, *52*, 3465-3468.

[21] D. Chen, X. Zhao, S. Chen, H. Li, X. Fu, Q. Wu, S. Li, Y. Li, B.-L. Su, R. S. Ruoff, *Carbon* **2014**, *68*, 755-762.

[22] S. Guo, S. Sun, *Journal of the American Chemical Society* **2012**, *134*, 2492-2495.

[23] J. Kim, Y. Lee, S. Sun, *Journal of the American Chemical Society* **2010**, *132*, 4996-4997.

[24] V. Mazumder, M. Chi, K. L. More, S. Sun, *Journal of the American Chemical Society* **2010**, *132*, 7848-7849.

[25] W. Chen, J. Kim, S. Sun, S. Chen, *The Journal of Physical Chemistry C* **2008**, *112*, 3891-3898.

[26] A. S. Aricò, S. Srinivasan, V. Antonucci, *DMFCs: From Fundamental Aspects to Technology Development, Fuel Cells* **2001**, *1*, 133-161.

[27] J. F. Watts, J. Wolstenholme, *An Introduction to Surface Analysis by XPS and AES , John Wolstenholme* **2003**.

[28] K. Jayasayee, V. A. T. Dam, T. Verhoeven, S. Celebi, F. A. de Bruijn, *The Journal of Physical Chemistry C* **2009**, *113*, 20371-20380.

[29] T. Toda, H. Igarashi, H. Uchida, M. Watanabe, *Journal of The Electrochemical Society* **1999**, *146*, 3750-3756.

[30] T. Okada, T. Abe, M. Kaneko, *Springer series in Material Science 111, Spinger-verlag: Berlin* **2009**.

[31] A. J. Bard, L. R. Faulkner, Electrochemical Methods Fundamentals and Applications, 2nd ed.; John Wiley & Sons, Inc.: New York, **2006.**

[32] H. S. Wroblowa, S. B. Qaderi, *Journal of Electroanalytical Chemistry* **1990**, *295*, 153-161.

Chapter 4
Low-Platinum based 3-D Hollow Nanocage Structure for Oxygen Reduction Reaction in Primary Zn-Air Battery*

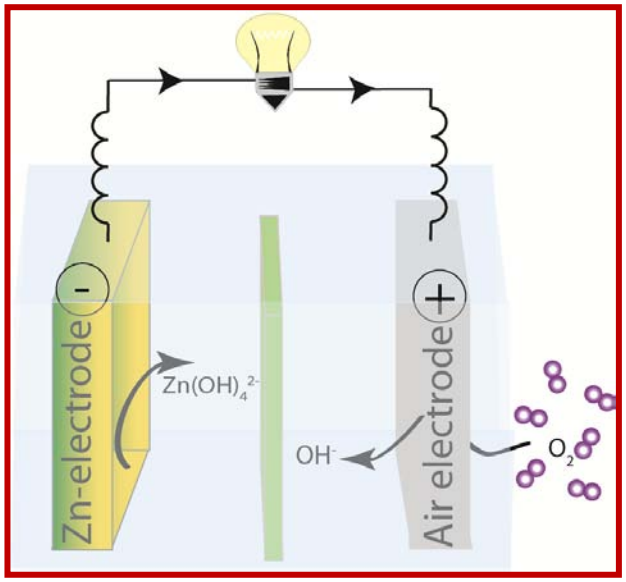

This chapter deals with the effective utilization of the intrinsic properties of a hollow 3-dimensinal (3-D) CuPt nanocage material (CuPt-NC) for devising effective cathode electrode for Zn-air battery owing to its remarkable oxygen reduction activity in alkaline medium. The key properties of the structure such as the higher active centers, surface area, and molecular accessibility along with its 3-D electrocatalytic surface have been highlighted. In conjunction, the mentioned structural properties of CuPt-NC have been utilized to screen its activity towards ORR in primary Zn-air battery as an air electrode. The steady state polarization and discharge profile have been recorded and explained thoroughly. All the results have been compared with respect to the performance characteristics of the commercially available 20 wt. % Pt/C based systems.

*The content of this chapter has been published in "***ACS Catalysis***, 2015, 5, 1445−1452*"
-Reprinted (adapted) with permission from (***ACS Catalysis,*** *2015, 5, 1445-1452)*. Copyright (2015) American Chemical Society.

4.1. Introduction

In recent days, metal-air batteries have attracted substantial research attention due to their applications in portable devices such as hearing aids, toy cars, flashlights, clocks, etc.[1-2] Among the available metal (M)-air batteries (M = Cd, Zn, Li, Al etc.), Zn-air battery is being widely examined due to the low cost, abundance and environmental benignity of Zn.[1-2] The Zn-air battery also enjoys high theoretical energy density and long shelf-life compared to the traditional aqueous batteries.[3,4] However, the prospect is limited by poor performance of the air electrode due to its sluggish ORR activity at the cathode, compared to the anodic oxidation of the Zn metal.[1-6] Hence, development of an efficient cathode catalyst for the Zn-air battery is an existing challenge in front of the scientific community.[1-6] Hitherto, alloys and core-shell structures of Pt-based metals in the supported form are found to be showing better activity for ORR.[7-13] Moreover, the limited-localized electronic interaction with the support or within the particles leads to support corrosion, which eventually leads to particle agglomeration during the actual operating conditions.[7-13] Along with this, the reactant distribution and its utilization are the added issues associated with these types of conventional materials.[7-13] Additionally, the tedious synthesis protocols involved in the synthesis of the nanostructured electrocatalysts significantly impede the prospects towards the wide-spread applications of many of these materials in the metal-air batteries. In the previous chapter (**Chapter 3**), I have highlighted the prospects of Cu@Pt/C and Fe_2O_3@Pt/C to serve as good ORR electrocatalysts compared to Pt/C. However, as mentioned above, these electrocatalysts possess limited localized electronic interaction with the carbon support and lesser intra-atomic connectivity with the separated phases (*i.e.* the core and the shell as separate phases within the structure). Hence, the structural tuning can help to utilize these electrocatalysts under the highly basic and potential conditions.

In view of that, while going through the recent literatures in the relevant areas, I found that researchers are ambitiously focusing in a different angle by constructing Pt-based materials possessing definite geometrical configuration and composition in order to get better activity with higher utilization.[14-21] Moreover, these non-zero dimensional structures make the inter-metallic nanocage structures less susceptible to dissolution and aggregation during the actual operating conditions compared to the available carbon supported catalysts.[22-30] Consequently, deploying alloys possessing porous nanocage structures could be an elegant solution to effectively tackle the issues related to the activity and utilization.[27-32] Recently, Yang *et al*[33] have reported the

synthesis of Pt-Ni nanoframes by employing chemical reduction of metal precursors followed by controlled thermal treatment. The formed Pt-Ni nanoframe structure has shown 36 and 22-fold enhanced mass and specific activity, respectively. Similarly, recently, many more researchers involved on the synthesis of non-zero cage structures based on Kirkendall effect and galvanic displacement method, and explored such materials for the application of ORR.[33-40] Many multi-metallic nanocage structures have shown improved performance and stability in fuel cell applications.[27-30,41-44] This property modulation is credited to the possible electronic changes, systematic atomic arrangement, presence of more voids and edges, higher surface-to-volume ratio and more accessible active sites etc.[22-40]

In most of the case, the adopted synthetic protocols such as, template assisted methods (hard, soft, sacrificial templates), chemical reduction methods etc. are very tedious and time demanding.[27-30,44] At the same time, the interruption and surface passivation of metal by the organic and/or inorganic structure directing agents make the chemistry very difficult to achieve the desired product with definite geometry.[27-30,42-44] In parallel, during bulk synthesis, controlling simultaneously the growth, size and geometry of the crystal is a tricky job. Therefore, achieving high and consistent energy and power densities with these types of inter-metallic electrocatalysts is a really difficult task. Most of the nanocage structures have been prepared with low energy density materials (such as Co-oxide, Mn-oxide, Mg-oxide, etc.).[27-30,42-43] Hence, the structural stability is less under actual operating conditions. Therefore, a key solution is to develop novel ORR electrocatalysts with high energy density materials (such as, Cu-Pt, Pd-Pt, Fe-Pt, etc) which could fulfill the requirement of efficient ORR activity along with higher energy output in Zn-air battery. Relatively, traditional batteries follow the complicated intercalation-deintercalation mechanism during charge-discharge process, which limits the actual achievable energy density. In this perspective, substitution of intercalation material (cathode electrode) with a catalytically active ORR and oxygen evolution reaction (OER) electrode may solve the existing energy density issue of the traditional storage devices.[1-4] In this context, metal-air batteries (mainly, Zn-air) can be a very good option, which can attain a very high energy density of 1100 Wh/kg, possibly due to the absence of intercalation mechanism. Herein, I demonstrate that utilization of a nanocage catalyst based on Cu and Pt (CuPt-NC) can serve as potential cathode electrode material for the Zn-air battery (**Scheme 4.1**) with enhanced activity and durability characteristics. Recently, Lou *et al* have synthesized a Cu-Pt nanocage structure, which was investigated

towards methanol oxidation.[42] The applications of such materials so far have been mainly restricted to the methanol oxidation.[14-16,42-43,45] However, I observed that these types of systems possess great potentials to tackle the sluggish electrode kinetics in metal-air batteries. Herein, I report how a primary Zn-air battery fabricated by using CuPt-NC structures as the cathode could outperform the cathode derived from the state-of-the-art Pt/C catalyst. CuPt-NC was prepared by the *in-situ* galvanic displacement reaction between Cu particles and Pt ions by solvothermal method.[42] Here, the peculiar morphology, the 3-D electrocatalytic surface and higher surface active area of CuPt-NC help the system to provide high ORR activity in alkaline medium, which eventually could be utilized in the battery system by deploying the material as the cathode catalyst. In addition, from the detailed investigation, I could realized that the activity modulation from the present system could be realized from the structural benefits of the 3-D nanocage structure of the materials, which provides low density, more active centers, larger accessible area, better intra-molecular connectivity and amended electronic structure within the system.

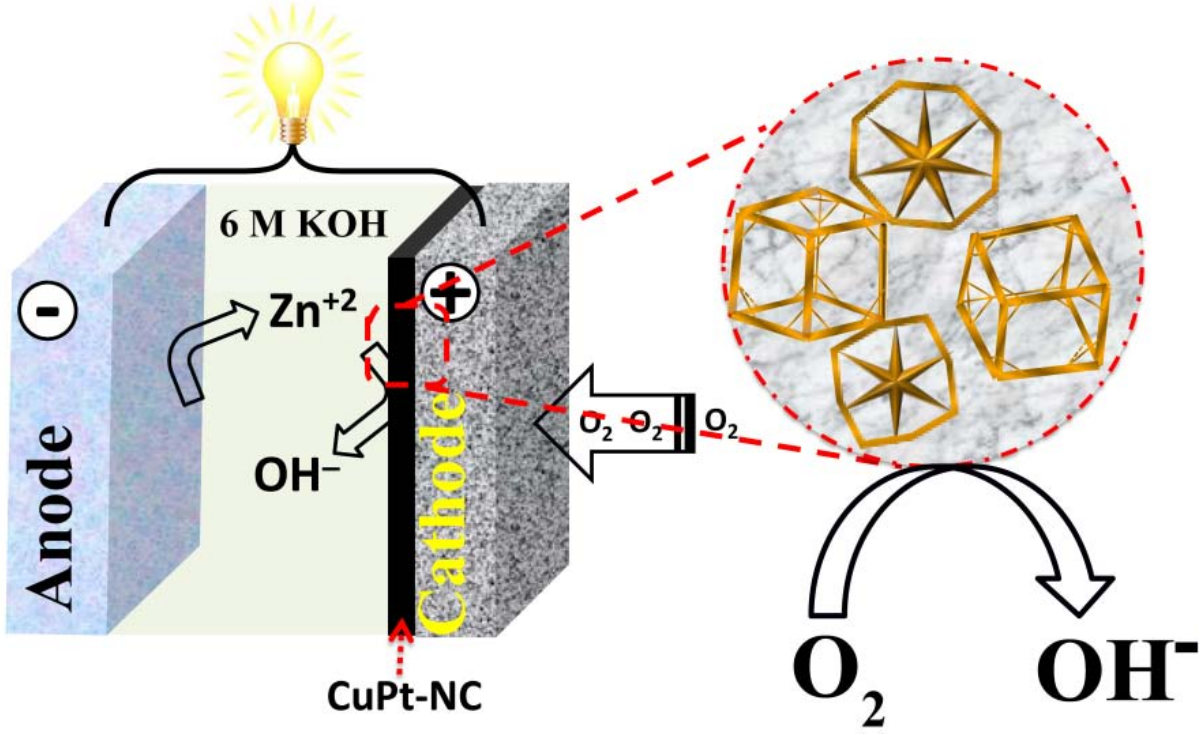

Scheme 4.1: *Schematic representation of a primary Zn-air battery with CuPt-NC as the cathode electrode.*

4.2. Experimental Section

4.2.1. Synthesis of Nanoengineered Cu-Pt Intermetallic Nanocage (CuPt-NC) Structures

8 wt. % of chloroplatinic acid solution was prepared in 200 mg of oleylamine, and 20 mg of copper acetylacetonate was dispersed in fresh 8 ml oleylamine by sonicating it in a Branson water bath sonicator. Subsequently, 50 mg of CTAB was added and the sonication was extended for further 30 min. The well dispersed solution was transferred into a 15 ml Teflon coated stainless steel autoclave and the mixture was subjected for heating at 180 ^{o}C for 24 h. Finally, the reaction mixture was centrifuged at 10,000 rpm and washed with toluene-ethanol (3:2) mixture and the material was dried at 60 ^{o}C in an oven. The material collected after this stage was used as such for further characterization.

4.2.2. Primary Zn-air Battery Testing

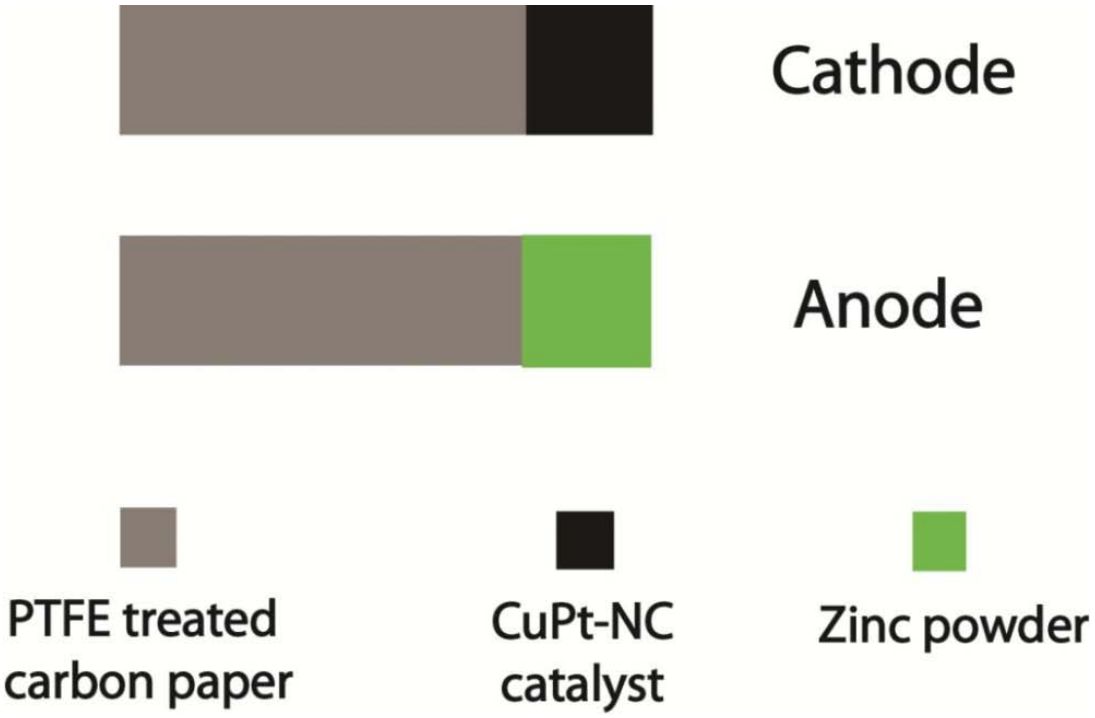

Figure 4.1: *Representation of the cathode and anode electrodes prepared by coating CuPt-NC and Zn-powder, respectively, on the polytetrafluoroethylene (PTFE) treated carbon paper.*

To construct the Zn-air battery, the air electrode was prepared by coating a dispersed solution of CuPt-NC in isopropyl alcohol onto the porous carbon paper (1cm^2) to achieve 2 mg$_{Pt}$/cm^2 loading and paired with Zn powder coated porous carbon paper (anode electrode) in 6 M

KOH, which acts as the electrolyte. The battery testing was performed at room temperature and the electrolyte was continuously purged with oxygen (0.2 slpm). The system showed initial open circuit voltage of 1.3-1.4 V. Moreover, the voltage stability of the Zn-air battery cell was tested at different discharge rates *viz* 20, 25, 30, and 35 mA/cm^2. The obtained results with CuPt-NC were compared with a system made by using commercially available 20 wt. % Pt/C (**Figure 4.11**) at the cathode, having similar loading. Similarly, the steady-state polarization curve was recorded with the same set-up under the continuous purging of oxygen at 5 mV/s (**Figure 4.12b**).[4] The electrodes were prepared by brush coating as shown in **Figure 4.1.**

4.3. Results and Discussion

4.3.1. TEM Analysis

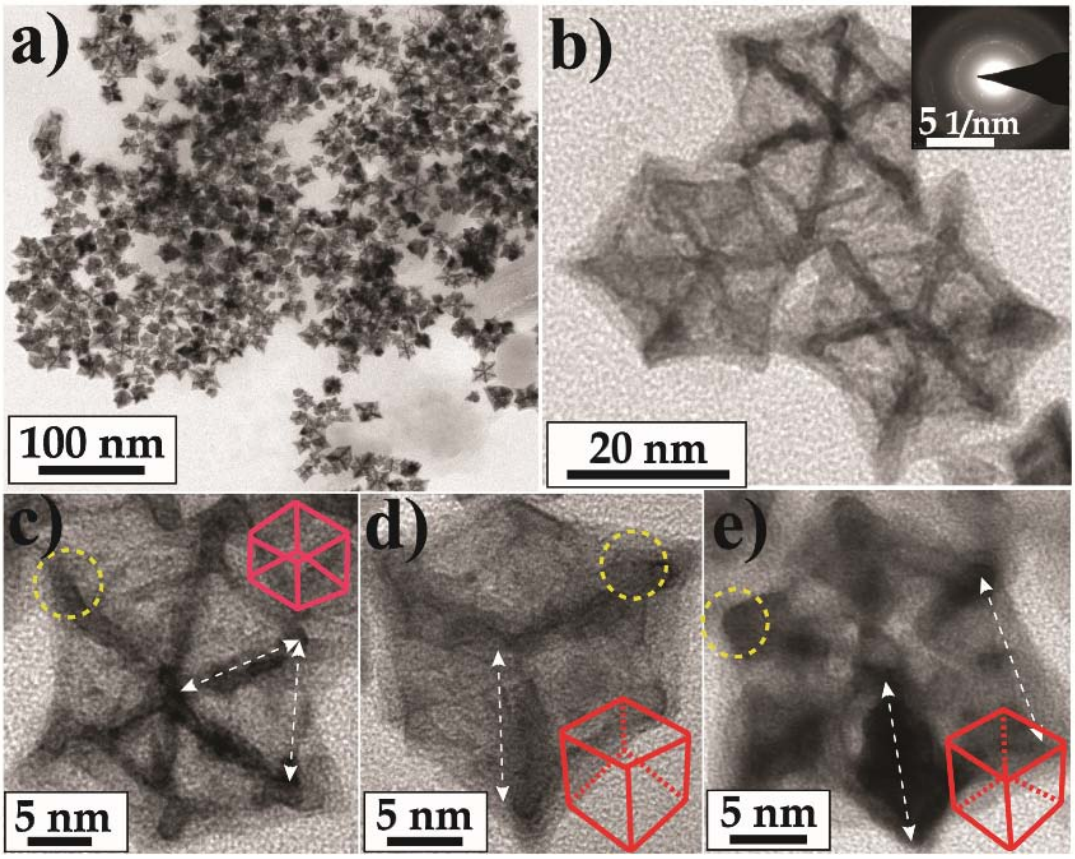

Figure 4.2: *TEM images of the CuPt-NC intermetallic nanocage structures, a) indicating well dispersion of CuPt-NC in solution, b) HR-TEM images of CuPt-NC; inset: SAED pattern and c-e) the hexagonal, cubical, and pentagonal structures of CuPt-NC with their representative model structured frameworks (inset), respectively.*

Figure 4.2a displays homogeneous and well-dispersed distribution of the nanoparticles of CuPt-NC in solution. High resolution TEM (HR-TEM) images of CuPt-NC are given in **Figure 4.2b** and **4.2c**. The structures are found to be well organized within the framework demarcated with distinguishing arms having clear edges and corners (shown in **Figure 4.2c-4.2e** with white two sided arrows and yellow circle). The HR-TEM images clearly indicate the formation of cubical, pentagonal and hexagonal structures (**Figure 4.2c-4.2e**) with an average size of ~20 nm. A close inspection of the TEM images (**Figure 4.2b**) reveal that these nanocages have an observable hollow structure (the model structures are shown in inset of **Figure 4.2c-4.2e**). However, some of the particles seem to be such as hexagonal stars because of their peculiar orientation. Moreover, the crystallinity of CuPt-NC is confirmed through selected area electron diffraction (SAED) pattern (**Figure 4.2b, inset**). It has been documented that, this kind of morphology will be formed due to complex chemistry between the metal precursors and the used surfactant and/or the reducing agent.[27-30,42-43]

4.3.2. XRD Analysis

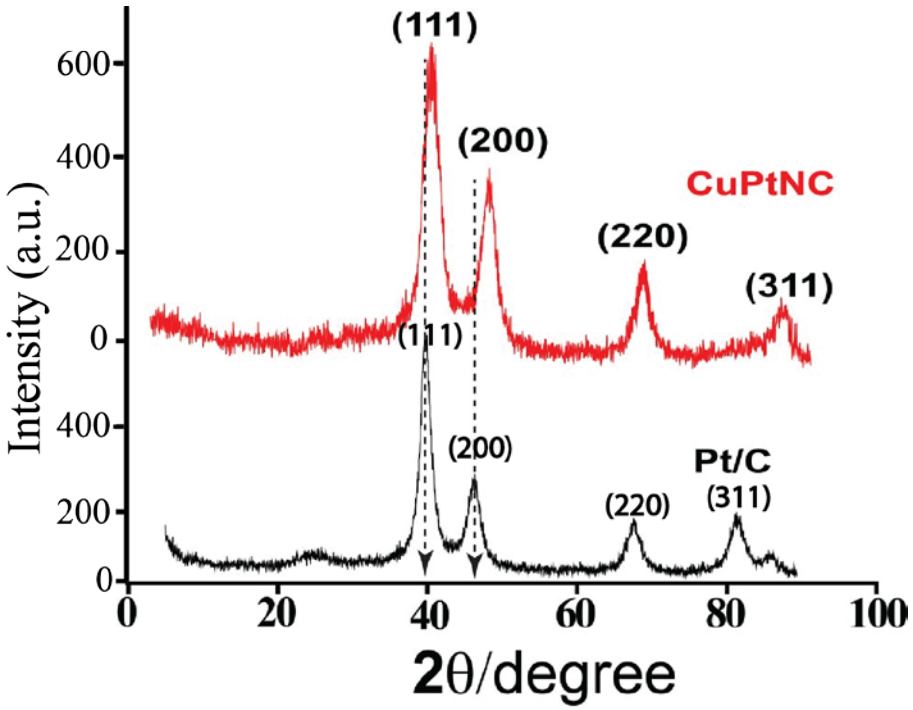

Figure 4.3: *Comparative X-ray diffraction patterns of 20 wt. % Pt/C and CuPt-NC.*

Comparative X-ray diffraction pattern of CuPt-NC and Pt/C is given in **Figure 4.3**. The well-distinguished peaks at 2θ = 39.9, 46.5, and 68.8^{o}, correspond to the (111), (200), and (220)

planes of the fcc crystal of Pt. Moreover, the clear difference in the diffraction peak of CuPt-NC compared to Pt/C validates the decrease in the d-spacing value (marked with the black colored dotted line in **Figure 4.3**).[42] However, as per our knowledge and compared with the literature reports, it seems that the (111/200) ratio is lower in case of alloys (1.24) compared to CuPt-NC (2.01).[42,46] The shift in the peaks certifies the lattice contraction, which is attributed to the change in the electronic structure as well as the geometrical nature of the Cu-Pt structure, which ultimately decreases the inter-atomic distance of the Pt atoms.[45]

4.3.3. XPS Analysis

The mutual interaction between Cu and Pt in the intermetallic structure and change in the electronic environment has also been confirmed through X-ray photoelectron spectroscopic (XPS) investigation (**Figure 4.4**). The full survey scan of CuPt-NC is given in **Figure 4.4a**. The presence of Cu, Pt, and O is marked in the figure.

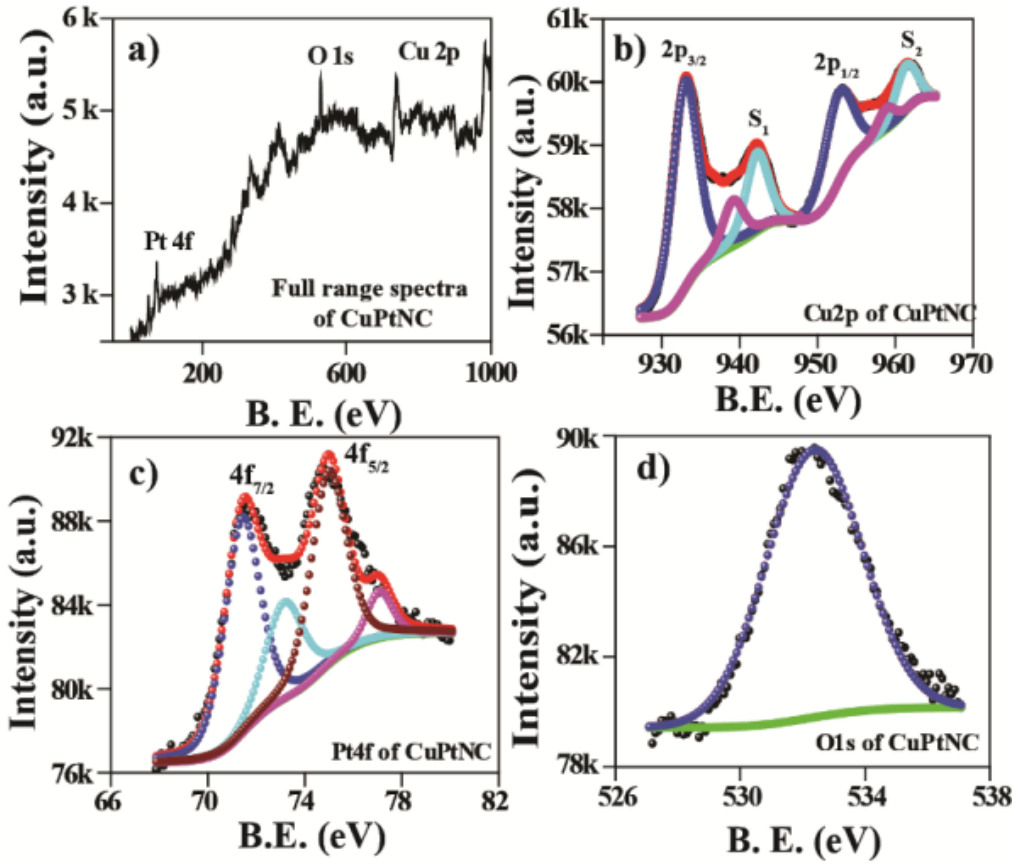

Figure 4.4: *XPS of CuPt-NC: a) full scan survey, b) Cu2p spectra, c) Pt4f spectra and d) O1s spectra.*

Subsequently, the deconvulated XPS of Cu is shown in **Figure 4.4b**, which gives two peaks at 933.08 and 953.20 eV, which are assigned to Cu $2p_{3/2}$ and $2p_{1/2}$, respectively. Moreover, the characteristic satellite peaks are observed at ~942 and ~962 eV of Cu$2p_{3/2}$ and $2p_{1/2}$, respectively. The satellite peaks also could be deconvoluted, which leads to the presence of two sub-peaks, which are attributed to the Cu present in the two different oxidation states.[41,49-50] Moreover, XPS of Pt shows the presence of four peaks originated from the spin-orbit splitting of Pt$4f_{7/2}$ and $4f_{5/2}$ (**Figure 4.4c**). The peaks at the binding energy of ~71.6 (Pt$4f_{7/2}$) and 74.9 eV (Pt$4f_{5/2}$) are attributed to the Pt^{o} state and the peaks at 72.8 and 76.5 eV are assigned to the Pt^{+x} state of the CuPt-NC structures. Whereas, in case of Pt/C, the $4f_{7/2}$ and $4f_{5/2}$ peaks are appeared at slightly lower binding energy, i.e., ~71.00 and ~74.10 eV (**Chapter 3, Section 3.3.4, Figure 3.9**). The relatively high intensity of Pt^{o} with respect to that of Pt^{+x} shows that the Pt in both the catalysts is principally metallic in nature. Moreover, the shift in the binding energy of Pt peaks for CuPt-NC indicates the effective charge transfer between Cu and Pt, possibly due to the change in the electronic structure of Pt in case of CuPt-NC.[42,47,49-50] XPS profiles of Pt 4f, C 1s, and O 1s of 20 wt. % Pt/C are shown in **Figure 3.9** (**Chapter 3, Section 3.3.4**). Moreover, the relative composition of the Cu to Pt in CuPt-NC has been calculated from the XPS data and is found to be 1:1.023. Subsequently, the Cu:Pt stoichiometry is found to be 3:1 in CuPt-NC. In detail, CuPt-NC is showing 46.44, 47.52 and 6.06 wt. % of Cu, Pt and O, respectively (**Figure 4.4**).

4.3.4. Concept of Nanoengineering

The nanoengineering of CuPt-NC is mainly associated with the complicated chemistry involved during the synthesis. The nanoengineering stands for the *in-situ* structural modification of the pre-formed Cu-nanocube (which acts as a self-sacrificial template) in presence of the Pt-ions. During the solvothermal reaction, initially, the Cu-nanocubes are formed, which are in nano-size. Later, the Pt-ions get reduced on the surface of the pre-formed Cu-nanocubes by *in-situ* galvanic displacement reaction between the Cu and Pt-ions accompanied by the Kirkendall effect. This finally ended with Cu-Pt nanocage structures with increased number of the active sites and improved contact between the electrolyte and the catalyst surfaces. This ultimately leads to the improvement in the electrocatalytic activity. Hence, this *in-situ* structural (chemical) modification of the self-sacrificial template (Cu) in presence of Pt-ions in nano-regime has been termed as nanoengineering.

4.3.5. Concept 3-D Electrocatalytic Surface

The formed nanocage structures possess open faceted beautiful hollow geometry with ordered atomic arrangement within the structure. As already shown in **Figure 4.2**, CuPt-NC are formed by interconnected arms of CuPt and arranged in to 3-D network. To get clear idea and to understand more easily, the model structures have also been shown in inset of **Figure 4.2c-4.2e**. It seems that the formed CuPt-NCs are hollow structures possessing open facets in all the directions. In addition, these open facets increase the overall active sites and provide easy molecular accessibility within the structure. In view of this, this open 3-D structure having facile molecular accessibility is termed as a 3-D electrocatalytic surface.[33,42-44]

4.3.6. Electrochemical Analysis

To investigate the electrochemical activity of CuPt-NC, we have carried out cyclic voltammetry (CV) and linear sweep voltammetry (LSV) in a 0.1 M KOH solution in a potential range of 0.1 to 1.3 V (vs. RHE) and 1.2 to 0.3 V (vs. RHE), respectively. The electrochemical activity of CuPt-NC has been compared with the commercial available Pt/C. **Figure 4.5a and 4.5b** are showing the comparative CV of CuPt-NC and Pt/C in an N_2- and O_2-saturated 0.1 M KOH. The deviation of voltammogram in O_2-atmosphere indicates ORR activity of the catalyst.

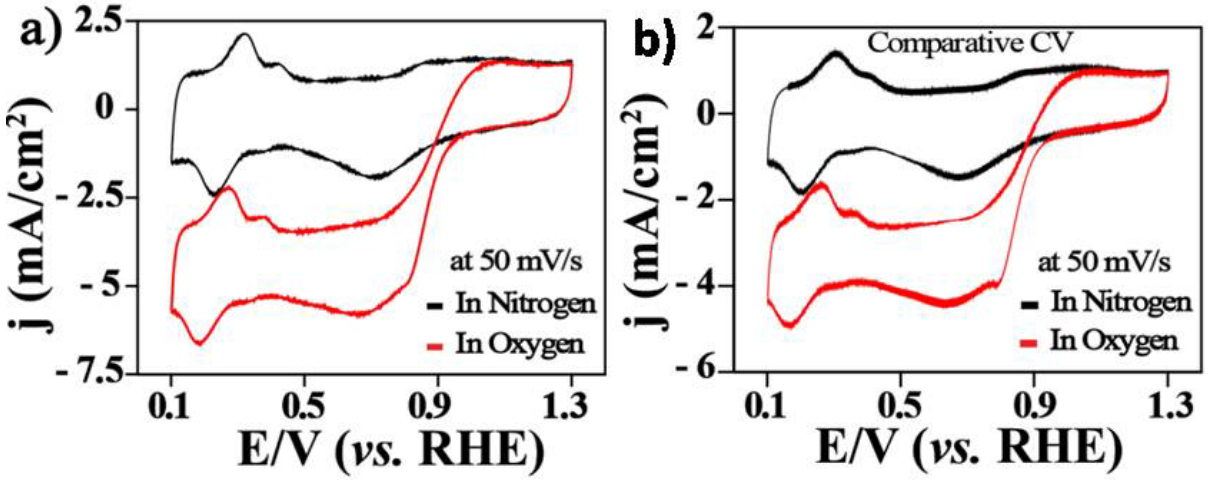

Figure 4.5: *Comparative CV profiles of (a) CuPt-NC, and (b) Pt/C, recorded in N_2- and O_2-saturated 0.1 M KOH, using Hg/HgO as the reference electrode and Pt-foil as the counter electrode. Finally, the data was normalized with respect to the reversible hydrogen electrode (RHE). Conditions: scan rate: 50 mV/s, rotation: 900 rpm.*

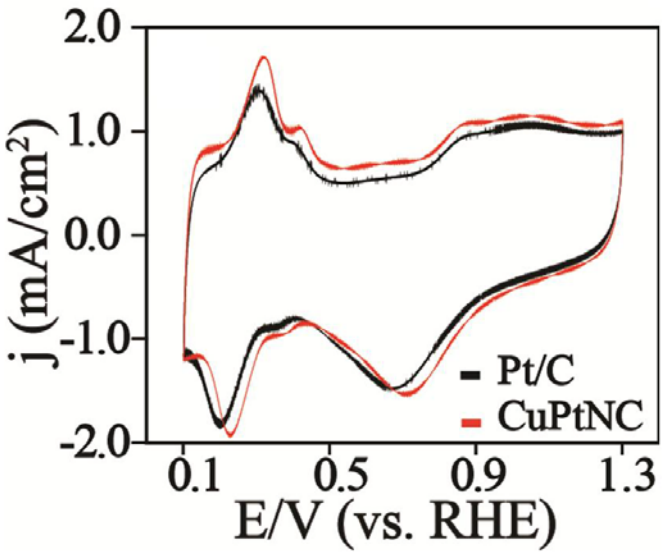

Figure 4.6: *Comparative CV of CuPt-NC with 20 wt. % Pt/C recorded in N_2-saturated 0.1 M KOH at 50 mV/s.*

Moreover, the comparative CV of CuPt-NC and Pt/C is presented in **Figure 4.6**. The CV features are similar to that of the polycrystalline Pt electrode.[42] In both the CVs, the hydrogen adsorption-desorption and oxygen reduction peak is appeared in the potential range of 0.1 to 0.4 V, and 0.6 to 1 V (vs. RHE), respectively. Peak integral of hydrogen desorption region gives the charge values equal to 1.43 mC and 1.23 mC for CuPt-NC and Pt/C, respectively. The electrochemical active surface area (ECSA) has been calculated by using **Equation 4.1**.[48,51]

$$ECSA\ (m^2/gm_{\text{-}Pt}) = [Q_{H\text{-}des}] / [0.21*Pt_{\text{-}loading}) \qquad (4.1)$$

where, $Q_{H\text{-}des}$ is the charge associated with hydrogen desorption in mC, 0.21 mC/cm^2 is a constant charge required to remove the monolayer of the adsorbed hydrogen layer, and Pt-loading is 0.01 mg. The obtained ECSA and roughness factor (RF) for CuPt-NC is 68 $m^2/g_{\text{-}Pt}$ and 34.65, whereas the corresponding values for Pt/C are 58.57 $m^2/g_{\text{-}Pt}$ and 29.85, respectively. The slight increment in ECSA for the former could be assigned to the higher number of accessible Pt active sites of CuPt-NC compared to Pt/C. CV result shows that CuPt-NC has positive onset potential shift as well as higher peak current density for oxygen reduction compared to Pt/C (**Figure 4.6**).

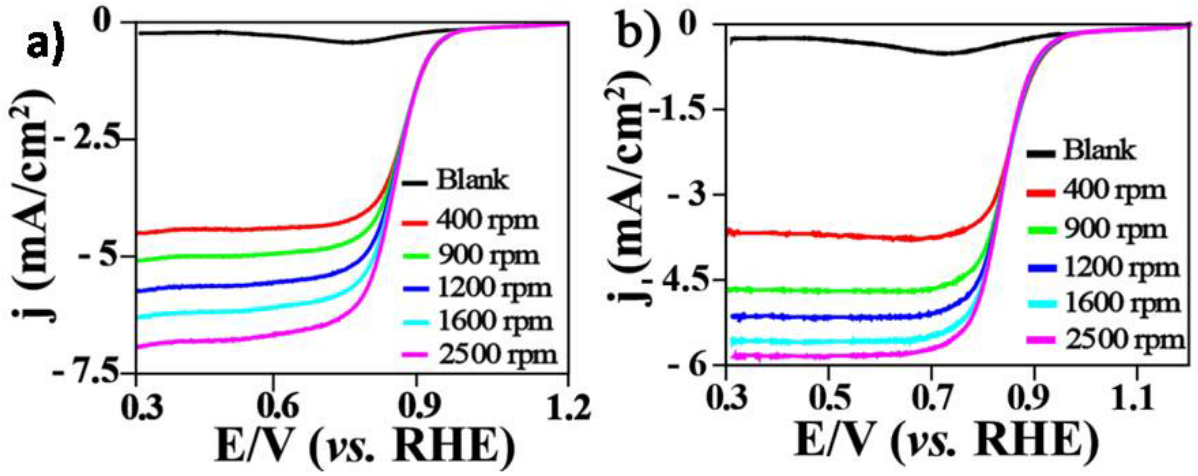

Figure 4.7: *Hydrodynamic voltammograms of (a) CuPt-NC and (b) Pt/C, recorded at different rotation rates of the working electrode (400 to 2500 rpm) in O_2-saturated 0.1 M KOH with scan rate of 10 mV/s.*

In addition, a hydrodynamic voltammogram for the ORR using RDE technique has been recorded by varying the rotation speed of the working electrode from 400 to 2500 rpm (**Figure 4.7a, 4.7b**). **Figure 4.7a and 4.7b** showing the hydrodynamic voltammograms of CuPt-NC and Pt/C, respectively recorded at different rotation of working electrode in O_2-saturated 0.1 M KOH with scan rate of 10 mV/s. It has been observed that the current increases with increasing the rotation speed of the working electrode, which clearly reveals the facile mass transport of oxygen to the electrode surface (details about the RDE and related equations are given in **Chapter 2, Section 2.3.2**).

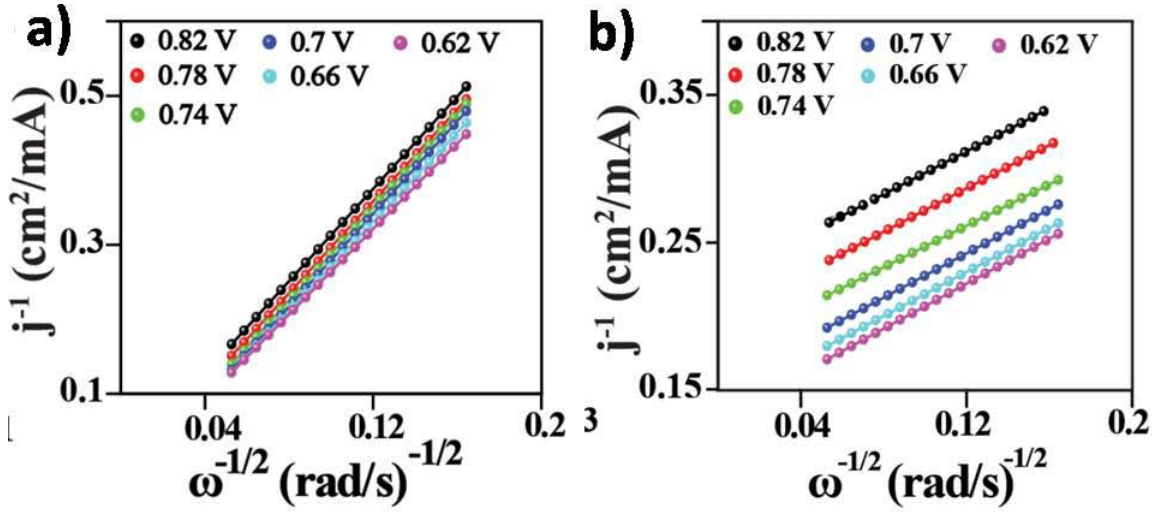

Figure 4.8: *K-L plots of (a) CuPt-NC, and (b) Pt/C, at different potentials.*

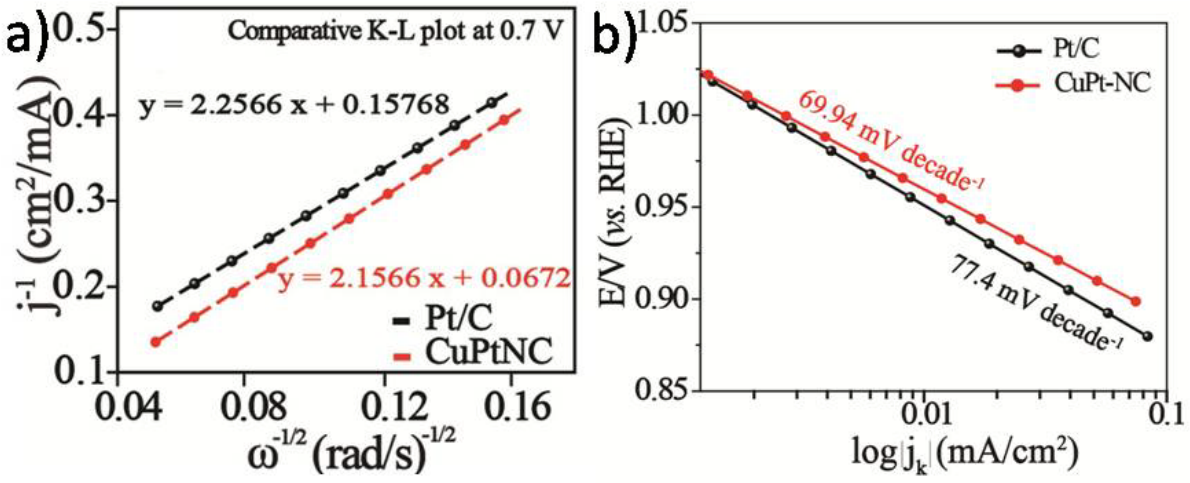

Figure 4.9: *Comparative (a) K-L plots at 0.7 V (vs. RHE), and (b) mass-corrected Tafel plots, of CuPt-NC and Pt/C. The Tafel slopes are calculated by the linear regression method.*

Moreover, the exact mechanism of the ORR has been confirmed through the Koutecky-Levich (K-L) analysis and the obtained K-L plots are shown in **Figure 4.8**. The K-L plots show good linearity, which is assigned to the first order kinetics of ORR and both the catalysts follow similar mechanistic pathway.[48] The number of electron (n) transferred during the reaction has been obtained from the slope of the K-L plot, which is found to be ~4 (**Figure 4.9a**). Moreover, the reciprocal of the intercept of the K-L plot provides the kinetic current (**Figure 4.9a**). It has been observed that CuPt-NC (1.49 x 10^{-3} mA) has shown one order improved kinetic current than that of Pt/C (6.34 x 10^{-4} mA), which highlights the structural benefit of the nanocage over spherical particles towards ORR.

Further insight on the mechanism of ORR and quality of the electrocatalyst can be obtained from Tafel analysis and mass and specific activity comparisons. In view of this, comparative mass transport corrected Tafel plots, which is a graph of E *vs.* log $|j_k|$), are given in **Figure 4.9b**. The currents were corrected for mass-diffusion to give kinetic current (j_k) in the mixed activation-diffusion region, which could be evaluated from **Equation 4.2**.[47,52-53]

$$j_k = (j * j_L) / (j_L - j) \qquad (4.2)$$

where, 'j_L//(j_L-j)'is the mass transfer correction factor. Importantly, **Equation 4.2** can be used for mass-correction when the reaction kinetic is of first order. The calculated Tafel slopes of Pt/C and CuPt-NC are found to be ~77.4 and ~69.94 mV/decade, respectively. It should be noted that,

the Tafel slope provides the indication of the actual mechanism takes place on the electrode surface and is related to the state of the adsorbed oxygen species and its coverage variation with respect to the potential. The lower Tafel slope obtained in the case of CuPt-NC stands out an important indicator of its improved performance, which originates from the facile oxygen adsorption and the subsequent reduction processes on the nanocage surface.[47]

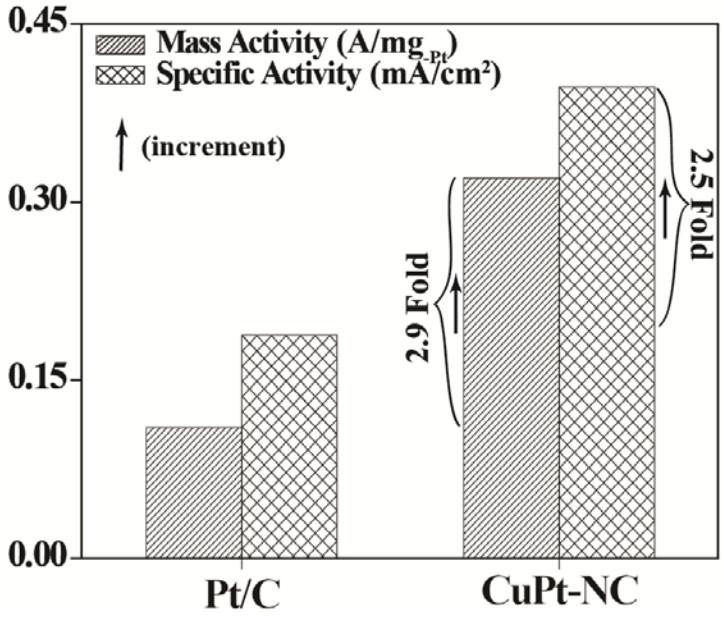

Figure 4.10: *Mass activity and specific activity at 0.9 V (vs. RHE) for Pt/C and CuPt-NC. At 0.9 V (vs. RHE), CuPt-NC is 2.9 fold more active on the basis of equivalent Pt mass compared to Pt/C. Furthermore, CuPt-NC exhibited a 2.5 fold improved specific ORR activity (at 0.9 V (vs. RHE)) compared to Pt/C.*

Furthermore, to understand the quality of the electrocatalyst, we have calculated the mass and specific activity of the Pt/C and CuPt-NC at 0.9 V (*vs.* RHE) as shown in **Figure 4.10**.The mass-corrected j_k value has been divided with the Pt-concentration (0.01 mg) in the coated sample to get the mass activity of Pt/C and CuPt-NC. Moreover, the specific activity of Pt/C and CuPt-NC has been derived by dividing the mass corrected j_k (at 0.9 V (*vs.* RHE) value with the ECSA. The obtained ECSA values for CuPt-NC and Pt/C are found to be 6.8095 cm^2 (68 m^2/g_{-Pt}) and 5.857 cm^2 (58 m^2/g_{-Pt}), respectively. Moreover, CuPt-NC displays a mass activity of 0.32 A/mg_{-Pt}, which is 2.9 fold higher than that of the Pt/C catalyst (0.1101 A/mg_{-Pt}), at 0.9 V (*vs.* RHE). Interestingly, this improvement could be due to the variation in active centered sites and difference in ECSA. Moreover, CuPt-NC displayed the specific activity (calculated at 0.9 V (*vs.*

RHE)) of 0.47 mA/cm^2, which is 2.5 fold better than the Pt/C (0.19 mA/cm^2) (**Figure 4.10**). This improved mass activity and specific activity of CuPt-NC over Pt/C is mainly credited to the well-defined atomic arrangement, overall structural integrity and higher number active centers of the open faceted nanocage framework.

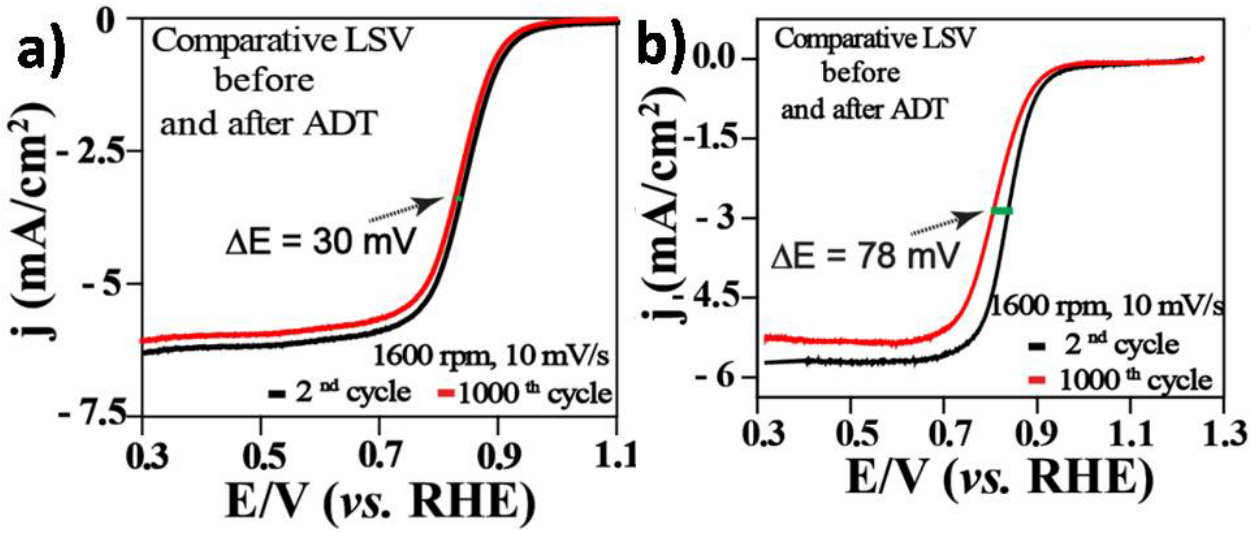

Figure 4.11: *Comparative LSVs before and after the 1000 cycles of (a) CuPt-NC and (b) Pt/C, recorded at 1600 rpm in O_2-satuared 0.1 M KOH. The half wave potential shift was observed to be 30 and 78 mV for CuPt-NC and Pt/C, respectively.*

To fulfill the desire for the effective utilization of CuPt-NC in a realistic application, the stability under electrochemical environment is an obligatory requirement. Therefore, ADT (accelerated durability test) has been performed by potential cycling (1000 cycles) in a potential window of 0.5 to 1.3 V (*vs*. RHE), with a voltage scan rate of 50 mV/s in oxygen saturated 0.1 M KOH solution, at room temperature. LSV has been recorded before and after ADT to investigate the performance degradation. **Figure 4.11a and 4.11b** show the comparative LSVs of CuPt-NC and Pt/C, before and after ADT, respectively. After 1000 cycles, the half-wave potential ($E_{1/2}$) is decreased by 30 and 78 mV for CuPt-NC and Pt/C, respectively (**Figure 4.11a, 4.11b, Table 4.1**). Also, the limiting current is found to be better for CuPt-NC compared to that of Pt/C (**Figure 4.11a, 4.11b, Table 4.1**). Moreover, CuPt-NC (onset potential is 0.95 V) has shown 50 mV of positive onset potential shift as compared to Pt/C (onset potential is 0.90 V) (**Figure 4.11a, 4.11b, Table 4.1**).

The difference in $E_{1/2}$ between the CuPt-NC and Pt/C systems is found to be 40 and 80 mV before and after ADT (**Table 4.1**). The observed higher limiting current for CuPt-NC compared to that of Pt/C could be attributed to the improved diffusion of oxygen and, subsequently, to its better interaction with the active sites located in CuPt-NC. Furthermore, both the catalysts follow the direct reduction mechanism of ORR involving the 4-electron transfer, which produces OH^- (**Figure 4.8 and 4.9a**). The better productivity of CuPt-NC is mainly attributed to its structure, which ultimately provides higher number of the catalytically active sites, easily accessible space and synergetic effect of Cu and Pt, etc. The sites are more favorable for the dissociative adsorption of oxygen during ORR in alkaline medium. Furthermore, to understand the exact cause behind the decrease in the limiting current and change in the half wave potential value, we have done the comparative compositional analysis of CuPt/NC by XPS study,[49-50] before and after the ADT test. CuPt-NC has shown 46.44, 47.52 and 6.06 wt. % of Cu, Pt and O, respectively, (**Figure 4.4**) before ADT. After ADT, the wt. % corresponding to Cu, Pt and O are found to be 46.14, 47.22 and 6.64, respectively (**Figure 4.12**).

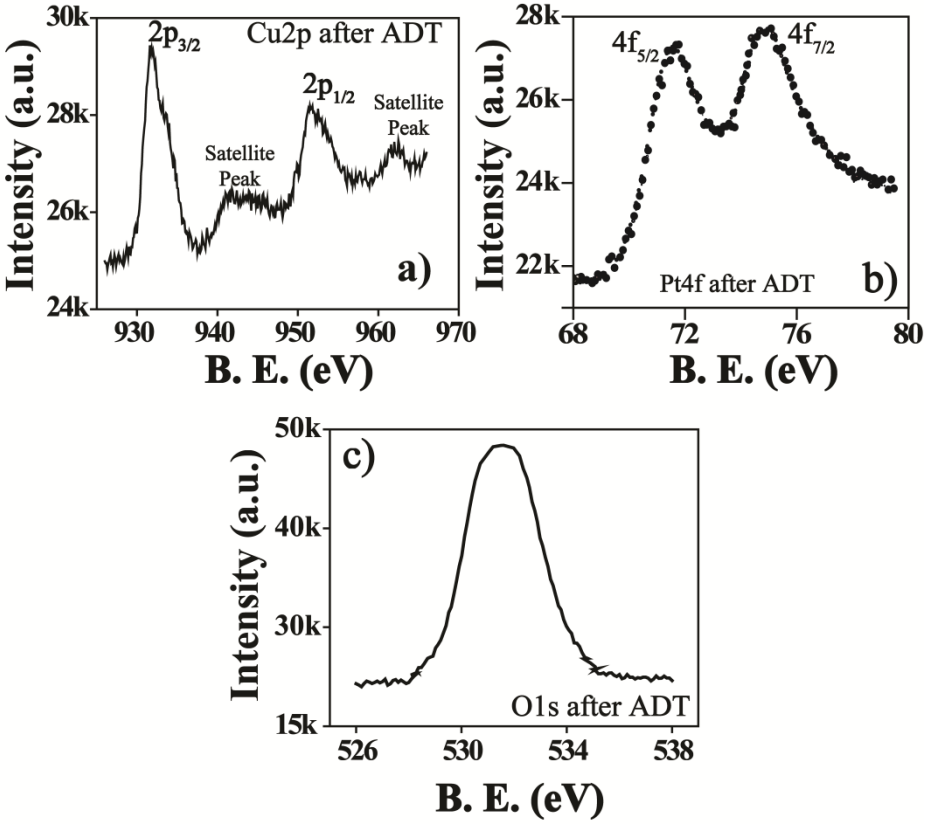

Figure 4.12: *XPS of CuPt-NC after 1000 cycle of ADT; a) Cu2p, b) Pt4f and c) O1s.*

A close analysis of the XPS data reveals that the relative composition of the metals (*i.e.* Cu:Pt) is nearly same (1:1.023) and the stoichiometric ratio is also found to be the same (Cu:Pt is 3:1) before and after ADT. However, more interestingly, the O wt. % is found to be slightly increased from 6.06 to 6.64 wt. %. This indicates higher oxidation of the surface metal atoms during ADT without affecting their relative metal composition (Cu:Pt =1:1.023) and stoichiometry (Cu_3Pt). In other words, the obtained results stand out as a proof for the structural integrity of the intermetallic hollow CuPt-NC structure. The increased oxygen wt. % at the surface might be a reason for the decrease in the half-wave potential and limiting current of CuPt-NC after the 1000 cycles of ADT because the increased O wt. % might be due to the higher oxidation of the active metal centers. On the other hand, in case of Pt/C, the main reason for the decrease in the limiting current is attributed to the higher oxidation of the carbon support under the potential cycling in a window of 0.5 to 1.3 V (*vs.* RHE). The oxidation of the support may leave naked Pt-nanoparticles, which results into aggregation of the particles, leading to a decrease in the surface-to-volume ratio and thereby the overall activity. Hence, the aggregation of Pt-particles in case of Pt/C and higher oxidation of active metal centers in case of CuPt-NC could be the reasons for the decrease in the limiting current.

4.3.7. Primary Zn-Air Battery Analysis

The superior ORR activity of CuPt-NC as evident from the RDE study, however, is not sufficient to conclude that the system can ensure an enhanced performance in practical Zn-air battery, because the concentration of the dissolved oxygen will be different in an electrolyte used for the LSV investigation (0.1M KOH) and the electrolyte used in the battery testing (6 M KOH). Along with this, the overall performance will also be decided by the formation of the effective triple-phase boundary, which could be effectively tackled in case of nanocage structure. Hence, it is necessary to analyze the material at similar electrolyte condition which is favorable for the Zn-air battery.

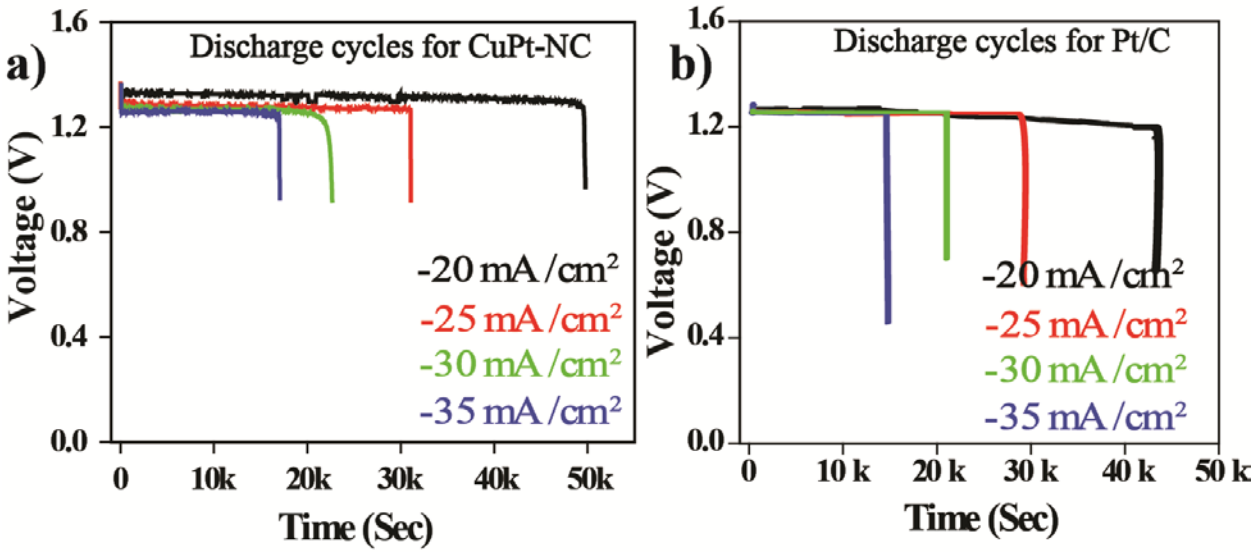

Figure 4.13: *Discharge test of the primary Zn-air battery performed with different discharge current densities (20 to 35 mA/cm^2) using cathode as (a), CuPt-NC coated carbon paper (2 mg$_{-Pt}$/cm^2) and (b) 20 wt % commercially available Pt/C coated carbon paper (2 mg$_{-Pt}$/cm^2). Conditions: anode = Zn powder coated carbon paper; electrolyte = 6 M KOH; active area = 1 cm^2.*

The fabricated Zn-air battery is composed of CuPt-NC as the air electrode material (cathode) and Zn-powder as the anode material and 6 M KOH as the electrolyte (**Scheme 4.1 and Figure 4.1**). Instead of using Ni-foil or any other kind of oxygen evolution (OER) materials, we coated CuPt-NC catalyst on a polytetrafluoroethylene (PTFE) treated carbon paper (active area = 1 cm^2), which avoids additional intrinsic electrochemical activity interference within the system. In principle, Zn undergoes oxidation at the anode and oxygen gets reduced at the cathode. Here, we have compared the performance of the CuPt-NC coated electrodes for ORR in the primary Zn-air battery with the commercially available Pt/C. The cathode Pt-loading was kept as 2 mg/cm^2 in both the systems. The detailed electrode fabrication is given in the experimental section. The Zn-powder and CuPt-NC coated carbon papers were dipped in 6 M KOH solution and oxygen was purged at the cathode side. The separately fabricated Zn-air battery set-ups with CuPt-NC and Pt/C as the air electrodes have shown an open circuit potential of ~1.4 and ~1.3 V (**Figure 4.13**), respectively.

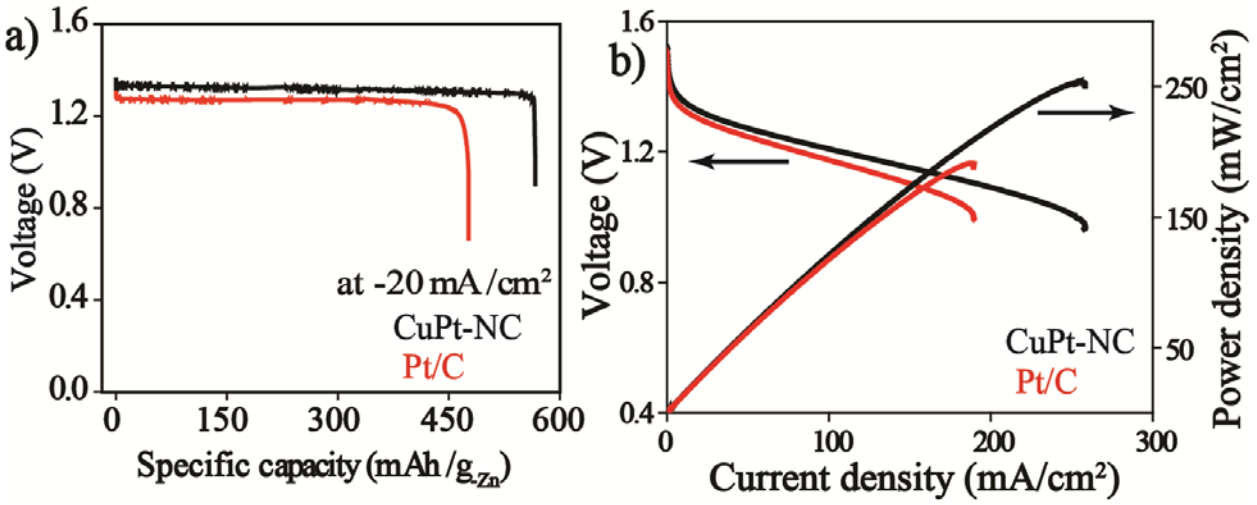

Figure 4.14: *(a) Comparative specific capacity vs. potential plot of CuPt-NC and 20 wt. % Pt/C at a discharge current density of 20 mA/cm^2. The plots in* ***Figure 4.14a*** *are made from the data of* ***Figure 4.13****, by normalizing the values with the amount of the Zn consumed (~0.5 g$_{-Zn}$) and(b) comparative steady-state polarization curves (I-V) and corresponding power density plots of the battery fabricated by using CuPt-NC and Pt/C as the cathode catalysts. Conditions: anode: Zn-powder coated carbon paper; cathode: Pt/C or CuPt-NC coated carbon paper (2 mg$_{-Pt}$/cm^2); electrolyte: 6 M KOH; active area: 1 cm^2.*

The improved open circuit potential in the case of the system having CuPt-NC as the cathode electrode is attributed to the higher number of the active center and ECSA possessed by CuPt-NC, which has already been confirmed through the cyclic voltammetric investigation. The comparative steady-state polarization curves of CuPt-NC and Pt/C as cathode electrode are shown in **Figure 4.14b**. CuPt-NC based device shows a current density of 253.8 mA/cm^2, whereas, the one based on Pt/C gives a current density of 188.8 mA/cm^2 at a voltage of 1 V (**Figure 4.14b**). Moreover, the peak power density is found to be 1.3 fold higher for CuPt-NC as air-electrode compared to Pt/C (**Figure 4.14b**). The improved current density at 1 V and peak power density of set-up fabricated with CuPt-NC as the air electrode compared to Pt/C. In addition, to investigate the robustness of the primary Zn-air batteries made with CuPt-NC over Pt/C, the system was subjected to galvanostatic discharge and the polarization curve was recorded at different discharge current rates ranging from 20 to 35 mA/cm^2. No abrupt potential drop is observed for long time, showing absence of any catastrophic failure of the integrated assembly with CuPt-NC as the cathode electrode (**Figure 4.13a**). The higher discharge stability obtained for CuPt-NC (~14 h, **Figure 4.13a**) compared to Pt/C (~12 h, **Figure 4.13b**), at a

discharge rate of 20 mA/cm^2, is attributed to the higher ORR activity of CuPt-NC in the battery and its inherent structural integrity. As the galvanostatic discharge continues, the Zn undergoes oxidation, becoming thinner and thinner. Ultimately, the electrolyte gets accumulated with more and more Zn-salts and battery eventually stops functioning once the whole Zn-metal is consumed (**Figure 4.13**). Besides, the specific capacity is found to be better for CuPt-NC compared to Pt/C (**Figure 4.14a**, discharge rate is 20 mA/cm^2). The specific capacity calculated by normalizing current with the mass of the consumed Zn[5] (~0.5 g) is 560 and 480 mAh/g$_{\text{-Zn}}$ for CuPt-NC and Pt/C, respectively. Correspondingly, CuPt-NC has shown high energy density of 728 Wh/kg$_{\text{-Zn}}$ compared to Pt/C (624 Wh/kg$_{\text{-Zn}}$). The superior activity for CuPt-NC is mainly credited of its peculiar structure, which helps the system to effectively maintain active center density and easily accessible space along with the electronic modulations affected in the system which facilitates effective dissociation of oxygen. Therefore, the obtained system could be developed with many more different metals and could be utilized for many more electrochemical applications such as metal-air battery, fuel cells, etc.

Table 4.1: *A summary of the electrochemical analysis.*

Sample Name	Before ADT			After ADT			% Decrease in Limiting Current Density	$\Delta E_{1/2}$ (V)	I_k @ 0.7 V (mA)
	Onset Potential (V)	$E_{1/2}$ (V)	Limiting Current Density (mA/cm^2)	Onset Potential (V)	$E_{1/2}$ (V)	Limiting Current Density (mA/cm^2)			
Pt/C	0.90	0.806	5.75	0.9	0.728	5.0	13%	0.078	6.34×10^{-4}
CuPt-NC	0.95	0.846	6.25	0.95	0.816	6.0	4%	0.030	1.49×10^{-3}

4.4. Conclusion

CuPt-NC intermetallic nanocage structures are synthesized by simple solvothermal method *via* an *in-situ* galvanic displacement reaction between Cu and Pt and its enhanced oxygen reduction activity and stability compared to Pt/C in alkaline solution could be explored. Interestingly, CuPt-NC has shown 2.9 fold improved mass activity and 2.5 fold improved specific ORR activity (at 0.9 V (*vs.* RHE)) than Pt/C. Utilization of CuPt-NC (250 mW/cm^2, 253.8 mA/cm^2 at 1V) as the air cathode in primary Zn-air battery delivered 1.30 and 1.34 fold

improved power density and current density at 1V, compared to the state-of-the-art Pt/C (190 mW/cm^2, 188.8 mA/cm^2 at 1V) catalyst. Moreover, in primary Zn-air battery testing, CuPt-NC led to a higher specific capacity and energy density (560 mAh/g_{-Zn}, 728 Wh/kg_{-Zn}, at a discharge rate of 20 mA/cm^2), which is superior compared to the performance of the system possessing Pt/C as the cathode (480 mAh/g_{-Zn}, 624 Wh/Kg_{-Zn}, at a discharge rate of 20 mA/cm^2). In particular, CuPt-NC, with its high density of surface defects, potentially offers more active site density for facilitating efficient dissociative adsorption of oxygen, resulting into improved ORR activity. The synergetic interaction between Pt and Cu also plays a favorable role for the efficient adsorption and bond polarization of oxygen. The primary Zn-air batteries prepared with CuPt-NC electrocatalyst are found to be very robust, which indicates the survivability of the system under the electrochemical environment.

4.5. References

[1] D. Linden, T. B. Reddy, *Handbooks of Batteries*, McGraw-Hill, New York, **2002**.

[2] Z. Chen, A. Yu, D. Higgins, H. Li, H. Wang, Z. Chen, *Nano Letters* **2012**, *12*, 1946-1952.

[3] J. –S. Lee, S. T. Kim, R. Cao, N. –S. Choi, M. Liu, K. T. Lee, J. Chao, *Advance Energy Materials* **2011**, *1*, 34-50.

[4] Y. Li, M. Gong, Y. Liang, J. Feng, J. –E. Kim, H. Wang, G. Hong, B. Zhang, H. Dai, *Nature Communications* **2013**, *4*, 1805, DOI: 10.1038/ncomms2812.

[5] G. Girishkumar, B. McCloskey, A. C. Luntz, S. Swanson, W. Wilcke, *The Journal of Physical Chemistry Letters* **2010**, *1*, 2193-2203.

[6] B. Scrosati, J. Hassoun, Y. –K. Sun, *Energy & Environmental Science.* **2011**, *4*, 3287-3295.

[7] B. Lim, T. Yu, Y. Xia, *Angewandte Chemie International Edition* **2010**, *49*, 9819-9820.

[8] D. Xu, Z. P. Liu, H. Z. Yang, Q. S. Liu, J. Zhang, J. Y. Fang, S. Z. Zou, K. Sun, *Angewandte Chemie International Edition* **2009**, *48*, 4217-4221.

[9] P. Strasser, S. Koh, T. Anniyev, J. Greeley, K. More, C. Yu, Z. Liu, S. Kaya, D. Nordlund, H. Ogasawara, M. F. Toney, A. Nilson, *Nature Chemistry* **2010**, *2*, 454-460.

[10] T. K. Sau, A. L. Rogach, F. Jackel, T. A. Klar, J. Feldmann, *Advanced Materials* **2010**, *22*, 1805-1825.

[11] J. Snyder, T. Fujita, M. W. Chen, J. Erlebacher, *Nature Materials* **2010**, *9*, 904-907.

[12] F. Barbir, *PEM Fuel Cells: Theory and Practice*, 2nd ed.; Elsevier: San Diego, CA, **2005.**

[13] L. Carrette, K. A. Friedrich, U. Stimming, *Fuel Cells*, **2001**, *1*, 5-39.

[14] Z. W. Chen, M. Waje, W. Z. Li, Y. S. Yan, *Angewandte Chemie International Edition* **2007**, *46*, 4060-4063.

[15] S. M. Alia, G. Zhang, D. Kisailus, D. S. Li, S. Gu, K. Jensen, Y. S. Yan, *Advanced Functional Materials* **2010**, *20*, 3742-3746.

[16] R. Wang, C. Xu, X. Bi, Y. Ding, *Energy & Environmental Science* **2012**, *5*, 5281-5286.

[17] K. Sasaki, J. X. Wang, H. Naohara, N. Marinkovic, K. More, H. Inada, R. R. Adzic, *Electrochimica. Acta.* **2010**, *55*, 2645-2652.

[18] N. V. Long, Y. Yang, C. M. Thi, N. V. Minh, Y. Cao, M. Nogami, *Nanoenergy*, **2013**, *2*, 636-676.

[19] P. C. Favilla, J. J. Acosta, C. E. Schvezov, D. J. Sercovich, J. R. Collet-Lacoste, *Chemical Engineering Science* **2013**, *101*, 27-34.

[20] X. Zhou, Y. Gan, J. Du, D. Tian, R. Zhang, C. Yang, Z. Dai, *Journal of Power Sources* **2013**, *232*, 310-322.

[21] G. Zhang, Z. –G. Shao, W. Lu, F. Xie, X. Qin, B. Yi, *Electrochimica Acta* **2013**, *103*, 66-76.

[22] J. W. Hong, S. W. Kang, B. S. Choi, D. Kim, S. B. Lee, S. W. Han, *ACS Nano* **2012**, *6*, 2410-2419.

[23] Y. –Y. Feng, G. –R. Zhang, J. –H. Ma, G. Liu, B. –Q. Xu, *Physical Chemistry Chemical Physics* **2011**, *13*, 3863-3872.

[24] J. Snyder, I. McCue, K. Livi, J. Erlebacher, *Journal of the American Chemical Society* **012**, *134*, 8633-8645.

[25] M. A. Mahmoud, W. Qian, M. A. El-Sayed, *Nano Letters* **2011**, *11*, 3285-3289.

[26] M. H. Oh, T. Yu, S. –H. Yu, B. Lim, K. –T. Ko, M. –G. Willinger, D. –H. Seo, B. H. Kim, M. G. Cho, J. –H. Park, K. Kang, Y. –E. Sung, N. Pinna, T. Hyeon, *Science* **2013**, *340*, 964-968.

[27] D. Wang, Y. Li, *Advanced Materials* **2011**, *23*, 1044-1060.

[28] R. Ferrando, J. Jellinek, R. L. Johnston, *Chemical Reviews* **2008**, *108*, 845-910.

[29] A. R. Tao, S. Habas, P. Yang, *Small* **2008**, *4*, 310-325.

[30] S. W. Kang, Y. W. Lee, Y. Park, B. –S. Choi, J. W. Hong, K. –H. Park, S. W. Han, *ACS Nano* **2013**, *7*, 7945-7955.

[31] Y. H. Bing, H. S. Liu, L. Zhang, D. Ghosh, J. J. Zhang, *Chemical Society Reviews* **2010**, *39*, 2184-2202.

[32] S. –I. Choi, R. S. Choi, W. Han, J. T. Park, *Chemistry-A European Journal* **2011**, *17*, 12280-12284.

[33] C. Chen, Y. Kang, Z. Huo, Z. Zhu, W. Huang, H. L. Xin, J. D. Snyder, D. Li, J.A . Herron, M. Mavrikakis, M. Chi, K. L. More, Y. Li, N. M. Markivic, G. A. Somorjai, P. Yang, V. R. Stamenkovic, *Science* **2014**, *343*, 1339-1343.

[34] Y. Yin, R. M. Rioux, C. K. Erdonmez, S. Hughes, G. A. Somorjai, A. P. Alivisatos, *Science* **2004**, *304*, 711-714.

[35] J. E. Macdonald, M. BarSadan, L. Houben, I. Popov, U. Banin, *Nature Materials* **2010**, *9*, 810-815.

[36] S. E. Skrabalak, J. Chen, Y. Sun, X. Lu, L. Au, C. M. Cobley, Y. Xia, *Accounts of Chemical Research* **2008**, *41*, 1587-1595.

[37] M. McEachran, D. Keogh, B. Pietrobon, N. Cathcart, I. Gourevich, N. Coombs, V. Kitaev, *Journal of the American Chemical Society* **2011**, *133*, 8066-8069.

[38] J. X. Wang, C. Ma, Y. Choi, D. Su, Y. Zhu, P. Liu, R. Si, M. B. Vukmirovic, Y. Zhang, R. R. Adzic, *Journal of the American Chemical Society* **2011**, *133*, 13551-13557.

[39] S. A. Johnson, P. J. Ollivier, T. E. Mallouk, *Science* **1999**, *283*, 963-965.

[40] M. S. Yavuz, Y. Cheng, J. Chen, C. M. Cobley, Q. Zhang, M. Rycenga, J. Xie, C. Kim, K. H. Song, A. G. Schwartz, L. V. Wang, Y. Xia, *Nature Materials* **2009**, *8*, 935-939.

[41] R. E. Davis, G. L. Horvath, C. W. Tobias, *Electrochimica Acta* **1967**, *12*, 287-297.

[42] B. Y. Xia, H. B. Wu, X. Wang, X. W. Lou, *Journal of the American Chemical Society* **2012**, *134*, 13934-13937.

[43] Z. Zhang, Y. Yang, F. Nosheen, P. Wang, J. Zhang, J. Zhuang, X. Wang, *Small* **2013**, *9*, 3063-3069.

[44] Y. Xu, B. Zhang, *Chemical Society Reviews* **2014**, *43*, 2439-2450.

[45] C. Susut, G. B. Chapman, G. Samjeske, M. Osawac, Y. Tong, *Physical Chemistry Chemical Physics* **2008**, *10*, 3712-3721.

[46] D. Wang, Y. Yu, H. L. Xin, R. Hovden, P. Ercius, J. A. Mundy, H. Chen, J. H. Richard, D. A. Muller, F. J. DiSalvo, H. D. Abruña, *Nano Letters* **2012,** *12*, 5230-5238.

[47] S. M. Unni, V. M. Dhavale, V. K. Pillai, S. Kurungot, *The Journal of Physical Chemistry C* **2009**, *114*, 14654-14661.

[48] A. J. Bard, L. R. Faulkner, *Electrochemical Methods Fundamentals and Applications*, 2nd ed.; John Wiley & Sons, Inc.: New York, **2006**.

[49] J. F. Moulder, W. F. Stickle, P. E. Sobol, K. D. Bomben, In *Handbook of X-ray Photoelectron Spectroscopy: A Reference Book of Standard Spectra for Identification and Interpretation of XPS Data*, 2nd ed.; J. C. Prairie and E. Minn, Physical Electronics, Division, Perkin-Elmer Corp., **1992.**

[50] J. F. Watts, J. Wolstenholme, *An Introduction to Surface Analysis by XPS and AES*, 2nd ed.; Wiley, New York, USA, **2003**.

[51] H. –J. Kim, D. –Y. Kim, H. Han, Y. –G. Shul, *The Journal of Power Sources* **2006**, 159, 484-490.

[52] N. R. Elezović, B. M. Babic, L. Gajić-Krstajic, V. Radmilovic, N. V. Krstajic, L. J. Vracar, *The Journal of Power Sources* **2010,**195, 3961-3968.

[53] S. L. Gojkovic, S. K. Zecevic, R. F. Savinell, *Journal of the Electrochemical Society* **1998**, 145, 3713-3720.

Chapter 5
Synthesis of Pt-free Core-Shell Electrocatalyst for Oxygen Reduction Reaction via Simple Water-in-Oil Emulsion Method*

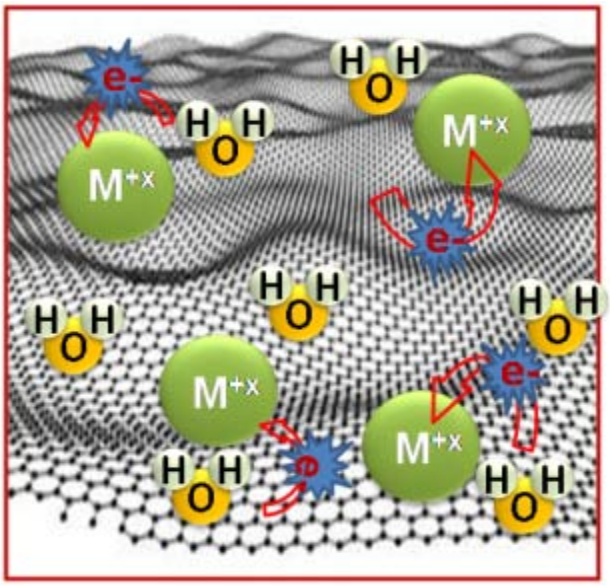

Simple water-in-oil (W/O) emulsion method developed for the synthesis of a core-shell structured Pt-free electrocatalyst is explained in this chapter. The core-shell nanoparticles prepared here possess nitrogen doped graphene (NGr) as the shell and Au nanoparticles as the core (Au@NGr).The key aspects of the process involve milder experimental conditions and very easy workups. The process guarantees distinct core-shell features of the formed nanoparticles. The growth of the core-shell structure is facilitated by the mutually assisted redox reaction happening within the emulsion droplet, which acts as a "nanoreactor". A detailed discussion on the possible interactions that could be existing between the Au nanoparticle and the covered carboneous shell around it and the role of such interactions to modulate the properties of the shell to favourably influence its oxygen reduction activity is included in this chapter. The chapter also includes a detailed discussion on the material characterization, which clearly unravels the structural and basic property characteristics of the materials. Finally, the chapter narrates the interesting oxygen reduction activity acquired by the system.

---

*The content of this chapter has been published in "***J. Mater. Chem. A.** *2014, 2, 1383-1390*"
- Reproduced by permission of The Royal Society of Chemistry
http://pubs.rsc.org/en/Content/ArticleLanding/2014/TA/c3ta14005a#!divAbstract

5.1. Introduction

Various low-Pt materials have been extensively investigated as cost-effective oxygen reduction electrocatalysts for polymer PEMFCs.[1-2]The last two chapters (**Chapter-3 and 4**) illustrate the structural and activity characteristics of low-Pt based core-shell (Cu@Pt and Fe_2O_3@Pt) and3-D hollow (CuPt-NC) structured electrocatalysts for ORR. Despite the excellent research progress in this direction, the ultimate target obviously is to make the electrode completely free from Pt. Recently, a number of studies have been focused on developing Pt-free electrocatalysts, and this area has become a hot research topic in the field of fuel cells.[3-5] Among these, heteroatom (N, P, B and S) doped electrocatalysts have generated a great deal of research interest.[6-8] Their capability for the ORR originates from the doped heteroatom in a graphitic network, which makes it *non-electron-neutral* and thus favours the molecular oxygen adsorption and eventually the reduction. Nevertheless, here, control of the activity and selectivity of the sites towards the desired ORR pathway involving four-electron ($4e^-$) transfer is a daunting task. The doping increases the disorderness in the catalyst with a concomitant increase in the number of the active sites for ORR.[6-9]The induced disorderness and more active sites are mainly attributed to the change in spin density and charge distribution of carbon atoms, thanks to the presence of heteroatom at next-door to it.[10-11]However, due to the dislocations, the overall electronic conductivity of the catalyst will get altered due to opening of band gap between the conduction and valence bands.[6-9]Moreover, the nitrogen doping in graphene frameworks shifts the Fermi level above the Dirac point,[12-13] and density of state near the Fermi level gets suppressed.[14-16]Apart from this, the synthesis method also alters the overall conductivity of the N-doped systems. Gong *et al.* observed that the conductance of graphene annealed in ammonia atmosphere was lower than that of pristine graphene due to the N-doping in a graphene framework, whereas the N-doping in a nitrogen atmosphere apparently did not alter the electronic properties of graphene.[15]Thus, the material accommodates the heteroatom with some compensation on its inherent electronic conductivity even though the mode of preparation plays a crucial role.[15-16]In addition, Anderson *et al.* investigated the oxygen reduction study on graphene, N-doped graphene and non-noble metal (like cobalt) based graphene systems[17-18] using DFT method. The authors found that the electroreduction of oxygen mainly leads to the formation of H_2O_2 by following the undesirable two electron pathway.

In parallel, Henkelman *et al.*[19] reported that the difference in the Fermi energy of core and shell entities decides the direction of charge redistribution. Generally, the charge gets transferred from the higher to lower Fermi energy.[19] Moreover, along with the charge redistribution, the adsorption and desorption rates of chemical species decide the activity of a catalyst. According to the Bronsted-Evans-Polanyi relationship, the energy barrier of reactions is linearly associated to the reaction energy.[20-21] In general, a chemical species like oxygen binds very strongly with non-noble metals (like Cu, Fe, Co, etc), with no barrier for dissociative adsorption. On the other hand, noble metals like Pt, Au, etc. bind oxygen weakly and have high barrier for dissociative adsorption.[9, 22-23] However, in the designing of the kinetic model of the surface chemistry by putting together the relationship between the product binding energy and energy barrier, a maxima in catalytic activity is found at an optimal compromise between the weak product binding energy and reaction barrier.[24-25] Also, Schmickler *et al*. investigated the importance of gold in alkaline fuel cells with supported evidences from energy calculations.[23]

In this context, gathering the intrinsic properties of gold and N-doped graphene in a single nanostructure system will be helpful to understand the effect of property modulations in influencing the parameters such as ohmic overpotential, electrical conductivity and oxygen reduction kinetics. Taking the advantage of the difference in the conductivity, electronegativity and Fermi energy of Au compared to carbon, herein, I tried to synthesis a Pt-free electrocatalyst, which can show nearly comparable activity to the 20 wt.% commercial Pt/C, without sacrificing the overall conductivity of the metal-graphene nanostructures. This is achieved by encapsulating nitrogen-doped graphene (NGr) on gold (Au) nanoparticle (hereinafter called Au@NGr) all the while keeping the Au concentration very low. Here, the role of the NGr shell is to reduce oxygen, while the Au core modulates the electronic conductivity[26] and the electrocatalytic activity of the NGr shell by triggering synergetic electronic interactions. The study leads to conclusive evidence on the highly influential role played by the core metal species in shifting the ORR kinetics of NGr towards the favourable four-electron ($4e^-$) pathway. This leads to a reduced content of hydrogen peroxide (H_2O_2) in alkaline environment apart from its contribution in enhancing the electrical conductivity. Therefore, over the low-Pt based electrocatalysts described in **Chapter 3 and 4**, the Pt-free Au@NGr could somewhat help to reduce the electrode cost in fuel cells as the Au concentration in the present case is significantly low.

5.2. Experimental Section

5.2.1. Synthesis of Gold@Nitrogen Doped Graphene (Au@NGr) Electrocatalyst

Gold@nitrogen-doped graphene (Au@NGr) core-shell nanostructures were synthesized by simple W/O emulsion technique without using any external reducing and capping agents in a size controlled manner (**Scheme 5.1**). Briefly, 4 mg of the as-synthesized NGr was mixed with 2 ml of aqueous solution of 100 mM$HAuCl_4$ and the mixture was sonicated for 30 min using a bath sonicator to form a homogenous solution. The dispersed solution was added drop-wise in previously taken fresh silicon oil (25 ml), under a strong magnetic stirring. Furthermore, the reaction mixture was maintained for 5 h under stirring at 750 rpm at room temperature to get a uniform distribution of emulsion droplets. At this stage, the color of the reaction mixture was turned from transparent to reddish, which is attributed to the formation of Au@NGr core-shell nanostructures.

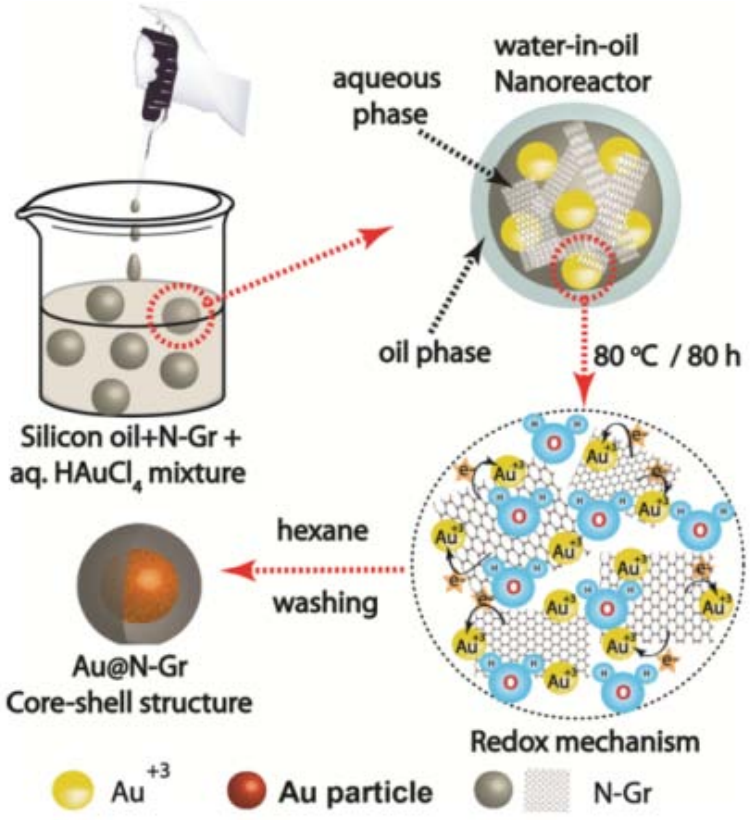

Scheme 5.1: *Schematic representation of the synthesis of Au@NGr core-shell nanoparticle by the micro-emulsion technique.*

Further, the W/O emulsion was transferred into a Petri dish, and was kept in an oven at 80 ^{o}C for 80 h. During this process, water in the emulsion droplets gets evaporated and crystallization of the solid components in the emulsion droplets occurs simultaneously. Finally, the formed Au@NGr core-shell nanostructures were centrifuged at 10000 rpm for 15 min and the mixture was washed with excess hexane to obtain oil-free Au@NGr core-shell nanostructures.

5.2.2 Synthesis of Gold@Graphene (Au@Gr) Electrocatalyst

In a similar way, gold@graphene (Au@Gr) sample was also prepared by using graphene (Gr), instead of NGr, in the abovementioned method (detailed synthesis procedures adopted for preparing GO, Gr, NGr, Au nanoparticles, and Au@Gr are given in **Chapter 2, Section 2.1.6-2.1.10**, respectively).

5.2.3. Calculation of Uncompensated Resistance for iR Compensation Study

a) Positive Feedback method:

The uncompensated resistance value has been calculated by positive feedback method, as described in the literature.[27]

The automatic compensation of resistance has been done on Bio-Logic instrument, by determining the resistance value using positive feedback method. Basically, at any potential, where no Faradaic reaction is happening, the Faradaic impedance is very large and can be taken as approximately an open circuit. By applying very small amount potential, where no Faradaic process takes place, the instantaneous change in the potential will takes place, and consequently the current drops to zero. Finally, the current value at time (t) equal to zero has been calculated by extrapolation, and used it to find the uncompensated resistance (iR_u). In between the reference and working electrode, the resistance (R_u) in series with capacitance (C_d) will be appeared. Therefore, in order to eliminate the C_d term, the feedback method is useful to get the resistance- free data. Here, the application of a small potential step (50 mV) across the reference and working electrode is given, where no Faradaic reaction occurs and hence the only current that flows in this region is charging current with an exponential decay. Finally the linear regression is performed at low time scale, as shown in **Figure 5.1a**. The current response should be

$$i(t) = (\Delta E / R_u) \exp(-t / R_u C_d) \quad (5.1)$$

The current at t = 0 can be interpreted as in **Equation 5.1**, where the exponential term of **Equation 5.1** (i.e. $-t/R_uC_d$), becomes equal to unity and capacitance will disappear. Finally **Equation 5.1** changes to,

$$i\,(0) = \left(\frac{\Delta E}{R_u}\right) \quad (5.2)$$

where, ΔE is known (50 mV) and R_u can be extracted after extrapolation at t = 0.

The plot of current (*i*) *vs.* time (*t*), extrapolation of graph at t = 0, gives the value of $\Delta E/R_u$.

Calculation:

$\Delta E/R_u = 0.85$ mA

$R_u = \Delta E/0.85$ mA

$= 50$ mV / 0.85 mA

R_u= 58.82 Ω

b) Impedance spectroscopy:

The uncompensated resistance value could also be calculated by impedance analysis. The dispersed sample is coated on the glassy carbon electrode surface, and was used as the working electrode. Moreover, the impedance spectra wasrecorded in a three-electrode system by using Hg/HgO as the reference electrode and platinum foil as the counter electrode in 0.1 M KOH. The plot is shown in **Figure 5.1b**. The X-axis intercept gives the value of resistance (58.2 Ohms), which was used for the automatic *iR* compensation study during RDE. The obtained resistance value is matching with the obtained resistance value by the positive feedback method.

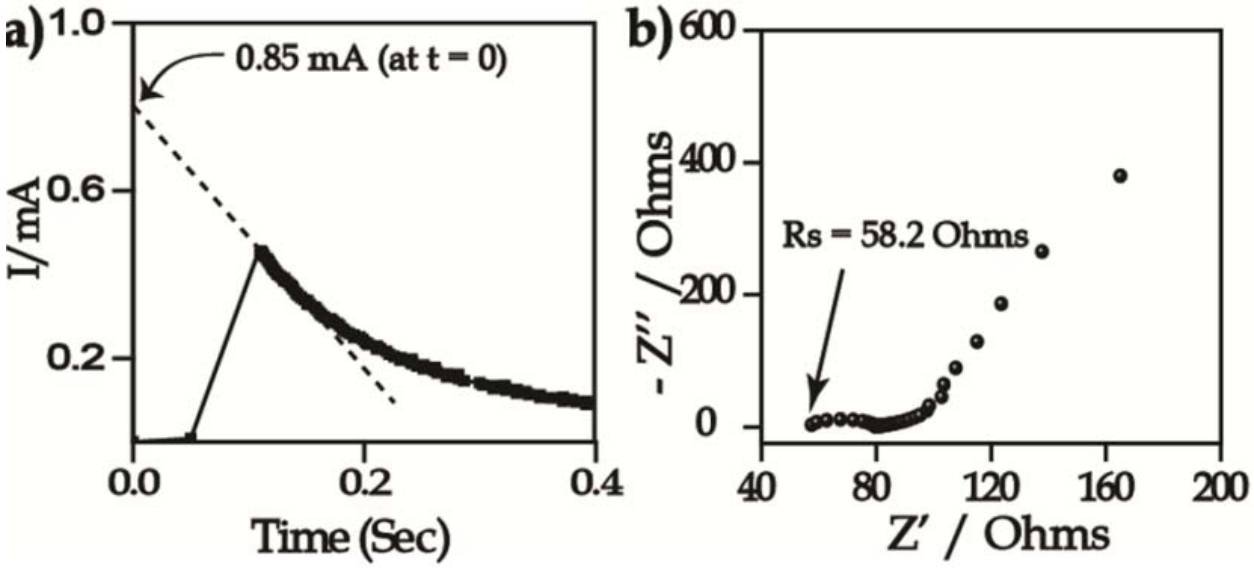

Figure 5.1: *Determination of the uncompensated resistance value by a) positive feedback method and b) impedance spectroscopy.*

5.3. Results and Discussion

5.3.1. Concept of Nanoreactor and Mechanism of Formation of Core-Shell Structures

During the synthesis of Au@NGr core-shell structured electrocatalyst by using W/O emulsion technique, numbers of water droplets were formed. These water droplets contain water dispersed Gr/NGr and Au^{+x} ions. These emulsion droplets will act as "*nanoreactors*", where the actual reaction takes place (**Scheme 5.1**). During the time bound heating process, water starts evaporating, and simultaneously, the metal ion and NGr undergo mutually assisted redox reaction,[28-32] leading to the formation of Au@NGr core-shell nanostructures. Importantly, during the reaction, the Gr gets distributed at the water-oil interface due to the larger surface area and flexible properties of Gr.[28-32] Mainly, three kinds of energies viz., surface energy (Es) created by bending of Gr layers, Vander Waals forces (Ev) between the Gr sheets, and gravitational potential energy (Eg) of metal nanoparticles will decide the final structure of the metal-Gr nanostructures.[28-32] However, for the formation of the core-shell structures, Ev is expected to dominate over Es and Eg.[28-32]

5.3.2. TEM Analysis

Figure 5.2a and **5.2e** show the TEM images of the well dispersed Au@Gr and Au@NGr core-shell nanostructures, respectively. The inset shows the magnified views of the selected particles, displaying the core-shell features with an average particle size of ~10 nm. The HR-TEM images of Au@Gr and Au@NGr are given in **Figure 5.2b** and **5.2f**, respectively. The *d*-spacing values of the core and shell have been calculated from the lattice fringes profiling (**Figure 5.2c and 5.2g**), which gives ~0.26 nm for the core for both Au@Gr and Au@NGr, which is attributed to Au. In the case of the shell, the *d*-values for Au@Gr and Au@NGr are ~0.33 and ~0.36 nm (**Figure 5.2c** and **5.2g**), respectively, which clearly indicate the coverage of the Au core in the corresponding samples by Gr and NGr. It has been reported that N-doping leads to an increase in the *d*-value due to incorporation of N-atoms in the graphene framework, which leads to the lattice expansion.[9] Insets of **Figure 5.2b** and **5.2f** show the selected area electron diffraction (SAED) patterns of Au@Gr and Au@NGr, respectively.

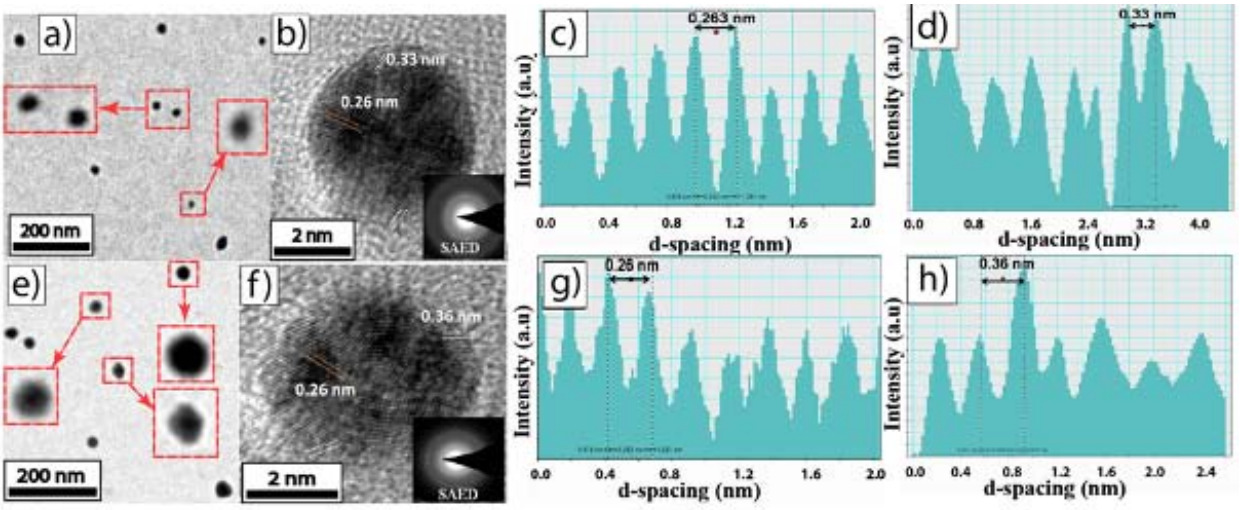

Figure 5.2: *TEM images of a) Au@Gr and e) Au@NGr nanoparticles and the inset gives the magnified image of the selected area highlighting the core-shell structure of the particles, HR-TEM images of b) Au@Gr and f) Au@NGr core-shell structure with lattice fringes (inset: SAED pattern), c and d) represent the lattice fringe profile of Au (core) and Gr (shell), respectively, indicating the core is Au and shell is Gr, g and h) represent the lattice fringe profile of Au (core) and NGr (shell), respectively, indicating the core is Au and shell is NGr.*

5.3.3. XRD Analysis

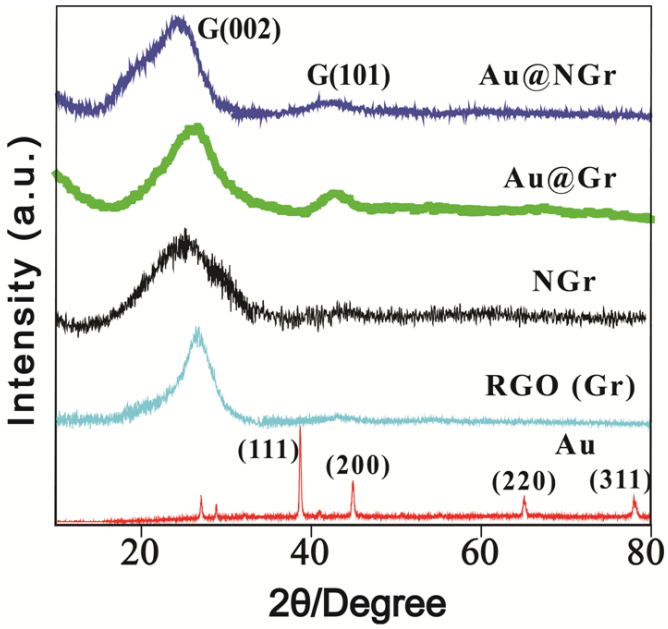

Figure 5.3:*Comparative full range XRD of Au nanoparticles, Gr, NGr, Au@Gr and Au@NGr core-shell nanoparticles. The G (002) peak showing a shift in the peak position after N-incorporation in the graphene framework.*

Figure 5.3 shows the comparative X-ray diffraction (XRD) of Gr, NGr, Au, Au@Gr and Au@NGr. In all the cases except Au, a strong reflection at $2\theta = \sim 26.5^{o} \pm 0.3^{o}$ is observed which is attributed to the G (002) graphitic plane. In case of NGr and Au@NGr, the same peak is shifted to lower 2θ values (~25^{o}) with broadening, indicating the incorporation of nitrogen atom in the graphene framework (**Figure 5.3**). Compared to NGr, the shift in the peak position in the case of Au@NGr is more and a similar trend, even though less pronounced, is also observed between Gr and Au@Gr. These shifts are attributed to the interaction of Au with the Gr shell, which is in well agreement with the calculated *d*-spacing values from TEM.

5.3.4. Raman Analysis

Raman spectroscopy serves as a powerful and non-destructive tool for the characterization of carbon based materials. A typical Raman spectrum of Gr shows a peak at 1345 cm^{-1} (D band), which corresponds to the breathing mode of K-point photons of A_{1g} symmetry allied with vibrations of the sp^3 carbon atoms.

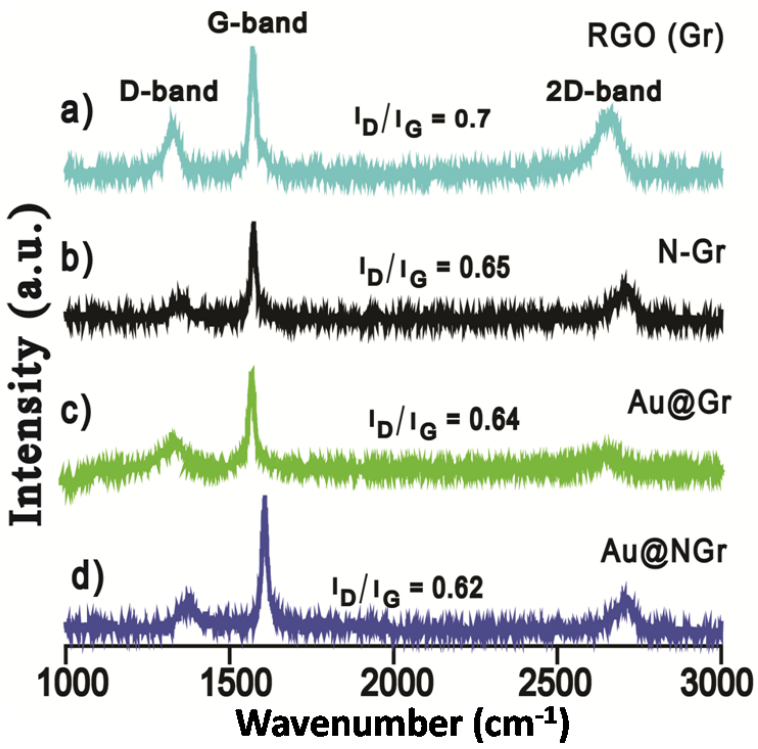

Figure 5.4: *Comparative Raman spectra of Gr, NGr, Au@Gr, and Au@NGr with their corresponding I_D/I_G ratios.*

Furthermore, a peak at 1590 cm^{-1} (G band)has also been identified, which is attributed to the in-plane vibration of the sp^2 carbon atoms in the hexagonal lattice (**Figure 5.4**).[33-34]Explicitly, the first-order Raman scattering processes are responsible for the G-band, whereas the double-resonance process and second order scattering results into the 2D and D bands.[9] Usually, the intensity ratio of D to G (I_D/I_G) is used to compare the structural order between the crystalline and amorphous graphitic systems. In the present case, the I_D/I_G ratios of the prepared samples follow the order: Gr (0.70) >NGr (0.65) >Au@Gr (0.64) >Au@NGr (0.62).The slight decrease in the I_D/I_G ratio from Gr to NGr is due to the incorporation of nitrogen in the Gr framework at 900 ^oC, where the oxygen functionalities of Gr might have reduced. Furthermore, the I_D/I_G ratio is still decreased when the Gr deposition occurs over Au and this is attributed to the expected interpenetration of the lattice fringes of the component phases.[9, 35] Additionally, the 2D bands of Gr in Au@Gr and Au@NGr are clearly shifted to a higher wave number, due to the interaction of Au with Gr/NGr, leading to the electron transfer from the core to the shell.[9, 35]

5.3.5. XPS Analysis

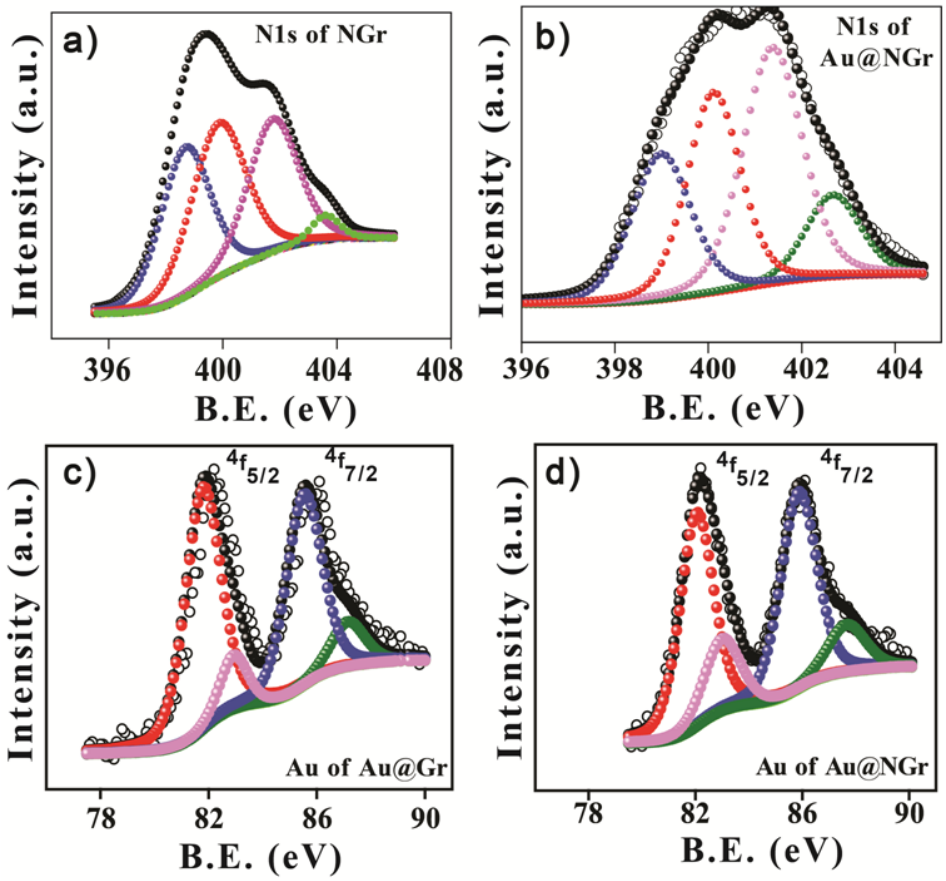

Figure 5.5:*a & b) N1s spectra of NGr and Au@NGr, respectively; c & d)Au4f deconvulated XPS of Au@Gr and Au@NGr, respectively.*

An understanding on the electronic interactions in the materials has been obtained by X-ray photoelectron spectroscopy (XPS). **Figure 5.5a** and **5.5b** show the deconvulated N1s spectra of NGr and Au@NGr, which reveal the presence of four types of nitrogen namely pyridinic-N, pyrrolic-N, graphitic-N and N-oxide, with a total N content of ~3.5 %. Basically, the nitrogen which possesses a lone pair of electrons is known to enhance the electron-donor property of the catalyst.[9, 35]As a result, it can weaken the O-O bond *via* the bonding between oxygen and nitrogen and/or the adjacent carbon atom, and in turn can facilitate the reduction of oxygen.[9-10, 36-39]

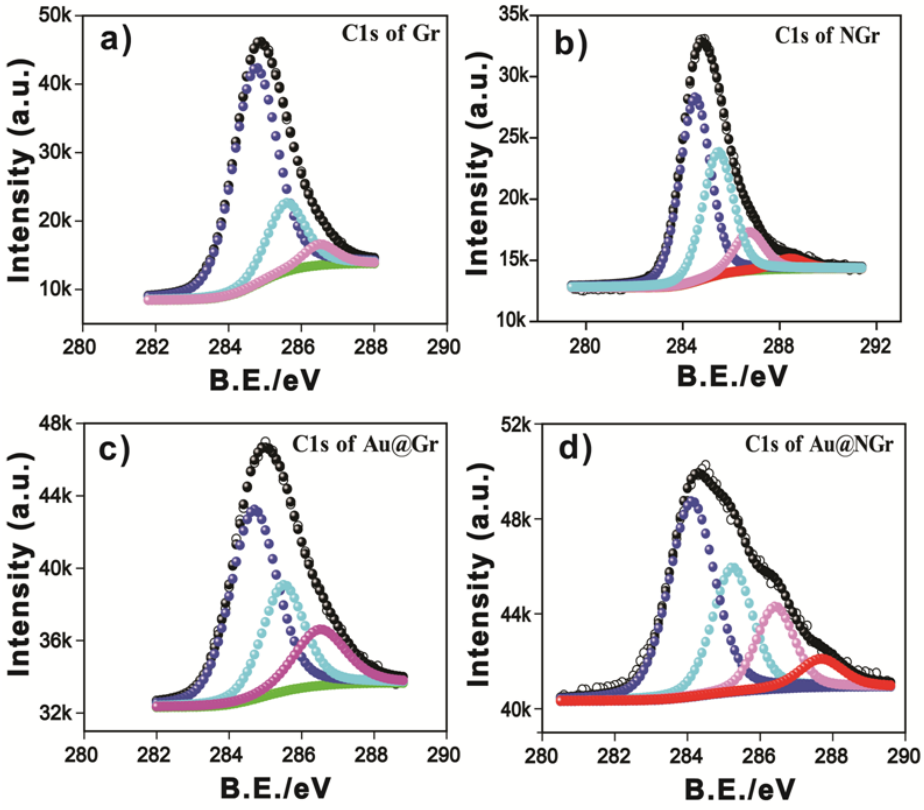

Figure 5.6:*DeconvulatedC1s XPS of Gr (a), NGr (b), Au@Gr (c), and Au@NGr (d).*

Figure 5.5c and 5.5d show the Au4f spectra of Au@Gr and Au@NGr. The higher shift in the binding energy of the Au4f peaks is attributed to the interaction of Au with the Gr/NGr shell. The interaction of the metal with carbon is still a matter of debate. Nevertheless, as reported, the delocalized p-orbital electrons (π electrons) of carbon overlap with the d-orbital of Au, indicating the partial covalent bonding characteristics.[35] This could be due to the d-orbital electron of the metal is shared with a π* anti-bonding orbital of the carbon. **Figure 5.6** shows the C1s spectra of Gr, NGr, Au@Gr and Au@NGr, which have been deconvoluted as per their spin-orbit splitting. The C1s spectra (**Figure 5.6c** and **5.6d**) of Au@Gr and Au@NGr, respectively show higher shifts in the binding energy compared to the C1s spectra of Gr (**Figure 5.6a**) and NGr ((**Figure 5.6b**), which is credited to the interaction of Au with the surface layer of Gr/NGr.

5.3.6. Electrical Conductivity Analysis

The change in the electronic configuration and interaction of Au with the Gr/NGr shell is reflected in the electrical conductivity as well (**Figure 5.7**). The measured conductivity follows

the order: Au@NGr (9.41 S/cm) >Au@Gr (6.03 S/cm) > Au (2.09 S/cm) >NGr (1.48 S/cm) >Gr (0.50 S/cm). The enhancement in the conductivity of Au@NGr and Au@Gr originates from the Au core and its interaction (dπ-pπ back bonding) with the surface carbon, which improves the interfacial charge transfer.[9, 35] The shift in Raman spectra (**Section 5.3.4, Figure 5.4**), as explained before, substantiates this kind of interfacial charge transfer from the Au core to the Gr shell. Moreover, the electronegativity of C (2.55) is slightly higher than Au (2.54), which is a determining factor in deciding the direction of the charge transfer. The detailed procedure of the electrical conductivity measurement is given in **Chapter 2, Section 2.2.6**.

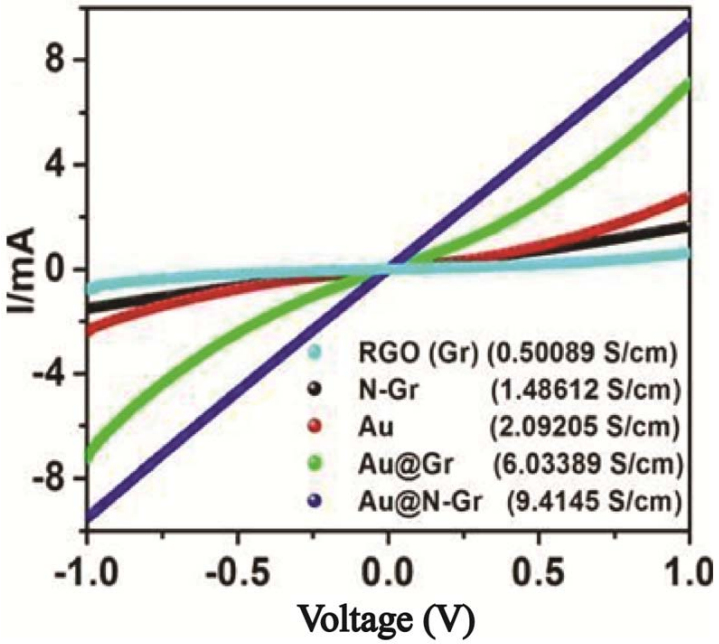

Figure 5.7: *Comparative electrical conductivity of the Au nanoparticles, Gr, NGr, Au@Gr, and Au@NGr.*

5.3.7. Electrochemical Study

The enhancement in the conductivity and lattice modulation of the Gr/NGr layer are also expected to bring in favourable changes in the ORR activity of the system. A preliminary screening of the electrocatalytic activity of all the samples towards ORR in alkaline media was carried out by cyclic voltammetry (CV). More specifically, nitrogen and oxygen saturated 0.1 M KOH aqueous solution was used as the electrolyte and current-voltage curves were recorded at a typical scan rate of 50 mV/s (**Figure 5.8**).

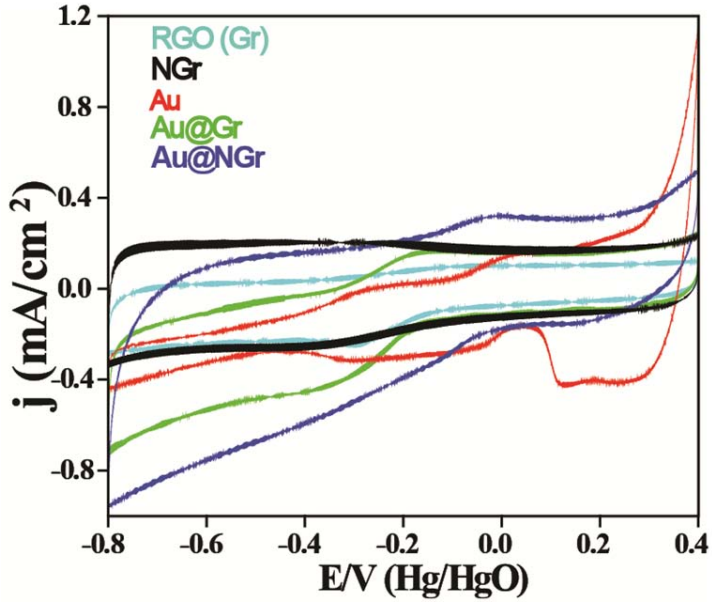

Figure 5.8: *Comparative cyclic voltammograms taken in N_2-saturated 0.1 M KOH electrolyte with a scan rate of 50 mV/s, after 70% iR compensation.*

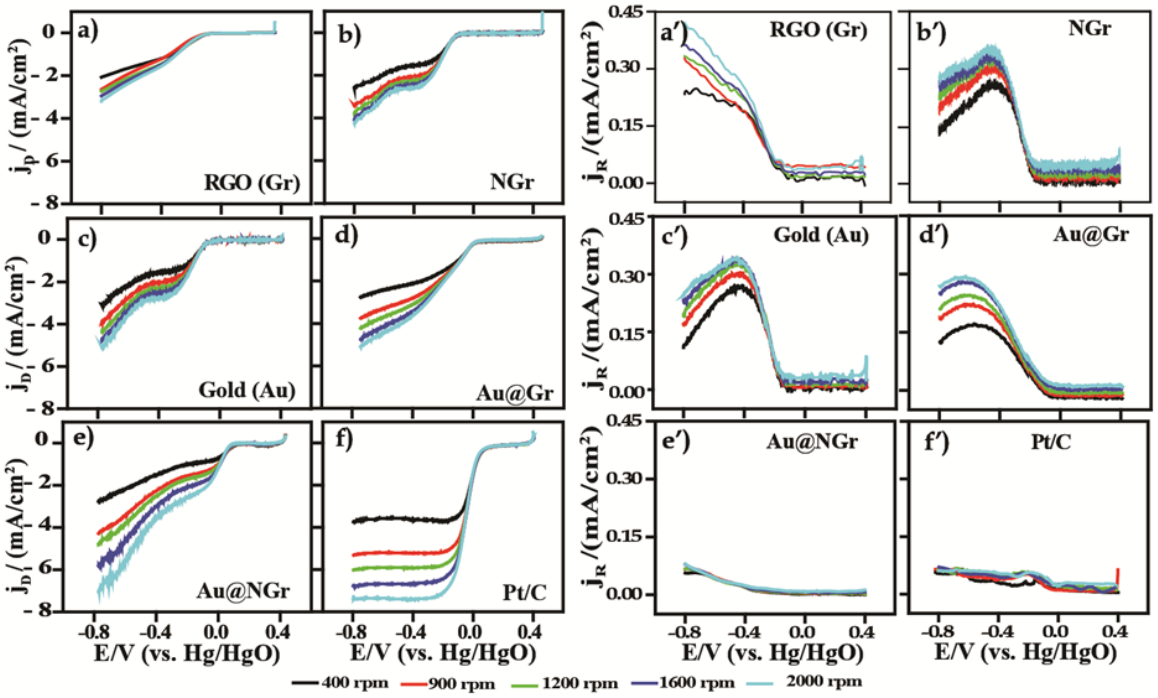

Figure 5.9: *a-f)70% iR compensated hydrodynamic voltammograms of the different prepared samples monitored for ORR. a'-f') current-voltage profile of the as prepared samples by monitoring the reaction occurring at a Pt ring electrode, held at 0.6 V (vs. Hg/HgO) during potential scan with varying rotation speeds of RRDE. Conditions: Scan rate: 10 mV/s; rotation speeds: 400, 900, 1200, 1600, and 2000 rpm; electrolyte: O_2-saturated 0.1 M KOH.*

A catalyst loading of 20 µg on a glassy carbon disk electrode was maintained in all the cases. Accordingly, **Figure 5.8** shows the comparative CV profiles of Gr, NGr, Au, Au@Gr, and Au@NGr taken in an N_2-saturated 0.1 M KOH. Furthermore, the capacitive nature of Au@Gr and Au@NGr as compared to the Au nanoparticles indicates that Au is encapsulated by Gr/NGr (**Figure 5.8**). Moreover, the gold-oxide peak at ~0.1 V (vs. Hg/HgO) is totally absent in the case of Au@Gr and Au@NGr, which also confirms the coverage of Au with Gr/NGr.

A quantitative estimation of the actual kinetics of ORR and H_2O_2 formation is made by recording hydrodynamic voltammograms using a rotating ring disk electrode (RRDE) set-up at a scan rate of 10 mV/s in O_2-saturated electrolyte (**Figure 5.9**). The measurement of the current was done at various electrode rotation speeds of 400, 900, 1200, 1600 and 2000 rpm, by applying a constant ring potential (E_R) of 0.6 V (vs. Hg/HgO). The rotation of the working electrode is expected to minimize the diffusion limitation effect.[35] As shown in **Figure 5.9a-5.9f**, from 400 to 2000 rpm, the potential regions under kinetic and oxygen mass transport limiting control are becoming more prominent and the current density increases.

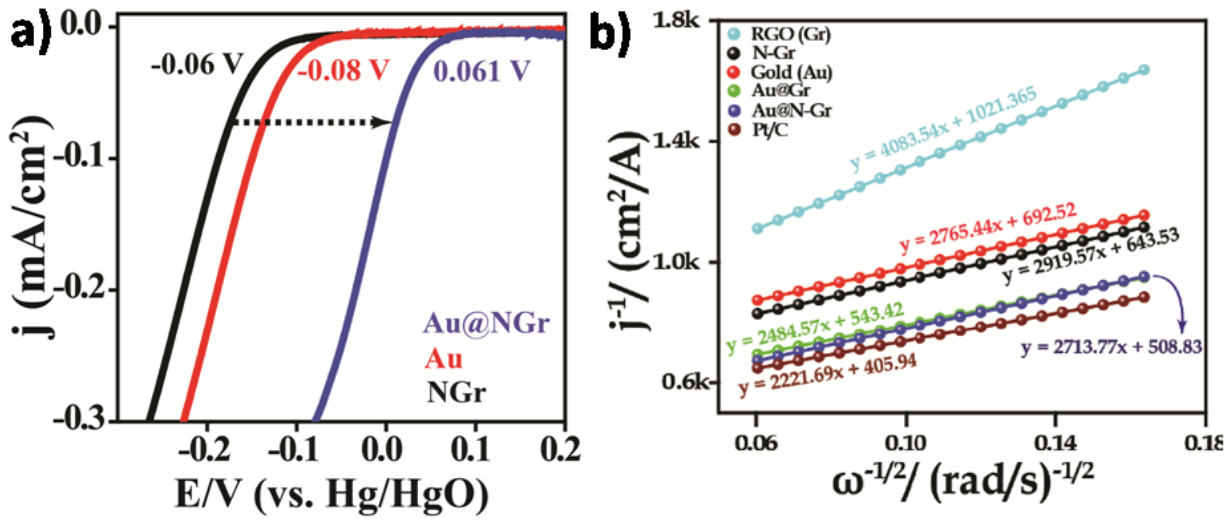

Figure 5.10: *a) Comparative hydrodynamic voltammograms at kinetic region for ORR of Au, NGr and Au@NGr performed in an O_2-saturated 0.1 M KOH solution at 1600 rpm with a scan rate of 10 mV/s and at a constant ring potential (E_R = 0.6 V, vs. Hg/HgO), b) Comparative Koutecky-Levich (K-L) plots at -0.32 V (vs. Hg/HgO) obtained from the iR-free RDE data.*

From the hydrodynamic voltammograms (**Figure 5.9a-5.9f**) and selective comparative graph of Au, NGr and Au@NGr (**Figure 5.10a**) at 1600 rpm indicates the better ORR performance of Au@NGr compared to the separate entities. The onset potential values (vs. Hg/HgO) for ORR are found in the order of Gr (-0.11 V) <NGr (-0.06 V) < Au (-0.08 V) <Au@Gr (0.015 V) <Au@NGr (0.061 V) <Pt/C (0.096 V). Thus, among the prepared samples, Au@NGr is a champion of the race. It is clear that the encapsulation on Au has helped NGr to reduce the overpotential. Even with the commercial Pt/C catalyst, the overpotential is higher by only 35 mV. However, the reduction of O_2 can be accomplished *via* a 4-electron (4e-) pathway leading to H_2O or a 2-electron (2e-) route giving H_2O_2. The later one decreases the cell potential in a PEMFC and accelerates the degradation of membrane and catalyst with the intervention of H_2O_2. Thus, the 4e- pathway is desired in ORR, but it is well documented that carbon based electrocatalysts show high yield of H_2O_2 compared to the Pt based ones.[10, 36-39]

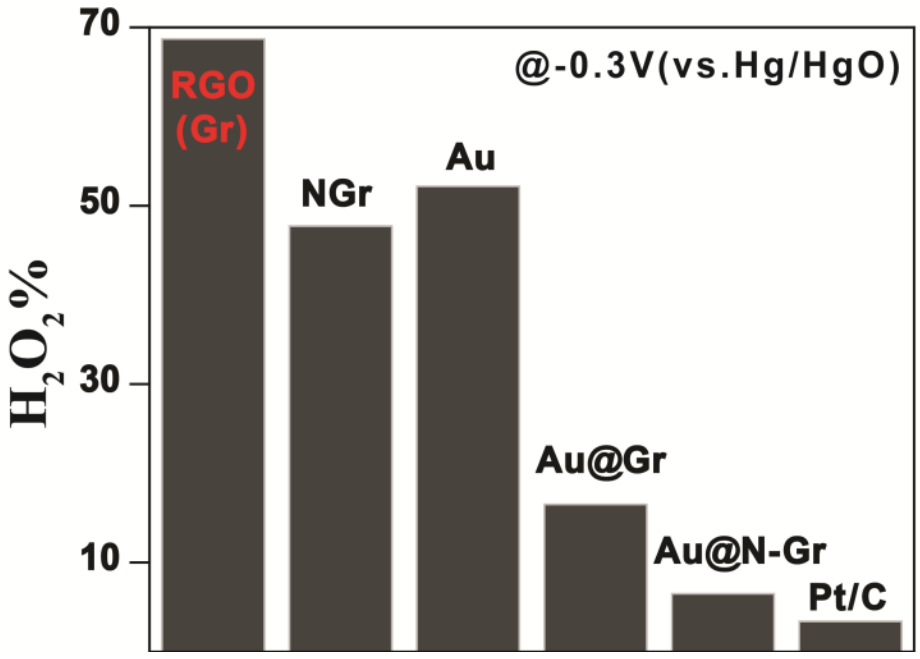

Figure 5.11. *Calculated hydrogen peroxide percentage over the various systems measured at -0.3 V (vs. Hg/HgO).*

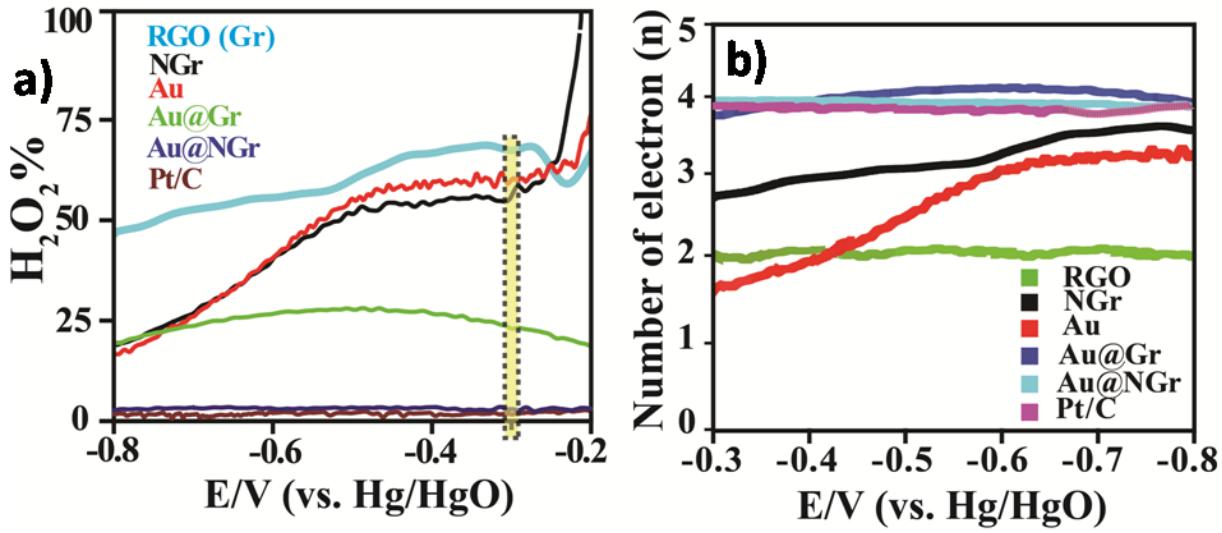

Figure 5.12: *a) Change in H_2O_2 percentage with respect to potential (calculated from the data presented in* ***Figure 5.9****) at 1600 rpm and b) number of electron transferred during the ORR study calculated by using* ***Equation 2.10****.*

To understand the actual mechanism, RRDE investigation was carried out by keeping the ring potential to 0.6 V (vs. Hg/HgO). The electron pathway of the electrocatalysts towards ORR was evaluated by calculating the yield of H_2O_2 by using **Equation 2.9** (details are given in **Chapter 2, Section 2.3.3**).[40]The ring current in **Figure 5.9a'-5.9f'**, which corresponds to the formation of H_2O_2, shows an increase in its yield in the kinetic region and exhibits a gradual increase in the diffusion region (< -0.2 V, vs. Hg/HgO).**Figure 5.12a**shows the change in the H_2O_2 percentage with respect to the potential during the ORR process. At -0.3 V (vs. Hg/HgO), Au@Gr gives a yield of 16.5 % for H_2O_2 which gets reduced to 6.5 % for Au@N-Gr. On the other hand, the H_2O_2 yield of RGO and NGr are 68.7 and 47.7 %, respectively. Moreover, Au itself gives 52.2 % of H_2O_2. This means that when Au is covered with Gr and N-Gr, the H_2O_2 % from Au has come down by 68 and 87 %, respectively (**Figure 5.11**). The enhanced ORR activity and the reduced H_2O_2 yield for Au@NGr is attributed to the favourable push towards the nearly 4e- pathway through the mutual interactions of the metallic core with the non-metallic shell (**Figure 5.12b**).

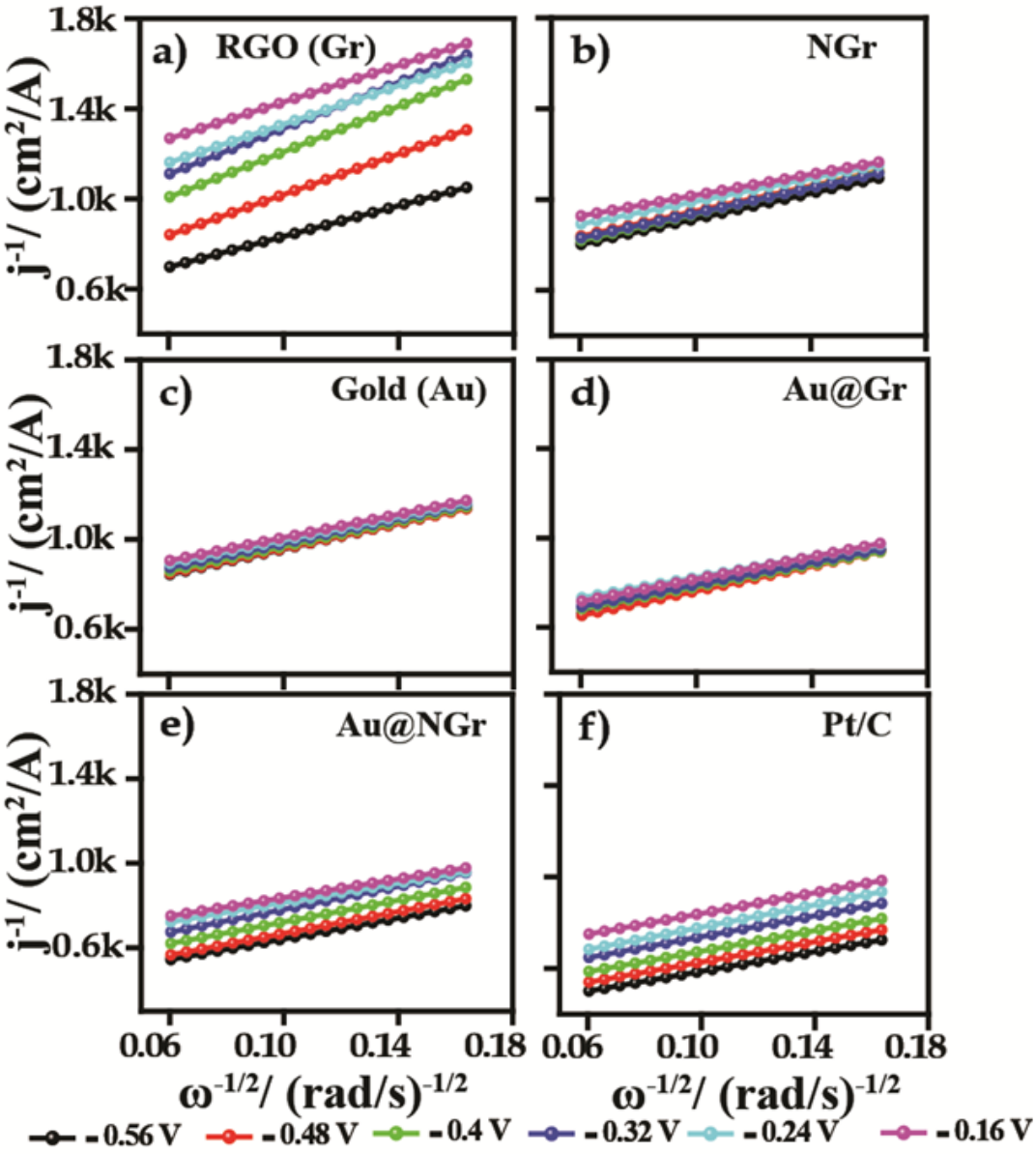

Figure 5.13: *K-L plots of a) RGO (Gr), b) NGr, c) Au, d) Au@Gr, e) Au@NGr, and f) Pt/C at different potentials generated from the iR corrected RDE data of* ***Figure 5.9a-5.9f****.*

Furthermore, to substantiate the obtained results from RRDE, mainly the transferred electron number and its co-relation with the H_2O_2 formation during ORR, we have separately examined the disk current data after iR compensation (70 %). The obtained RDE plots (**Figure 5.9a-5.9f**) have three different regions, namely, diffusion-controlled region (~-0.3 to -0.8 V), mixed diffusion-kinetic limitation region (-0.3 to -0.1 V) and kinetic region or Tafel region (> -

0.1 V). The obtained current (j) is a combination of diffusion-limiting (j_L), film diffusion (j_f) and kinetic (j_k) (detailed explanation with equations is provided **in Chapter 2, Section 2.3.2**).

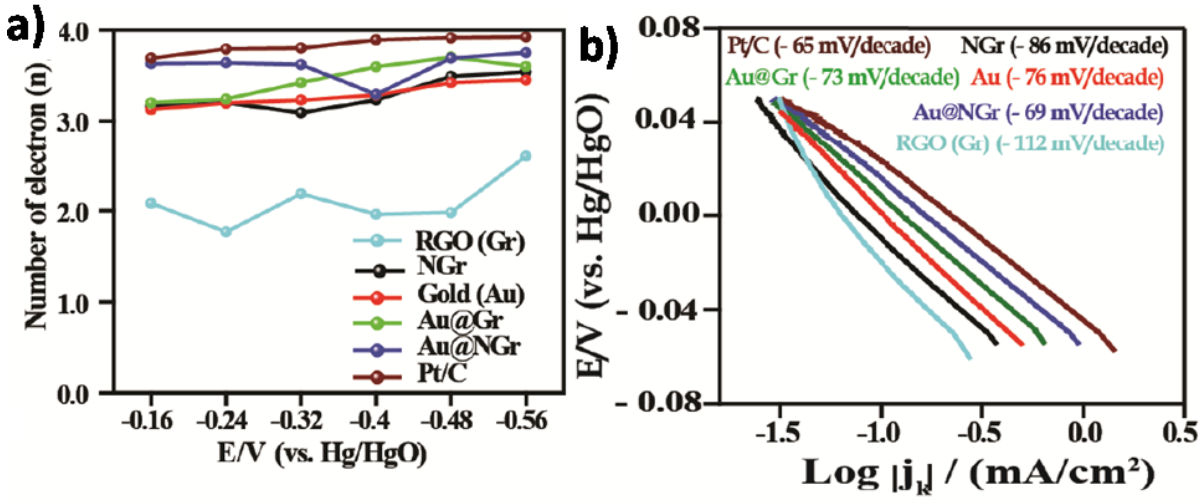

Figure 5.14: *a) Number of electron transferred during ORR at different potentials calculated from the K-L plots, b) comparative mass corrected Tafel plots for ORR obtained from the iR corrected ORR data, at low current density region. The kinetic current density calculated by RDE analysis is used for generating the Tafel plots.*

The total current obtained under various rotating rate is plotted in the form of current density (j^{-1}) versus angular rotation ($\omega^{-1/2}$) and a straight line with good linearity has been obtained in **Figure 5.13**at different potentials. The slopes remain approximately constant over the potential range from -0.16 to -0.56 V (vs. Hg/HgO) for Pt/C, Au@NGr and Au@Gr, which suggest that the electron transfer numbers for ORR at different electrode potentials remain similar in these systems. However, slight deviations in the slopes with potential have been noticed in the case of Au, Gr and NGr, which is in accordance with the RRDE results. Linearity and parallel behaviour of the plots are usually taken as an indication of first-order reaction kinetics with respect to the concentration of dissolved oxygen. Moreover, the comparative K-L plots are shown in **Figure 5.10b**. The number of electron exchanged during ORR for each catalyst has been deduced from the slope of the straight lines. The calculated n values for Pt/C, Au@Gr and Au@NGr fall in the range of ~3.4 to 4, whereas, in case of Gr (RGO), NGr and Au the value ranges from 2.1 to 3.4 (**Figure 5.14a**), which is in well harmony with the results obtained from RRDE. The results thus indicate that Au@Gr and Au@NGr reduce the oxygen

molecule into water, whereas, the n values of Gr (RGO), NGr, and Au are showing that oxygen molecule gets reduced with the formation of higher amounts of H_2O_2 compared to the core-shell structures.

The mass transport corrected Tafel plots (E Vs. log $|j_k|$) are shown in **Figure 5.14b**for the entire synthesized samples alongwith 20 wt. % Pt/C. The measured current values were corrected for diffusion to give kinetic current (j_k) in the mixed activation-diffusion region, as calculated from **Equation 5.3**.[41-42]

$$j_k = j * j_L/(j_L - j) \qquad (5.3)$$

where, $j_L/(j_L-j)$ is the mass transfer correction factor. This equation is valid only for the first order kinetic reactions. TheTafel slopes for Pt/C and Au@NGr are -65 and -69 mV/decade, respectively. However, Gr, NGr, and Au show higher Tafel slope compared to Au@NGr (**Table 5.1**). The Tafel slope is an indication of the actual mechanism on the electrode surface, which can be co-related with the changing nature of the adsorbed O_2 species and its coverage variation with respect to potential. Moreover, the higher Tafel slope of Gr, NGr and Au compared to Au@NGr gives a judgment of decreased ORR rate, which may be due to the insufficient coverage of adsorbed intermediates. In contrast, the core-shell structures show nearly same Tafel slope values, attributed to the similar adsorption mechanism and coverage of the adsorbed species and subsequently its effective reduction.[43]

The mass-transport corrected plots have thus given additional information of improved kinetic current for Au@NGr in comparison to all other synthesized samples. The calculated n value from K-L plots and mass-transport corrected results support the obtained RRDE results. Moreover, the change in the nature of RDE curve for Gr, NGr and Au compared to Pt/C, may be due to the less number of electrons involved during ORR, which is directly reflected from the yield of H_2O_2 and Tafel slopes as well. In contrast to this, the Au@NGr core-shell has shown better activity towards ORR with favourable electron pathway. Overall, the better ORR activity calculated from the *iR* compensated RDE data and reduced H_2O_2 yield for Au@NGr can be attributed to the healthy talk between the core metal with the covered NGr shell. The interaction of the phases through the transfer of electrons from the core to shell due to the π–backbonding effect, further helps to improve oxygen adsorption prior to its reduction.

Table 5.1:*Summary of the electrochemical results.*

	RGO (Gr)	NGr	Gold (Au)	Au@Gr	Au@NGr	Pt/C
Electrical conductivity (S/cm)	**0.5**	**1.48**	**2.09**	**6.03**	**9.41**	**--**
Onset potential (V) (Vs. Hg/HgO)	**-0.11**	**-0.06**	**-0.08**	**0.015**	**0.061**	**0.096**
n values @ -0.32 V, from iR free RDE data	**2.18**	**3.17**	**3.24**	**3.49**	**3.69**	**3.89**
Tafel slope from mass-corrected plots (mV/decade)	**-112**	**-86**	**-76**	**-73**	**-69**	**-65**
H_2O_2 % @-0.3 V (vs. Hg/HgO)	**68.7**	**47.7**	**52.2**	**16.5**	**6.5**	**2.9**

5.4. Conclusion

The synthesis of an efficient core-shell structured electrocatalyst possessing NGr as the shell and Au nanoparticle as the core (Au@NGr) through a simple W/O emulsion technique has been demonstrated successfully. The proposed process involves milder experimental conditions and very easy workups which guarantees the formation of distinct core-shell features of the metal-graphene nanoparticles. The system showed enhanced electrical conductivity and significantly reduced overpotential for ORR compared to NGr and even Au as independent entities. Apart from this, the study revealed the critical role played by a highly conducting metal core, in its low concentration, in influencing the active sites located at the shell layer to shift the reaction kinetics to the favourable ~4e- reduction pathway. Thus, the pertaining issue of the high ohmic drop on the heteroatom doped system could be effectively tackled by adopting this method for synthesizing many more non-noble metal based systems.

5.5. References

[1] K. Sasaki, H. Naohara, Y. Choi, Y. Cai, W.-F. Chen, P. Liu, R. R. Adzic, *Nature Communications***2012**, *3*, 1115.

[2] S. Guo, D. Li, H. Zhu, S. Zhang, N. M. Markovic, V. R. Stamenkovic, S. Sun, *Angewandte Chemie International Edition* **2013**, *52*, 3465-3468.

[3] J. L. Fernández, D. A. Walsh, A. J. Bard, *Journal of the American Chemical Society* **2004**, *127*, 357-365.

[4] C. Xu, Y. Zhang, L. Wang, L. Xu, X. Bian, H. Ma, Y. Ding, *Chemistry of Materials* **2009**, *21*, 3110-3116.

[5] J. L. Fernández, V. Raghuveer, A. Manthiram, A. J. Bard, *Journal of the American Chemical Society* **2005**, *127*, 13100-13101.

[6] W. Chen, S. Chen, *Angewandte Chemie International Edition* **2009**, *48*, 4386-4389.

[7] R. Silva, D. Voiry, M. Chhowalla, T. Asefa, *Journal of the American Chemical Society***2013**, *135*, 7823-7826.

[8] X. Sun, Y. Zhang, P. Song, J. Pan, L. Zhuang, W. Xu, W. Xing, *ACS Catalysis* **2013**, *3*, 1726-1729.

[9] H. Wang, T. Maiyalagan, X. Wang, *ACS Catalysis* **2012**, *2*, 781-794.

[10] L. Zhang, Z. Xia, *The Journal of Physical Chemistry C* **2011**, *115*, 11170-11176.

[11] M. N. Groves, A. S. W. Chan, C. Malardier-Jugroot, M. Jugroot, *Chemical Physics Letters* **2009**, *481*, 214-219.

[12] A. Lherbier, X. Blase, Y.-M. Niquet, F. Triozon, S. Roche, *Physical Review Letters* **2008**, *101*, 036808.

[13] N. Amir, C. H. Mark, S. Tamar, *Nanotechnology* **2013**, *24*, 505715.

[14] M. Deifallah, P. F. McMillan, F. Corà, *The Journal of Physical Chemistry C* **2008**, *112*, 5447-5453.

[15] B. Guo, Q. Liu, E. Chen, H. Zhu, L. Fang, J. R. Gong, *Nano Letters***2010**, *10*, 4975-4980.

[16] D. Wei, Y. Liu, Y. Wang, H. Zhang, L. Huang, G. Yu, *Nano Letters* **2009**, *9*, 1752-1758.

[17] E. Vayner, A. B. Anderson, *The Journal of Physical Chemistry C* **2007**, *111*, 9330-9336.

[18] K. A. Kurak, A. B. Anderson, *The Journal of Physical Chemistry C* **2009**, *113*, 6730-6734.

[19] W. Tang, G. Henkelman, *The Journal of Chemical Physics* **2009**, *130*, 194504.

[20] J. N. Brönsted, *Chemical Reviews (Washington, D.C.)* **1928**, 231.

[21] M. G. Evans, M. Polanyi, *Transactions of the Faraday Society* **1938**, *34*, 11-24.

[22] B. Hammer, J. K. Nørskov, *Chemisorption and Reactivity on Supported Clusters and Thin Film* **1976**, 285.

[23] P. Quaino, N. B. Luque, R. Nazmutdinov, E. Santos, W. Schmickler, *Angewandte Chemie International Edition* **2012**, *51*, 12997-13000.

[24] J. K. Nørskov, T. Bligaard, A. Logadottir, S. Bahn, L. B. Hansen, M. Bollinger, H. Bengaard, B. Hammer, Z. Sljivancanin, M. Mavrikakis, Y. Xu, S. Dahl, C. J. H. Jacobsen, *Journal of Catalysis* **2002**, 275.

[25] T. Bligaard, J. K. Nørskov, S. Dahl, J. Matthiesen, C. H. Christensen, J. Sehested, *Journal of Catalysis* **2004**, *224*, 206.

[26] S. B. Wang, M. S. Hu, S. J. Chang, C. W. Chong, H. C. Han, B. R. Huang, L. C. Chen, K. H. Chen, *Nanoscale* **2012**, *4*, 3660-3664.

[27] P. He, L. R. Faulkner, *Analytical Chemistry* **1986**, *58*, 517-523.

[28] H. Huang, H. Zhang, Z. Ma, Y. Liu, H. Ming, H. Li, Z. Kang, *Nanoscale* **2012**, *4*, 4964-4967.

[29] B. Viswanath, P. Kundu, B. Mukherjee, N. Ravishankar, *Nanotechnology* **2008**, *19*, 195603.

[30] J. G. Radich, P. V. Kamat, *ACS Nano* **2013**, *7*, 5546-5557.

[31] B. Viswanath, P. Kundu, A. Halder, N. Ravishankar, *The Journal of Physical Chemistry C* **2009**, *113*, 16866-16883.

[32] Z.-L. Wang, J.-M. Yan, H.-L. Wang, Y. Ping, Q. Jiang, *Journal of Materials Chemistry A* **2013**, *1*, 12721-12725.

[33] W. Zhang, J. Cui, C. A. Tao, Y. Wu, Z. Li, L. Ma, Y. Wen, G. Li, *Angewandte Chemie* **2009**, *48*, 5864-5868.

[34] G. Wang, J. Yang, J. Park, X. Gou, B. Wang, H. Liu, J. Yao, *The Journal of Physical Chemistry C* **2008**, *112*, 8192-8195.

[35] A. Z. AlZahrani, G. P. Srivastava, *Brazilian Journal of Physics* **2009**, *39*, 694-698.

[36] T. Okada, T. Abe, M. Kaneko, *Springer series in Material Science 111, Spinger-verlag: Berlin* **2009**.

[37] K. Gong, F. Du, Z. Xia, M. Durstock, L. Dai, *Science* **2009**, *323*, 760-764.

[38] R. Liu, D. Wu, X. Feng, K. Mullen, *Angewandte Chemie International Edition***2010**, *49*, 2565-2569.

[39] S. Wang, L. Zhang, Z. Xia, A. Roy, D. W. Chang, J.-B. Baek, L. Dai, *Angewandte Chemie International Edition* **2012**, *51*, 1.

[40] A. J. Bard, L. R. Faulkner, Electrochemical Methods Fundamentals and Applications, 2nd ed.; John Wiley & Sons, Inc.: New York, **2006.**

[41] N. R. Elezović, B. M. Babić, L. Gajić-Krstajić, V. Radmilović, N. V. Krstajić, L. J. Vračar, *Journal of Power Sources* **2010**, *195*, 3961-3968.

[42] S. L. Gojković, S. K. Zečević, R. F. Savinell, *Journal of The Electrochemical Society* **1998**, *145*, 3713-3720.

[43] S. M. Unni, V. M. Dhavale, V. K. Pillai, S. Kurungot, *The Journal of Physical Chemistry C* **2010**, *114*, 14654-14661.

Chapter 6
Pt-Free 3-Dimentional N-doped Graphene Interpenetrated Ni-Nanocages: Efficient and Stable Water-to-Dioxygen Electrocatalyst*

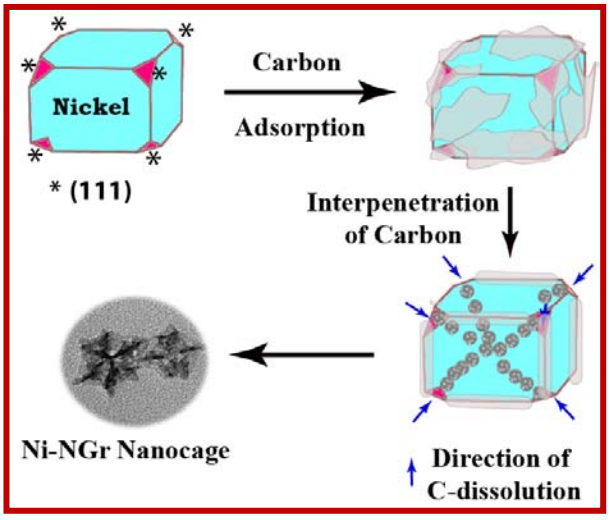

The present chapter describes the solid state chemistry in a nano-regime of W/O emulsion to get the beautiful 3-dimentional (3-D) Pt-free structure for electrochemical water oxidation reaction. Mainly, the synthesis of a nitrogen-doped graphene (NGr) interpenetrated 3-D Ni-nanocage (Ni-NGr) electrocatalyst has been explained. The morphology of Ni-NGr electrocatalyst has been confirmed by using TEM and SEM. Later, the correlation of adsorption of NGr and subsequent interpenetration through the specific surface plane of nickel particles as well as the concomitant interaction of N and C with Ni in the nano-regime has been explored explicitly by using spectroscopic techniques like, XPS, Raman, etc. Apart from the synergistic interactions between Ni, N, and C, the role of overall integrity of the structure and its intra-molecular connectivity within the framework for achieving better oxygen evolution characteristics has been explained. Finally, the quantification of evolved oxygen has been done by gas chromatography.

*The content of this chapter has been published in "***Nanoscale***, 2014, 6, 13179–13187*"

- Reproduced by permission of The Royal Society of Chemistry

http://pubs.rsc.org/en/Content/ArticleLanding/2014/NR/c4nr03578j#!divAbstract

6.1. Introduction

Oxygen evolution reaction (OER) is gaining substantial attention due to its growing importance in several energy conversion and storage devices, such as metal-air batteries, water splitting, etc.[1-2] The water splitting reaction proceeds *via* two half reactions: the anodic OER and the cathodic hydrogen evolution reaction (HER). The anodic oxidation reaction, *i.e.* OER, is more complicated as it involves a four electron oxidation path in which two water molecules get oxidized to form one oxygen molecule.[3-4] Hence, the overall efficiency of electrolytic water splitting is mainly held back due to the higher anodic overpotential of OER. Consequently, development of promising OER electrocatalysts is a challenging task compared to the HER catalysts. The oxides of ruthenium and iridium have been currently considered as optimal electrocatalysts having efficient OER activity. However, even these catalysts operate with overpotential higher than 200 mV at a practical current density of 10 mA/cm^2.[5-7] 10 mA/cm^2 is the current density required to achieve a splitting efficiency of 10 % with one sun illumination for solar-to-fuel conversion.[8] However, the cost and scarcity are the major challenges of these systems, which hamper the prospects of their commercialization. Moreover, efficient OER electrocatalysts have great urge in the field of sustainable energy devices in order to maintain high overall efficiencies of the systems where multiple processes are integrated to meet the efficiency requirements and challenges.[1-2]

A review of literature suggests that multi-metallic structures of Co, Ni, Fe, Ru–Co, and Ir–Ni, have been widely explored for OER.[8] Moreover, the nickel based electrocatalysts (Ni–Co, Ni– Mo, or the spinels like $NiCo_2O_4$, etc.) have been reported as active catalysts for multiple reactions, including OER and ORR in alkaline medium and as better oxidation electrocatalysts for alcohols and amines.[9-11] However, stability is the major concern in the way of the real commercialization of these OER catalysts. Moreover, the inter- and/or intra-metallic interaction within the structure has not been explored. Along with this, the synthesis techniques like sputtering, thermal decomposition, immersion process, etc. make the processes less viable for scale-up.[8, 12-18] In conjunction, the surface passivation, corrosion of metals and supports and degradation of materials lead to performance loss during long-term tests. Recently, Ni based multi-metallic heterostructures (oxides, hydroxides etc.) have been introduced as potential substitutes to the precious metal based electrocatalysts.[8, 12-28] These morphologies reveal

beautiful geometry and they also have high surface area and voids, which pave their use as electrocatalysts in the field of energy devices.[21-28] Unfortunately, the limited-localized electronic interaction of these structures with a support material (carbon) causes carbon corrosion, and eventually the inherent structural properties get disturbed during the long-term tests.[21-28] In addition, the separate N-doped graphene (NGr) or metal decorated NGr/Gr may not be a good solution due to its limited electronic interaction with/within the framework and has low molecular accessibility.[9-11, 29-34] Specifically, Ni, Fe etc. decorated on NGr show the innate carbon interpenetration property.[35-40]

Therefore, systematic control of the reaction parameters during synthesis could be possible to obtain new structured catalysts. In that view, I have tried to utilize the synthetic protocol adopted in **Chapter 5** by changing the metal precursor and reaction parameters to achieve a 3-D hollow structured electrocatalyst for electrocatalytic applications. Hence, dispersing NGr and Ni in an aqueous nanodroplet, and the advantage of the dissolution property of one component into the other trigger the solid-state reaction and eventually lead to the formation of new morphologies with precise control on the size of the particles. I have observed that the reaction between Ni and NGr in nano-droplets leads to the formation of Ni–NGr nanocage structures possessing unique three-dimensional (3D) architecture. The overall structural and electronic modulations acquired by the new morphology help the system to function as an efficient OER catalyst which displays a significantly reduced overpotential for the reaction.

6.2. Experimental Section

6.2.1. Synthesis of Ni-NGr Nanocage Structures

For the synthesis of the Ni-based nanocage structures, a homogeneous mixture of NGr (4 mg) and an aqueous solution of $NiCl_2$ (2 ml, 100 mM) was obtained by sonicating the mixture for 30 min using a Branson bath sonicator. This well dispersed solution was added drop-wise in previously taken fresh silicon oil (25 ml), under strong magnetic stirring (750 rpm) at room temperature. Moreover, the reaction mixture was maintained for 5 h at room temperature for uniform distribution of the emulsion droplets. Furthermore, the W/O emulsion was transferred into a Petri dish, and was kept in an oven at 80 °C for 80 h. The formed Ni-NGr nanocage structures were centrifuged at 10 000 rpm for 15 min and were washed several times with hexane

to remove the silicon oil and the material was dried under a lamp (**Scheme 6.1**). Furthermore, to understand the role of nitrogen, I have prepared a Ni-Gr sample by employing a similar synthetic procedure with RGO (Gr), instead of NGr, and ended with spherical particles (a TEM image is shown in **Figure 6.3**) (detailed synthesis procedures adopted for preparing graphene oxide (GO), reduced graphene oxide (Gr), NGr, Ni-Gr particles, and Ni-nanoparticles are given in **Chapter 2, Section 2.1.7, 2.1.8, 2.1.13** and **2.1.14**, respectively).

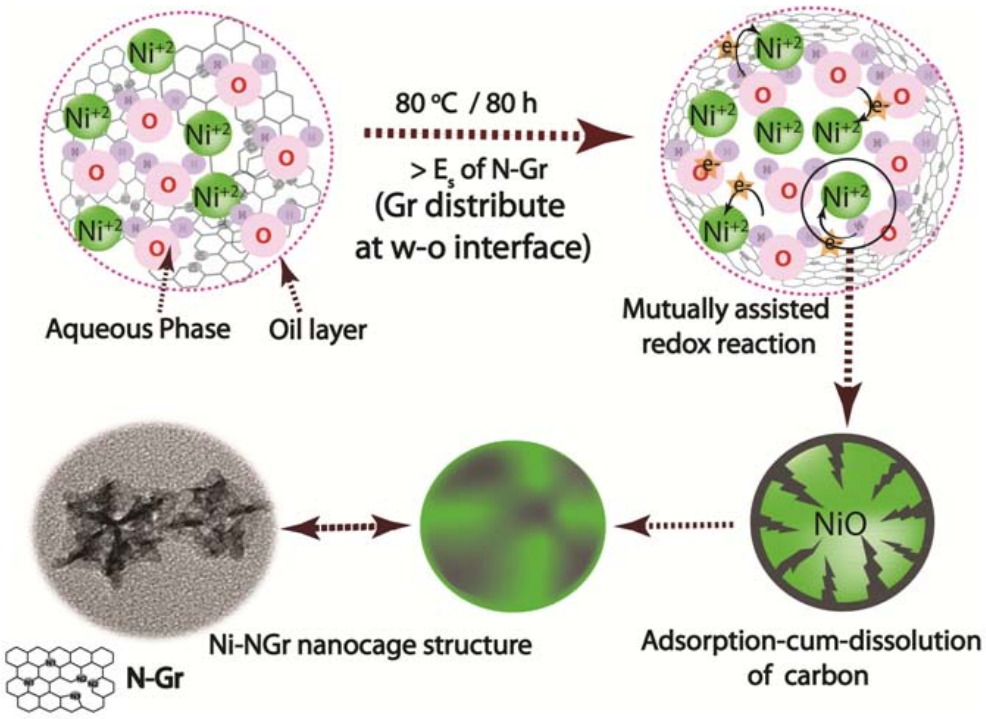

Scheme 6.1: *Schematic illustration for the synthesis of Ni–NGr nanocage particles.*

6.2.2. Gas Chromatography (GC)

Oxygen evolution measurements were performed in a gas closed electrochemical cell assembly having 25 ml capacity. 0.1 M KOH (12 ml) was used as the electrolyte and the catalyst coated glassy carbon electrode (GCE) was used as the working electrode. Along with that, a Pt-flag and Hg/HgO were used as the counter and reference electrodes, respectively. The catalyst slurry was prepared by sonicating 5 mg Ni-NGr in a 1 ml ethanol–water (3:2) mixture. Out of it, 40 µl was drop-coated on the GCE surface (area = 0.19625 cm^2). Furthermore, to investigate the oxygen evolution activity, the chronoamperometry profile was recorded by applying a constant potential of 1.5 V (vs. RHE). The amount of O_2 evolved was determined using a gas

chromatograph (GC) (Agilent Technologies, 7890A). Nitrogen was used as the carrier gas. The data were collected for 1 h with an interval of 15 min (2 cycles). The evolving gas mixture was taken in a 500 µl gas tight syringe and was subsequently injected into the GC.

Calculation:

(1) O_2 (ml) = (peak area × slope × dead volume)/injection volume.

(2) Moles of O_2 per g = [(O_2 (ml)/22400)/weight of the catalyst] × 1000.

6.3. Results and Discussion

6.3.1. Concept of Nanoreactor

During the synthetic process, plenty of aqueous droplets were dispersed in oil, wherein $NiCl_2$ was dissolved and NGr was dispersed. During time bound heating, the water starts evaporating in a nano-sized water droplet. As a result, because of the higher surface area (Es) and flexible nature of NGr, it will tend to distribute at the W/O interface. Finally, the formation of the nanocage is facilitated by the mutually assisted redox reaction of $NiCl_2$ and NGr followed by adsorption and subsequent interpenetration of carbon in nickel particles within the tiny water droplets in the oil phase (**Scheme 6.1**) which acts as the nanoreactors and controls the growth process.

6.3.2. TEM and SEM Analysis

A structural illustration of the Ni–NGr nanocage is carried out by transmission electron microscopy (TEM) (**Figure 6.1**). **Figure 6.1a** and **6.1b** show the well dispersed nanocage structures, with clear dimensions having an average size of ~20 nm ± 2 nm, with cubical and hexagonal structures. The ends of the Ni-arms seem to be connected through the metal oxide layer, which is clearly observed in **Figure 6.1a** and **6.1b**. The presence of Ni-oxide has been confirmed by XPS, as explained in **Section 6.3.5**. HR-TEM and dark field images of Ni–NGr nanocages are presented in **Figure 6.1c** and **Figure 6.2**, respectively. The separately calculated d-spacing values of each side from the lattice fringe profile of Ni-NGr (**Figure 6.1d–6.1f**) are in the range of 0.23-0.28 nm, which is attributed to the carbon interpenetration (dissolution) in the nickel lattice. The dark-field image (**Figure 6.3**) of Ni-NGr nanocages clearly indicates the difference in Z-contrast, the white shiny part could be due to Ni, and the surrounding low

contrast may be because of the combined effect of nickel oxide and/or adsorbed carbon.[41] Furthermore, as mentioned in **Section 6.2.1**, to understand the role of nitrogen, Ni–Gr sample is also prepared. The morphology of Ni-Gr has been found to be spherical in nature with approximate size around 10-15 nm (**Figure 6.3**).

The well distribution of C, O, N and Ni in a Ni-NGr nanocage structure was observed by SEM elemental mapping (**Figure 6.1**). The **Figure 6.1g** provides the SEM image of Ni-NGr at 500 nm. Moreover, SEM mapping of Ni-NGr nanocage structure shown in **Figure 6.1g** for carbon, oxygen and Ni elements has been done and the images are provided in **Figure 6.1h-6.1j**, respectively. The elemental mapping indicates the better distribution of C, O and Ni in Ni-NGr.

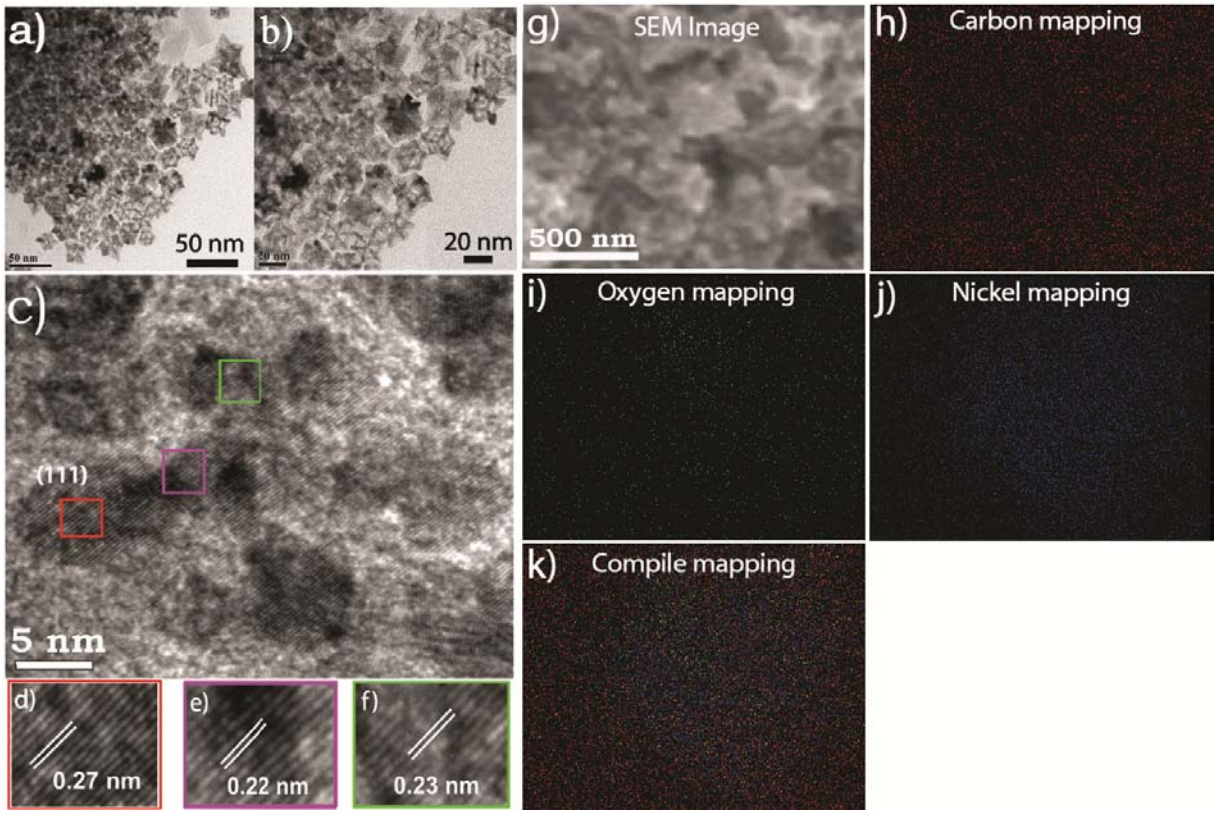

Figure 6.1: *TEM images of Ni–NGr nanocage structures: (a–b) solution dispersed at lower and higher magnifications, respectively, (c) HR-TEM image with lattice fringes, (d–f) lattice constant of the particular selected areas of (c), g) SEM image of Ni-NGr and h-k) SEM elemental mapping of Ni-NGr.*

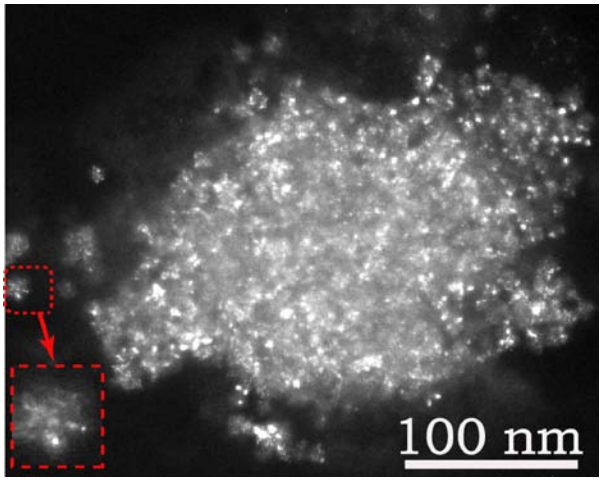

Figure 6.2: *Dark field image of Ni-NGr. Inset shows the magnified image of a single Ni-NGr nanocage structure.*

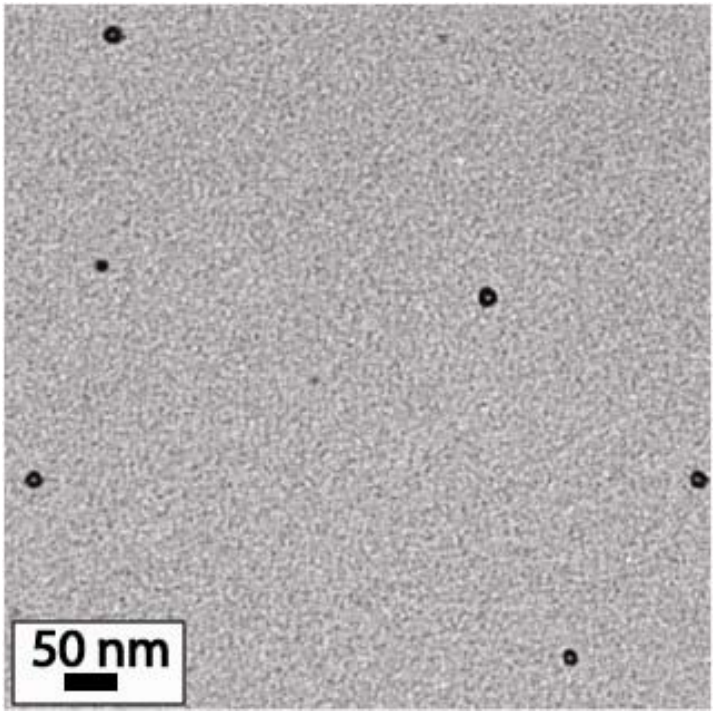

Figure 6.3: *TEM image of Ni-Gr showing the formation of spherical particles rather than nanocages. Particle size is around 20-25 nm. This gives a clear idea of the important role played by nitrogen during the Ni-NGr nanocage synthesis.*

6.3.3. XRD Analysis

The characteristic diffraction peaks in the X-ray diffraction (XRD) pattern give an idea about the presence of Ni-oxide and Ni-carbide (**Figure 6.4**) in Ni–NGr. **Figure 6.4** shows

comparative X-ray diffraction (XRD) patterns of graphite, Gr, NGr, $NiCl_2$ and Ni-NGr. The peak obtained at a 2θ of ~25° is attributed to the graphitic reflection of the (002) plane which is found to be shifted in the case of NGr and even for Ni-NGr, by approximately 0.5° and 0.6°, respectively. This peak shift can be directly correlated with the d-spacing values, which clearly indicates the lattice expansion in the case of Ni-NGr compared to the rest. This also could be taken as indirect evidence of the N-doping in the graphene framework.[42-43] The characteristic peaks of the oxide and carbides are marked in the XRD pattern of Ni-NGr.

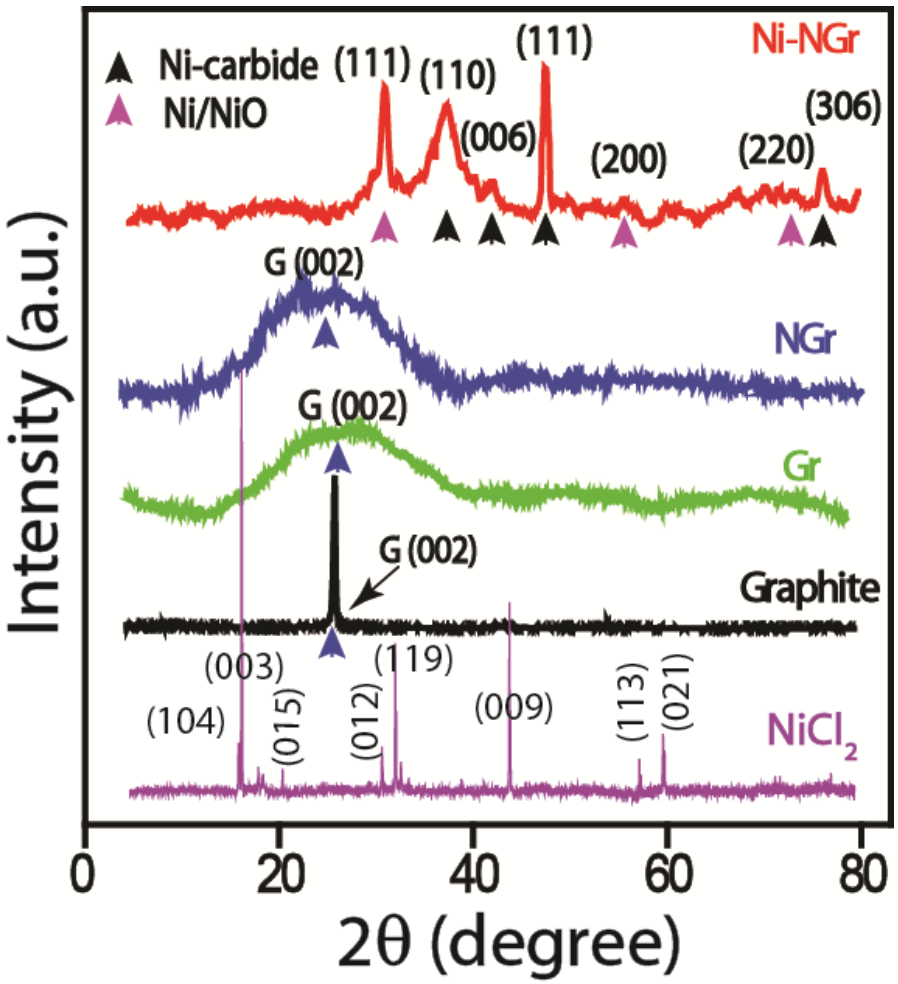

Figure 6.4: *Comparative XRD patterns of $NiCl_2$, graphite, Gr, NGr, and Ni–NGr.*

6.3.4. Raman Analysis

Comparative Raman spectra of $NiCl_2$, RGO (Gr), NGr, Ni–NGr, and a physical mixture of $NiCl_2$ and NGr ($NiCl_2$+NGr) are provided in **Figure 6.5**. In general, the Stokes phonon energy

shift caused by laser excitation creates the main two peaks at nearly ~1320 and ~1596 cm^{-1}, which could be assigned to the defective (D-band) and graphitic (G-band) nature of the carbon.[44-45] In the present case, a substantial shift in the positions of the G and D bands was observed in the case of both Ni-NGr and NGr. The peaks appearing at a lower wavenumber in the case of $NiCl_2$, $NiCl_2$+NGr and Ni-NGr could be attributed to the transverse and longitudinal optical (TO and LO, respectively) phonon modes of Ni.[46-47] However, the 6 cm^{-1} shift in the graphitic peak of NGr (1590 cm^{-1}) compared to RGO (Gr) (1596 cm^{-1}) indicates the effective nitrogen doping in the graphene framework.

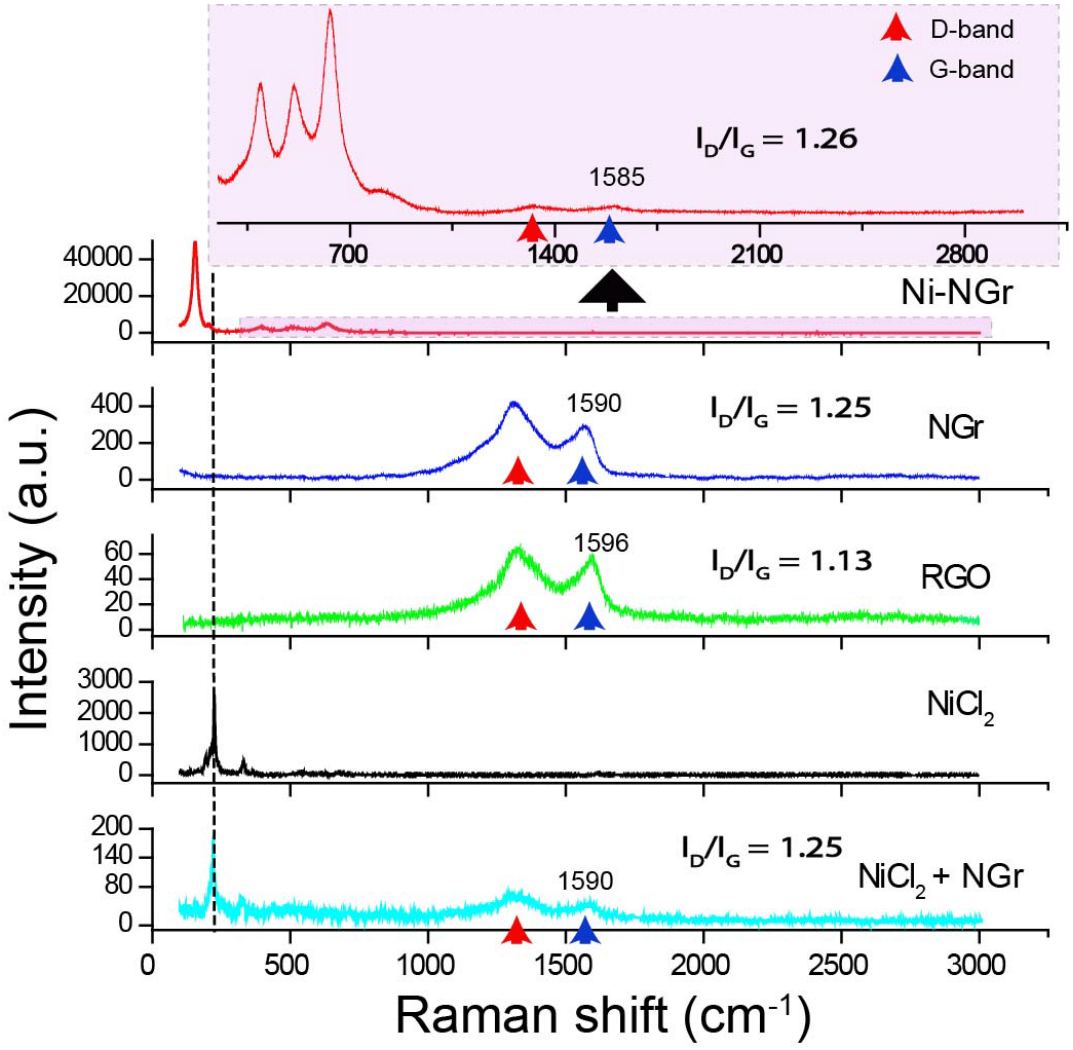

Figure 6.5: *Comparative Raman spectra of RGO (Gr), NGr, $NiCl_2$, Ni-NGr, and physically mixed $NiCl_2$ and NGr ($NiCl_2$+NGr).*

Furthermore, the same peak is again shifted to a lower wavenumber by 5 cm^{-1} for Ni-NGr (1585 cm^{-1}) compared to NGr alone, which could be due to the charge transfer between the Ni and NGr. Conversely, this also could be accounted for the interaction of the Ni-N/C/O in Ni-NGr[44-45] (confirmed by XPS, explained in **Section 6.3.5**). In parallel, the calculated I_D/I_G ratio is found to be in the order of RGO (Gr) (1.13) < NGr (1.25) < Ni-NGr (1.26). The NGr interpenetrated Ni, *i.e.* Ni-NGr, showed more defects than NGr, which could be attributed to the formation of nickel carbide and/or the Ni-N bond which changes the structural and electronic configuration of NGr in Ni-NGr. This type of interaction of Ni with carbon and formation of Ni-carbide has already been reported by John Thong *et al.*[44] On the other hand, the oxygen functional groups present at the edges of the graphene sheets will interact with the Ni-ions and will lead to the oxidation at the particular site, which can eventually facilitate the rupturing and/or cutting of the graphene sheets. This also could increase the number of defects in graphene. [44-45] Moreover, the Raman spectrum of Ni-NGr has shown multiple peaks at 395.5, 508.7, 632.93, and 805.9 cm^{-1}, which are assigned to the TO, LO, 2TO, and TO + LO phonon modes, respectively.[46-47] Subsequently, the shift in the peaks at the lower wavenumber substantiates the charge transfer between the Ni and N and/or C in Ni-NGr.

6.3.5. XPS Analysis

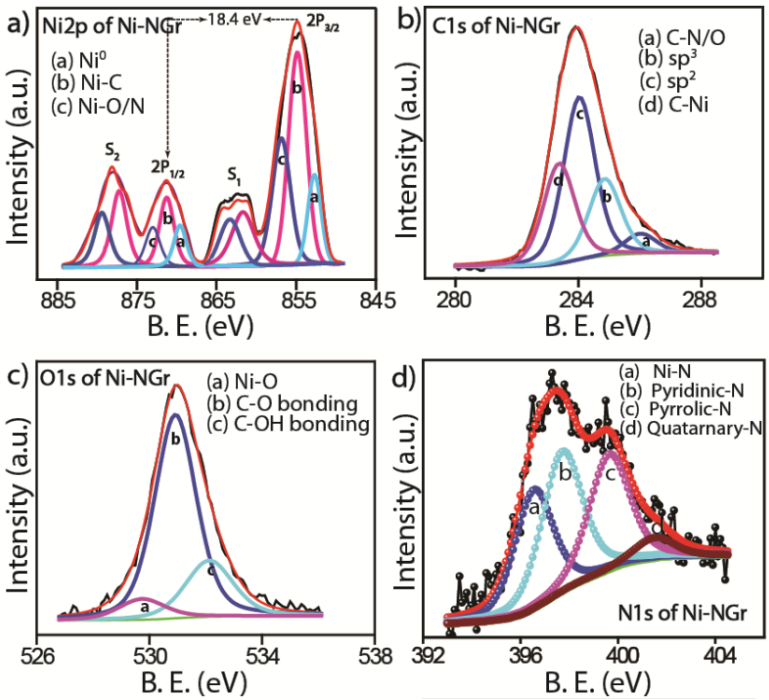

Figure 6.6: *Deconvoluted XPS of a) Ni 2p, b) C1s, c) O 1s and d) N 1s of the Ni-NGr nanocage structure.*

Furthermore, the XPS also gives additional proof of formation of the nickel-carbon bond, evidenced by the characteristic peak of Ni-C bonding at ~283.5 eV in C 1s spectra (**Figure 6.6b**) of Ni-NGr.[48-49] Along with this, the XPS of Ni 2p and O 1s of Ni-NGr are provided in **Figure 6.6a** and **Figure 6.6c**, respectively. The Ni 2p spectra show two peaks, one at 855.9 and another at 874.5 eV of $2p_{3/2}$ and $2p_{1/2}$, respectively, along with their corresponding satellite (S_1 and S_2) peaks. Moreover, the difference between the Ni $2p_{3/2}$ and Ni $2p_{1/2}$ peaks is found to be 18.4 eV and the occurrence of the satellite peaks is attributed to the presence of oxide/carbide of nickel in the Ni-NGr system.[48-49] On the other hand, the higher binding energy shift (~4–6 eV) of Ni $2p_{3/2}$ and $2p_{1/2}$ of Ni-NGr compared to that of $NiCl_2$ (**Figure 6.7d**) is attributed to the change in the electronic configuration of Ni present in Ni-NGr, which substantiates the interaction between the Ni and N/C/O.[48-49]

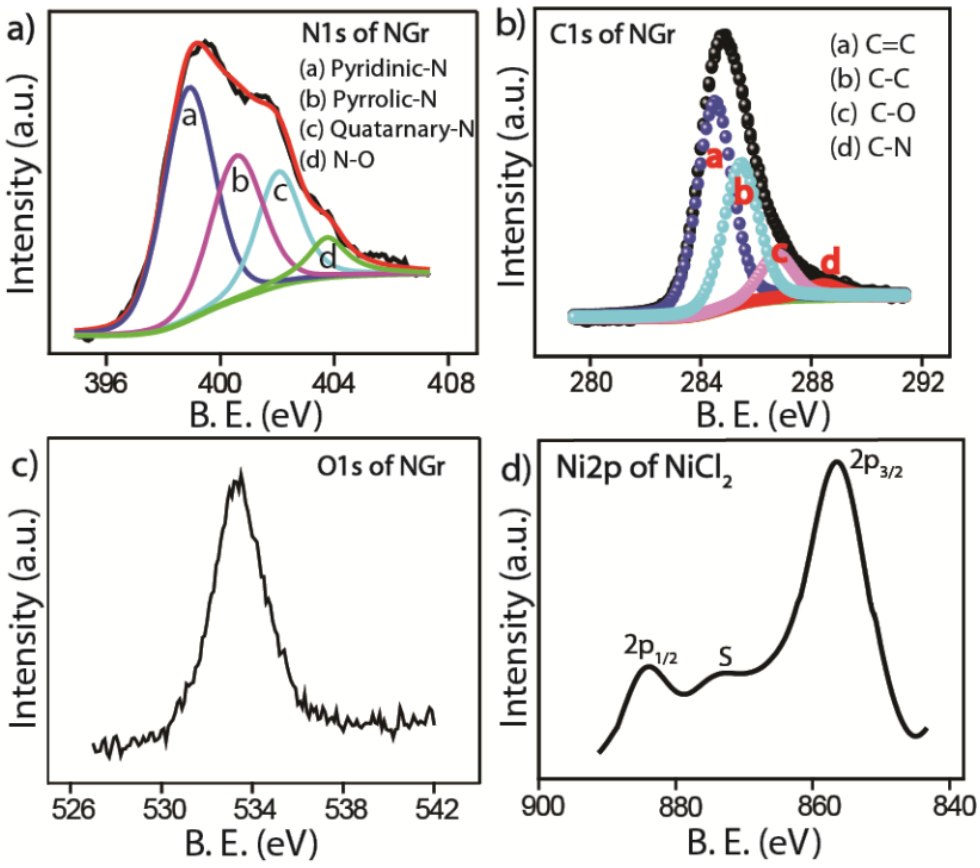

Figure 6.7: *XPS of a) N 1s, b) C1s, c) O 1s of NGr and d) XPS of Ni 2p of $NiCl_2$ precursor used for the synthesis of Ni-NGr.*

For comparison, XPS spectra of N1s, C1s, and O1s of NGr are provided in **Figure 6.7a-6.7c**, respectively. More importantly, the number of defective sites seemed to be more as observed in C1s of NGr (**Figure 6.7b**) compared to Ni-NGr (**Figure 6.6b**). However, the Raman investigation highlights a slight variation in the I_D/I_G ratio (**Section 6.3.4**). Overall, the defects in NGr are due to the combined effects of functional groups, N-doping and change in the bond length after the N-doping. Conversely, in the case of Ni-NGr, the carbon is in coordination with the Ni and N (which has been confirmed by XPS, **Figure 6.6**). Therefore, only the type of the defect is changed in Ni-NGr compared to NGr. Similarly, the presence of a low binding energy peak (< 398 eV) in N1s of Ni-NGr (**Figure 6.6d**) also gives the evidence of the interaction between the N and Ni.

6.3.6. Mechanism of Formation of Ni-NGr Nanocage Structure

More importantly, to understand the exact mechanism of the formation of Ni-NGr nanocage structures, a similar synthetic protocol using Gr instead of NGr was followed and ended up with spherical particles (**Figure 6.3**). This means that the presence of nitrogen has a crucial role in the formation of the Ni-NGr nanocage structure. Moreover, nickel has higher carbon solubility and also, it forms ordered surface carbide.[35-40] In fact, during the entire synthesis process, the carbon of the NGr gets adsorbed on the *in situ* formed nickel nanoparticles, because of the dominance of van der Waals forces (Ev) between the NGr layers compared to the gravitational potential energy of metal nanoparticles and the surface energy of NGr. The dominating role played by the van der Waals interaction in forming the graphene based core-shell structure has already been reported by Kang *et al*.[50] Consequently, the presence of nitrogen may increase Ev of the NGr layer as well as the pressure built by the water vapors in the oil phase leads to controlled and/or enhanced interpenetration (dissolution/diffusion) of the carbon in the nickel crystal structure. Besides, the nitrogen in NGr has a lone pair of electrons which could act as a source of electrons (higher electron density) and may be donated to the Ni^{2+} with its eventual reduction.[50-55] On the other hand, NGr will undergo self-oxidation, which is termed here as a "mutually assisted redox reaction". [50-55] Therefore, the interaction between the nitrogen of NGr and Ni^{2+} may assist the easy carbon dissolution in the Ni-matrix.[44-45], [50-55] In general, the carbon dissolution/diffusion in a metal takes place at higher temperatures. However, in our case, the presence of a hetero-atom and interfacial tension at the water-oil interface is

expected to reduce the activation barrier for the carbon dissolution/diffusion. This could be the reason for obtaining the nickel nanocage structures at a relatively low temperature. In conjunction, I tried to correlate the present situation with the surface plane energy of nickel for the adsorption followed by interpenetration properties of the adsorbed entities (like carbon). Essentially, during actual formation of the nanocage structure, atoms of adsorbed entities (*i.e.* carbon) move into the lattice sites of nickel, effectively causing position switching between them.[41, 56-57] During high scale diffusion, there will be a flux of atoms (carbon) in one direction and a flux of vacancies (created due to the reaction of three/four Ni atoms with one C-atom) in the other, which may be depending on the surface energy of the crystal plane of the substrate (nickel).[35-41,56-57] Furthermore, based on the literature reports, the surface plane energy and adsorption-cum interpenetration of carbon in nickel are in the order of Ni (111) > Ni (110) > Ni (100) (**Table 6.1**).[58]

Table 6.1: *Desorption energy per carbon atom (E_{des}) and activation energy (ΔE_a) for carbon diffusion of nickel surface.*[58]

Surface plane	**Surface energy (J/m^2)**	**Desorption energy (E_{des}) in eV**	**Activation energy (ΔE_a) in eV**
111	2.02	6.28	~0.4
100	2.23	7.61	~2.1
110	2.29	6.76	~0.4
311	**2.31**		

Hence, more carbon interpenetration, *i.e.* dissolution/diffusion, may take place in the mentioned order of the Ni crystal plane and the flux of vacancies (vacancies created due to formation of Ni_3C or Ni_4C) in the other direction. This kind of phenomenon has already been explained by Gu *et al.* for Mn–Zn ferrite structures and by Li *et al*. for constructing a Au island on the Pt-Ni nanoframe as a tri-metallic nanoframe catalyst.[56-57,41] In addition, the presence of nitrogen may help in minimizing the activation barrier for the adsorption of carbon and subsequent interpenetration in the nickel matrix[59-60] which resulted into a fancy, high surface area, highly active 3D Ni-NGr nanocage structure for OER. The engineered Ni-NGr nanocage shows the well

ordered inter-connected atomic arrangement and wide-directional electronic interaction within the structure (which could be clearly observed in TEM, shown in **Figure 6.1**), which may help in improving the overall structural integrity during actual performance investigation. Moreover, it also improves the tolerance towards oxidizing conditions during the real applications.[61-62]

6.3.7. Electrochemical Study

To evaluate the electrochemical activity of the synthesized Ni-NGr electrocatalyst for water oxidation, experiments with cyclic voltammetry (CV) and linear sweep voltammetry (LSV) have been carried out in aqueous 0.1 M KOH solution. The CV is scanned in a potential window of 0.7 to 1.7 V (vs. RHE). Ni-NGr has shown the characteristic property of oxygen evolution with lower overpotential. **Figure 6.8** shows the comparative CV of NGr and Ni-NGr performed in N_2-saturated 0.1 M KOH.

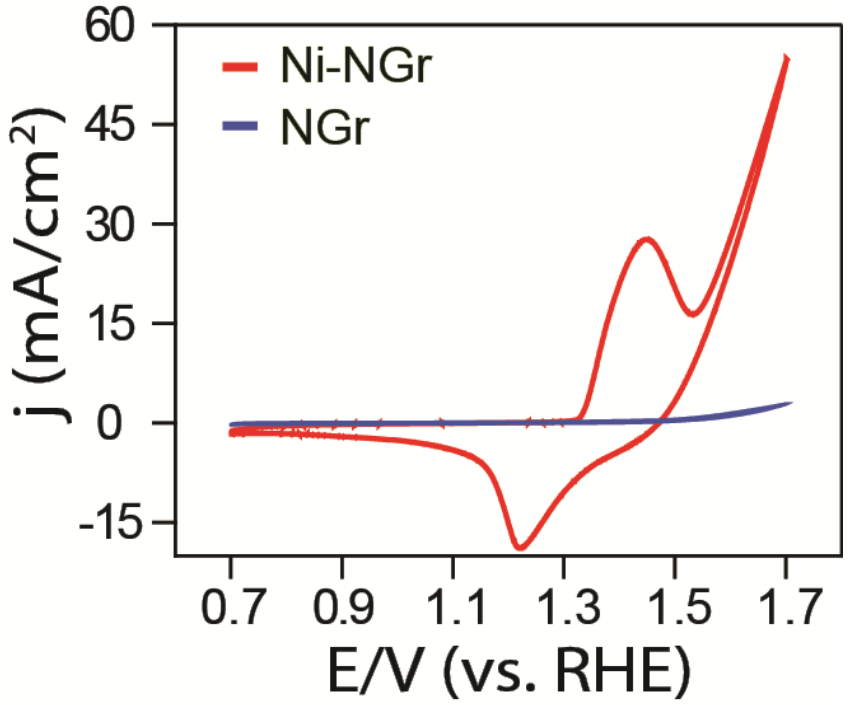

Figure 6.8: *Comparative CV of NGr and Ni-NGr. Conditions: electrolyte: 0.1 M KOH, scan rate: 50 mV/s, potential window: 0.7 to 1.7 V (vs. RHE).*

The peak at ~1.42 V during the anodic scan is the characteristic oxidation peak of the active Ni-center, which is followed by a sharp augment in current due to the oxygen evolution (**Figure 6.8 and 6.9b**). [12-18] The probable mechanism of OER on the Ni-active center (A) is given in **Figure**

6.9a. In brief, the active center (A) will form hydroxide (A-OH), followed by chemical association between OH_{ads} and OH^-, with the reaction involving two electrochemical steps, *viz.* OH^- discharge and O^-_{ads} discharge, which finally leads to the evolution of oxygen.

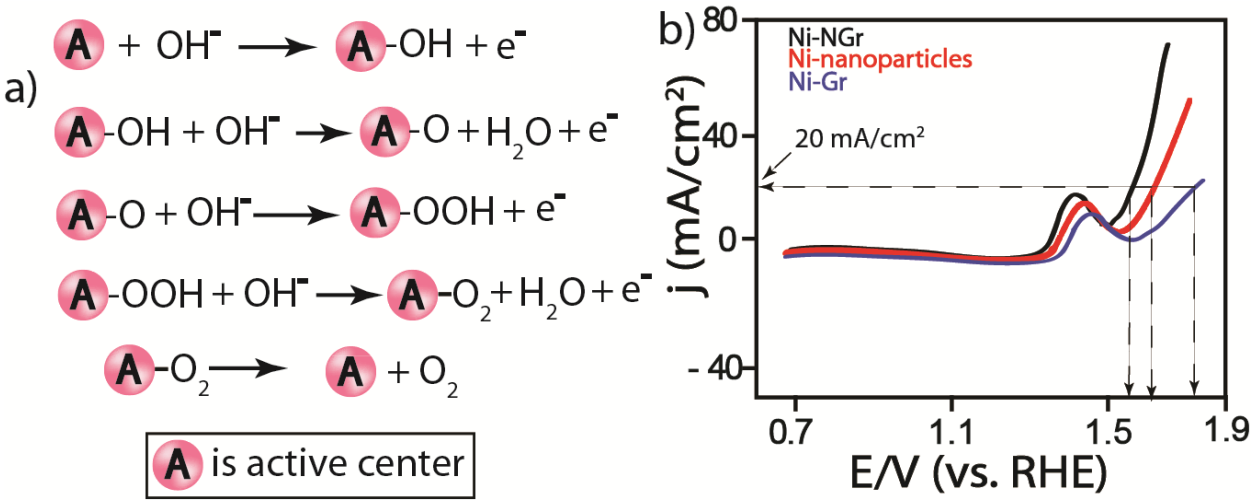

Figure 6.9: *a) Mechanism of OER in alkaline medium and b) comparative LSV of Nickel nanoparticles, Ni-Gr, and Ni-NGr recorded in N_2-saturated 0.1M KOH at 1600 rpm. The calculated overpotential at 20 mA/cm^2 for Ni-nanoparticles, Ni-Gr and Ni-NGr is ~370, 570, and 290 mV. The OER current is seem to be in the order of Ni-NGr > Ni-nanoparticles > Ni-Gr.*

The electrochemical surface active area (ESCA) was deduced from the electrochemical double layer capacitance (C_{dl}) of the catalytically active surface.[63] The calculation of C_{dl} is done by measuring the non-Faradaic capacitive current associated with double layer charging by merely recording the scan rate dependent CV as shown in **Figure 6.10a and 6.10c**.[63-64] To obtain the double layer charging from CV, at first, the potential window corresponding to the non-Faradaic contribution is determined from static CV. Principally, this potential window will be of ~0.1 V, centered at the open circuit potential (OCP) of the system. The CV of the Ni-NGr electrocatalyst in the non-Faradaic potential window is displayed in **Figure 6.10a**, and the C_{dl} is calculated using **Equation 6.1**.

$$i = \upsilon\, C_{dl} \qquad (6.1)$$

where '*i*' is the measured cathodic/anodic current and 'υ' is the scan rate. The plot of *i* vs. υ gives a straight line with C_{dl} as a slope (**Figure 6.10b**). The obtained C_{dl} is 0.1985 mF for Ni-NGr.

Moreover, the ratio of C_{dl} to the specific capacitance (C_s) will directly give the ESCA, and it is found to be 7.26 cm^2 for Ni-NGr (the used Cs value is 27 $\mu F/cm^2$).

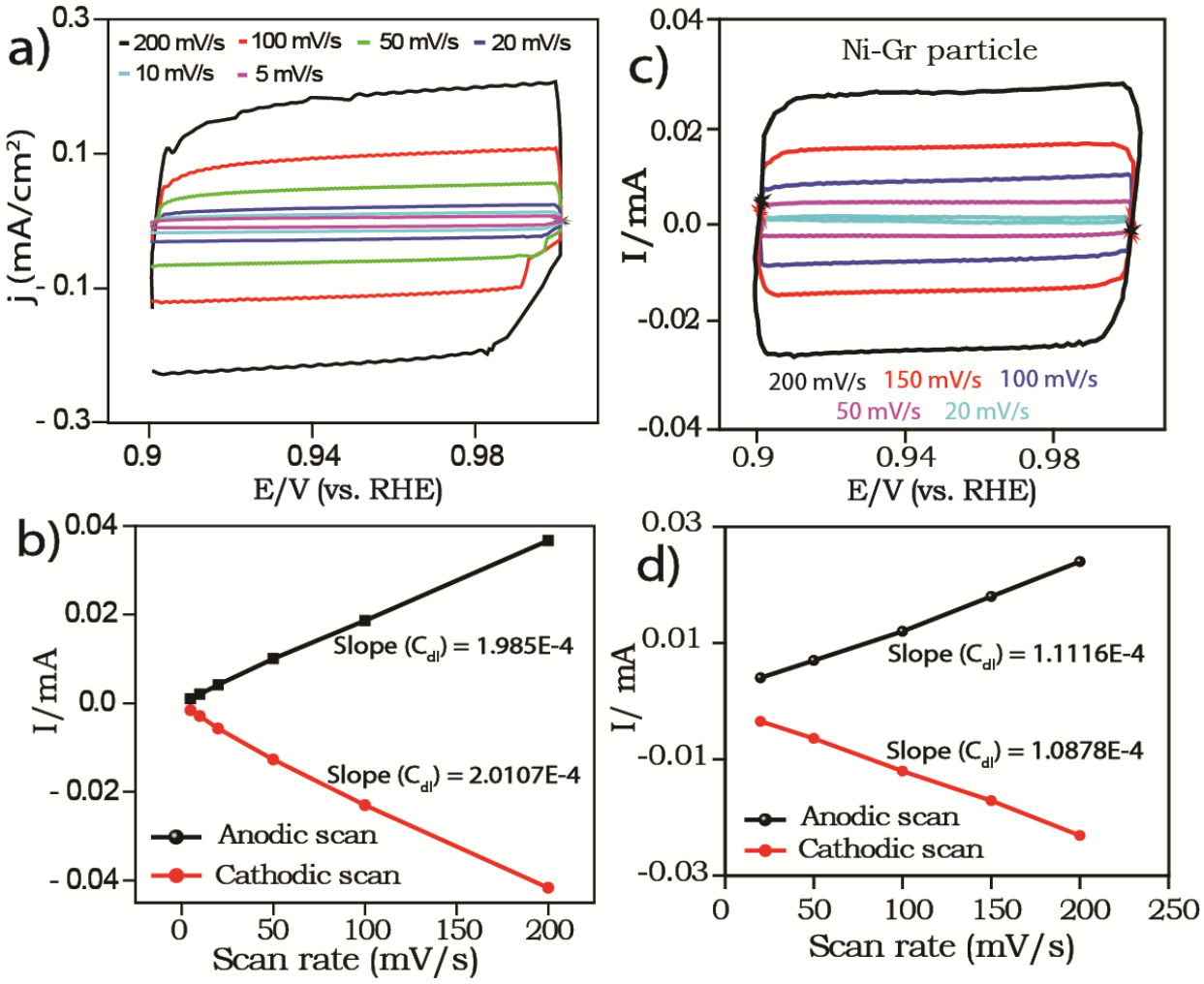

Figure 6.10: *Cyclic voltammograms performed in the non-Faradaic potential window (0.9 to 1 V (vs. RHE)) at varying scan rates in a nitrogen saturated 0.1 M KOH electrolyte of (a) Ni-NGr, (c) Ni-Gr and (b and d) plot of anodic and cathodic current vs. scan rate at 0.95 V (vs. RHE) of (a), and (c), respectively.*

As per the literature, the typical C_s values reported for metals in alkaline medium are in the range of 22-130 $\mu F/cm^2$,[34, 65-76] and for the Ni-based electrocatalysts they fall in the range of 23-28 $\mu F/cm^2$ (**Table 6.2**).[34, 65-76] C_s is the capacitance of an atomically smooth planar surface of the material per unit area under the similar electrolyte conditions. Moreover, the roughness factor (RF) is obtained by taking the ratio of ESCA to the geometrical surface area of the electrode

(0.19625 cm^2), and is found to be 36 ± 3. Furthermore, to investigate the importance of the nanocage structure and chemical combination, ESCA and RF of the Ni-Gr particles were determined using a similar method. Ni-Gr showed the ESCA and RF values of 4.11 cm^2 and 20.9, respectively (**Figure 6.10c and 6.10d**).

Table 6.2: *Reported specific capacitance (C_S) for Ni-based materials and platinum in alkaline medium.*

Ni-based electrocatalyst	Electrolyte concentration	C_s (mF/cm^2)	Reference
Ni	1 M NaOH	0.03	[73]
Ni	0.5 M KOH	0.04	[55]
Ni	31% KOH	0.03	[72]
Ni	4 N KOH	0.022	[68-69]
Ni-Co	1 M NaOH	0.026	[34]
Pt	1M KOH	0.028	[75]
Pt/C	1M KOH	0.03	[76]

The 1.7 order improved ESCA and RF of Ni-NGr nanocages compared to Ni-Gr particles is mainly credited to their 3D morphology with controlled chemical composition, higher molecular accessible space, higher surface-to-volume ratio and more number of active sites. Importantly, it is just to be noted that the calculated ESCA and RF are the precision average values of three independent measurements with standard deviations of 0.03 and 1.73, respectively. These measurements are a sign of precision of the measurements and not obligatorily meticulous to the obtained ESCA and RF. The estimated values must be considered only for comparing the surface roughness. LSVs of NGr and Ni-NGr were recorded to monitor the anodic reaction by scanning in a potential window of 0.7 to 1.9 V and 0.7 to 1.7 V (vs. RHE), respectively. The onset potential is found to be 1.7 V (**Figure 6.12**) and 1.5 V (**Figure 6.11a and 6.9b**) (vs. RHE) for NGr and Ni-NGr, respectively. The overpotential calculated at 20 mA/cm^2 for the Ni-NGr nanocage is found to be ~290 mV, which is even less compared to the literature data of the Ni-based electrocatalysts (~400 mV)[8] which are reported at a lower current density of 10 mA/cm^2

(tabulated in **Table 6.3**). In short, the reported Ni-based electrocatalysts might give 10% efficiency for water splitting with one sun illumination to convert solar energy to fuel; conversely, double efficiency could be obtained from Ni-NGr even at a lower overpotential.[8]

Table 6.3: *Reported overpotential values for Ni-based electrocatalysts.*[8]

Electrocatalyst	Electrolyte concentration and catalyst synthesis method	Overpotential (mV)	Reference
NiO_x	1 M NaOH (Electrochemical deposition on Ni substrate and reported at 16 mA/cm^2)	420	[77]
$NiCeO_x$	1 M NaOH (Electrochemical deposition on Ni substrate and reported at 16 mA/cm^2)	280 mV	[77]
$NiCoO_x$	5 M KOH (Electrochemical deposited on Cu substrate and reported at 10 mA/cm^2)	400 mV	[78]
$NiCuO_x$	1 M NaOH (Electrochemical deposited onto Ni substrate and reported at 100 mA/cm^2 and 80^{0}C)	420 mV	[79]
$NiFeO_x$	1 M NaOH (Electrochemical deposited onto Pt and reported at 100 mA/cm^2)	290 mV	[80]
$NiFe_2O_4$	1M KOH (Hard template method and reported at 10 mA/cm^2)	360 mV	[81]
Ni-NGr nanocage	W/O emulsion technique	270 mV	Present work

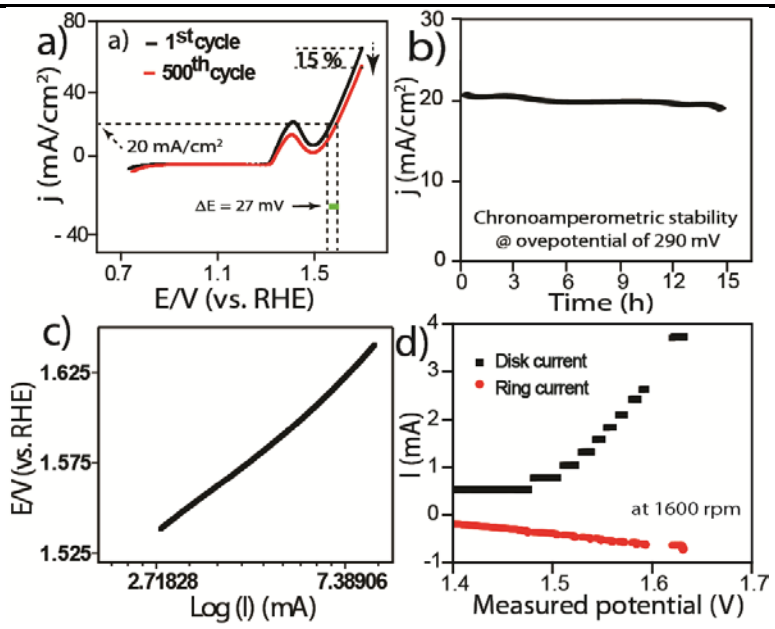

Figure 6.11: *(a) O_2-evolution curve of Ni-NGr nanocages before and after cycle stability performed in a potential window of 0.7 to 1.7 V (vs. RHE), in a 0.1 M KOH electrolyte, (b) chronoamperometric stability profile performed at overpotential of ~290 mV for 15 h, (c) Tafel plot of Ni-NGr, and (d) rotating ring disk electrode (RRDE) study for OER of Ni-NGr nanocages, recorded in 0.1M KOH at 1600 rpm. The disk electrode is subjected to a series of current steps, and the corresponding potentials are measured.*

Consequently, the Tafel slope (**Figure 6.11c**) was obtained by plotting the log I *vs.* potential, and is found to be ~69 mV per decade. The Tafel slope directly gives an idea about the good intrinsic electrocatalytic activity. For comparison, the anodic LSV scan of Ni-nanoparticles and Ni-Gr (**Figure 6.9b**) was recorded. The obtained overpotential of the samples at 20 mA/cm^2 is in the order of Ni-NGr (~290 mV) < Ni-nanoparticles (~370 mV) < Ni-Gr (~570 mV). The obtained results in terms of lower overpotential and higher current signify the importance of the nanocage structures over the Ni-nanoparticles and Ni-Gr. Moreover, cyclic stability (**Figure 6.11a**) was confirmed by anodic potential scanning for 500 cycles and a chronoamperometric (**Figure 6.11b**) study at a practical overpotential value (*i.e.* required to achieve the 20 mA/cm^2 current density) for 15 h. From the chronoamperometric investigation, it was found that the current density is steady up to 15 h at the applied overpotential (η = 290 mV). However, in potential cycling, nearly 15 % decrease in the current is observed after 500 cycles, which is showing good stability under the operating conditions. The observed overpotential (η) at the current density of 20 mA/cm^2 is found to be ~290 mV before the stability test (*i.e.* $\eta_{n=1}$ = 290 mV, where, n = number of cycles) and after 500 potential cycles, η is found to be increased to 317 mV (*i.e.* $\eta_{n=500}$ is 317 mV).

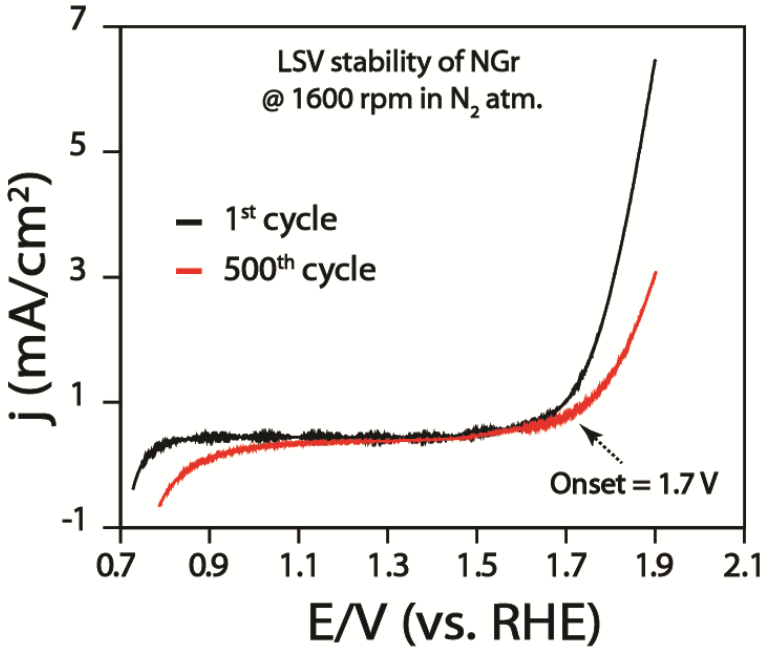

Figure 6.12: *LSV OER stability of NGr recorded in nitrogen saturated 0.1M KOH at 1600 rpm. The overpotential is around 470 mV (at onset). The current is also very low for OER.*

Therefore, the percentage of overpotential increment after the 500 cycles is 8.5 at 20 mA/cm^2, which is far better than the available reports.[8] The better activity and stability of Ni-NGr nanocages is attributed mainly to a high surface-to-volume ratio, and 3D surface molecular accessibility, which provide more active sites. The exact reason for the increase of overpotential after 500 cycles and the decrease in the current after the 15 h chronoamperometric test could be the electrode surface passivation due to the evolved oxygen and/or formation of nickel oxyhydroxide.

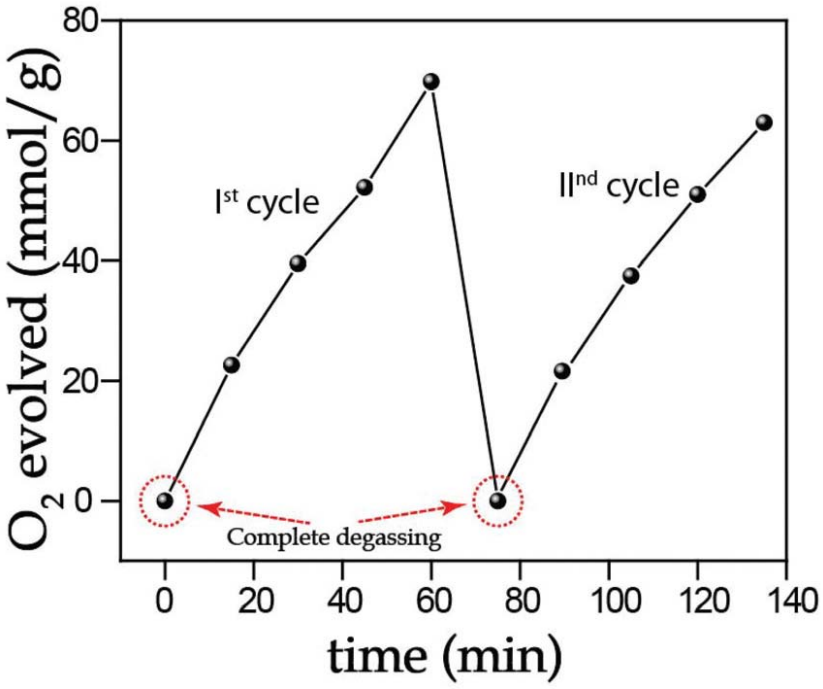

Figure 6.13: *Quantitative analysis of the evolved oxygen and cycle stability evaluation of the catalyst by gas chromatography during the electrochemical water oxidation.*

Finally, a gas tight electrochemical cell assembly has been constructed for the quantification of the generated oxygen during the electrochemical water oxidation. The quantification was done by analyzing the gas sample from headspace of the assembly using the gas chromatography (GC) technique. Mainly, before starting the experiment, the electrolyte was purged with N_2 for 30 min and complete gas evacuation was ensured by applying vacuum for 10 min. Afterwards, GC spectrum was recorded and confirmed the absence of any gas in the assembly. Subsequent to this, the system was subjected to a chronoamperometric testing at 1.5 V (vs. RHE) and the generated oxygen was recorded by GC for 1 h with an interval of 15 min,

named the Ist cycle in **Figure 6.13**. A systematic increase in the amount of oxygen is observed from 0 to 70 mmol/h/g. Furthermore, to understand the stability of the catalyst, the assembly was completely evacuated and made free from the gas and the same experiment was repeated, termed as the IInd cycle in **Figure 6.13**. The amount of O_2 generated is almost the same in both the cycles, which highlights the higher stability of the catalyst under the operating conditions.

To understand the efficiency of Ni-NGr for OER, RRDE investigation has been done. Mainly, the Faradaic efficiency (ε) measurement was done by applying a current step from 2 to 15 mA/cm^2 to the carbon disk and the corresponding voltage was measured (**Figure 6.11d**). During the measurement, the rotation speed of the RRDE was kept at 1600 rpm. The oxygen evolution from the carbon disk was monitored by reducing it on the Pt ring, whose potential was kept constant at 1.3 V (vs. RHE). The Faradaic efficiency was calculated by using **Equation 6.2**, and is found to be 0.9 at 15 mA/cm^2.[3-4]

$$\text{Faradaic efficiency } (\varepsilon) = 2*I_R / I_D*N \qquad (6.2)$$

where, I_R is the ring current, I_D is 2.7 mA, is the constant disk current for a 0.2646 cm^2 disk electrode to get minimum current density of 10 mA/cm^2 and N is the collection efficiency (0.37).

6.4. Conclusion

Ni-NGr nanocage structure was synthesized by a simple W/O emulsion technique by optimizing the reaction occurring inside the nanoreactors of the aqueous droplets. Ni-NGr showed a significantly reduced overpotential for OER at the practical current density of 20 mA/cm^2 compared to the literature results. Moreover, the chronoamperometry evaluation highlighted its better sustainability in alkaline medium. Nearly 70 mmol/h/g of oxygen was generated after 1 h and the catalyst displayed good reproducibility in the second cycle as well. Ni-NGr is relatively cheap and it displays excellent corrosion resistance properties in the aqueous alkaline system. Hence, it offers an efficient and cheap alternative to the energy intensive and expensive Ru/Ir-oxide catalysts. The method demonstrated here can be useful to synthesize many more multi-metallic nanocage structures for ORR, OER, alcohol oxidation, etc. Still, the exact type of nitrogen which triggers the formation of the nanocage structure is an open question for further studies.

6.5. References

[1] J. Rossmeisl, Z. W. Qu, H. Zhu, G. J. Kroes, J. K. Nørskov, *Journal of Electroanalytical Chemistry* **2007**, *607*, 83-89.

[2] J. Divisek, P. Malinowski, J. Mergel, H. Schmitz, *International Journal of Hydrogen Energy* **1988**, *13*, 141-150.

[3] J. K. Hurst, *Science* **2010**, *328*, 315-316.

[4] M. W. Kanan, D. G. Nocera, *Science* **2008**, *321*, 1072-1075.

[5] M. G. Walter, E. L. Warren, J. R. McKone, S. W. Boettcher, Q. Mi, E. A. Santori, N. S. Lewis, *Chemical Reviews* **2010**, *110*, 6446-6473.

[6] T. R. Cook, D. K. Dogutan, S. Y. Reece, Y. Surendranath, T. S. Teets, D. G. Nocera, *Chemical Reviews* **2010**, *110*, 6474-6502.

[7] Y. Matsumoto, E. Sato, *Materials Chemistry and Physics* **1986**, *14*, 397-426.

[8] C. C. L. McCrory, S. Jung, J. C. Peters, T. F. Jaramillo, *Journal of the American Chemical Society* **2013**, *135*, 16977-16987.

[9] R. N. Singh, M. Hamdani, J. F. Koenig, G. Poillerat, J. L. Gautier, P. Chartier, *Journal of Appliled Electrochemistry* **1990**, *20*, 442-446.

[10] V. Rashkova, S. Kitova, I. Konstantinov, T. Vitanov, *Electrochimica Acta* **2002**, *47*, 1555-1560.

[11] R. N. Singh, J. F. Koenig, G. Poillerat, P. Chartier, *Journal of The Electrochemical Society* **1990**, *137*, 1408-1413.

[12] M. Gong, Y. Li, H. Wang, Y. Liang, J. Z. Wu, J. Zhou, J. Wang, T. Regier, F. Wei, H. Dai, *Journal of the American Chemical Society* **2013**, *135*, 8452-8455.

[13] M. W. Louie, A. T. Bell, *Journal of the American Chemical Society* **2013**, *135*, 12329-12337.

[14] K. Fominykh, J. M. Feckl, J. Sicklinger, M. Döblinger, S. Böcklein, J. Ziegler, L. Peter, J. Rathousky, E.-W. Scheidt, T. Bein, D. Fattakhova-Rohlfing, *Advanced Functional Materials* **2014**, *24*, 3123-3129.

[15] D. Wang, Y. Li, *Advanced Materials* **2011**, *23*, 1044-1060.

[16] R. Ferrando, J. Jellinek, R. L. Johnston, *Chemical Reviews* **2008**, *108*, 845-910.

[17] A. R. Tao, S. Habas, P. Yang, *Small* **2008**, *4*, 310-325.

[18] S. W. Kang, Y. W. Lee, Y. Park, B.-S. Choi, J. W. Hong, K.-H. Park, S. W. Han, *ACS Nano* **2013**, *7*, 7945-7955.

[19] J. Wang, H.-x. Zhong, Y.-l. Qin, X.-b. Zhang, *Angewandte Chemie International Edition* **2013**, *52*, 5248-5253.

[20] S. Chen, J. Duan, M. Jaroniec, S.-Z. Qiao, *Advanced Materials* **2014**, *26*, 2925-2930.

[21] M. H. Huang, S. Rej, S.-C. Hsu, *Chemical Communications* **2014**, *50*, 1634-1644.

[22] H. Zhang, M. Jin, Y. Xia, *Chemical Society Reviews* **2012**, *41*, 8035-8049.

[23] B. Y. Xia, H. B. Wu, X. Wang, X. W. Lou, *Journal of the American Chemical Society* **2012**, *134*, 13934-13937.

[24] F. Saleem, Z. Zhang, B. Xu, X. Xu, P. He, X. Wang, *Journal of the American Chemical Society* **2013**, *135*, 18304-18307.

[25] E. Taylor, S. Chen, J. Tao, L. Wu, Y. Zhu, J. Chen, *ChemSusChem* **2013**, *6*, 1863-1867.

[26] C. J. DeSantis, S. E. Skrabalak, *Langmuir* **2012**, *28*, 9055-9062.

[27] S.-B. Wang, W. Zhu, J. Ke, J. Gu, A.-X. Yin, Y.-W. Zhang, C.-H. Yan, *Chemical Communications* **2013**, *49*, 7168-7170.

[28] C. J. DeSantis, A. C. Sue, M. M. Bower, S. E. Skrabalak, *ACS Nano* **2012**, *6*, 2617-2628.

[29] L. A. De Faria, M. Prestat, J. F. Koenig, P. Chartier, S. Trasatti, *Electrochimica Acta* **1998**, *44*, 1481-1489.

[30] W. J. King, A. C. C. Tseung, *Electrochimica Acta* **1974**, *19*, 485-491.

[31] M. R. G. De Chialvo, A. C. Chialvo, *Electrochimica Acta* **1993**, *38*, 2247-2252.

[32] C.-C. Hu, Y.-S. Lee, T.-C. Wen, *Materials Chemistry and Physics* **1997**, *48*, 246-254.

[33] S. C. Thomas, V. I. Birss, *Journal of The Electrochemical Society* **1997**, *144*, 558-566.

[34] G. Wu, N. Li, D.-R. Zhou, K. Mitsuo, B.-Q. Xu, *Journal of Solid State Chemistry* **2004**, *177*, 3682-3692.

[35] V. K. Portnoi, A. V. Leonov, S. N. Mudretsova, S. A. Fedotov, *The Physics of Metals and Metallography* **2010**, *109*, 153-161.

[36] X. Li, W. Cai, L. Colombo, R. S. Ruoff, *Nano Letters* **2009**, *9*, 4268-4272.

[37] M. Eizenberg, J. M. Blakely, *Surface Science* **1979**, *82*, 228-236.

[38] M. Diarra, A. Zappelli, H. Amara, F. Ducastelle, C. Bichara, *Physical Review Letters* **2012**, *109*, 185501.

[39] M. Diarra, H. Amara, F. Ducastelle, C. Bichara, *physica status solidi (b)* **2012**, *249*, 2629-2634.

[40] J.-S. Lee, G. S. Park, S. T. Kim, M. Liu, J. Cho, *Angewandte Chemie International Edition* **2013**, *52*, 1026-1030.

[41] Y. Wu, D. Wang, G. Zhou, R. Yu, C. Chen, Y. Li, *Journal of the American Chemical Society* **2014**, *136*, 11594-11597.

[42] Y. Li, Y. Zhao, H. Cheng, Y. Hu, G. Shi, L. Dai, L. Qu, *Journal of the American Chemical Society* **2011**, *134*, 15-18.

[43] H. Wang, T. Maiyalagan, X. Wang, *ACS Catalysis* **2012**, *2*, 781-794.

[44] W. S. Leong, C. T. Nai, J. T. L. Thong, *Nano Letters* **2014**, *14*, 3840-3847.

[45] M. Balaceanu, A. Vladescu, M. Braic, C. N. Zoita, I. Feraru, V. Braic, *Optoelectronics and Advanced Materials-Rapid Communications* **2010**, *4*, 2167-2171.

[46] K. R. Krishnadas, P. R. Sajanlal, T. Pradeep, *The Journal of Physical Chemistry C* **2011**, *115*, 4483-4490.

[47] B. Varghese, M. V. Reddy, Z. Yanwu, C. S. Lit, T. C. Hoong, G. V. Subba Rao, B. V. R. Chowdari, A. T. S. Wee, C. T. Lim, C.-H. Sow, *Chemistry of Materials* **2008**, *20*, 3360-3367.

[48] I. M. Chan, F. C. Hong, *Thin Solid Films* **2004**, *450*, 304-311.

[49] A. Achour, A. A. El Mel, N. Bouts, E. Gautron, E. Grigore, B. Angleraud, L. Le Brizoual, P. Y. Tessier, M. A. Djouadi, *Diamond and Related Materials* **2013**, *34*, 76-83.

[50] H. Huang, H. Zhang, Z. Ma, Y. Liu, H. Ming, H. Li, Z. Kang, *Nanoscale* **2012**, *4*, 4964-4967.

[51] F. Banhart, *Nanoscale* **2009**, *1*, 201-213.

[52] B. Viswanath, P. Kundu, B. Mukherjee, N. Ravishankar, *Nanotechnology* **2008**, *19*, 195603.

[53] J. G. Radich, P. V. Kamat, *ACS Nano* **2013**, *7*, 5546-5557.

[54] B. Viswanath, P. Kundu, A. Halder, N. Ravishankar, *The Journal of Physical Chemistry C* **2009**, *113*, 16866-16883.

[55] Z.-L. Wang, J.-M. Yan, H.-L. Wang, Y. Ping, Q. Jiang, *Journal of Materials Chemistry A* **2013**, *1*, 12721-12725.

[56] J. Xie, C. Yan, Y. Zhang, N. Gu, *Chemistry of Materials* **2013**, *25*, 3702-3709.

[57] Y.-A. Zhu, Y.-C. Dai, D. Chen, W.-K. Yuan, *Carbon* **2007**, *45*, 21-27.

[58] S. Hong, Y.-H. Shin, J. Ihm, *Japanese Journal of Applied Physics* **2002**, *41*, 6142.

[59] V. Di Noto, E. Negro, S. Polizzi, F. Agresti, G. A. Giffin, *ChemSusChem* **2012**, *5*, 2451-2459.

[60] X. Gu, Case Western Reserve University **2007**.

[61] V. Di Noto, E. Negro, *Electrochimica Acta* **2010**, *55*, 7564-7574.

[62] V. Di Noto, E. Negro, M. Piga, L. Piga, S. Lavina, G. Pace, *ECS Transactions* **2007**, *11*, 249-260.

[63] S. Trasatti, O. A. Petrii, *Pure and Applied Chemistry* **1991**, *63*, 711-734.

[64] J. D. Benck, Z. Chen, L. Y. Kuritzky, A. J. Forman, T. F. Jaramillo, *ACS Catalysis* **2012**, *2*, 1916-1923.

[65] S. Iseki, K. Ohashi, S. Nagaura, *Electrochimica Acta* **1972**, *17*, 2249-2265.

[66] W. A. Badawy, A. G. Gad-Allah, H. A. Abd El-Rahman, M. M. Abouromia, *Surface and Coatings Technology* **1986**, *27*, 187-196.

[67] T. A. Centeno, F. Stoeckli, *Journal of Power Sources* **2006**, *154*, 314-320.

[68] J. L. Weininger, M. W. Breiter, *Journal of The Electrochemical Society* **1963**, *110*, 484-490.

[69] J. L. Weininger, M. W. Breiter, *Journal of The Electrochemical Society* **1964**, *111*, 707-712.

[70] R. N. O'Brien, P. Seto, *Journal of Electroanalytical Chemistry and Interfacial Electrochemistry* **1968**, *18*, 219-230.

[71] N. A. Hampson, R. J. Latham, J. B. Lee, K. I. Macdonald, *Journal of Electroanalytical Chemistry and Interfacial Electrochemistry* **1971**, *31*, 57-62.

[72] E. G. Gagnon, *Journal of The Electrochemical Society* **1973**, *120*, 1052-1056.

[73] A. Lasia, A. Rami, *Journal of Electroanalytical Chemistry and Interfacial Electrochemistry* **1990**, *294*, 123-141.

[74] P. Gu, L. Bai, L. Gao, R. Brousseau, B. E. Conway, *Electrochimica Acta* **1992**, *37*, 2145-2154.

[75] L. Bai, L. Gao, B. E. Conway, *Journal of the Chemical Society, Faraday Transactions* **1993**, *89*, 235-242.

[76] J. Fournier, L. Brossard, J. Y. Tilquin, R. Coʎté, J. P. Dodelet, D. Guay, H. Ménard, *Journal of The Electrochemical Society* **1996**, *143*, 919-926.

[77] D. A. Corrigan, R. M. Bendert, *Journal of The Electrochemical Society* **1989**, *136*, 723-728.

[78] J. C. K. Ho, D. L. Piron, *Journal of Applied Electrochemistry* **1996**, *26*, 515-521.

[79] X. Li, F. C. Walsh, D. Pletcher, *Physical Chemistry Chemical Physics* **2011**, *13*, 1162-1167.

[80] M. D. Merrill, R. C. Dougherty, *The Journal of Physical Chemistry C* **2008**, *112*, 3655-3666.

[81] J. Landon, E. Demeter, N. İnoğlu, C. Keturakis, I. E. Wachs, R. Vasić, A. I. Frenkel, J. R. Kitchin, *ACS Catalysis* **2012**, *2*, 1793-1801.

Chapter 7
Summary and Conclusions

This chapter gives an overview on the important observations and conclusions along with the future prospects of the work described in the thesis. Development of the *in situ* modification-cum-anchoring strategy for obtaining low-Pt based core-shell structures dispersed on carbon support substrate is an important achievement of the work. Several advantages of this approach such as direct anchoring of the nanoparticles, *in situ* functionalization of the support substrate, controlled formation of continuous thin Pt-shell on the surface of the non-noble metal core and the application of these catalysts in the field of PEMFCs have been thoroughly discussed. The significance of low-Pt and Pt-free 3-D hollow nanocage structured electrocatalysts possessing multifunctional characteristics to address the challenges existing in the area of performance improvement is also covered in the thesis. Another key highlight of the work is the synthesis of a non-Pt based core-shell structured electrocatalyst possessing a graphene shell and demonstration of its benefits in attaining modulated performance characteristics for oxygen reduction. The thesis also deals with the viability of the water-in-oil (W/O) emulsion technique in order to build various types of nanostructured Pt-free electrocatalysts by making use of the complex chemistry involved in nano regime of the water droplet. This chapter gives a concise summary of the key aspects of the work illustrated in the thesis. The main aspects with respect to the synthesis strategies adopted, structural features attained and performance modulations achieved are highlighted in the chapter.

Polymer electrolyte membrane fuel cells (PEMFCs) and Zn-air batteries offer the prospects to fulfil the future energy demands of the world, because of their many fascinating features like noise-free operation, substantial reduction in pollution and better efficiency etc. Conversely, the use of expensive platinum (Pt) and its sluggish ORR activity are the bottleneck in the field of marketization, especially in the case of PEMFCs. Therefore, the electrocatalysts need special attention as they play a decisive role in deciding the performance and cost aspects of PEMFCs and metal-air batteries. Hence, there is a clear urge to develop suitable low-Pt and Pt-free electrocatalysts for PEMFCs and metal-air batteries without affecting their performance and stability. Looking closely at the fundamental aspects of the metal structures and their correlation with the size, there exists good opportunity to build novel nanostructured electrocatalysts possessing higher surface-to-volume ratio with better dispersion on the support substrate. In addition, structural modulation of bi-metallic systems consisting the noble metal Pt with less expensive transition metals such as Cu, Fe, Ni, etc. in the form of alloy, core-shell, and hollow nanocage etc. can help to resolve the issues related to cost and performance in comparison to the state-of-the-art Pt/C. Along with this, various nanostructured Pt-free systems such as metal-carbon core-shell and hollow nanocages structures have immense potential to evolve as efficient cost effective materials for energy applications by effectively tackling their physico-chemical characteristics.

The works demonstrated in the thesis stand out as a concerted effort to overcome some of the pertinent issues associated with the existing noble metal based electrocatalysts which are being used for various energy related applications such as PEMFCs, metal-air batteries, water splitting etc. The key strategy in this work involves synthesis of different engineered nanostructures *via* logical selection of the reducing agents, metal precursors, synthesis protocols and reaction parameters. A controlled interplay of many of these parameters is found to be assisting in attaining various types of nanostructured activity modulated and cost-effective electrocatalysts, which have great potential to bring in redefined performance characteristics and cost benefits for devising systems for energy applications.

The major accomplishments of the present investigations can be summarized as follows:

1. Surface Modification-cum-Anchoring Strategy for the Synthesis of Low-Pt Core-Shell Electrocatalysts for Oxygen Reduction Reaction.

Even though there are several reports on synthesizing core-shell nanoparticles, development of carbon supported core-shell nanoparticles is still a challenging task owing to the counteracting inter-species interactions within the system. Pre-formed core-shell nanoparticles generally will not give proper dispersion owing to the weak interaction between carbon and reduced surface of the core-shell particles (*ex situ* method). However, in this case, the core-shell features of the nanoparticles will be intact. On the other hand, attempts for simultaneous preparation and dispersion of core-shell nanoparticles on carbon cause more individual metal particle dispersion than the formation and dispersion of the core-shell particles due to preferential adsorption of the respective metal ions on the active sites of carbon (*in situ* method). This means that, maintaining high dispersion while retaining the core-shell characteristics of the species is an exigent task. To overcome this issue, a novel strategy could be developed where the reduction process itself gives a means to interlink the core-shell particles with the carbon surface. **Chapter 3** deals with this work. This one pot synthesis of *in situ* modification of the support substrate and *ex situ* dispersion of the as formed core-shell structures is termed as surface-modification-cum-anchoring (SMcA) strategy in this thesis.

Main achievements of the work and future scope pertaining to the work are highlighted below:

- The SMcA approach as illustrated in **Chapter 3** deals with an effective one-pot synthesis strategy for developing well dispersed carbon supported core-shell nanoparticles of Pt possessing remarkable electrocatalytic activities.

- The chronological addition of the metal precursors and reducing agent (here, ascorbic acid (AA)) is found to be critical because the oxidation products of AA during the metal ion reduction play decisive role in functionalizing the carbon surface and thereafter in anchoring the so formed core-shell particles on the surface. Therefore, excellent core-shell features and high dispersion can be simultaneously ensured in this process. By employing the SMcA approach, Cu@Pt/C and Fe_2O_3@Pt/C electrocatalysts could be synthesized which possess core-shell features as well as good dispersion on the carbon substrate. Both the electrocatalysts delivered better ORR activity compared to Pt/C.

- Among the prepared catalysts, Fe_2O_3@Pt/C has delivered better ECSA and ORR activity compared to Cu@Pt/C. Most importantly, Fe_2O_3@Pt/C has shown higher performance for ORR at significantly low-Pt loading, possibly due to the less ohmic overpotential by the oxidic core moiety when the coating thickness is less. Therefore, in a system that possesses a less conductive core material, *i.e*. Fe_2O_3, it is mandatory to prevent the electrode thickness from exceeding a threshold level owing to the greater dominance of the core material with its higher mass fraction in the system. Exceeding the thickness beyond a threshold level upsets the ECSA, oxygen reduction kinetics, and polarization characteristics. On the other hand, in optimized systems, the core-shell (Fe_2O_3@Pt/C) material clearly outperforms the conventional Pt/C, leaving a great scope in the development of high performance, cost-effective low-Pt electrocatalysts possessing excellent electrochemical stability.

- Overall, the realization of high-performance thin electrodes is expected to make radical changes in the design aspects of PEMFCs along with its potential to develop miniature cells for various niche applications.

2. Low-Platinum based 3-D Hollow Nanocage Structure for Oxygen Reduction Reaction in Primary Zn-Air Battery.

The thesis also deals with successful utilization of a Cu-Pt nanocage (CuPt-NC), which has a 3-D structural morphology, as a potential ORR electrocatalyst for primary Zn-air battery applications. **Chapter 4** in the thesis is dedicated for highlighting the key aspects of this work. The key specialities of the nanocage morphology are the availability and exposure of higher number of active sites along with better molecular accessibility within the single crystal structure of CuPt-NC.

The key aspects of the work are highlighted as below:

- CuPt-NC with its high density of surface defects, potentially offers more active sites for facilitating efficient dissociative adsorption of oxygen, resulting into an improved ORR activity. The nanocage structure offers 3-D molecular accessibility, higher surface-to-volume ratio, more electro-active centers and the interconnected arms which make the

nanostructure more stable and energetic for electrochemical applications. This could not be observed in the case of simple metal nanoparticles.

- Mainly, the oxygen reduction electrocatalyst decides the overall efficiency of the metal-air batteries. However, issues related to reactant accessibility and stability of the presently used Pt-electrocatalysts hinder the commercial viability of such systems. Therefore, to improve the performance of the energy storage devices, the concerns related to accessibility, activity and stability have to be sorted out. The strategy developed here effectively deals with this issue as the 3-D structure with easy accessibility favourably influences to achieve better oxygen reduction activity with higher stability in actual operating conditions.

- The fabricated battery set-up with CuPt-NC as the air-electrode showed higher open circuit potential (~1.4 V) compared to the one with Pt/C (~1.3 V), and led to higher specific capacity and energy density (560 mAh/g_{-Zn}, 728 Wh/kg_{-Zn}, at -20 mA/cm^2), which are superior compared to the performance of the Pt/C based system (480 mAh/g_{-Zn}, 624 Wh/Kg_{-Zn}, at -20 mA/cm^2).

- Such engineered structures with property modulation have far reaching effects in devising active cost-effective oxygen reduction catalysts for metal-air batteries and other potential electrochemical devices where oxygen reduction activity dictates the overall efficiency such as fuel cells.

3. Synthesis of Pt-free Core-Shell Electrocatalyst for Oxygen Reduction Reaction *via* Simple Water-in-Oil Emulsion Method

Heteroatom doped (such as N, P, S and B) carbon nanostructures have attained substantial attention in recent years due to their excellent oxygen reduction activities under extreme electrochemical conditions. Very close or matching onset potentials for oxygen reduction compared to Pt have been reported on some of these materials. One important drawback of many heteroatoms doped and functionalized carbon nanomaterials is a significant compensation in terms of the electrical conductivity. The pre-oxidative treatments, multisteps involved during the synthesis and use of capping and reducing agents adversely affect the electrical conductivity. Under these tricky circumstances, the overall conductivity of these

materials gets affected, which, eventually, leads to higher ohmic drops in ORR. Since minimization of ohmic drop in the current (I)-voltage (V) polarization is essential in order to meet the operating power demands from a cell if such issues not properly addressed, the activity of the heteroatom doped catalysts will not be pronounced beyond a certain limit. **Chapter 5** explains how this issue could be tackled by using nitrogen doped graphene (NGr) deposited over Au nanoparticles to form core-shell structure. Here, the Au nanoparticle is encapsulated by NGr, where Au acts as the core and NGr as the shell. The Au concentration was maintained to be very low (10 wt. % Au and 90 wt. % NGr) and well featured core-shell nanoparticles were generated with good yield by adopting very simple water-in-oil (W/O) emulsion method.

The main highlights of this work are as follows:

- The method adopted here is unique and easily scalable. Reaction occurs within the droplets of the W/O "nanoreactors" as temperature goes up and stirring maintains the droplets size to be tiny and uniform. Finally, evaporation of water leads to encapsulation of Au with NGr (Au@NGr) giving good yield of the core-shell material.

- Excellent core-shell features could be realized by TEM, XRD and electrochemical methods. Very good control over size and thicknesses of the core-shell phases is also achieved. A continuous layer of NGr and Gr is maintained throughout the surface of the Au nanoparticles, and in each particle, the Au phase is found to located nearly at the center.

- Interestingly, an enhancement in the electrical conductivity of Au@NGr compared to Gr, NGr, Au@Gr (Au encapsulated with undoped Gr) and even Au nanoparticles could be observed. This is an important achievement as it has a significant role in minimizing the ohmic overpotential during electrochemical oxygen reduction process. Thus, the pertaining issue of the high ohmic drop on the heteroatom doped system could be effectively resolved here.

- Similar to the electrical conductivity, a substantial reduction in the overpotential for oxygen reduction is also observed in the case of Au@NGr compared to NGr and Au particles as separate entities. This attributes to the modulations imparted by the core-shell interactions. Valid evidences on such interactions could be gained through XRD,

HRTEM, Raman and XPS analyses. The cyclic voltammetric, rotating ring-disk electrode and linear sweep voltammetric analyses shed light on the improvement of catalytic efficiency by the core-shell material.

- The strategy adopted here opens up a great scope for adopting new ways to develop cost-effective metal-graphene core-shell nanoparticles. The study highlights the crucial role played by a highly conducting metal core, in its low concentration, in influencing the active sites located at the graphene shell layer to shift the reaction kinetics to the favorable four electron reduction pathway. As a future prospective, a large number of metal-Gr core shell systems can be developed by adopting the same strategy, which is cost-effective and easily scalable.

3. Pt-Free 3-Dimentional N-doped Graphene Interpenetrated Ni-Nanocages as an Efficient and Stable Water-to-Dioxygen Electrocatalyst

Oxygen evolution reaction (OER) has achieved popularity for various energy conversion and storage applications, such as, solar to fuel conversion devices, water splitting, metal-air battery, etc. However, the total efficiency of the system is decided by the OER active material. The Ir-oxide and Ru-oxide based systems are considered to be the best for OER. However, the cost and scarcity are the major challenges of these systems, which hamper the prospects of their commercialization. **Chapter 6** of the thesis deals with the employment of a water-in-oil (W/O) emulsion technique to synthesize Ni-nitrogen doped graphene (Ni-NGr) based nanocage structure, which is cheap, cost effective and also highly active for OER.

The key aspects related to the process, structure and activity are summarized below:

- The process described is simple and easily scalable. The reaction is executed inside the water droplets of an emulsion formed by water and oil. The water droplets act as the "nanoreactors" where mutually assisted redox reaction of Ni^{+2} and nitrogen-doped graphene takes place, leading to the size controlled formation of the Ni-NGr nanocage structures.

- The tendency of carbon to get dissolved in Ni is the driving force for the formation of the Ni-NGr nanocage structure. A controlled interplay of the carbon dissolution property of

Ni and its dependency on the adsorption energy on the different crystal planes during the redox reaction inside the tiny water droplet lead to fancy Ni-NGr nanocage morphology with a higher surface-to-volume ratio and 3-D surface molecular accessibility.

- Normally, in the case of metal particles, the molecular accessible areas or sites are less compared to the nanocage structures. Ni-NGr offers 3-D molecular accessibility, higher surface-to-volume ratio, more electro-active centers and the interconnected arms which make the nanostructures more stable and energetic for the electrochemical applications.

- Ni-NGr nanocage structure has shown a lower overpotential of ~290 mV for OER at a higher current density of 20 mA/cm^2. Ni-NGr has shown only 29 mV (at 20 mA/cm^2) increment in overpotential after 500 potential cycles. This along with chronoamperometric investigation at higher current density (20 mA/cm^2) confirms the better sustainability of such system in alkaline medium. The generated oxygen has been quantified by gas chromatography, and is found to be ~70 mmol/h. The amount of oxygen generated is almost same in the second cycle as well, which validates the high stability of the system.

- The modulations affected in Ni-NGr has far reaching advantages in devising active cost-effective catalysts for water splitting to convert solar-to-fuel and as an oxygen evolution catalyst for metal-air batteries and other potential electrochemical devices.

❖ Future Prospects

Based on the aforementioned key aspects of the prepared samples (Low-Pt and Pt-free) related to their synthesis, structure and performance, they can possess additional advantages in the field of water splitting, solar cells, batteries and transistor etc. The synthesized Cu-Pt and Fe-Pt based core-shell and CuPt-NC structures can be effectively utilized as counter electrodes in the field of solar cells. Moreover, the fundamental understanding of variation in performance characteristics of PEMFCs with electrode thickness while dealing with the core-shell structured catalysts possessing less conductive cores stands out as an important guideline to design membrane electrode assemblies (MEAs) to develop miniature PEMFCs for various niche applications. In addition, the synthesized Ni-NGr nanocage structure can possibly be utilized as a

cathode electrode in combination with ORR catalysts in Zn-air batteries to convert the ZnO to Zn, which makes the system electronically rechargable.

Despite the material aspects, the synthetic approaches developed during the course of the study can find additional benefits in building different types of electrocatalysts. Mainly, the SMcA approach offers enough scope to design different shaped nanostructures of various transition metals with desired properties. We believe that apart from Cu or Fe (core) and Pt (shell), the SMcA approach can be extended to synthesize other potential metallic and semiconducting nanostructures for different energy conversion and storage devices such as solar-to-fuel conversion, water-splitting, CO_2-reduction, alcohol and amine oxidations etc. Moreover, the W/O emulsion technique can play major role in achieving ultra-low resistance across the metal-graphene contact in the field of graphene transistors, which has great future. This similar protocol (W/O emulsion) can be extended to build many more different metal-carbon based hetero-structures possessing higher surface area and hollow structures for the electrocatalysis. In addition, the high conducting and wide band gap hybrid materials can be synthesized by tuning the surface of metal-oxide with carbon layer.

Especially, in case of Ni-NGr nanocage structures, a theoretical study can help to predict the exact mechanism and the role of nitrogen in building this kind of structures which can help to build other potential materials. In conjunction, the exact type of nitrogen which triggers the formation of the nanocage structure is still an open question for further studies.

List of Publications

1. **Vishal M. Dhavale**, Sreekuttan M. Unni, Husain N. Kagalwala, Vijayamohanan K. Pillai, Sreekumar Kurungot, "*Ex-situ Dispersion of Core–Shell Nanoparticles of Cu-Pt on an In situ Modified Carbon Surface and their Enhanced Electrocatalytic Activities*", ***Chemical Communication***, **2011**, 47, 3951–3953.

2. **Vishal M Dhavale**, Sreekumar Kurungot, "*Tuning the Performance of Low-Pt Polymer Electrolyte Membrane Fuel Cell Electrodes Derived from Fe_2O_3@Pt/C Core–Shell Catalyst Prepared by an in Situ Anchoring Strategy*," ***Journal of Physical Chemistry-C***, **2012**, 116, 13, 7318–7326.

3. **Vishal M. Dhavale**, Sachin S. Gaikwad, Sreekumar Kurungot, "*Activated Nitrogen Doped Graphene Shell Towards Electrochemical Oxygen Reduction Reaction by its Encapsulation on Au Nanoparticle (Au@N-Gr) in Water-in-Oil "Nanoreactors"*, ***Journal of Material Chemistry-A***, **2014**, 2, 1383-1390.

4. **Vishal M. Dhavale**, Sachin S. Gaikwad, Leena K George, R. Nandini Devi, Sreekumar Kurungot," *Nitrogen-Doped Graphene Interpenetrated 3-D Ni-Nanocage: Efficient and Stable Water-to-Dioxygen Electrocatalyst,"* ***Nanoscale***, **2014**, 6, 13179-13187.

5. Pradip Pachfule,[$] **Vishal M. Dhavale**,[$] Sharath Kandambeth, Sreekumar Kurungot, Rahul Banerjee, "*Porous-Organic-Framework-Templated Nitrogen-Rich Porous Carbon as a More Proficient Electrocatalyst than Pt/C for the Electrochemical Reduction of Oxygen*", ***Chemistry-A European Journal***, **2013,** 19, 974-980. ([$]***These authors contributed equally to this work***).

6. **Vishal M. Dhavale**, Sreekumar Kurungot, "*Cu-Pt Nanocage with 3-D Electrocatalytic Surface as an Efficient Oxygen Reduction Electrocatalyst for Primary Zn-Air Battery"*, ***ACS Catalysis***, **2015**, 5, 1445−1452.

7. Sreekuttan M. Unni, **Vishal M. Dhavale**, Vijayamohanan K. Pillai, Sreekumar Kurungot, "*High Pt Utilization Electrodes for Polymer Electrolyte Membrane Fuel Cells by Dispersing*

Pt Particles Formed by a Preprecipitation Method on Carbon "Polished" with Polypyrrole", ***Journal of Physical Chemistry-C***, **2010**, 114, 14654–14661.

8. Santosh Singh, **Vishal M. Dhavale**, Sreekumar Kurungot,"*Low-Surface Energy Plane Exposed Co_3O_4 Nanocubes Supported on Nitrogen-Doped Graphene as an Electrocatalyst for Efficient Water Oxidation"*, ***ACS Applied Materials and Interfaces***, **2015,** 7, 442-451.

9. Anurag Sunda, **Vishal M. Dhavale**, Sreekumar Kurungot, Arun Venkatnathan, "*Structure and Dynamics of Benzyl-NX_3 (X = Me, Et) Trifluoromethanesulfonate Ionic Liquids"*, ***Journal of Physical Chemistry-B***, **2014**, 118, 1831–1838

10. Chinmay G. Nardele, **Vishal M. Dhavale**, K. Sreekumar, S. K. Asha, "*Ionic Conductivity Probed in Main Chain Liquid Crystalline Azobenzene Polyesters*", ***Journal of Polymer Science Part-A: Polymer Chemistry,*** **2015,** 53, 629-641.

11. Rahul S. Diggikar, **Vishal M. Dhavale**, Dhanraj B. Shinde, Nihal S. Kanbargi, Milind V. Kulkarni, Bharat B. Kale, "*Morphology Controlled Synthesis of LiV_2O_5/Ag Nanocomposite Nanotubes with Enhanced Electrochemical Performance"*, ***RSC Advances***, **2012**, 2, 3231-3233.

12. A. B. Deshmukh, Vinayak S. Kale, **Vishal M. Dhavale**, Sreekumar Kurungot, Vijayamohanan K. Pillai, Manjusha V. Shelke, "*Direct Transfer of Micro-Molded Electrodes for Enhanced Mass Transport and Water Management in PEMFC"*, ***Electrochemistry Communications***, **2010**, 12, 1638-1641.

13. D. B. Shinde, **Vishal M. Dhavale**, Sreekumar Kurungot, Vijayamohanan K. Pillai, "*Electrochemical preparation of nitrogen-doped graphene quantum dots and their size-dependent electrocatalytic activity for oxygen reduction*", ***Bulletin of Materials Science***, **2015**, 2, 1-8.

14. Mrigendra Dubey, Ashish Kumar, **Vishal M Dhavale**, Sreekumar Kurungot, Daya Shankar Pandey, "*Water Affluent Homochiral MOF: An Efficient Container for Proton Conductance"*, ***Inorganic Chemistry***, Under Revision.

15. **Vishal M. Dhavale**, Santosh Singh, Sreekumar Kurungot, "Fe-Fe_2O_3 Deposited N-doped Graphene as an Activity Modulated Pt-Free Electrocatalyst for Oxygen Reduction Reaction," ***Chemical Communications***, Submitted.

16. Shalini S, **Vishal M. Dhavale**, Sreekumar Kurungot, Vaidhyanathan Ramanathan, "Tuning proton conduction via stoichiometric loading of coordinating proton carriers", ***Journal of Materials Chemistry A***, Submitted.

17. Santosh Singh, **Vishal M. Dhavale**, Sreekumar Kurungot, "*Surface Energy Confined Co_3O_4 Nanoparticles Supported on Nitrogen Doped Graphene: Efficient Oxygen Reduction Electrocatalyst for Mechanical Rechargeable Zinc-Air Battery*", ***ACS Applied Materials and Interfaces***, Submitted.

18. Shyamapada Nandi, **Vishal M. Dhavale**, Sorout Shalini, Ulrike-Werner-Zwanziger, Harpreet Singh, Sreekumar Kurungot, Ramanathan Vaidhyanathan, "*Taking notes from MOF: Lithium assisted proton conduction at 150 °C in a microporous triazine-phenol polymer*", ***Journal of the American Chemical Society***, Submitted.

Erratum